HOKKAIDO UNIVERSITY

Title	A Study on the Excited Triplet States of Octahedral Hexamolybdenum(II) Clusters
Author(s)	,
Citation	. ( ) 13663
Issue Date	2019-03-25
DOI	10.14943/doctoral.k13663
Doc URL	http://hdl.handle.net/2115/77004
Type	theses (doctoral)
File Information	Soichiro_Akagi.pdf

Instructions for use

A Study on the Excited Triplet States of Octahedral Hexamolybdenum(II) Clusters

Soichiro Akagi

Graduate School of Chemical Sciences and Engineering,
Department of Chemical Sciences and Engineering,
HOKKAIDO UNIVERSITY (2019)

Chapter 1. General Introduction

Chapter 2. Experiments and Methodologies

Chapter 3. Redox, Spectroscopic, and Photophysical Properties of $[\{Mo_6X_8\}Y_6]^{2-}$ (X, Y = Cl, Br, or I)

Chapter 4. Redox, Spectroscopic, and Photophysical Properties of $[\{Mo_6X_8\}(RCOO)_6]^{2-}$
(X = Br or I, RCOO = Carboxylate)

Chapter 1

General Introduction

1–1. Phosphorescent Transition Metal Complex

Human beings have been attracted by light and relevant colors over the centuries, and the human society now a day is surrounded and highlighted by a variety of colors. During the past a few decades, light is not only the accessories of our daily lives but also has become to play important roles in industries as sustainable and clean energy resources in future. Scientists have devoted their efforts to convert a light energy to an electrical energy alternatively based on chemistry.[1–5] Indeed, solar cells and optoelectronic devices are developing rapidly and become small and high-performances during the past twenty years. Among various compounds, a hybrid compound composed of a transition metal ion and an organic compound(s) called ligand, transition metal complex, is interested very much as a material for light-energy conversion. As the most interesting feature of a transition metal complex, the d-orbital energy level of a metal ion can be controlled arbitrarily by nature of a ligand(s). Since the energy gap between the d orbital and the d*/π* orbital characterizes primarily various properties of a transition metal complex such as luminescence and magnetism, an appropriate combination of a metal ion with a ligand(s) enables fine tuning of various chemical and physical properties. As representative examples are shown in Figure 1-1, the emission color of an iridium(III) complex can be tuned from blue to red by an appropriate choice of the ligands, reflecting the difference in the electronic structures or energy level of the ligands.[6–8] Besides iridium(III) complexes,[6–12] since ruthenium(II),[13–16] rhenium(II),[17–20] platinum(II),[21–25] copper(I),[26–28] silver(I),[29–33] and gold(I)[34,35] complexes show relatively intense luminescence in the visible region, the fundamental luminescence properties of these complexes and their applications to solar cells or optoelectronic devices have been actively investigated by many scientists.

Luminescence is the radiative process from the electronically excited state of a molecule to the ground state and classified into fluorescence and phosphorescence by the spin multiplicity of the excited state as shown in Figure 1-2. Light excitation of the lowest-energy ground singlet state (S_0) of a molecule can convert to the
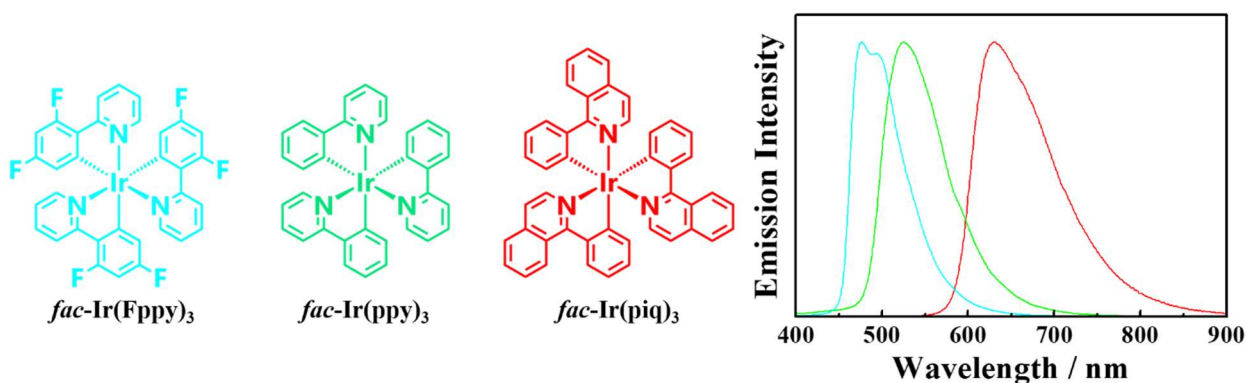
Figure 1-1. Structures and emission spectra of representative cyclometalated Ir(III) complexes. Fppy, ppy, or piq represents 2-(2,4-difluorophenyl)pyridine, 2-phenylpyridine, or 1-phenylisoquinoline, respectively. The colors of the structure and the emission spectra correspond to the emission colors. The complexes are synthesized according to refs. 6–8, and the emission data are recorded on the instruments described in §2-4.

higher-energy excited singlet states (S_n: $n > 1$) and, subsequently, the excited molecule experiences the thermal energy relaxation from the S_n states to the lowest-energy excited singlet state (S_1), which is known as internal conversion (IC). The radiative process from the S_1 state to the S_0 state is called fluorescence and the most of aromatic compounds show fluorescence. In the case of a transition metal complex, the S_n state undergoes easily spin inversion (i.e., intersystem crossing: ISC) and this produces the corresponding excited triplet state (T_n: $n > 1$). The T_n states relax energetically to the lowest-energy excited triplet state (T_1). The electronic transition from the T_1 state to the S_0 state often accompanies luminescence called phosphorescence. In the case of an ordinary organic molecule, although the energy level of the S_1 state is higher than that of the T_1 state, the electronic transition from the S_1 state to the T_1 state does not proceed owing to the spin selection rule. However, since a transition metal complex experiences an internal magnetic field due to relatively strong spin-orbit coupling (SOC) by the presence of a heavy atom, the spin selection rule is broken partly. Furthermore, the IC and ISC processes of a molecule proceed in a femto- to pico-second time scale, while the fluorescence process is in a nano-second time scale. In the case of $[Ru(bpy)_3]^{2+}$ (bpy = 4,4'-bipyridine) in water, for example, the S_n state undergoes IC to the S_1 state in ~20 ps and, subsequently, the S_1 state is converted to the T_1 state through ISC in ~15 fs.[36,37] Therefore, the electronic transition between different spin-multiplicity excited states of a transition metal complex is partially allowed and such a transition metal complex shows phosphorescence alone. There are three spin-sublevels in the T_1 state, while these levels are degenerated in energy for an ordinary molecule
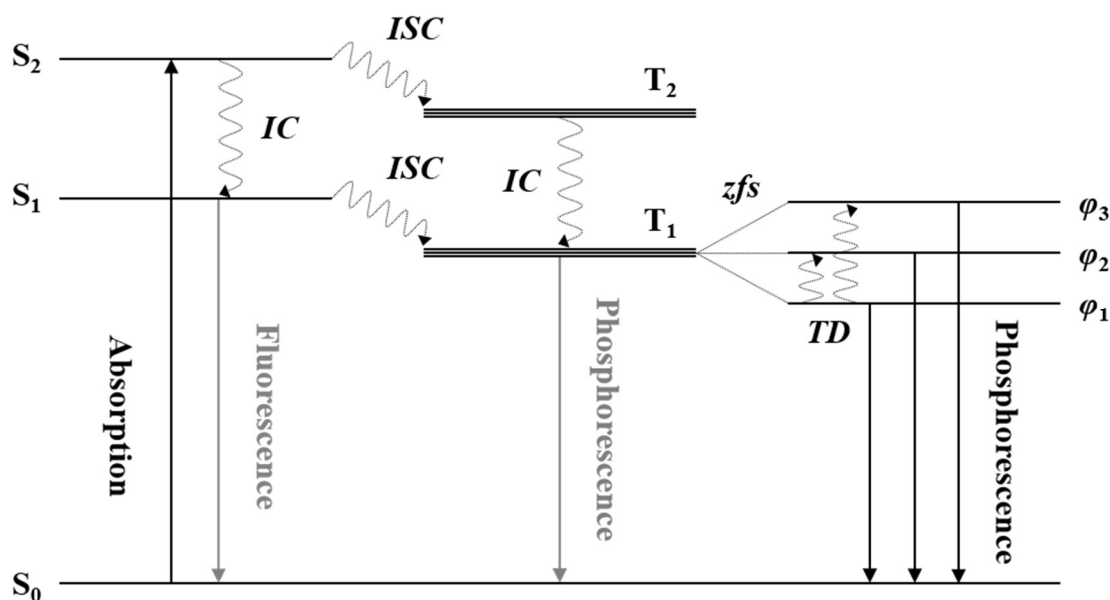
Figure 1-2. Schematic illustration of the emission mechanism of a molecule. The processes related closely to those of an ordinary transition metal complex are shown by the black lines. IC, ISC, TD, or zfs is the abbreviation of internal conversion, intersystem crossing, thermal deactivation, or zero-magnetic-filed splitting, respectively. S_n, T_n, and φ_n represents nth singlet, triplet state, and spin-sublevels in the T_1 state, respectively.

and, therefore, the T_1 state is regarded as one level. In the case of a transition metal complex having a heavy atom element, however, the degenerated T_1 state splits into the spin sublevels owing to large SOC, where the energy splitting between the spin-sublevels is called zero-magnetic-field splitting.

1–2. Zero-Magnetic-Field Splitting
1-2-1. Fundamental Theory of zfs

According to the second-order perturbation theory, zfs in the T_1 state of a molecule is responsible for both spin-spin and spin-orbit coupling as given by eq. 1-1,[38]

$$H = H_{ee} + H_{SO} \qquad (1\text{-}1)$$

where H_{ee} and H_{SO} are the Hamiltonians of spin-spin and spin-orbit coupling, respectively. It has been reported that the magnetic field generated by spin-spin coupling is quite small and the zfs energy by spin-spin coupling alone does not exceed 0.1 cm^{-1}, though spin-spin coupling certainly plays a role in zfs of a molecule.[39] In the case of an ordinary organic compound without a heavy atom element, spin-spin coupling is the dominant factor determining the zfs energy of the molecule. For example, the zfs energy of the T_1 state of benzene is reported to be 0.02 cm^{-1}.[40] In the case of a transition metal complex with a heavy atom element(s), on the other hand, since spin-orbit coupling is significantly strong compared to spin-spin coupling and the contribution of spin-spin coupling to the zfs energy is negligibly small, spin-orbit coupling plays a decisive role in determining the zfs energy of a transition metal complex.[39]

In the case of a transition metal complex, since the characteristics of the spin-sublevels (i.e., notation of the state) split energetically by zfs in the T_1 state are determined by the space group of the T_1 state, one should consider the assignment of the T_1 state. Electron repulsion between the two electrons in the highest-occupied molecular orbital (HOMO) and the lowest-energy unoccupied MO (LUMO) of a molecule results in several excited triplet states (T_n), in which the electron configurations of HOMO and LUMO determine the symmetry and multiplicity of each T_n. In the case of a d^6 metal atom, as an example, there are several possible configurations such as (e_g: HOMO, t_{1u}: LUMO), (t_{2g}: HOMO, t_{1u}: LUMO), (t_{2u}: HOMO, t_{1u}: LUMO), and so forth, and the T_n states provided by these configurations are (T_{2u}, T_{1u}), (T_{2u}, T_{1u}, E_u, A_{2u}), (T_{2g}, T_{1g}, E_g, A_{2g}), and so forth, respectively.[41]

In spin-orbit coupling (SOC), a spin-angular momentum change upon spin inversion (i.e., ISC as an example) is compensated by an orbital-angular momentum change. The Hamiltonian of SOC is given by eq. 1-2,[42]

$$H_{SO} = \sum_i \zeta(r_i) s_i \cdot l_i \qquad (1\text{-}2)$$

where $\zeta(r_i)$ is a spin-orbit coupling parameter and, s_i and l_i are the spin- and orbital-angular momentum operators for an electron i, respectively. In the case of a transition metal complex, the nucleus of a metal ion (core) and its

valence electrons play a role in determining the orbital- and spin angular momenta, respectively. As predicted from eq. 1-2, the multiplicity of each spin-sublevel in the T_1 state is therefore determined as the product of the matrix elements of the core and valence electrons for a given molecular symmetry.[43] In the case of $[Ru(bpy)_3]^{2+}$, as an example, since the T_1 state is assigned to T_{2g} and possesses D_3 symmetry, the T_1 state splits into the three spin-sublevels assigned to A_1 (φ_1), E (φ_2), and A_2 (φ_3).[43]

1-2-2. Experimental Evaluation of zfs Energy

Three experimental methods are known to observe and determine the zfs energy in the T_1 state of a molecule: electron-paramagnetic resonance (EPR) and high-resolution emission spectroscopy as direct observation methods and the analysis of temperature (T)-dependent phosphorescence as an indirect method. Although one cannot determine the zfs energies in the T_1 states of all compounds by the one method, these three experimental methods cover complementary to evaluate the zfs energies in the T_1 states of various compounds.

EPR spectroscopy is the method to observe microwave absorption of an unpaired electron system and used to detect and characterize organic radicals or metal ions, while the method also allows to determine the zfs energy in the T_1 state of a molecule. Upon microwave irradiation, the unpaired electron in the lower-energy state is excited to the higher-energy state, whose energy of the absorbed microwave corresponds to the energy gap between the two states. In the case of the T_1 state of a molecule, one can evaluate the energy gap between the spin-sublevels by observing microwave absorption between the spin-sublevels (see Figure 1-3 for the schematic illustration). Since EPR is spectroscopy for an unpaired electron system, this is a powerful tool to
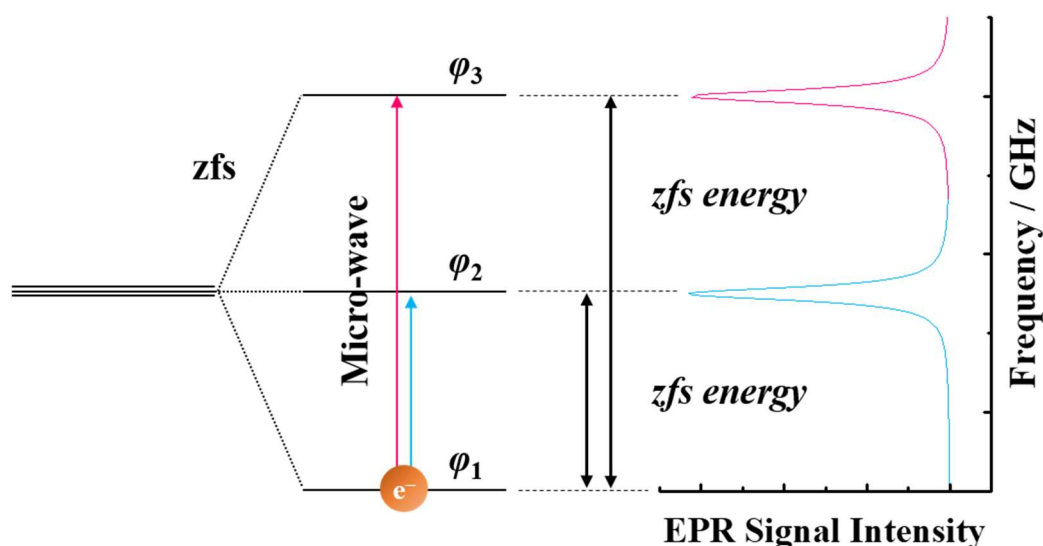
Figure 1-3. Schematic illustration of EPR spectroscopy to determine the zfs energies in the T_1 state of a molecule. The left and right panels represent the energy diagram of the T_1 state and the EPR spectrum. The energy difference between the EPR signals represented by blue and red curves corresponds to that between φ_2 and φ_3.

determine the zfs energy of a molecule possessing an open-shell electron structure such as a paramagnetic ion, organic radical in the ground doublet state (D_0), and a phosphorescence molecule in the T_1 state. Furthermore, different from the other methods described later, an EPR method does not require any special experimental conditions such as extremely low temperature. However, the method can be adopted only for a molecule whose energy splitting between the levels is less than 1 cm^{-1} owing to relatively low-energy nature of a microwave (i.e., microwave frequency is up to 300 GHz = 1 cm^{-1}).

Since the emission transition from each spin-sublevel in the T_1 state of a molecule proceeds to the corresponding S_0 state, the higher-energy spin-sublevel (φ_n) shows the higher-energy emission reflecting the zfs energy between φ_n. Furthermore, φ_n levels are under thermal equilibria and the contribution of the higher-energy spin-sublevel to the observed emission becomes large upon temperature (T)-elevation. It is important to note that each spin-sublevel possesses an inherent emission maximum energy ($\tilde{v}_n$) and the observed emission is the superposition of the φ_n emissions. High-resolution emission spectroscopy is the method to determine the zfs energies in the T_1 state of a molecule directly from the observed emission spectrum at a given T (see Figure 1-4 for the schematic illustration).[44] The direct determination of the zfs energies based on an emission spectrum is in general impossible, since an emission energy is distributed thermally to several vibrational levels in the S_0 state in the range of a few hundreds to a few thousands cm^{-1} (i.e., full-width-at-half-maximum: *fwhm*), while the zfs energies are in general below a few tens of wavenumber. As an example, the *fwhm* value of the emission spectrum of Pt(thpy)$_2$ (thpy = 2-(2-thienyl)pyridine) in *n*-butyronitrile at 1.3 K is around 400 cm^{-1}, while the zfs
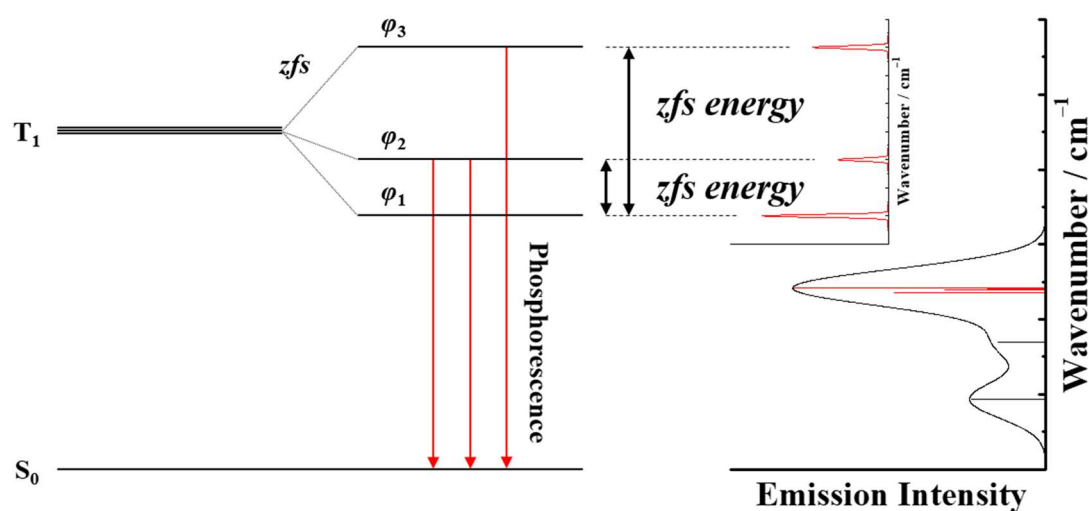
Figure 1-4. Schematic illustration of high-resolution emission spectroscopy to determine the zfs energies in the T_1 state of a molecule. The left and right panels show the energy diagram of the triplet state and the high-resolution/usual emission spectra at an extremely low temperature, respectively. The red curves in the right panel represent the high-resolution emission spectrum corresponding to the emission from the spin-sublevels. The enlarged emission spectrum is also shown in the right panel.

energy in the T_1 state of the complex is 4.3 cm^{-1}. In the case of high-resolution emission spectroscopy, a special technique is employed to decrease the *fwhm* value of an emission spectrum and, thus, a targeted molecule is dissolved or dispersed homogeneously in an *n*-alkane matrix called Shpol'skii matrix. It has been reported that a planar aromatic compound dissolved in an *n*-alkane matrix at extremely low temperature shows a very sharp emission spectrum (i.e., *fwhm* = 1–5 cm^{-1}).[45] The very sharp emission spectrum mentioned above is due to highly suppressed molecular vibrations in a non-polar solvent at low temperature. The interaction between the surroundings and a sample molecule can assist to arrange to a specific molecular vibration, while many vibrational modes in the S_0 state of the molecule in a polar matrix would participate for the emission transition and, thus the *fwhm* value would be large.[45] The effects of a Shpol'skii matrix on a emission spectrum have been confirmed for various platinum(II) complexes.[44] For example, although the *fwhm* value of the emission spectrum of Pt(thpy)$_2$ at 1.3 K in *n*-butyronitrile is around 400 cm^{-1}, that in *n*-octane decreases to 2–3 cm^{-1}. Since an ordinary transition metal complex shows a zfs energy in a few tens cm^{-1}, high-resolution vibrational spectroscopy is quite powerful to determine the zfs energies of a transition metal complex. However, this method can be adopted only for the luminescent molecules with a small dipole moment in the T_1 state.

The emission transition probabilities from the spin-sublevels in the T_1 state to the S_0 state are sensitive to the multiplicities of the spin-sublevels and this is reflected on the radiative rate constants of the spin-sublevels (k_r^n). Since the emission lifetime (τ_n) and emission quantum yield (Φ_n) of each spin-sublevel depend on k_r^n, these parameters are inherent to the spin-sublevels. Furthermore, the contributions of the spin-sublevels to the spectroscopic and photophysical parameters of a compound are determined by the thermal Boltzmann distributions at a given T and, therefore, the observed emission characteristics at a given T are the Boltzmann distribution- and multiplicity-weighted sum of the φ_n emissions, resulting in the T-dependences of the emission characteristics: spin-sublevel (φ_n) model, see Figure 1-5 for schematic illustration.[41,43,46–49] At an extremely low temperature, it is important to note that the spin-sublevels in the T_1 state are not thermally equilibrated and each φ_n emission is observed individually, resulting in multi-exponential emission decay profiles, called spin alignment. In the case of a transition metal complex, although ISC from the S_1 state proceeds to each spin-sublevel, spin-lattice relaxation from the higher-energy φ_n to the lower-energy φ_n takes place much faster than the phosphorescence lifetime of each φ_n and, therefore, the population of each spin-sublevel at a given T follows thermal Boltzmann distributions. At an extremely low temperature, spin-lattice relaxation between φ_n becomes slower than the phosphorescence process of each φ_n, leading to the observation of individual φ_n emissions.[50]

According to the φ_n model, the T-dependence of the emission lifetime ($\tau(T)$) is given by eq. 1-3,

$$\tau(T) = \frac{\sum g_n \exp\left(\dfrac{-\Delta E_{1n}}{k_B T}\right)}{\sum \dfrac{g_n}{\tau_n} \exp\left(\dfrac{-\Delta E_{1n}}{k_B T}\right)}$$

(1-3)

where g_n, τ_n and k_B are the multiplicity, the emission lifetime of each φ_n and the Boltzmann constant, respectively, and ΔE_{1n} is the energy separation between φ_1 and φ_n. The analysis of the $\tau(T)$ data by eq. 1-1 can provide the emission parameters inherent to each spin-sublevel and the zfs energies, ΔE_{1n}. As an example, the T-dependent emission lifetime (τ_n) and emission quantum yield (Φ_n) of the T$_1$ state of [Ru(bpy)$_3$]$^{2+}$ evaluated by the φ_n model are shown in Figure 1-6 together with the energy diagram of the T$_1$ state of the complex.[48] As seen in the figure, the observed emission lifetime decreases upon T-elevation, while the emission quantum yield increases with an
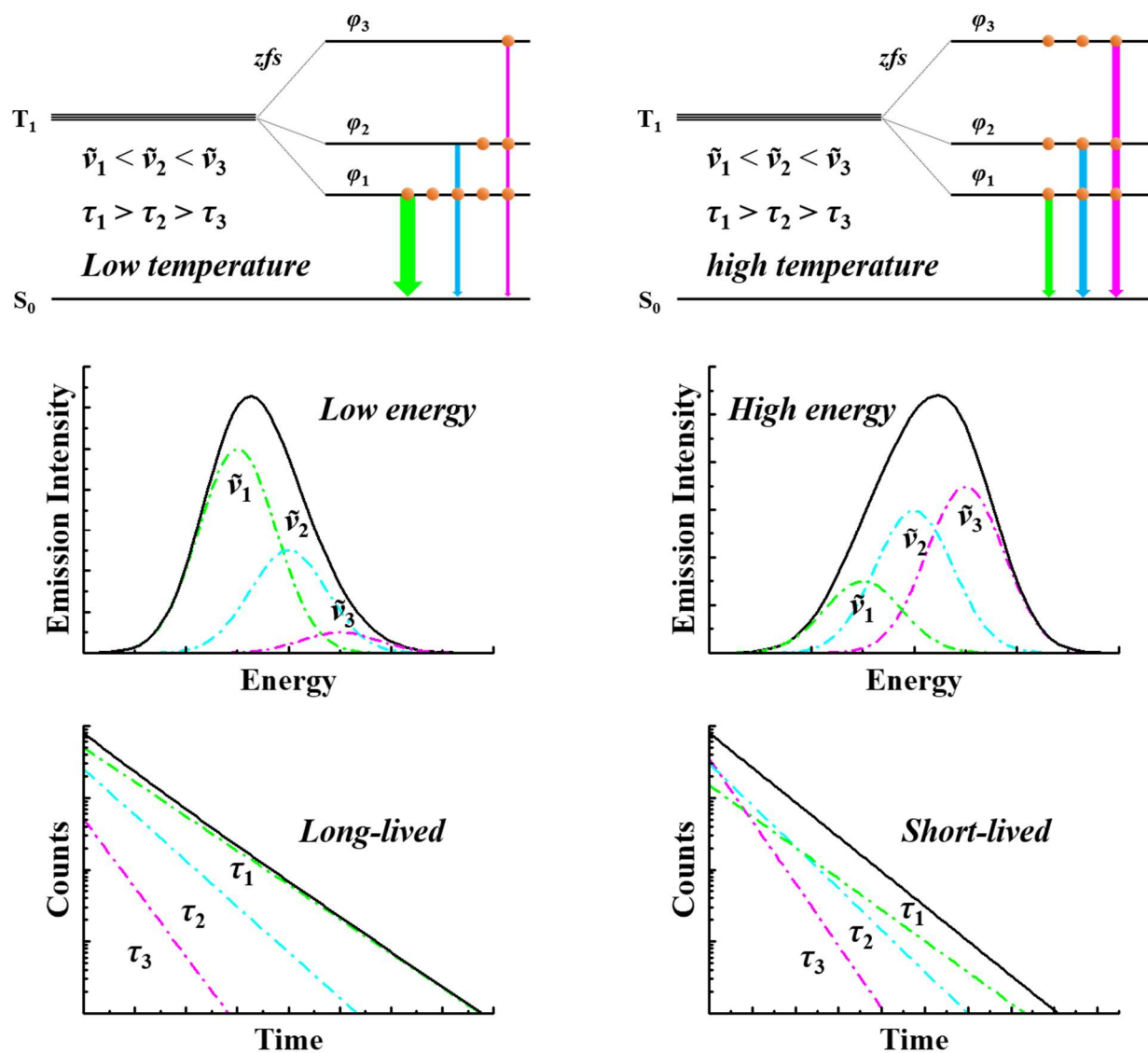
Figure 1-5. Schematic illustration of the spin-sublevel model and emission at a given temperature (left: low temperature, right: high temperature). The upper, middle, and lower panels represent the energy diagram of the spin-sublevels, the emission spectra and emission decay profiles of the spin-sublevels at a given temperature, respectively. The orange circles in the upper panels represent the thermal Boltzmann population of the spin-sublevel. The black and colored spectra or emission decay profiles in the middle or lower panels, respectively, are the observed emission spectra or decay profiles from the T$_1$ states and those from the spin-sublevels, respectively.
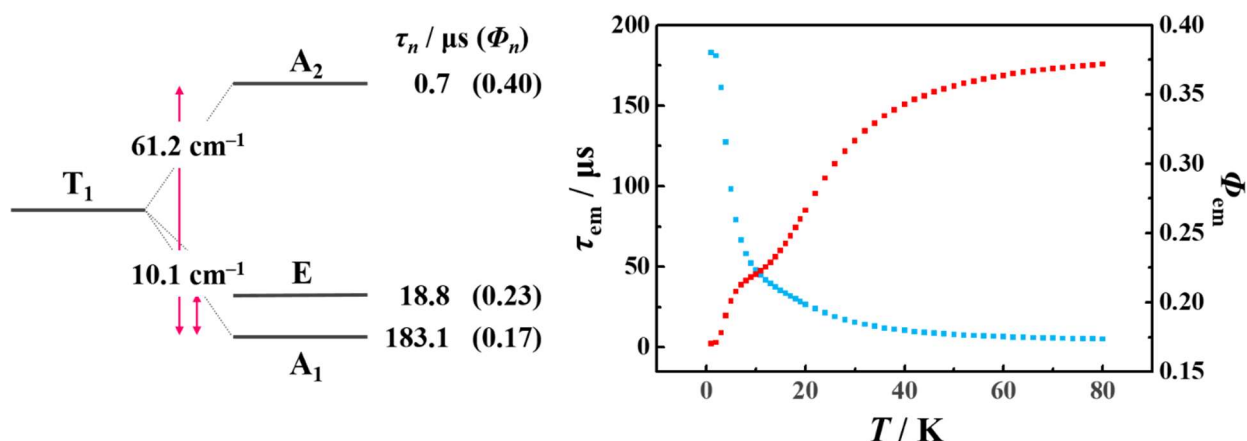
Figure 1-6. Energy diagram (right panel) and *T*-dependent emission lifetime (blue) and emission quantum yield (red) of $[Ru(bpy)_3](PF_6)$. The data were reproduced from ref. 48.

increase in temperature. Furthermore, the analysis of the *T*-dependent emission data can provide ΔE_{1n}, τ_n, and Φ_n of $[Ru(bpy)_3]^{2+}$ to be $(\Delta E_{13}, \Delta E_{12}) = (61.2, 10.1)$ cm^{-1}, $(\tau_3, \tau_2, \tau_1) = (0.68, 18.8, 183.1)$ µs, and $(\Phi_3, \Phi_2, \Phi_1) = (0.40, 0.23, 0.17)$.[48] The analysis of $\tau(T)$ data based on the φ_n model and eq. 1-3 is thus quite useful to reveal the emission properties of each spin-sublevel in the T_1 state of a compound. However, since this method relies on thermal distributions between φ_n, it is impossible to determine a small zfs energy below 3 cm^{-1}. Judging from the Boltzmann factor ($k_B T$) at 4 K (i.e., liquified He temperature) to be 2.78 cm^{-1}, the zfs energy in the T_1 state smaller than 2.78 cm^{-1} cannot be determined since the populations of the spin-sublevels are thermally equilibrated above 4 K.

1-2-3. zfs in the Excited Triplet States of Transition Metal Complexes

Among various transition metal complexes, zfs in the T_1 states of octahedral-coordinated d^6 metal complexes (Ru(II), Os(II), Rh(III), Ir(III), and Re(V)) and planer-coordinated d^8 metal complexes (Pd(II) and Pt(II)) have been investigated based on high-resolution spectroscopy or analysis of *T*-dependent emission characteristics.[43,48–69] The zfs energies reported for the T_1 states of these complexes are as follows: Ru(II) = 30–64,[43,48,49] Os(II) = 64–221,[51,52] Rh(III) = 0.12,[53] Ir(II) = 23–170,[54–59] Re(V) = ~2,[60] Pd(II) = ~0.01,[61] and Pt(II) = ~0.01–47 cm^{-1}.[62–69] These data indicate that the complex with a heavier metal ion shows a larger zfs energy. For a given metal ion, furthermore, the electronic structures of a ligand(s) also influence largely the zfs energy. Among these metal complexes, zfs in the T_1 states of platinum(II) complexes has been studied very widely and Yersin et al. have reported that the larger is the zfs energy, the shorter is the observed emission lifetime at ambient temperature as shown in Figure 1-7.[69] Since it is generally known that the emission lifetime of a transition metal complex decreases in the sequence $^3\pi\pi^*$ (i.e., ligand center (LC) or intraligand charge transfer (ILCT)) > ^{3}MLCT (metal-to-ligand charge transfer) excited states, it has been demonstrated that the zfs energy in the T_1 state of a transition metal complex increases in the sequence $^3\pi\pi^*$ < admixture of $^3\pi\pi^*$ and
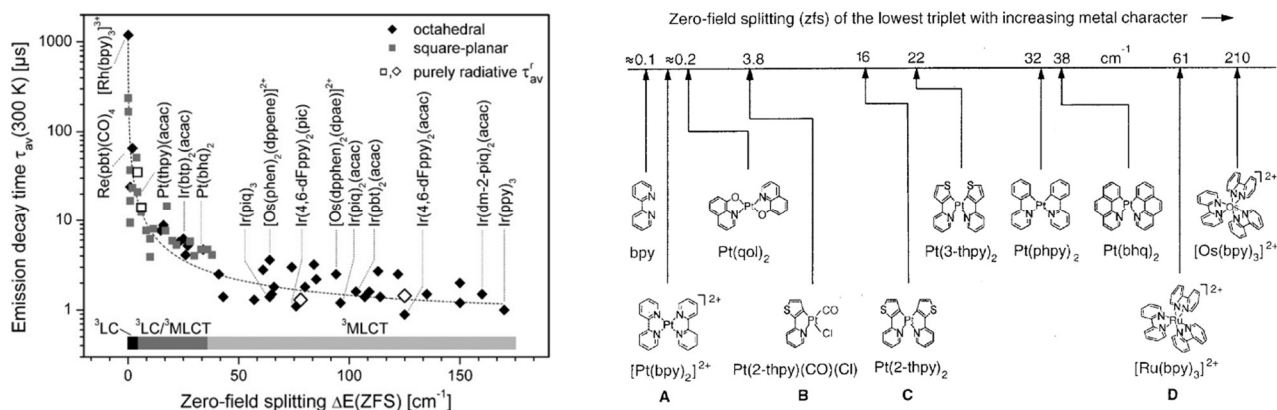
Figure 1-7. Relationship between the zfs energy and emission lifetime (left panel) or metal character (right panel) in the T_1 state of a transition metal complex. The graphs are taken from refs. 69 and 70.

^{3}MLCT < ^{3}MLCT excited states. These data indicate that the d-electron character in the T_1 state plays an important role in determining the zfs energy of a transition metal complex as shown in Figure 1-7.[69] These findings are very important to discuss further the relationships between the zfs energy and the emission characteristics in the T_1 state of a transition metal complex.

1–3. Octahedral Hexanuclear Metal Clusters

The zfs energy in the T_1 state of an ordinary transition metal complex is small compared to the k_BT value at ambient temperature and, therefore, zfs in the T_1 state hardly influences the emission characteristics at ambient temperature, while those at low temperature are sensitive to zfs in the T_1 state. Among various transition metal complexes, it has been reported that an octahedral hexamolybdenum(II) cluster, $[\{Mo_6Cl_8\}Cl_6]^{2-}$, shows very large T-dependent emission characteristics and the zfs energy in the T_1 state of the complex is as large as ~650 cm^{-1}, which is much larger than those of other transition metal complexes.[41,46,47] These characteristic zfs energy and T-dependent emission of $[\{Mo_6Cl_8\}Cl_6]^{2-}$ demonstrate clearly that the emission characteristics of a hexamolybdenum(II) cluster would be determined primarily by zfs in the T_1 state.

The structure of an octahedral hexanuclear metal cluster with the general formula of $[\{Mo_6(\mu_3\text{-}X_8)\}L_6]^{n-}$ (X = halide, L = inorganic and organic ligand) is shown in Figure 1-8. An octahedral hexamolybdenum(II) cluster ($[\{Mo_6X_8\}L_6]^{n-}$) has six molybdenum(II) ions and eight bridging ligands (X: Cl, Br, or I), which compose of the cluster core $\{Mo_6X_8\}^{4+}$, and six terminal ligands (L) extend to the outer-ward of the molybdenum(II) octahedron. Besides hexanuclear molybdenum(II) clusters, low-oxidized d^4 metal ions, tungsten(II) and rhenium(III), also produce octahedral hexanuclear metal clusters.[71,72] Although high-temperature reaction conditions are necessary to prepare an $\{M_6E_8\}^{4+}$ unit, various terminal ligands can be introduced easily to an $\{M_6(\mu_3\text{-}E_8)\}^{4+}$ (M = d^4 metal ion, E = bridging ligand) core. Since the metal ions and the bridging ligands are connected strongly with each other forming an $\{M_6E_8\}^{4+}$ unit, the cluster shows in general high-photochemical,
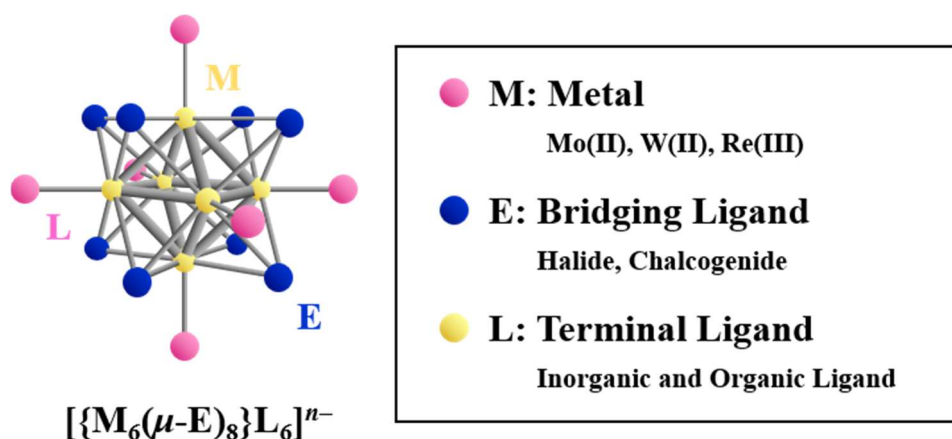
Figure 1-8. Structure of an octahedral hexamolybdenum(II) cluster.

-thermal, and -chemical stabilities.[73] Furthermore, it has been known that a series of the octahedral hexanuclear metal clusters in both solution and crystalline phases show long-lived emission in the visible-near infrared region at ambient temperature. As examples, the emission maximum wavelength (λ_{em}), emission lifetime (τ_{em}), and emission quantum yield (Φ_{em}) of $[\{Mo_6Cl_8\}Cl_6]^{2-}$, $[\{W_6Cl_8\}Cl_6]^{2-}$, or $[\{Re_6S_8\}Cl_6]^{2-}$ in CH_3CN at 298 K are as follows: λ_{em} (Mo(II), W(II), or Re(III), respectively) = 805, 833, or 770 nm, τ_{em} = 180, 1.5, or 6.3 μs, and Φ_{em} = 0.19, 0.017, or 0.039.[74–76] Besides the high stability and long-lived red phosphorescence, since molybdenum has advantages in terms of element strategy compared to rare metals, a variety of octahedral hexamolybdenu(II) clusters have been hitherto synthesized as possible candidates for photofunctional materials.[77–106] Furthermore, hexamolybdenum(II) clusters have been also studied widely in the research fields of bio-imaging, X-ray sensitizers, optoelectronic devices, and so forth, owing to the relatively long-lived and intense red emission compared to the emissions from hexatungsten(II) and hexarhenium(III) clusters as shown in Figure 1-9.[107–111] However, since a family of an octahedral hexanuclear metal cluster is less emissive than other transition metal complexes represented by cyclometalated iridium(III) and polypyridine ruthenium(II) complexes, the emission properties of an octahedral hexanuclear metal cluster should be improved toward the utilization of the clusters as photofunctional materials. The emission characteristics of an octahedral hexanuclear metal cluster would be governed by zfs in the T_1 state as described above and, therefore, it is necessary to obtain detailed information on the factors governing zfs in the T_1 state to improve the emission properties of an octahedral hexanuclear metal cluster.

1–4.   Purpose and Outline of the Thesis

Zero-magnetic-field splitting (zfs) in the T_1 state of a transition metal complex is responsible for spin-orbit coupling (SOC) as described in §1-2-1 and the strength of SOC in the T_1 state is dependent of nature of constituting atoms of a molecule. Furthermore, it has been suggested that the emission characteristics of a
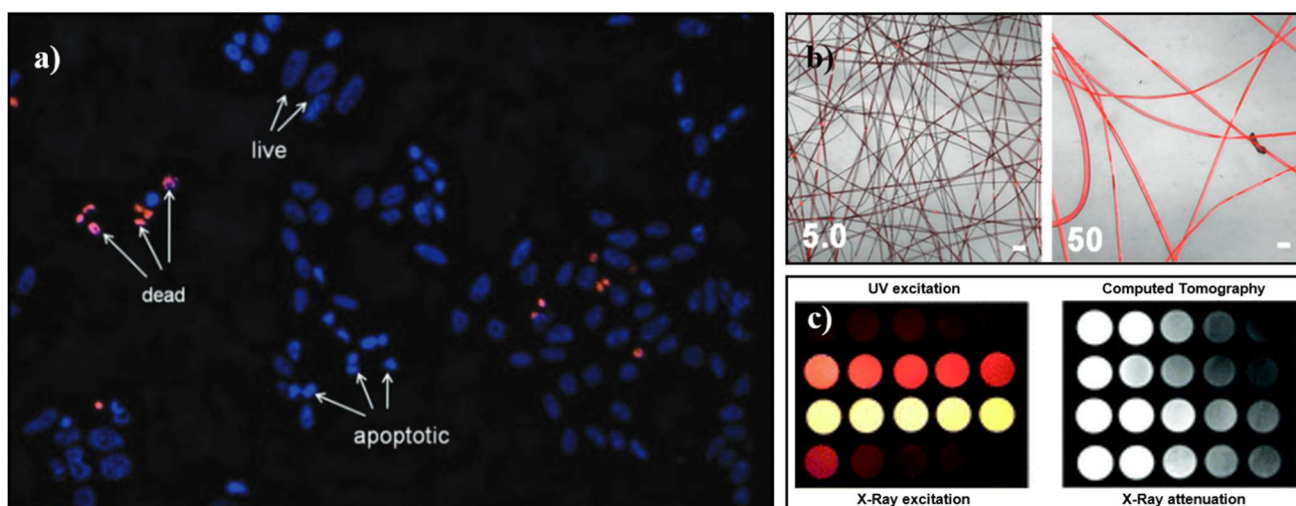
Figure 1-9. Applications of octahedral hexamolybdenum(II) clusters. a, b, and c show applications of the clusters to bioimaging, an optoelectronic material, and a radiosensitizer, respectively. The figures a, b, and, c are taken from ref. 107, 108, and 109, respectively.

transition metal complex are related to the relevant zfs energy (§1-2-2), although a quantitative discussion on such a relationship has not been hitherto reported. These results suggest a possibility of controlling the emission properties of a transition metal complex through the relevant zfs energy in the T_1 state and, therefore, nature of the constituting atoms of the complex. In order to pursue such a study, an octahedral hexamolybdenum(II) cluster, $[\{Mo_6X_8\}L_6]^{2-}$ (X = Cl (atomic number (Z) = 17), Br (35), or I (53)), is an ideal molecular system, since the clusters show intense and long-lived emission in both solution and crystalline phases. Furthermore, one can introduce a series of terminal ligands (L = X (Cl, Br, or I), aliphatic and aromatic carboxylates, aromatic sulfonates, and so forth in $[\{Mo_6X_8\}L_6]^{2-}$), suggesting a possibility of synthetic tuning of the strength of SOC and, thus, zfs in the T_1 state of the cluster.

The main purpose of the present study is the elucidation of the factors governing zfs in the T_1 states of hexamolybdenum(II) clusters by systematic investigations on the *T*-dependent emission characteristics of the clusters and the relevant zfs parameters in the T_1 states. On the basis of the emission parameters inherent to the spin-sublevels in the T_1 state, furthermore, the photophysical properties of a series of octahedral hexamolybdenum(II) clusters are discussed. The factors governing zfs in the T_1 states of hexamolybdenum(II) clusters are also checked for zfs in the T_1 states of ordinary transition metal complexes, platinum(II) complexes.

The thesis is composed of six chapters. In Chapter 1, the research background and purpose of the thesis are described. As the key aspects into the present study, furthermore, the emission mechanisms and the theoretical background of zfs in the T_1 state of a transition metal complex are discussed. The chapter also describes possible experimental approaches to determine the zfs energy in the T_1 state of a transition metal complex. The structural and emission characteristics of the targeted complexes in the research, octahedral hexamolybdenum(II) clusters, are introduced.

Chapter 2 describes the synthetic procedures of the octahedral hexamolybdenum(II) clusters and cyclometalated platinum(II) complexes. The details of the physical measurements, the four spin-sublevel (Φ_n) model for the *T*-dependent emission characteristics of an octahedral hexamolybdenum(II) cluster, and computational chemistry are also described.

Chapter 3 describes the electrochemical, spectroscopic, and photophysical properties of the nine terminal halide clusters, $[\{Mo_6X_8\}Y_6]^{2-}$ (X, Y = Cl, Br, or I), in solution or crystalline phases at 298 K, and the results are discussed in terms of the bridging and terminal ligand effects on the properties. The *T*-dependent emission characteristics of the nine clusters in 3 K < *T* < 300 K and their analysis by the Φ_n model are described in detail. As a very important finding of the present study, the emission characteristics of the clusters at 298 K have been shown to be governed by zfs in the T_1 states.

Chapter 4 describes the X-ray structural, electrochemical, and photophysical properties of the terminal carboxylate clusters, $[\{Mo_6X_8\}(RCOO)_6]^{2-}$ (X, Y = Cl, Br, or I), in solution or crystalline phases at 298 K. As an important finding, it has been demonstrated that the bond length between the Mo atom and the ligating O atom in the carboxylate, the redox potentials, and the emission characteristics (emission energy, emission lifetime, and emission quantum yield) of the clusters are shown to be controlled synthetically by the electron-donating ability of the terminal carboxylate ligand, irrespective of nature of the bridging ligand, X = Br or I. Furthermore, the analysis of the *T*-dependent emission characteristics of the clusters by the Φ_n model has revealed that the emission maximum energy of the cluster is governed by the relevant zfs energies in the T_1 state and it has been shown that this explains very well the terminal ligand dependences of the photophysical properties.

In Chapter 5, the factors governing the zfs energies of the octahedral hexamolybdenum(II) clusters are discussed in detail based on the analytical results of the *T*-dependent emission characteristics of the clusters by the spin-sublevel model described in Chapters 3 and 4. Quite importantly, the present study has found for the first time that the zfs energies correlate very well with the ^{95}Mo NMR chemical shift of $[\{Mo_6X_8\}Y_6]^{2-}$ (X = Y = Cl, Br, or I) or the acid dissociation constant of the carboxylic acid in $[\{Mo_6Br_8\}L_6]^{2-}$ (L = carboxylate), indicating the importance of the effective nuclear charge on the Mo atom(s) in determining the zfs energies of the octahedral hexamolybdenum(II) cluster. Furthermore, it has been demonstrated that the effective nuclear charge on the Mo atom(s) also governs the photophysical properties of the cluster. As the most interesting point, the zfs energies and the photophysical properties of the platinum(II) complexes are also explained by the similar context to those of the hexamolybdenum(II) clusters mentioned above as revealed by both the experimental and computational results. Thus, the thesis has demonstrated that the zfs energies and phosphorescence properties of a luminescence transition metal complex could be controlled synthetically by the effective nuclear charge on the metal atom(s).

Chapter 6 describes the principal conclusions and future perspective of the present study.

1–5.   References

(1)   Hagfeldt, A.; Boschloo, G.; Sun, L.; Kloo, L.; Pettersson, H. Dye-sensitized Solar Cell. *Chem. Rev.* **2010**, *110*, 6595–6663.

(2)   Carey, G. H.; Abdelhady, A. L.; Ning, Z.; Thon, S. M.; Bakr, O. M.; Sargent, E. H. Colloidal Quantum Dot Solar Cells. *Chem. Rev.* **2015**, *115*, 12732–12763.

(3)   Ueno, K.; Oshikiri, T.; Sun, Q.; Shi, X.; Misawa, H. Solid-state Plasmonic Solar Cells. *Chem. Rev.* **2018**, *118*, 2955–2933.

(4)   Xu, H.; Chen, R.; Sun. Q.; Lai, W.; Su, Q.; Huang, W.; Liu, X. Recent Progress in Metal-organic Complexes for Optoelectronic Applications. *Chem. Soc. Rev.* **2014**, *43*, 3259–3302.

(5)   Grimsdale, A. C.; Chan, K. L.; Martin, R. E.; Jokisz, P. G.; Holmes, A. B. Synthesis of Light-emitting Conjugated Polymers for Applications in Electroluminescent Devices. *Chem. Rev.* **2009**, *109*, 897–1091.

(6)   Tamayo, A. B.; Alleyne, B. D.; Djurovich, P. I.; Lamansky, S.; Tsyba, I.; Ho, N. N.; Bau, R.; Thompson, M. E. Synthesis and Characterization of Facial and Meridional Tris-cyclometalated Iridium(III) Complexes. *J. Am. Chem. Soc.* **2003**, *125*, 7377–7387.

(7)   King, K. A.; Spellane P. J; Watts, R. J. Excited-state Properties of a Triply Ortho-metalated Iridium(III) Complex. *J. Am. Chem. Soc.* **1985**, *107*, 1431–1432.

(8)   Tsuboyama, A.; Iwawaki, H.; Furugori, M.; Mukaide, T.; Kamatani, J.; Igawa, S.; Moriyama, T.; Miura, S.; Takiguchi, T.; Okada, S.; Hoshino, M.; Ueno, Kazunori. Homoleptic Cyclometalated Iridium Complexes with Highly Efficient Red Phosphorescence and Application to Organic Light-emitting Diode. *J. Am. Chem. Soc.* **2003**, *125*, 12971–12979.

(9)   Lamansky, S.; Djurovich, P; Murphy, D.; Abdel-Razzaq, F.; Kwong, R.; Tsyba, I.; Bortz, M.; Mui, B.; Bau, R.; Thompson, M. E. Synthesis and Characterization of Phosphorescent Cyclometalated Iridium Complexes. *Inorg. Chem.* **2001**, *40*, 1704–1711.

(10)   Zanoni, K. P. S.; Sanematsu, M. S.; Iha, N. Y. M. Photophysical Characterization of [Ir(ppy)$_2$(dmb)][PF$_6$] Towards Application in Light-emitting Electrochemical Cells (LECs). *Inorg. Chem. Commun.* **2014**, *43*, 162–164.

(11)   Baldo, M. A.; Lamansky, S.; Burrows, P. E.; Thompson, M. E.; Forrest, S. R. Very High-Efficiency Green Organic Light-emitting Devices Based on Electrophosphorescence. *Appl. Phys. Lett.* **1999**, *75*, 4–6.

(12)   Adachi, C.; Baldo, M. A.; Thompson, M. E.; Forrest, S. R. Nearly 100% Internal Phosphorescence Efficiency in an Organic Light-emitting Device. *J. Appl. Phys.* **2001**, *90*, 5048–5051.

(13)   Casper, J. V.; Meyer, T. J. Photochemistry of Ru(bpy)$_3{}^{2+}$. Solvent Effects. *J. Am. Chem. Soc.* **1983**, *105*, 5583–5590.

(14)   Nakagawa, A.; Sakuda, E.; Ito, A.; Kitamura, N. Remarkably Intense Emission from Ruthenium(II)

Complexes with Multiple Borane Centers. *Inorg*. *Chem*. **2015**, *54*, 10287–10295.

(15)　Hu, Y.; Maclennan, A.; Sham, T. K.; Electronic Structure and Optical Luminescence Studies of Ru Based OLED Compounds. *J*. *Lumin*. **2015**, *166*, 143–147.

(16)　O'Regan, B.; Grätzel, M. A Low-cost, High-efficiency Solar Cell Based on Dye-sensitized Colloidal TiO_2 Films. *Nature* **1991**, *353*, 737–740.

(17)　Sacksteder, L.; Zipp, A. P.; Brown, E. A.; Streich, J.; Demas, J. N.; DeGraff, B. A. Luminescence Studied of Pyridine α-Diimine Rhenium(I) Tricarbonyl Complexes. *Inorg*. *Chem*. **1990**, *29*, 4335–4340.

(18)　Sato, S.; Matubara, Y.; Koike, K.; Falkenström, M.; Katayama, T.; Ishibashi, Y.; Miyasaka, H.; Taniguchi, S.; Chosrowjan, H.; Mataga, N.; Fukazawa, N.; Koshihara, S.; Onda, K.; Ishitani, O. Photochemistry of *fac*-[Re(bpy)(CO)$_3$Cl]. *Chem*. *Eur*. *J*. **2012**, *18*, 15722–15734.

(19)　Morimoto, T.; Nakajima, T.; Sawa, S.; Nakanishi, R.; Imori, D.; Ishitani, O. CO_2 Capture by Rhenium(I) Complex with the Aid of Triethanolamine. *J*. *Am*. *Chem*. *Soc*. **2013**, *135*, 16825–16828.

(20)　Zhao, G.-W.; Zhao, J.-H.; Hu, Y.-X.; Zhang, D.-Y.; Li, X. Recent Advantages of Neutral Rhenium(I) Tricarbonyl Complexes for Application in Organic Light-emitting Diodes. *Synth*. *Met*. **2016**, *212*, 131–141.

(21)　Maestri, M.; Sandrini, D.; Balzani, V. Luminescence of Ortho-metallated Platinum(II) Complexes. *Chem*. *Phys*. *Lett*. **1985**, *122*, 375–379.

(22)　Brooks, J.; Babayan, Y.; Lamansky, S.; Djirovich, P. I.; Tsyba, I.; Bau, R.; Thompson, M. E. Synthesis and Characterization of Phosphorescent Cyclometalated Platinum Complexes. *Inorg*. *Chem*. **2002**, *41*, 3055–3066.

(23)　Unger, Y.; Meyer, D.; Molt, O.; Schildknecht, C.; Münster, I.; Wagenblast, G.; Strassner, T. *Angew*. *Chem*. *Int*. *Ed*. **2010**, *49*, 10214–10216.

(24)　Che, C.-M.; Kwok, C.-C.; Lai, S.-W.; Rausch, A. F; Finkenzeller, W. J.; Zhu, N.; Yersin, H. Photophysical Properties and OLED Applications of Phosphorescent Platinum(II) Schiff Base Complexes. *Chem*. *Eur*. *J*. **2010**, *16*, 233–247.

(25)　Vezzu, D. A. K.; Deaton, J. C.: Jones, J. S.; Bartolotti, L.; Harris, C. F.; Marchetti, A. P.; Kondakova, M.; Pike, R. D.; Huo, S. Highly Luminescent Tetradentate Bis-cyclometalated Platinum Complexes: Design Synthesis, Structure Photophysics, and Electroluminescence Application. *Inorg*. *Chem*. **2010**, *49*, 5107–5119.

(26)　Ford, P. C.; Cariati, E.; Bourassa, J. Photoluminescence Properties of Multinuclear Copper(I) Compounds. *Chem*. *Rev*. **1999**, *99*, 3625–3647.

(27)　Czerwieniec, R.; Yu, J.; Yersin, H. Blue-light Emission of Cu(I) Complexes and Singlet Harvesting. *Inorg*. *Chem*. **2011**, *50*, 8293–8301.

(28)　Tsuge, K.; Chishina, Y.; Hashiguchi, H.; Sasaki, Y.; Kato, M.; Ishizaka, S.; Kitamura, N. Luminescent

Copper(I) Complexes with Halogenido-bridged Dimeric Core. *Coord. Chem. Rev.* **2016**, *306*, 636–651.

(29)   Henary, M.; Zink, J. I. Luminescence from the Chair and Cube Isomers of Ag$_4$I$_4$(PPh$_3$)$_4$. *Inorg. Chem.* **1991**, *30*, 3111–3112.

(30)   Omary, M. A.; Rawashdeh-Omary, M. A.; Gonser, M. W. A.; Elbjeirami, O.; Grimes, T.; Cundari, T. R.; Diyabalanage, H. V. K.; Gamage, C. S. P.; Dias, H. V. R. Metal Effect on the Supramolecular Structure, Photophysics, and Acid-Base Character of Trinuclear Pyrazolato Coinage Metal Complexes. *Inorg. Chem.* **2005**, *44*, 8200–8210.

(31)   Pucci, D.; Barberio, G.; Bellusci, A.; Crispini, A.; La Deda, M.; Ghedini, M.; Szerb, E. I. Induction of Columnar Mesomorphism in Tetracoordinated Ionic Silver(I) Complexes Based on Chelate 4,4'-Disubstituted 2,2'-Bipyridines. *Eur. J. Inorg. Chem.* **2005**, 2457–2463.

(32)   Lin, Y.-Y.; Lai, S.-W.; Che, C.-M.; Fu, W.-F.; Zhou, Z.-Y.; Zhu, N. Structural Variations and Spectroscopic Properties of Luminescent Mono- and Multinuclear Silver(I) and Copper(I) Complexes Bearing Phosphine and Cyanide Ligands. *Inorg. Chem.* **2005**, *44*, 1511–1524.

(33)   Tong, G. S. M.; Kui, S. C. F.; Chao, H.-Y.; Zhu, N.; Che, C.-M. The $^3[nd\sigma*(n+1)p\sigma]$ Emissions of Linear Silver(I) and Gold(I) Chains with Bridging Phosphine Ligands. *Chem. Eur. J.* **2009**, *15*, 10777–10789.

(34)   Seki, T.; Sakurada, K.; Ito, H. Controlling Mechano- and Seeding-Triggered Single-crystal-to-single-crystal Phase Transition: Molecular Domino with a Disconnection of Aurophilic Bonds. *Angew. Chem. Int. Ed.* **2013**, *52*, 12828–12832.

(35)   Seki, T.; Takamatsu, Y; Ito, H. A Screening Approach for the Discovery of Mechanochromic Gold(I) Isocyanide Complexes with Crystal-to-Crystal Phase Transitions. *J. Am. Chem. Soc.* **2016**, *138*, 6252–6260.

(36)   Cannizzo, A.; van Mourik, F.; Gawelda, W.; Zgrablic, G.; Bressler, C.; Chergui, M. Broadband Femtosecond Fluorescence Spectroscopy of [Ru(bpy)$_3$]$^{2+}$. *Angew. Chem. Int. Ed.* **2006**, *45*, 3174–3176.

(37)   Cooley, L. F.; Bergquist, P.; Kelley, D. F. Determination of Exciton Hopping Rates in Ruthenium(II) Tris(bipyridine) Complexes by Picosecond Polarized Absorption Spectroscopy. *J. Am. Chem. Soc.* **1990**, *112*, 2612–2617.

(38)   Griffith, J. S. *The Theory of Transition Metal Ions*; Cambridge University Press: Cambridge, **1964**.

(39)   Harriman, J. E.; *Theoretical Foundations of Electron Spin Resonance*; Academic Press: New York, **1978**.

(40)   Vergragt, P. J.; van der Waals, J. H. Distortion of the triplet State of Benzene in a Borazole Host. A Study by Microwave Induced Delayed Phosphorescence at 1.2 K. *Chem. Phys. Lett.* **1976**, *42*, 193–196.

(41)   Azumi, T.; Saito, Y. Electronic Structures of the Lower Triplet Sublevels of Hexanuclear Molybdenum(II) Chloride Cluster. *J. Phys. Chem.* **1988**, *92*, 1715–1721.

(42)   Condon, E. U.; Shortley, G. H. *The Theory of Atomic Spectra*; Cambridge University Press: London, **1953**.

(43) Harrigan, R. W.; Crosby, G. A. Symmetry Assignments of the Lowest CT Excited States of Ruthenium(II) Complexes Via a Proposed Electronic Coupling. *J. Chem. Phys*. **1973**, *59*, 3468–3476.

(44) Yersin, H.; Donges, D. Low-lying Electronic States and Photophysical Properties of Organometallic Pd(II) and Pt(II) Compounds. Modern Research Trends Presented in Detailed Case Studies. *Top. Curr. Chem*. **2000**, *214*, 81–190.

(45) Lamotte, M.; Merle, A. M.; Joussot-Dubien, J. Multiplet Strucure of the Emission Bands of Coronene and Perylene in *n*-Heptane Single Crystal. *Chem. Phys. Lett*. **1975**, *35*, 410–416.

(46) Kitamura, N.; Kuwahara, Y.; Ueda, Y.; Itoh, Y.; Ishizaka, S.; Sasaki, Y.; Tsuge, K.; Akagi, S. Excited Triplet States of $[\{Mo_6Cl_8\}Cl_6]^{2-}$, $[\{W_6Cl_8\}Cl_6]^{2-}$, and $[\{Re_6S_8\}Cl_6]^{4-}$ Clusters. *Bull. Chem. Soc. Jpn*. **2017**, *90*, 1164–1173.

(47) Miki, H.; Ikeyama, T.; Sasaki, Y.; Azumi, T. Phosphorescence from the Triplet Spin Sublevels of a Hexanuclear Molybdenum(II) Chloride Cluster Ion, $[Mo_6Cl_{14}]^{2-}$. Relative Radiative Rate Constants for Emitting Sublevels. *J. Phys. Chem*. **1992**, *96*, 3236–3239.

(48) Hager, G. D.; Crosby, G. A. Charge Transfer Excited States of Ruthenium(II) Complexes. I. Quantum Yield and Decay Measurement. *J. Am. Chem. Soc*. **1975**, *97*, 7031–7037.

(49) Hager, G. D.; Watts, R. J.; Crosby, G. A. Charge-transfer Excited States of Ruthenium(II) Complexes. II. Relationship of Level Parameters to Molecular Structure. *J. Am. Chem. Soc.* **1975**, *97*, 7037–7042.

(50) Homeier, H. H. H.; Strasser, J.; Yersin, H. Spin-lattice Relaxation in Metal-organic Platinum(II) Complexes. *Chem. Phys. Lett*. **2000**, *316*, 280–284.

(51) Huber, P.; Yersin. H. Highly Resolved Emission of $[Os(bpy\text{-}h_8)_n(bhy\text{-}d_8)_{3-n}]^{2+}$ ($n = 0$–3): Evidence for Electronic Delocalization. *J. Phys. Chem*. **1993**, *97*, 12705–12709.

(52) Kober, E. M.; Casper, J. V.; Lumpkin, R. S.; Meyer, T. J. Application of the Energy Gap Law to Excited-state Decay of Osmium-polypyridine Complexes: Calculation of Relative Nonradiative Decay Rates from Emission Spectral Profiles. *J. Phys. Chem*. **1986**, *90*, 3722–3734.

(53) Humbs, W.; Yersin, H. Characterization of the Lowest Excited States of $[Rh(bpy\text{-}h_8)_n(bhy\text{-}d_8)_{3-n}]^{3+}$ by Highly Resolved Emission and Excitation Spectra. *Inorg. Chem*. **1996**, *35*, 2220–2228.

(54) Mak, C. S. K.; Pentlehner, D.; Stich, M.; Wolfbeis, O. S.; Chan, W. K.; Yersin, H. Exceptional Oxygen Sensing Capabilities and Triplet State Properties of Ir(ppy-NPh₂)₃. *Chem. Mater*. **2009**, *21*, 2173–2175.

(55) Rausch, A. F.; Thompson, M. E.; Yersin. H. Matrix Effects on the Triplet State of the OLED Emitter Ir(4,6-dFppy)₂(pic) (FIrpic): Investigations by Hi-Resolution Optical Spectroscopy. *Inorg. Chem*. **2009**, *48*, 1928–1937.

(56) Deaton, J. C.; Young, R. H.; Lenhard, J. R.; Rajeswaran, M.; Huo, S. Photophysical Properties of the Series *fac*- and *mer*-(1-Phenylisoquinolinato-N-C²')$_x$(2-phenlpyridinato-N^C²')$_{3-x}$ Iridium(III) ($x = 1$–3). *Inorg. Chem*. **2010**, *49*, 9151–9161.

(57)   Marchetti, A. P.; Deaton, J. C.; Young, R. H. Narrow-line and Broadband Spectra of Iridium(III) Complexes in a Shpol'skii Matrix and an Amorphous Host. *J. Phys. Chem. A* **2006**, *110*, 9828–9838.

(58)   Rausch, A. F.; Thompson. M. E.; Yersin H. Blue Light Emitting Ir(III) Compounds for OLEDs – New Insights into Ancillary Ligand Effects on the Emitting Triplet State. *J. Phys. Chem. A* **2009**, *113*, 5927–5932.

(59)   Hofbeck, T.; Yerisn, H. The Triplet State of *fac*-Ir(ppy)$_3$. *Inorg. Chem.* **2010**, *49*, 9290–9299.

(60)   Czerwieniec, R.; Finkenzeller, W. J.; Hofbeck, T.; Starukhin, A.; Wedel, A.; Yersin, H. Photophysical Properties of Re(pbt)(CO)$_4$ Studied by High Resolution Spectroscopy. *Chem. Phys. Lett.* **2009**, *468*, 205–210.

(61)   Donges, D.; Nagle, J. K.; Yersin, H. Characterization of Intraligand Charge Transfer Transitions in Pd(qol)$_2$, Pt(qol)$_2$ and Pt(qtl)$_2$ Investigated by Shpol'skii Spectroscopy. *J. Lumin.* **1997**, *72–74*, 658–659.

(62)   Kozhevnikov, D. N.; Kozhevnikov, V. N.; Ustinova, M. M.; Santoro, A.; Bruce, D. W.; Koenig, B.; Czerwieniec, R.; Fischer, T.; Zabel, M.; Yersin, H. Synthesis of Cyclometallated Platinum Complexes with Substituted Thienylpyridines and Detailed Characterization of Their Luminescence Properties. *Inorg. Chem.* **2009**, *48*, 4179–4189.

(63)   Rausch, A. F.; Monkowius, U. W.; Zabel, M.; Yersin, H. Bright Sky-blue Phosphorescence of [*n*-Bu$_4$N][Pt(4,6-dFppy)(CN)$_2$]: Synthesis, Crystal Structure, and Detailed Photophysical Studies. *Inorg. Chem.* **2010**, *49*, 7818–7825.

(64)   Yersin, H.; Donges, D.; Humbs, W.; Strasser, J.; Sitters, R.; Glasbeek, M. Organometallic Pt(II) Compounds. A Complementary Study of a Triplet Emitter Based on Optical High-resolution and Optically Detected Magnetic Resonance Spectroscopy. *Inorg. Chem.* **2002**, *41*, 4915–4922.

(65)   Fischer, T.; Czerwieniec, R.; Hofbeck, T.; Osminina, M. M.; Yersin, H. Triplet State Properties of A Red Light Emitting [Pt(s-thpy)(acac)] Compounds. *Chem. Phys. Lett.* **2010**, *486*, 53–59.

(66)   Rausch, A. F.; Thompson, M. E.; Yersin, H. Triplet State Relaxation Processes of the OLED Emitter Pt(4,6-dFppy)(acac). *Chem. Phys. Lett.* **2009**, *468*, 46–51.

(67)   Rausch, A. F.; Murphy, L.; Williams, J. A. G.; Yersin, H. Probing the Excited State Properties of the Highly Phosphorescent Pt(dpyb)Cl Compound by High-resolution Optical Spectroscopy. *Inorg. Chem.* **2009**, *48*, 11407–11414.

(68)   Bossi, A.; Rausch, A. F.; Leitl, M. J.; Czerwieniec, R. Whited, M. T.; Djurovich, P. I.; Yersin, H.; Thompson, M. E. Photophysical Properties of Cyclometalated Pt(II) Complexes: Counterintuitive Blue Shift in Emission with an Expanded Ligand System. *Inorg. Chem.* **2013**, *52*, 12403–12415.

(69)   Yersin, H.; Rausch, A. F.; Czerwieniec, R.; Hoftback, T.; Fischer, T. The Triplet State of Organo-Transition Metal Compounds. Triplet Harvesting and Singlet Harvesting for Efficient OLEDs. *Coord. Chem. Rev.* **2011**, *255*, 2622–2652.

(70)   Yersin, H.; Strasser, J. Triplets in Metal-Organic Compounds. Chemical Tunability of Relaxation Dynamics. *Coord. Chem. Rev*. **2000**, *208*, 331–364.

(71)   Hogue, R. D.; McCarley, R. E. Chemistry of Polynuclear Metal halides. V. Reactions and Characterization of Compounds Containing Tungsten Halide Cluster Species. *Inorg. Chem*. **1970**, *9*, 1354–1360.

(72)   Leduc, L.; Perrin, A.; Sergent, M. Structure du Dichlorure et Octaséléniure D'hexarhénium, $Re_6Se_8Cl_2$: Composé Bidimensionnel à Clusters Octaédriques Re_6. *Acta Crystallogr. Sec. C* **1983**, *39*, 1503–1506.

(73)   Dorman, W. C.; McCarley, R. E. Chemistry of Polynuclear Metal Halides. XII. Preparation of Molybdenum and Tungsten $M_6X_8^{4+}$ Clusters by Reduction of Higher Halides in Molten Sodium Halide-aluminum Halide Mixtures. *Inorg. Chem*. **1974**, *13*, 491–493.

(74)   Maverick, A. W.; Najdzionek, J. S.; MacKenzie, D.; Nocera, D. G.; Gray, H. B. Spectroscopic, Electrochemical, and Photochemical Properties of Molybdenum(II) and Tungsten(II) Halide Cluster. *J. Am. Chem. Soc*. **1983**, *105*, 1878–1882.

(75)   Zietlow, T. C.; Nocera, D. G.; Gray, H. B. Photophysics and Electrochemistry of Hexanuclear Tungsten Halide Clusters. *Inorg. Chem*. **1986**, *25*, 1351–1353.

(76)   Yoshimura, T.; Ishizaka, S.; Umakoshi, K.; Sasaki, Y.; Kim, H.-B.; Kitamura, N. Hexarhenium(III) Clusters $[Re_6(\mu_3\text{-}S)_8X_6]^{4-}$ ($X^- = Cl^-$, Br^-, I^-) are Luminescent at Room Temperature. *Chem. Lett*. **1999**, *28*, 697–698.

(77)   Zheng, Z.; Gray, T. G.; Holm, R. H. Synthesis and Structures of Solvated Monoclusters and Bridged Di- and Triclusters Based on the Cubic Building Block $[Re_6S_8]^{2+}$. *Inorg. Chem*. **1999**, *38*, 4888–4895.

(78)   Yoshimura, T.; Umakoshi, K.; Sasaki, Y.; Sykes, A. G. Synthesis, Structures, and Redox Properties of Octa(μ_3-sulfido)hexarhenium(III) Complexes Having Terminal Pyridine Ligands. *Inorg. Chem*. **1999**, *38*, 5557–5564.

(79)   Yoshimura, T.; Ishizaka, S.; Sasaki, Y.; Kim, H.-B.; Kitamura, N. Unusual Capping Chalcogenide Dependence of the Luminescence Quantum Yield of the Hexarhenium(III) Cyano Complexes $[Re_6(\mu_3\text{-}E)_8(CN)_6]^{4-}$, $E^{2-} = Se^{2-} > S^{2-} > Te^{2-}$. *Chem. Lett*. **1999**, *28*, 1121–1122.

(80)   Yoshimura, T.; Umakoshi, K.; Sasaki, Y.; Ishizaka, S.; Sasaki, Y.; Kim, H.-B.; Kitamura, N. Emission and Metal^ and Ligand-centered-redox Characteristics of the Hexarhenium(III) Clusters *trans*- and *cis*-$[Re_6(\mu_3\text{-}S)_8Cl_4(L)_6]^{2-}$, Where L Is a Pyridine Derivative or Pyrazine. *Inorg. Chem*. **2000**, *39*, 1765–1772.

(81)   Itasaka, A.; Abe, M.; Yoshimura, T.; Tsuge, K.; Suzuki, M.; Imamura, T.; Sasaki, Y. Octahedral Arrangement of Porphyrin Moieties Around Hexarhenium(III) Cluster Cores: Structure of (μ_3-Selenido)hexa(5-(4-pyridyl)-10,15,20-tritolylporpyrin)-hexrhenium(III) (2+). *Angew. Chem. Int. Ed*. **2002**, *41*, 463–466.

(82)   Selby, H. D.; Roland, B. K.; Zheng, Z. Ligand-bridged Oligomeric and Supramolecular Arrays of the

Hexanuclear Rhenium Selenide Clusters–Exploratory Synthesis, Structural Characterization, and Property Investigation. *Acc. Chem. Rus*. **2003**, *36*, 933–944.

(83)   Yoshimura, T.; Chen, Z.-N.; Itasaka, A.; Abe, M.; Sasaki, Y.; Ishizaka, S. Kitamura, N. Preparation, Structures, and Redox and Emission Characteristics of the Isothiocyanate Complexes of Hexarhenium(III) Clusters $[Re_6(\mu_3-E)_8(NCS)_6]^{4-}$ (E = S, Se). *Inorg. Chem.* **2003**, *42*, 4857–4863.

(84)   Pilet, G.; Cordier, S.; Golhen, S.; Perrin, C.; Ouahab, L.; Perrin, A. Syntheses and Structures of Two New $M_6L^i_8(N_3)^a_6$Cluster-unit Based Compounds: $Cs_4Re_6S_8(N_3)_6 \cdot H_2O$ and $Na_2Mo_6Br_8(N_3)_6 \cdot 2H_2O$. *Solid State Sci.* **2003**, *5*, 1263–1270.

(85)   Yarovoi, S.; Mironov, Y. V.; Naumov, D. Y.; Gatilov, Y. V.; Kozlova, S. G.; Kim, S.-J.; Fedorov, V. E. Octahedral Hexahydroxo Rhenium Cluster Complexes $[Re_6Q_8(OH)_6]^{4-}$ (Q = S, Se): Synthesis, Structure, and Properties. *Eur. J. Inorg. Chem*. **2005**, 3945–3949.

(86)   Mironov, Y. V.; Brylev, K. A.; Shestopalov, M. A.; Yarovoi, S. S.; Fedorov, V. E.; Spies, H.; Pietzsch, H.-J.; Stephan, H.; Geipel, G.; Bernhard, G.; Kraus, W. Octahedral Rhenium Cluster Complexes with Organic Ligands: Synthesis, Structure and Properties of $[Re_6Q_8(3,5-Me_2PzH)_6]Br_2 \cdot 2(3,5-Me_2PzH)$ (Q = S, Se). *Inorg. Chim. Acta* **2006**, *359*, 1129–1134.

(87)   Orto, P. J.; Nichol, G. S.; Wang, R.; Zheng, Z. Cluster Carbonyls of $[Re_6(\mu_3-Se)_8]^{2-}$ Core. *Inorg. Chem.* **2007**, *46*, 8436–8438.

(88)   Harder, K.; Preetz, W. Darstellung und spektroskopische Charakterisierung des Clusteranions $[(Mo_6Cl_8{}^i)(CF_3COO)_6{}^a]^{2-}$. *Zeit. Anorg. Allg. Chem.* **1992**, *612*, 97–100.

(89)   Braack, P.; Simsek, M. K.; Preetz, W. Darstellung, Kristallstrukturen und Schwingungsspektren von $[(Mo_6X^i_8)Y^a_6]^{2-}$; X^i=Cl, Br; Y^a=NO_3, NO_2. *Zeit. Anorg. Allg. Chem.* **1998**, *624*, 375–380.

(90)   Sokolov, M. N.; Mihailov, M. A.; Peresypkina, E. V.; Brylev, K. A.; Kitamura, N.; Fedin, V. P. Highly luminescent complexes $[Mo_6X_8(n-C_3F_7COO)_6]^{2-}$ (X = Br, I). *Dalton Trans.* **2011**, *40*, 6375–6377.

(91)   Sokolov, M. N.; Mikhailov, M. A.; Abramov, P. A.; Fedin, V. P. Crystal Structures of Two Solvates of Molybdenum Octahedral Clusters: $(Bu_4N)_2[Mo_6Cl_8(O_3SC_6H_4CH_3)_6] \cdot 2CH_3CN$ and $(Bu_4N)_2[Mo_6Cl_8(O_3SC_6H_4CH_3)_6] \cdot 2CH_2Cl_2$. *J. Struct. Chem.* **2012**, *53*, 197–201.

(92)   Efremova, O. A.; Shestopalov, M. A.; Chirtsova, N. A.; Smolentsev, A. I.; Mironov, Y. V.; Kitamura, N.; Brylev, K. A.; Sutherland, A. J. A Highly Emissive Inorganic Hexamolybdenum Cluster Complex as a Handy Precursor for the Preparation of New Luminescent Materials. *Dalton Trans.* **2014**, *43*, 6021–6025.

(93)   Mikhailov, M. A.; Brylev, K. A.; Virovets, A. V.; Gallyamov, M. R.; Novozhilov, I. N.; Sokolov, M. N. Complexes of $\{Mo_6I_8\}$ with Nitrophenolates: Synthesis and Luminescence. *New J. Chem.* **2016**, *40*, 1162–1168.

(94)   Simsek, M. K.; Preetz, W. Darstellung, Kristallstrukturen, Schwingungsspektren und Normal-

koordinatenanalyse von $(TBA)_2[(Mo_6X^i_8)Y_a^6]$; X^i = Cl, Br; Y^a = NCO, NCSe. *Zeit. Anorg. Allg. Chem.* **1997**, *623*, 515–523.

(95)   Simsek, M. K.; Bublitz, D.; Preetz, W. Darstellung, Kristallstrukturen, Schwingungsspektren und Normalkoordinatenanalyse von $[(Mo_6Br^i_8)Y_a^6]^{2-}$; Y^a = CN, NCS. *Zeit. Anorg. Allg. Chem.* **1997**, *623*, 1885–1891.

(96)   Bublitz, D.; Preetz, W.; Simsek, M. K. Darstellung, Kristallstrukturen und spektroskopische Eigenschaften der Clusteranionen $[(Mo_6X^i_8)(N_3)^a_6]2-$; X^i = Cl, Br. *Zeit. Anorg. Allg. Chem.* **1997**, *623*, 1–7.

(97)   Mery, D.; Plault, L.; Ornelas, C.; Ruiz, J.; Nlate, S.; Astruc, D.; Blais, J. C.; Rodrigues, J.; Cordier, S.; Kirakci, K.; Perrin, C. The Simple Hexapyridine Cluster $[Mo_6Br_8Py_6][OSO_2CF_3]_4$ and Substituted Hexapyridine Clusters Including a Cluster-cored Polyolefin Dendrimer. *Inorg. Chem.* **2006**, *45*, 1156–1167.

(98)   Hamer, A. D.; Smith, T. J.; Walton, R. A. Complex Halides of the Transition Metals. XXI. Evidence for the Existence of Tertiary Phosphine Derivatives of the New Octachlorohexamolybdate(2+) Cluster Cation. *Inorg. Chem.* **1976**, *15*, 1014–1017.

(99)   Saito, T.; Yamamoto, N.; Nagase, T.; Tsuboi, T.; Kobayashi, K.; Yamagata, T.; Imoto, H.; Unoura, K. Molecular Models of the Superconducting Chevrel Phases: Syntheses and Structures of $[Mo_6X_8(PEt_3)_6]$ and $[PPN][Mo_6X_8(PEt_3)_6]$ (X = S, Se; PPN = $(Ph_3P)_2N$). *Inorg. Chem.* **1990**, *29*, 764–770.

(100) Szczepura, L. F.; Ketcham, K. A.; Ooro, B. A.; Edwards, J. A.; Templeton, J. N.; Cedeno, D. L.; Jircitano, A. J. Synthesis and Study of Hexanuclear Molybdenum Clusters Containing Thiolate Ligands. *Inorg. Chem.* **2008**, *47*, 7271–7278.

(101) Szczepura, L. A.; Edwards, J. A.; Cedeno, D. L. Luminescent Properties of Hexanuclear Molybdenum(II) Chloride Clusters Containing Thiolate Ligands. *J. Cluster Sci.* **2009**, *20*, 105–112.

(102) Sokolov, M. N.; Mikhailov, M. A.; Brylev, K. A.; Virovets, A. V.; Vicent, C.; Kompankov, N. B.; Kitamura, N.; Fedin, V. P. Alkynyl Complexes of High-Valence Clusters. Synthesis and Luminescence Properties of $[Mo_6I_8(C{\equiv}CC(O)OMe)_6]^{2-}$, the First Complex with Exclusively Organometallic Outer Ligands in the Family of Octahedral $\{M_6X_8\}$ Clusters. *Inorg. Chem.* **2013**, *52*, 12477–12481.

(103) Sokolov, M. N.; Mikhailov, M. A.; Virovets, A. V.; Brylev, K. A.; Bredikhin, R. A.; Maksimov, A. M.; Platonov, V. E.; Fedin, V. P. Synthesis, Structure, and Luminescence of the Octahedral Molybdenum Cluster $[Mo_6I_8(SC_6F_4H)_6]^{2-}$. *Russ. Chem. Bull.* **2013**, *62*, 1764–1767.

(104) Johnston, D. H.; Gaswick, D. C.; Lonergan, M. C.; Stern, C. L.; Shriver, D. F. Preparation of Bis(tetrabutylammonium)   Octa(μ_3-chloro)hexakis(trifluoromehtanesulfonato)-octahedro-hexamolybdate(2–), $(Bu_4N)_2[Mo_6Cl^i_8(CF_3SO_3)^a_6]$: A Versatile Starting Material for Substituted Mo(II) Clusters Containing the $[Mo_6Cl^i_8]^{4+}$ Core. *Inorg. Chem.* **1992**, *31*, 1869–1873.

(105)   Sokolov, M. N.; Brylev, K. A.; Abramov, P. A.; Gallyamov, M. R.; Novozhilov, I. N.; Kitamura, N.; Mikhaylov, M. A. Complexes with a $\{W_6I_8\}^{4+}$ Clusters with Carboxylates: Preparation, Electrochemistry, and Luminescence. *Eur. J. Inorg. Chem.* **2017**, 4131–4137.

(106)   Fuhrmann, A.-D.; Seyboldt, A.; Enseling, D.; Jüstel, T.; Meyer, H.-J. Preparation and Luminescence of Cluster Compounds $[W_6Br_8L_6]^{2-}$ with L = CF_3COO and $C_7H_7SO_3$. *Zeit. Anorg. Allg. Chem.* **2017**, *643*, 1451–1455.

(107)   Solovieva, A. O.; Vorotnikov, Y. A.; Trifonova, K. E.; Efremova, O. A.; Krasilnikova, A. A.; Brylev, K. A.; Vorontsova, E. V.; Avrorov, P. A.; Shestopalov, L. V.; Poveshchenko, A. F.; Mironov, Y. V.; Shestopalov, M. A. Cellular Internalization, Bioimaging and Dark and Photodynamic Cytotoxicity of Silica Nanoparticles Doped by $[Mo_6I_8]^{4+}$ Metal Clusters. *J. Mater. Chem. B* **2016**, *4*, 4839–4846.

(108)   Efremova, O. A.; Brylev, K. A.; Vorotnikov, Y. A.; Vejsadová, L.; Shestopalov, M. A.; Topham, P.; Kim, S.-J.; Kitamura, N.; Sutherland. Photoluminescent Materials Based on PMMA and Highly-Emissive Octahedral Molybdenum Cluster. *J. Mater. Chem. C* **2016**, 497–503.

(109)   Evtushok, D. V.; Melnikov, A. R.; Vorotnikova, N. A.; Vorotnikov, Y. A.; Ryadun, A. A.; Kuratieva, N. V.; Kozyr, K. V.; Obedinskaya, N. R.; Kretov, E. I.; Novozhilov, I. N.; Mironov, Y. V.; Stass, D. V.; Efremova, O. A.; Shestopalov, M. A. A Comparative Study of Optical Properties and X-ray Induced Luminescence of Octahedral Molybdenum and Tungsten Cluster Complexes. *Dalton Trans.* **2017**, *46*, 11738–11747.

(110)   Kirakci, K.; Kubát, P.; Fejfarová, K.; Martinčík, J.; Nikl, M.; Lang, K. X-ray Inducible Luminescence and Singlet Oxygen Sensitization by an Octahedral Molybdenum Cluster Compound: A New Class of Nanoscintillators. *Inorg. Chem.* 2016, *55*, 803–809.

(111)   Amela-Cortes, M.; Molard, Y.; Paofai, S.; Desert, A.; Duvail, J.-L.; Naumov, N. G.; Cordier, S. Versatility of the Ionic Assembling Method to Design Highly Luminescent PMMA Nanocomposites Containing $[M_6Q^i_8L^a_6]^{n-}$ Octahedral Nano-building Blocks. *Dalton Trans.* **2016**, *45*, 237-245.

Chapter 2

Experiments and Methodologies

2-1. Introduction

This thesis targets to study the phosphorescence properties and the lowest-energy excited triplet (T_1) states of octahedral hexamolybdenum(II) clusters in special references to elucidate the zero-magnetic-field splitting (zfs) parameters in the T_1 states. Since a transition metal complex shows a significantly large zfs energy in the T_1 state compared to an ordinary organic compound, the emission characteristics of the transition metal complex are influenced largely by temperature (*T*, from extremely low T to ambient *T*) through the strength of spin-orbit coupling (SOC) and zfs experienced by the excited state. Quantitative and systematic studies on the zfs energy and the effects of nature of the atom(s) composed of a transition metal complex are thus primarily important to understand the emission characteristics of a transition metal complex in the T_1 state toward molecular design of photofunctional materials.

For systematic and detailed investigations on the T_1 state of a transition metal complex, this thesis focuses on both bridging and terminal ligands structures in an octahedral hexamolybdenum(II) cluster and, therefore, various hexamolybdenum(II) clusters having a series of bridging and terminal ligands have been synthesized: $[\{Mo_6X_8\}Y_6]^{2-}$ (X, Y = Cl, Br, or I) and $[\{Mo_6X_8\}(RCOO)_6]^{2-}$ (X = Br or I. RCOO = various carboxylates: pivalate, acetate, 4-methoxybenzoate, 3,5-dimethybenzoate, benzoate, 3,5-dimethoxybenzoate, 1-naphthoate, 4-cyanobenzoate, 2-furoate, 4-nitrobenzoate, 3,5-dinitrobenzoate, pentafluorobenzoate, or trifluoroacetate). Furthermore, platinum(II) complexes were also synthesized to check the general validity of the experimental results given by the studies on the T_1 states of the octahedral hexamolybdenum(II) clusters. In this chapter, the synthesis of the cluster complexes, the apparatus used for the physical measurements, and the analytical methods for the *T*-dependent emission data are described.

2-2. Materials and Characterization

Molybdenum and bismuth powders, CsX (X = Br or I), $AgNO_3$, NaOH, acetic acid, 3,5-dimethylbenzoic acid, benzoic acid, 1-naphthoic acid, trifluoroacetic acid, K_2PtCl_4, benzo[*h*]quinoline, and tetra-*n*-butylammonium hexafluorophosphate ($TBA^+(PF_6)^-$) were purchased from Wako Pure Chemical Co., Ltd. Pivalic acid, 4-methoxybenzoic acid, 4-cyanobenzoic acid, 2-furoic acid, 3,5-dinitrobenzoic acid, TBA^+X^- (X = Cl, Br, or I), 2-phenylpyridine, acetylacetone, and dipivaloylmethane were obtained from Tokyo Chemical Industry Co., Ltd. $MoCl_5$, 3,5-dimethoxybenzoic acid, 4-nitrobenzoic acid, pentafluorobenzoic acid, and heptafluorobutylic acid were purchased from Sigma-Aldrich Co., Ltd. All of these chemicals used for the synthesis of hexamolybdenum(II) clusters or Pt(II) complexes were used as received. 2-(2-Thienyl)pyridine was prepared according to the literature.[1] All of the solvents used for the synthesis were obtained from Wako Pure Chemical Co., Ltd. and used without further purification. Spectroscopic grade acetone and CH_3CN were purchased from Wako Pure Chemical Co., Ltd. and distilled prior to use. $TBAPF_6$ was recrystallized from ethanol and dried prior to use.

Electron spray ionization mass spectroscopy (ESI-MS) and FT ^{1}H/^{195}Pt NMR measurements were conducted by using a micromassZQ spectrometer (Waters Co.) and a 270 MHz JME-EX or 400 MHz JNM-ECZ spectrometer (JEOL Ltd.), respectively. For ^{1}H NMR and ^{195}Pt NMR spectroscopies, tetramethylsilane (in CDCl$_3$, 0 ppm) and potassium tetrachloroplatinate (in D$_2$O, –1618 ppm) were used as internal and external standards, respectively, for determining the chemical shifts of the NMR signals in ppm. Elemental analysis was carried out in Instrumental Analysis Division, Global Facility Center, Creative Research Institute, Hokkaido University.

2-3.   Synthesis

2-3-1. Synthesis of [{Mo$_6$X$_8$}X$_6$]$^{2-}$ (X = Cl).

The TBA salt of [{Mo$_6$Cl$_8$}Cl$_6$]$^{2-}$ (**1Cl**) as a starting material for the synthesis of [{Mo$_6$Cl$_8$}Y$_6$]$^{2-}$ was prepared by the reduction of the highly oxidized state of molybdenum chloride by a metal powder as follow.[2] MoCl$_5$ (5.0 g, 16 mmol) and a Bi powder (6.3 g, 30 mmol) were introduced into a glass ampoule (50 mm (inner diameter) × 200 mm (length)) and dried in *vacuo* at liquid nitrogen temperature. The sealed ampoule was heated at 240ºC in a furnace for 2 h and, then, at 350ºC for further 26 h. The brown solids were removed from the ampoule and washed with conc. HCl aq. and ethanol until the filtrate became colorless. The crude product dispersed in boiled conc. HCl aq. was refluxed for 3h and, then, the mixture was filtered still hot. The yellow needle crystals precipitated upon cooling were collected by filtration and dissolved in ethanol. To a solution was added 14 g of TBA$^+$Cl$^-$ (50 mmol), yielding the yellow precipitates. The precipitates were then dissolved in a minimum amount of acetone, and slow diffusion of diethyl ether vapor to the solution gave 3.1 g of pure crystals. (TBA)$_2$[{Mo$_6$Cl$_8$}Cl$_6$] (**1Cl**): Yield = 3.1 g (75%). Anal. Calcd. for Mo$_6$Cl$_{14}$C$_{32}$H$_{72}$N$_2$: C, 24.69; H, 4.67; N, 1.80. Found: C, 25.05; H, 4.88; N, 1.20. ESI-MS (CH$_3$CN) for Mo$_6$Cl$_{14}$: *m/z* 535 (M–2TBA).

2-3-2. Synthesis of [{Mo$_6$X$_8$}X$_6$]$^{2-}$ (X = Br or I).

The TBA salts of [{Mo$_6$Br$_8$}Br$_6$]$^{2-}$ (**2Br**) and [{Mo$_6$I$_8$}I$_6$]$^{2-}$ (**3I**) as starting materials for the synthesis of {Mo$_6$Br$_8$}$^{4+}$- and {Mo$_6$I$_8$}$^{4+}$-core clusters, respectively, were prepared by direct halogenation of a molybdenum powder by Br$_2$ or I$_2$.[3] An Mo powder (1.0 g, 10 mmol), X$_2$ (10 mmol, X = Br or I), and CsX (10 mmol) were introduced into a quartz ampoule (40 mm (inner diameter) × 120 mm (length)) and dried in *vacuo* at liquid nitrogen temperature. The sealed ampoule was heated at 500ºC in a furnace for 4 h. Then, the temperature was raised to 850ºC during 2 h and kept for 48 h. The brown to black solids were removed from the ampoule and washed with ethanol until the filtrate became colorless. The crude products were added into 500 mL of acetone in the presence of TBA$^+$X$^-$ (30 mmol) and the mixture was stirred for 1 day. After filtering out the by-products, the filtrate was evaporated to dryness. The crude products washed by ethanol were then dissolved in a minimum amount of acetone, and slow diffusion of diethyl ether vapor to the solution gave pure crystals.

(TBA)$_2$[{Mo$_6$Br$_8$}Br$_6$] (**2Br**): Yield = 2.3 g (63%). Anal. Calcd. for Mo$_6$Br$_{14}$C$_{32}$H$_{72}$N$_2$: C, 17.64; H, 3.33; N, 1.29. Found: C, 17.42; H, 3.11; N, 1.18. ESI-MS (CH$_3$CN) for Mo$_6$Br$_{14}$: *m/z* 847 (M–2TBA).

(TBA)$_2$[{Mo$_6$I$_8$}I$_6$] (**3I**): Yield = 1.8 g (38%).. Anal. Calcd. for Mo$_6$I$_{14}$C$_{32}$H$_{72}$N$_2$: C, 13.55; H, 2.56; N, 0.99. Found: C, 13.42; H, 2.36; N, 0.91. ESI-MS (CH$_3$CN) for Mo$_6$I$_{14}$: *m/z* 1176 (M–2TBA).

2-3-3. Synthesis of Terminal Halide Clusters: [{Mo$_6$X$_8$}Y$_6$]$^{2-}$ (X, Y = Cl, Br, or I).

The TBA salt of [{Mo$_6$X$_8$}Y$_6$]$^{2-}$ (X, Y = Cl, Br, or I) was synthesized by the terminal ligand exchange reaction between (TBA)$_2$[{Mo$_6$X$_8$}X$_6$] (**1Cl**, **2Br**, or **3I**) and a given HY acid.[4] Typically, 300 mg of (TBA)$_2$[{Mo$_6$X$_8$}X$_6$] dissolved in a concentrated HY acid-ethanol mixture (v/v = 9/1) was heated at reflux temperature over 4 h. Upon cooling, yellow or orange precipitates produced were collected by filtration and washed successively with cold conc. HY and ethanol until the filtrate became colorless. The residues were then dissolved in a minimum amount of acetone, and slow diffusion of diethyl ether vapor to the solution gave pure crystals.

(TBA)$_2$[{Mo$_6$Cl$_8$}Br$_6$] (**2Cl**): Yield = 292 mg (83%). Anal. Calcd. for Mo$_6$Cl$_8$Br$_6$C$_{32}$H$_{72}$N$_2$: C, 21.08; H, 3.99; N, 1.54. Found: C, 20.99; H, 3.66; N, 1.32. ESI-MS (CH$_3$CN) for Mo$_6$Cl$_8$Br$_6$: *m/z* 669 ([M – 2TBA]$^{2+}$).

(TBA)$_2$[{Mo$_6$Cl$_8$}I$_6$] (**3Cl**): Yield = 325 mg (80%). Anal. Calcd. for Mo$_6$Cl$_8$I$_6$C$_{32}$H$_{72}$N$_2$: C, 18.25; H, 3.45; N, 1.33. Found: C, 18.26; H, 3.55; N, 1.28. ESI-MS (CH$_3$CN) for Mo$_6$Cl$_8$I$_6$: *m/z* 810 ([M – 2TBA]$^{2+}$).

(TBA)$_2$[{Mo$_6$Br$_8$}Cl$_6$] (**1Br**): Yield = 240 mg (91%). Anal. Calcd. for Mo$_6$Br$_8$Cl$_6$C$_{32}$H$_{72}$N$_2$: C, 20.01; H, 3.80; N, 1.47. Found: C, 20.12; H, 3.63; N, 1.66. ESI-MS (CH$_3$CN) for Mo$_6$Br$_8$Cl$_6$: *m/z* 713 ([M – 2TBA]$^{2+}$).

(TBA)$_2$[{Mo$_6$Br$_8$}I$_6$] (**3Br**): Yield = 264 mg (78%). Anal. Calcd. for Mo$_6$Br$_8$I$_6$C$_{32}$H$_{72}$N$_2$: C, 15.62; H, 2.95; N, 1.14. Found: C, 15.66; H, 3.01; N, 1.22. ESI-MS (CH$_3$CN) for Mo$_6$Br$_8$I$_6$: *m/z* 988 ([M – 2TBA]$^{2+}$).

(TBA)$_2$[{Mo$_6$I$_8$}Cl$_6$] (**1I**): Yield = 184 mg (76%). Anal. Calcd. for Mo$_6$I$_8$Cl$_6$C$_{32}$H$_{72}$N$_2$: C, 16.80; H, 3.17; N, 1.22. Found: C, 16.91; H, 3.19; N, 1.26. ESI-MS (CH$_3$CN) for Mo$_6$I$_8$Cl$_6$: *m/z* 901 ([M – 2TBA]$^{2+}$).

(TBA)$_2$[{Mo$_6$I$_8$}Br$_6$] (**2I**): Yield = 238 mg (88%). Anal. Calcd. for Mo$_6$I$_8$Br$_6$C$_{32}$H$_{72}$N$_2$: C, 15.04; H, 2.84; N, 1.10. Found: C, 15.22; H, 2.81; N, 0.99. ESI-MS (CH$_3$CN) for Mo$_6$I$_8$Br$_6$: *m/z* 1035 ([M – 2TBA]$^{2+}$).

(TBA)$_2$[{Mo$_6$X$_8$}Y$_6$]			
*n*X	X		
	Cl	Br	I
Y Cl (*n* = 1)	1Cl	1Br	1I
Br (*n* = 2)	2Cl	2Br	2I
I (*n* = 3)	3Cl	3Br	3I
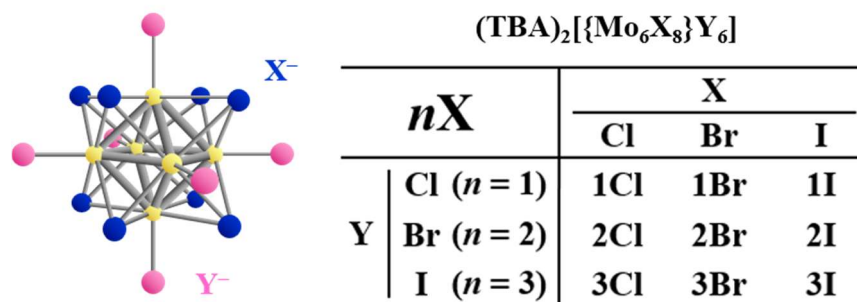
Chart 2-1. Structures and abbreviations of halide clusters [{Mo$_6$X$_8$}Y$_6$]$^{2-}$.

2-3-4. Synthesis of Terminal Carboxylate Clusters: [{Mo₆X₈}(RCOO)₆]²⁻ (RCOO = Carboxylate).

The TBA salt of $[\{Mo_6X_8\}(RCOO)_6]^{2-}$ (X = Br or I) was prepared by the reaction between $(TBA)_2[\{Mo_6X_8\}X_6]$ (X = Br (**2Br**) or I (**3I**)) and the relevant silver benzoate (RCOOAg) in acetone at room temperature.[5] RCOOAg was prepared by adding an ethanol-water mixture (3:1, v/v, 20 mL) of $AgNO_3$ (0.8 eq. to RCOOH) to an ethanol-water mixture (3:1, v/v, 40 mL) of RCOOH (500 mg) in the presence of an aqueous NaOH solution (10 mL, 0.9 eq. to RCOOH) in the dark. The white RCOOAg precipitates collected were washed thoroughly with an ethanol-water mixture and dried (yield = 45–81%), which were used without further purification for the following reaction. An acetone (for **4X**, **5X**, **7X**, **8X**, **11Br**, **13X**, **14Br**, and **15X–17X**) or methylene chloride (for **6Br**, **9Br**, **10X**, and **12Br**) solution (10 mL) of $(TBA)_2[\{Mo_6X_8\}X_6]$ (X = Br or I, 92 μmol) and a given RCOOAg (6–7 eq.) was stirred at room temperature for one week in the dark. The precipitates were removed by filtration and the yellow/orange filtrate was left under room light for further one day. The black precipitates were filtered off by using a membrane filter (pore size = 0.45 μm) and the filtrate was evaporated to dryness, giving orange solids. Single crystals of the cluster suitable for X-ray analysis were obtained by slow diffusion of diethyl ether to the acetone (**4X**, **5X**, **7X**, **8X**, **11Br**, **13X**, **14Br**, and **15X–17X**) or methylene chloride (**6Br**, **9Br**, **10X**, and **12Br**) solution of the crude product.

$(TBA)_2[\{Mo_6Cl_8\}(C_3F_7COO)_6]$ (**17Cl**): Yield: 53 mg (22%). Anal. Calcd. For $Mo_6Cl_8C_{56}H_{72}N_2O_{12}F_{42}$: C, 25.7; H, 2.8; N, 1.1. Found C, 25.7; H, 2.5; N, 0.9. ESI-MS (CH_3CN) for $Mo_6Cl_8C_{24}O_{12}F_{42}$: m/z 1069 ($[M - 2TBA]^{2+}$).

$(TBA)_2[Mo_6Br_8((CH_3)_3CCOO)_6]$ (**4Br**): Yield = 148 mg (79%). Anal. Calcd for $Mo_6Br_8C_{62}H_{126}N_2O_{12}$: C, 32.3; H, 5.5; N, 1.2. Found: C, 32.5; H, 5.2; N, 1.1. ^{1}H NMR (d_6-acetone, normalized to 24 H of the methyl groups in TBA, ppm) δ = 1.10 (s, 54H). ESI-MS (CH_3CN) for $Mo_6Br_8C_{30}H_{54}O_{12}$: m/z 911 ($[M - 2TBA]^{2+}$).

$(TBA)_2[Mo_6Br_8(CH_3COO)_6]$ (**5Br**): Yield = 181 mg (85%). Anal. Calcd for $Mo_6Br_8C_{44}H_{90}N_2O_{12}$: C, 25.7; H, 4.4; N, 1.4. Found: C, 25.6; H, 4.2; N, 1.2. ^{1}H NMR (d_6-acetone, normalized to 24 H of the methyl groups in TBA, ppm): δ = 1.87 (s, 18H). ESI-MS (CH_3CN) for $Mo_6Br_8C_{12}H_{18}O_{12}$: m/z 785 ($[M - 2TBA]^{2+}$).

$(TBA)_2[\{Mo_6Br_8\}(4-(OCH_3)-C_6H_3COO)_6]$ (**6Br**): Yield = 197 mg (82%). ^{1}H NMR (d_6-acetone, normalized to 24 H of the methyl groups in TBA, ppm) δ = 7.97 (d, 12H), 6.88 (d 12H), 3.81 (s, 18H) Anal. Calcd. for $Mo_6Br_8C_{80}H_{114}N_2O_{18}\cdot0.7CH_2Cl_2$: C, 36.36; H, 4.36; N, 1.05; Br, 23.98. Found: C, 36.10; H, 4.25; N, 1.03; Br, 24.73. ESI-MS (CH_3CN): m/z 1061 ($[M - 2TBA]^{2+}$).

$(TBA)_2[Mo_6Br_8(3,5-(CH_3)-C_6H_3COO)_6]$ (**7Br**): Yield = 169 mg (71%). Anal. Calcd for $Mo_6Br_8C_{86}H_{126}N_2O_{12}\cdot0.2CH_2Cl_2$: C, 36.93; H, 4.54; N, 1.00; Br, 22.80. Found: C, 39.4; H, 4.8; N, 1.0 %. ^{1}H NMR (d_6-acetone, normalized to 24 H of the methyl groups in TBA, ppm): δ = 7.65 (s, 12H), 6.99 (s, 6H), 2.28 (s, 36H). ESI-MS (CH_3CN) for $Mo_6Br_8C_{54}H_{54}O_{12}$: m/z 1055 ($[M - 2TBA]^{2+}$).

$(TBA)_2[Mo_6Br_8(C_6H_5COO)_6]$ (**8Br**): Yield = 167 mg (75%). Anal. Calcd for $Mo_6Br_8C_{74}H_{102}N_2O_{12}$: C, 36.6; H, 4.2; N, 1.2. Found: C, 36.4; H, 4.2; N, 1.1 %. ^{1}H NMR (d_6-acetone, normalized to 24 H of the methyl groups in TBA, ppm): δ = 8.03 (d, 12H), 7.38–7.32 (m, 18H). ESI-MS (CH_3CN) for $Mo_6Br_8C_{54}H_{54}O_{12}$: m/z 971 ([M –

2TBA]$^{2+}$).

(TBA)$_2$[{Mo$_6$Br$_8$}(3,5-(OCH$_3$)-C$_6$H$_3$COO)$_6$] (**9Br**): Yield = 156 mg (61%). ^{1}H NMR (d_6-acetone, normalized to 24 H of the methyl groups in TBA, ppm) δ = 7.21 (d, 12H), 6.48 (t, 6H), 3.77 (s, 36H). Anal. Calcd. for Mo$_6$Br$_8$C$_{86}$H$_{126}$N$_2$O$_{24}$: C, 37.07; H, 4.56; N, 1.00; Br, 22.94. Found: C, 36.65; H, 4.44: N, 0.90; Br, 22.95. ESI-MS (CH$_3$CN) for Mo$_6$Br$_8$C$_{54}$H$_{54}$O$_{24}$: *m/z* 1151 ([M – 2TBA]$^{2+}$).

(TBA)$_2$[Mo$_6$Br$_8$(C$_{10}$H$_7$COO)$_6$] (**10Br**): Yield = 216 mg (86%). Anal. Calcd for Mo$_6$Br$_8$C$_{98}$H$_{120}$N$_2$O$_{12}$: C, 43.1; H, 4.4; N, 1.0. Found: C, 43.0; H, 4.2; N, 0.9 %. ^{1}H NMR (d_6-acetone, normalized to 24 H of the methyl groups in TBA, ppm): δ = 9.23 (d, 6H), 8.16 (d, 6H), 7.17 (m, 12H). ESI-MS (CH$_3$CN) for Mo$_6$Br$_8$C$_{66}$H$_{48}$O$_{12}$: *m/z* 1124 ([M – 2TBA]$^{2+}$).

(TBA)$_2$[{Mo$_6$Br$_8$}(4-(CN)-C$_6$H$_4$COO)$_6$] (**11Br**): Yield = 218 mg (92%). ^{1}H NMR (d_6-acetone, normalized to 24 H of the methyl groups in TBA, ppm) δ = 8.38 (d, 12H), 8.03 (d, 12H). Anal. Calcd. for Mo$_6$Br$_8$C$_{80}$H$_{96}$N$_8$O$_{12}$: C, 37.29; H, 3.76; N, 4.35; Br, 24.81. Found: C, 37.00; H, 3.65; N, 4.11; Br, 23.94. ESI-MS (CH$_3$CN) for Mo$_6$Br$_8$C$_{48}$H$_{24}$N$_6$O$_{12}$: *m/z* 1046 ([M – 2TBA]$^{2+}$).

(TBA)$_2$[{Mo$_6$Br$_8$}(4-(NO$_2$)-C$_6$H$_4$COO)$_6$] (**12Br**): Yield = 223 mg (90%). ^{1}H NMR (d_6-DMSO, normalized to 24 H of the methyl groups in TBA, ppm) δ = 8.28 (d, 12H), 8.11 (d, 12H). Anal. Calcd. for Mo$_6$Br$_8$C$_{74}$H$_{96}$N$_8$O$_{24}$·0.2CH$_2$Cl$_2$: C, 32.84; H, 3.58; N, 4.13; Br, 23.56. Found: C, 32.62; H, 3.48; N, 4.11; Br, 23.69. ESI-MS (CH$_3$CN) for Mo$_6$Br$_8$C$_{42}$H$_{24}$N$_6$O$_{24}$: *m/z* 1106 ([M – 2TBA]$^{2+}$).

(TBA)$_2$[Mo$_6$Br$_8$(C$_4$H$_3$OCOO)$_6$] (**13Br**): Yield = 187 mg (86 %). Anal. Calcd for Mo$_6$Br$_8$C$_{62}$H$_{90}$N$_2$O$_{18}$: C, 31.5; H, 3.8; N, 1.2. Found: C, 31.2; H, 3.7; N, 1.1. ^{1}H NMR (d_6-acetone, normalized to 24 H of the methyl groups in TBA, ppm): δ = 7.49 (s, 6H), 6.88–6.83 (m, 12H), 6.42 (s 6H). ESI-MS (CH$_3$CN) for Mo$_6$Br$_8$C$_{30}$H$_{18}$O$_{18}$: *m/z* 941 ([M – 2TBA]$^{2+}$).

(TBA)$_2$[{Mo$_6$Br$_8$}(3,5-(NO$_2$)-C$_6$H$_3$COO)$_6$] (**14Br**): Yield = 244 mg (89%). ^{1}H NMR (d_6-acetone, normalized to 24 H of the methyl groups in TBA, ppm) δ = 8.97 (d, 6H), 8.95 (d, 12H). Anal. Calcd. for Mo$_6$Br$_8$C$_{74}$H$_{90}$N$_{14}$O$_{36}$: C, 29.96; H, 3.06; N, 6.61; Br, 21.55. Found: C, 29.88; H, 2.99; N, 6.34; Br, 21.03. ESI-MS (CH$_3$CN) for Mo$_6$Br$_8$C$_{42}$H$_{18}$N$_{12}$O$_{36}$: *m/z* 1240 ([M – 2TBA]$^{2+}$).

(TBA)$_2$[Mo$_6$Br$_8$(C$_6$F$_5$COO)$_6$] (**15Br**): Yield = 199 mg (73%). Anal. Calcd for Mo$_6$Br$_8$C$_{74}$H$_{72}$F$_{30}$N$_2$O$_{12}$: C, 30.0; H, 2.5; N, 0.9. Found: C, 29.9; H, 2.5; N, 1.0 %. ESI-MS (CH$_3$CN) for Mo$_6$Br$_8$C$_{42}$F$_{30}$O$_{12}$: *m/z* 1241 ([M – 2TBA]$^{2+}$).

(TBA)$_2$[Mo$_6$Br$_8$(CF$_3$COO)$_6$] (**16Br**): Yield = 192 mg (88%). Anal. Calcd for Mo$_6$Br$_8$C$_{98}$H$_{114}$N$_2$O$_{12}$: C, 22.2; H, 3.1; N, 1.2. Found: C, 22.2; H, 2.9; N, 1.0 %. ESI-MS (CH$_3$CN) for Mo$_6$Br$_8$C$_{12}$F$_{18}$O$_{12}$: *m/z* 946 ([M – 2TBA]$^{2+}$).

(TBA)$_2$[Mo$_6$Br$_8$(*n*-C$_3$F$_7$COO)$_6$] (**18Br**) Yield = 165 mg (60%). Anal. Calcd for Mo$_6$Br$_8$C$_{56}$H$_{72}$F$_{42}$N$_2$O$_{12}$: C, 22.6; H, 2.4; N, 0.9. Found: C, 22.8; H, 2.3; N, 0.9 %. ESI-MS (CH$_3$CN) for Mo$_6$Br$_8$C$_{24}$F$_{42}$O$_{12}$: *m/z* 1247 ([M – 2TBA]$^{2+}$).

(TBA)$_2$[{Mo$_6$I$_8$}((CH$_3$)$_3$CCOO)$_6$] (**4I**): Yield = 80 mg (61%). Anal. Calcd. for Mo$_6$I$_8$C$_{62}$H$_{126}$N$_2$O$_{12}$: C, 27.8; H,

4.7; N, 1.0. Found C, 27.3; H, 4.5; N, 1.0. ^{1}H NMR (CD$_3$CN, normalized to 24 H of the methyl groups in TBA, ppm): δ = 1.03 (s, 54H). ESI-MS (CH$_3$CN) for Mo$_6$I$_8$C$_{30}$H$_{54}$O$_{12}$: *m/z* 1099 ([M – 2TBA]$^{2+}$).

(TBA)$_2$[{Mo$_6$I$_8$}(CH$_3$COO)$_6$] (**5I**): Yield = 70 mg (40%). Anal. Calcd. for Mo$_6$I$_8$C$_{44}$H$_{90}$N$_2$O$_{12}$: C, 21.7; H, 3.7; N, 1.2. Found C, 21.8; H, 3.8; N, 1.2. ^{1}H NMR (*d*$_6$-DMSO, normalized to 24 H from the methyl groups in TBA, ppm): δ = 1.76 (s, 18H). ESI-MS (CH$_3$CN) for Mo$_6$I$_8$C$_{12}$H$_{18}$O$_{12}$: *m/z* 973 ([M – 2TBA]$^{2+}$).

(TBA)$_2$[Mo$_6$I$_8$(3,5-(CH$_3$)-C$_6$H$_3$COO)$_6$] (**7I**): Yield = 212 mg (78%). Anal. Calcd for Mo$_6$I$_8$C$_{86}$H$_{126}$N$_2$O$_{12}$: C, 34.7; H, 4.3; N, 0.9. Found: C, 34.5; H, 4.1; N, 0.8 %. ^{1}H NMR (*d*$_6$-acetone, normalized to 24 H of the methyl groups in TBA, ppm): δ = 7.61 (s, 12H), 6.97 (s, 6H), 2.27 (s, 36H). ESI-MS (CH$_3$CN) for Mo$_6$I$_8$C$_{54}$H$_{54}$O$_{12}$: *m/z* 1243 ([M – 2TBA]$^{2+}$).

(TBA)$_2$[{Mo$_6$I$_8$}(C$_6$H$_5$COO)$_6$] (**8I**): Yield = 90 mg (43%). Anal. Calcd. for Mo$_6$I$_8$C$_{74}$H$_{102}$N$_2$O$_{12}$: C, 31.7; H, 3.7; N, 1.0. Found: C, 31.8; H, 3.9; N, 1.1. ^{1}H NMR (CD$_3$CN, normalized to 24 H from the methyl groups in TBA, ppm): δ = 7.94 (d, 12H), 7.44–7.36 (m, 18H). ESI-MS (CH$_3$CN) for Mo$_6$I$_8$C$_{42}$H$_{30}$O$_{12}$: *m/z* 1159 ([M – 2TBA]$^{2+}$).

(TBA)$_2$[{Mo$_6$I$_8$}(C$_{10}$H$_7$COO)$_6$] (**10I**): Yield = 110 mg (59%). Anal. Calcd. for Mo$_6$I$_8$C$_{98}$H$_{114}$N$_2$O$_{12}$: C, 37.9; H, 3.7; N, 0.9. Found: C, 37.6; H, 3.6; N, 0.9. ^{1}H NMR (CD$_3$CN, normalized to 24 H from the methyl groups in TBA, ppm): δ = 8.93 (d, 6H), 7.95–7.87 (m, 18H), 7.53–7.47 (m, 18H). ESI-MS (CH$_3$CN) for Mo$_6$I$_8$C$_{66}$H$_{42}$O$_{12}$: *m/z* 1309 ([M – 2TBA]$^{2+}$).

(TBA)$_2$[{Mo$_6$I$_8$}(C$_4$H$_3$OCOO)$_6$] (**13I**): Yield = 108 mg (66%). Anal. Calcd. for Mo$_6$I$_8$C$_{62}$H$_{90}$N$_2$O$_{18}$: C 27.1; H 3.3; N 1.0. Found C 26.8; H 3.3; N 1.0. ^{1}H NMR (CD$_3$CN, normalized to 24 H from the methyl groups in TBA, ppm): δ = 7.49 (s, 6H), 6.83–6.81 (m, 6H), 6.44–6.43 (m, 6H). ESI-MS (CH$_3$CN) for Mo$_6$I$_8$C$_{30}$H$_{18}$O$_{18}$: *m/z* 1129 ([M – 2TBA]$^{2+}$).

(TBA)$_2$[Mo$_6$I$_8$(C$_6$F$_5$COO)$_6$] (**15I**): Yield = 160 mg (52 %). Anal. Calcd for Mo$_6$I$_8$C$_{72}$H$_{72}$F$_{30}$N$_2$O$_{12}$: C, 26.6; H, 2.2; N, 0.9. Found: C, 26.5; H, 2.0; N, 0.7. ESI-MS (CH$_3$CN) for Mo$_6$I$_8$C$_{40}$F$_{30}$O$_{12}$: *m/z* 1417 ([M – 2TBA]$^{2+}$).
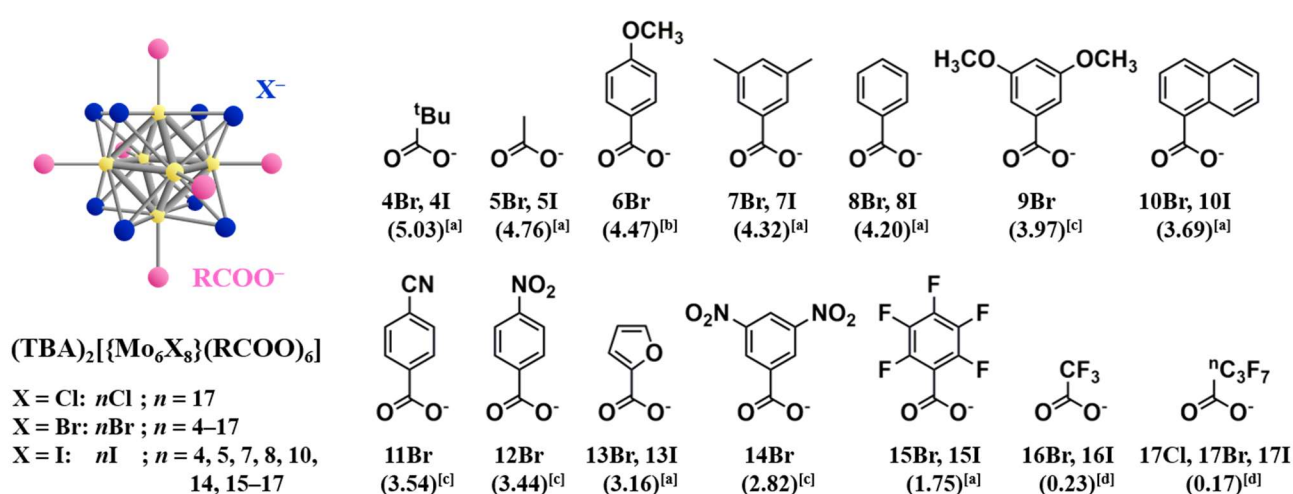
Chart 2-2. Ligand structures and abbreviations of terminal carboxylate clusters [{Mo$_6$X$_8$}(RCOO)$_6$]$^{2-}$.

(TBA)$_2$[{Mo$_6$I$_8$}(CF$_3$COO)$_6$] (**16I**): Yield: 142 mg (70%). Anal. Calcd. For Mo$_6$I$_8$C$_{44}$H$_{72}$N$_2$O$_{12}$F$_{18}$: C, 19.2; H, 2.6; N, 1.0. Found C, 19.3; H, 2.6; N, 1.0. ESI-MS (CH$_3$CN) for Mo$_6$I$_8$C$_{12}$O$_{12}$F$_{18}$: *m/z* 1135 ([M − 2TBA]$^{2+}$).

(TBA)$_2$[{Mo$_6$I$_8$}(C$_3$F$_7$COO)$_6$] (**17I**): Yield: 120 mg (56%). Anal. Calcd. For Mo$_6$I$_8$C$_{56}$H$_{72}$N$_2$O$_{12}$F$_{42}$: C, 20.1; H, 2.2; N, 0.8. Found C, 20.3; H, 2.3; N, 0.9. ESI-MS (CH$_3$CN) for Mo$_6$I$_8$C$_{24}$O$_{12}$F$_{42}$: *m/z* 1435 ([M − 2TBA]$^{2+}$).

2-3-5. Synthesis of Platinum(II) Complexes [Pt(*C^N*)(*O^O*)] (*C^N* = Cyclometalate Ligand).

[Pt(*L*)(*O^O*)] complexes (**1Pt**–**3Pt**) were prepared by a microwave-assisted method as described below.[6] A cyclometalate ligand (0.241 mmol) was dissolved in 10 mL of a 2-ethoxyethanol/water solution (3/1 = v/v) of K$_2$PtCl$_4$ (100 mg, 0.241 mmol). The solution deaerated by purging an Ar gas stream was heated at 60ºC for 1 min under microwave irradiation (150–200 W) and then, the container was cooled immediately to room temperature by an ice bath. After the heating-cooling procedures mentioned above being performed three times, 20 mL of water was added dropwise to the solution. The yellow to green precipitates were collected by filtration and dried in *vacuo*. The chloro-bridged dimer as the product was used for the following reaction without further purification. The powder of the chloro-bridged dimer (1 eq.) was suspended in 10 mL of a 2-ethoxyethanol/water mixture (3/1 = v/v) in the presence of both CH$_3$COONa (10 eq.) and dipivaloylmethane (dpm, for **1Pt**) or acetylacetone (acac, for **2Pt** and **3Pt**) (2 eq.). The mixture deaerated by purging an Ar gas stream was heated at 60°C for 10 min under microwave irradiation (150–200 W). Addition of an excess amount of water to the reaction mixture yielded yellow to green precipitates. The precipitates washed thoroughly with water were purified by silica-gel column chromatography with dichloromethane as an eluent. The eluent was concentrated by evaporation and, then, methanol was diffused slowly to the solution, yielding the yellow to green crystals.

[Pt(bhq)(dpm)] (**1Pt**): Yield = 43 mg (32%). ^{1}H NMR (CDCl$_3$, ppm) δ = 9.12 (d, 1H), 8.27 (d, 1H), 7.82–7.75 (m, 2H), 7.58 (d, 2H), 7.52 (d, 1H), 7.45 (dd, 1H), 5.87 (s, 1H), 1.32 (d, 18H). ^{195}Pt NMR (CDCl$_3$, ppm) δ = − 2770. ESI-MS (CH$_3$CN) for PtC$_{24}$H$_{27}$NO$_2$: *m/z* 556 ([M+H]$^+$).

[Pt(thpy)(acac)] (**2Pt**): Yield = 26 mg (24%). ^{1}H NMR (CDCl$_3$, ppm) δ = 8.80 (d, 1H), 7.67 (td, 1H), 7.49 (d, 1H), 7.29 (t, 1H), 7.20 (d, 1H), 6.92 (td, 1H), 5.48 (s, 1H), 2.00 (d, 6H). ^{195}Pt NMR (CDCl$_3$, ppm) δ = –2790. ESI-MS (CH$_3$CN) for PtC$_{14}$H$_{13}$NO$_2$S: *m/z* 454 ([M+H]$^+$).
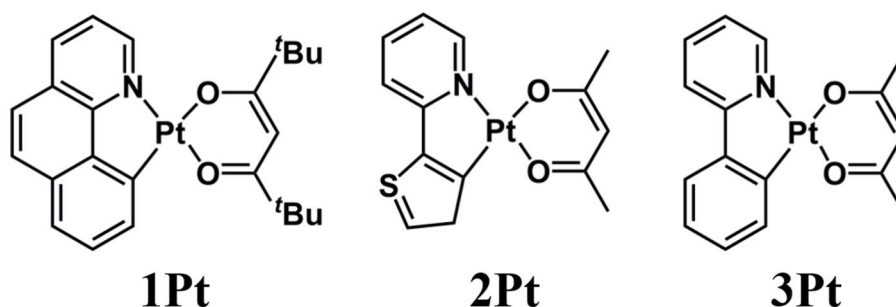

1Pt　　　　**2Pt**　　　　**3Pt**

Chart 2-3. Structures and abbreviations of platinum(II) complexes [Pt(*C^N*)(*O^O*)] and [Pt(*N^N-O^O*)].

[Pt(ppy)(acac)] (**3Pt**): Yield = 31 mg (29%). ^{1}H NMR (CDCl$_3$, ppm) δ = 9.00 (d, 1H), 7.80 (td, 1H), 7.62 (d, 2H), 7.44 (dd, 1H), 7.21 (td, 1H), 7.13–7.08 (m, 2H), 5.48 (s, 1H), 2.01 (d, 6H). [195]Pt NMR (CDCl$_3$, ppm) δ = –2870. ESI-MS (CH$_3$CN) for PtC$_{16}$H$_{15}$NO$_2$: *m/z* 448 ([M+H]$^+$).

2-3-6. Preparations of the Clusters Dispersed in Polymer Matrices.

The present study employed a polyethyleneglycol dimethacrylate (PEG-DMA) matrix as a medium for *T*-controlled (3–300 K) spectroscopic and photophysical experiments, since a PEG-DMA matrix was highly transparent in the wavelength region studied and could be prepared conveniently.[8,9] Polyethyleneglycol dimethacrylate 550 purchased from Sigma-Aldrich Co., Ltd. was purified by passing through an aluminum column with acetone as an eluent. A mixture of polyethyleneglycol dimethacrylate 550 (~10 mL), a cluster complex dissolved in a minimum amount of acetone (~5×10^{-5} mol/dm^3), and 2,2-azobis(2,4-dimethylvaleronitrile) (10 wt%, purchased from Wako Pure Chemical Co., Ltd. and used as supplied) as a polymerization initiator in a Pyrex tube (inner diameter = 1 mm) was degassed *in vacuo* and, then, the solution was allowed polymerization at 50ºC for 5 h in a water bath. The cluster sample in the tube was evacuated thoroughly prior to *T*-controlled spectroscopic and photophysical measurements to remove volatile chemicals and the resultant PEG-DMA block was isolated from the tube as a sample.

2-4.   Physical Measurements

Cyclic (CV) and differential pulse voltammetries (DPV) were carried out by using an ALS/701D electrochemical analyzer (ALS Co., Ltd.) at 298K. The acetone solutions of **1X**–**17X** (1.0×10^{-3} M (= mol/dm^3)) containing 0.1 M TBA$^+$(PF$_6$)$^-$ as a supporting electrolyte were deaerated by purging an Ar-gas stream prior to the measurements. The working, auxiliary, and reference electrodes were glassy carbon (ALS Co., Ltd., area: 7.1 mm^2), platinum wire, and AgNO$_3$/Ag electrodes, respectively. The electrode potentials were calibrated with that of a ferrocenium/ferrocene (Fc$^+$/Fc) redox couple in acetone. The potential sweep rate was set 100 mV/s in CV, and DPV was conducted with 50 mV height pulses (0.02 s duration) being stepped by 4 mV intervals (2.0 s interval between the two pulses). The redox potentials were evaluated by the peak values of the differential pulse voltammograms.

Absorption and corrected emission spectra of the clusters in acetone or CH$_3$CN were recorded on a UV-vis spectrophotometer (Hitachi Ltd., U-3900) and a red-sensitive multichannel photodetector (Hamamatsu Photonics K.K., PMA-12), respectively. For time-resolved emission spectroscopy, a pulsed Nd^{3+}:YAG laser (LOTIS TII Ltd., LS-2127, 355 nm, pulse-width ~10 ns) was used as an excitation light source. The excitation laser power was set 100 μJ/pulse or < 10 μJ/pulse for the lifetime measurements of the clusters in acetone (298 K) or crystalline phases (3 K < *T* < 300 K), respectively. The emission lifetimes of the clusters were determined by using a streak scope (Hamamatsu Photonics K.K., C4334) at 355 nm laser pulse excitation. The absolute

emission quantum yields of the clusters in both solution (acetone or CH_3CN) and crystalline phases were determined by using a C9920-02 system equipped with an integration sphere and a red-sensitive PMA-12 photodetector (Hamamatsu Photonics K.K.)[10] at 400 nm excitation. The absorbance of the sample solution was set < 0.05 at the excitation wavelength and the solution was deaerated thoroughly by purging an Ar-gas stream for 20 min prior to the experiments. For emission spectroscopy in the solid state, a cluster sample was placed between two non-fluorescent quartz plates, and the sample was deaerated by purging an Ar-gas stream prior to the experiments. For *T*-controlled experiments in 3 K < *T* < 300 K, the sample cluster dispersed in polymer matrices or crystalline samples placed between two quartz plates was set in a liquid-He cryostat system (Oxford Instruments, OptistatCF) to control the sample temperature in ±0.1 K.

2-5.   Single Crystal X-ray Diffraction Measurements

X-Ray diffraction data were accumulated by using an AFC-7R Mercury CCD (Rigaku Corp.) with graphite monochromated Mo Kα radiation ($\lambda = 0.7108$ Å) or XtaLAB Synergy Hypix diffractometer (Rigaku Corp.) with graphite monochromated Cu Kα radiation ($\lambda = 1.5418$ Å). Each single crystal was mounted on a MicroMount using a paraffin oil. The crystal was cooled to –123 °C using an N_2-gas-flow type temperature controller. Diffraction data were collected by CrysAlis PRO software.[11] The structures were solved by the direct method with SHELXT.[12] Structural refinement was done by full-matrix least-squares treatment using SHELXL2013.[13] Non-hydrogen atoms were refined anisotropically, and the positions of hydrogen atoms were refined using riding model. All calculations were conducted using Olex 2 crystallographic software package.[14] Cambridge Crystallographic Data Center (CCDC) numbers: 1501863 (**4Br**), 1501864 (**5Br**), 1848452 (**6Br**), 1501865 (**7Br**), 1522264 (**8Br**), 1848453 (**9Br**), 1501866 (**10Br**), 1848454 (**11Br**), 1848453 (**12Br**), 1501867 (**13Br**), 1522263 (**14Br**) 1501868 (**15Br**), 899509 (**16Br**),[15] 783750 (**17Br**),[5] 1027966 (**5I**), 1501869 (**7I**), 1472152 (**8I**), 1027965 (**10I**), 1027964 (**13I**), 1501870 (**15I**), 783751 (**16I**),[16], 783751 (**17I**).[5]

2-6.   Analysis of Temperature-Dependent Emission

The lowest-energy excited triplet (T_1) state of an octahedral hexamolybdenum(II) cluster having O_h symmetry is assigned to $^3T_{1u}$ originated from (t_{2g}, t_{1u}) configuration. Owing to SOC, the $^3T_{1u}$ state splits into five spin-sublevels (Φ_n), E_u, B_{2u}, E_u, T_{1u}, and A_{2u}, as shown in Scheme 2-1.[17,18] In the approximation of the first-order SOC, T_{2u} and E_u located in the lowest energy are degenerate. The T_{1u} and A_{1u} sublevels are located above T_{2u} and E_u and, thus, the energy order is T_{2u}, E_u < T_{1u} < A_{1u}. By considering the second-order SOC, the degeneracy between T_{2u} and E_u is lifted, giving rise to splitting into two sublevels with T_{2u} being lower in energy than E_u. Baudron et al. reported that a 23-electron oxidized cluster, $[\{Re_6S_8\}(CN)_6]^{3-}$, regarded as the electronic structure similar to that in the excited state of a hexamolybdenum(II) cluster, experienced Jahn-Teller distortion.[19] On the basis of low temperature X-ray studies, they showed that the *trans*-[Re-to-Re] distances in

the cluster core varied in different manners and this gave rise to symmetry lowering of the cluster from O_h to D_{4h} or D_{2h} at low temperature. Gray et al. also reported symmetry lowering from O_h to D_{4h} in the excited states of various haxarhenium(III) clusters.[20] Furthermore, Costuas et al. have demonstrated that $[\{Mo_6Br_8\}Br_6]^{2-}$ is distorted structurally from O_h to C_j or D_{3d} symmetry.[21] Assuming symmetry lowering from O_h to D_{4h} as an example, the lowest-energy lying T_{2u} state of the cluster is predicted to split into E_u and B_{2u} though the energy order of E_u and B_{2u} is unknown. The sequence of the splitting energy of the lowest-energy (Φ_1, E_u or B_{2u}) and higher-energy spin sublevels (Φ_2–Φ_5, ΔE_{1n}; $n = 2$–5) is predicted to be $\Delta E_{12} < \Delta E_{13} < \Delta E_{14} < \Delta E_{15}$ since the E_u (Φ_3) or B_{2u} (Φ_2) state is generated by second-order SOC or Jahn-Teller distortion, respectively

Among the five spin-sublevels, only T_{1u} (Φ_4) can couple with the ground state by an electronically-allowed dipole transition and, therefore, is emissive with a short emission lifetime (τ_{em}), while the emission transitions from other spin-sublevels to the ground state are forbidden and gain allowed characters only by vibronic coupling.[18] At low T, population of E_u (or B_{2u}, Φ_1) is dominant and, therefore, the observed τ_{em} value associated with the whole excited triplet state could be very long owing to forbidden transition. On the other hand, thermal population from E_u (or B_{2u}, Φ_1) to T_{1u} (Φ_4) should give rise to a decrease in τ_{em}.[17] Furthermore, since T_{1u} is emissive, while the emission from A_{1u} (Φ_5) is forbidden as mentioned above, the emission from A_{1u} (Φ_5) would be screened by relatively intense emission from T_{1u} (Φ_4) and, therefore, will not be observed experimentally. In total, four spin-sublevels (Φ_n, $n = 1$–4) contribute to the emission characteristics of the cluster. The photophysical properties of the clusters therefore should be explained by the four-spin-sublevel model in Scheme 2-1.

According to the four-spin-sublevel model, the T-dependent τ_{em} data ($\tau(T)$) of a cluster can be expressed by the Boltzmann-factor weighted sum of τ_n given by eq. 2-1,[17,18]
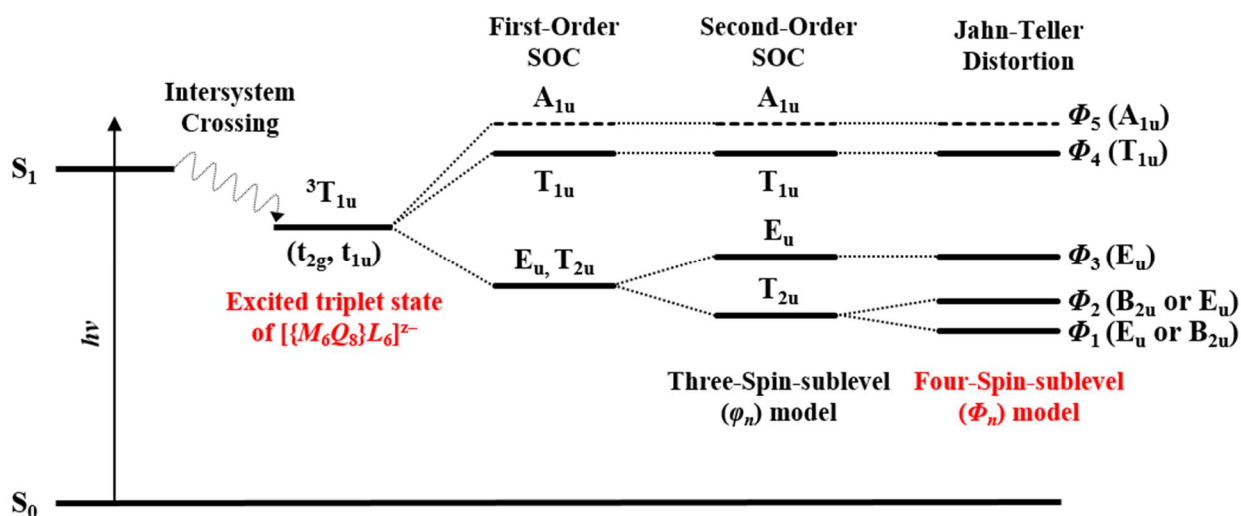
Scheme 2-1. Excited triplet state spin-sublevel (Φ_n) model for the emission from octahedral hexametal clusters.

$$\tau(T) = \frac{\Sigma g_n \exp(-\Delta E_{1n}/k_BT)}{\Sigma \dfrac{g_n \exp(-\Delta E_{1n}/k_BT)}{\tau_n}} \tag{2-1}$$

where g_n and τ_n are the multiplicity ($g_1 = g_3 = 2$, $g_2 = 1$, and $g_4 = 3$) and the emission lifetime of each Φ_n ($n = 1$–4), respectively, and ΔE_{1n} is the energy separation between the Φ_1 and Φ_n spin-sublevels.

Upon evaluation of the ΔE_{1n} values by the analysis of the $\tau(T)$ data by eq. 2-1, the emission spectrum of the cluster at a given T can be simulated as the Boltzmann-factor weighted sum of the Φ_n emission spectrum by eq. 2-2,[19]

$$I(\tilde{v}, T) = k_r^1 F(\tilde{v} - \tilde{v}_1) + k_r^2 F(\tilde{v} - \tilde{v}_2) \exp(-\frac{\Delta E_{12}}{k_BT})$$

$$+ k_r^3 F(\tilde{v} - \tilde{v}_3) \exp(-\frac{\Delta E_{13}}{k_BT}) + k_r^4 F(\tilde{v} - \tilde{v}_4) \exp(-\frac{\Delta E_{14}}{k_BT}) \tag{2-2}$$

where k_r^n is the radiative rate constant of Φ_n relative to that of Φ_1 (i.e., $k_r^1 = 1.0$). $F(\tilde{v} - \tilde{v}_n)$ and $\tilde{v}_n$ are a spectral Gaussian function and the emission maximum energy of each Φ_n, respectively, and $F(\tilde{v} - \tilde{v}_n)$ is given by eq. 2-3,[19]

$$F(\tilde{v} - \tilde{v}_n) = \frac{1}{fwhm(\Phi_n)\sqrt{\dfrac{\pi}{2}}} \exp\left[-2\left(\frac{\tilde{v} - \tilde{v}_n}{fwhm(\Phi_n)}\right)^2\right] \tag{2-3}$$

where $fwhm(\Phi_n)$ represents the full-width at half maximum (*fwhm*) of the emission spectrum of each Φ_n. Since the thermal fluctuation of each Φ_n level becomes large with increasing in T, the present study assumes that $fwhm(\Phi_n)$ at a given T is the same for $n = 1$–4 but varies with T.

2-7.   Computational Chemistry

Density functional theory (DFT), as implemented in Gaussian 09W program,[22] was used for all calculations. The split-valence triple-zeta basis sets, SDD[23,24] and 6-311G++(d,p),[25] were used for platinum and other elements, respectively. DFT calculations employed long range correlation type B3LYP functional based on Coulomb-attenuating method (CAM-B3LYP).[26] The high spin states (triplet) were calculated by unrestricted-CAM-B3LYP. Vibrational frequency calculations were carried out to confirm the optimized structures as global minimum energy (i.e., no imaginary frequencies). Natural population analysis was carried out for the optimized structures with the same level of theory.[27] In all DFT calculations, the ultrafine integration grid was used.

2-8.   Summary and Conclusions

This chapter described the synthesis of the octahedral hexamolybdenum(II) clusters and cyclometalated platinum(II) complexes studied in this thesis. All of the complexes including the novel twenty-one octahedral

hexamolybdenum(II) clusters were synthesized successfully by the similar procedures to those in the previous reports. Furthermore, the details on the physical measurements, the computational chemistry, and the four spin-sublevel model for the analysis of the *T*-dependent emission from an octahedral hexametal cluster were described. The fundamental idea of the analysis of *T*-dependent emissions is same with that by Azumi et al. on the three spin-sublevel model. However, the present study has demonstrated that Jan-Teller distortion in the excited state of the cluster plays an important role and the participation of the four spin-sublevel has been shown to be essential to explain the *T*-dependent emission of the cluster in 3 K < *T* < 300 K, instead of the three-spin-sublevel model by Azumi et al. The study has shown that the *T*-dependence of the *fwhm* value of the emission spectrum of the spin-sublevel is also very important to reproduce the observed emission spectrum of the cluster at a given *T*.

2-9.　References

(1)　Pospech, J.; Tlili, A.; Spannenberg, A.; Neumann, H.; Beller, M. Regioselective Ruthenium-catalyzed Carbonylative Direct Arylation of Five-membered and Condensed Heterocycles. *Chem. Eur. J.* **2014**, *20*, 3135–3141

(2)　Kolesnichenko, V.; Messerle, L. Facile Reduction of Tungsten Halides with Nonconventional, Mild Reductants. 2. Four Convenient, High-Yield Solid-State Synthesis of the Hexatungsten Dodecachloride Clusters W_6Cl_{12} and $(H_3O)_2[W_6(\mu_3\text{-}Cl)_8Cl_6](OH_2)_x$, Including New Cation-Assisted Ternary Routes. *Inorg. Chem.* **1998**, *37*, 3660–3663.

(3)　Sheldon, J. C. Bromo- and Iodo-Molybdenum(II) Compounds. *J. Chem. Soc.* **1962**, 410–415.

(4)　Hogue, R. D.; McCarley, R. E. Chemistry of Polynuclear Metal Halides. V. Reactions and Characterization of Compounds Containing Tungsten Halide Cluster Species. *Inorg. Chem.* **1970**, *7*, 1354–360.

(5)　Sokolov, M. N.; Mihailov, M. A.; Peresypkina, E. V.; Brylev, K. A.; Kitamura, N.; Fedin, V. P. Highly Luminescent Complexes $[Mo_6X_8(n\text{-}C_3F_7COO)_6]^{2-}$ (X = Br, I). *Dalton Trans.* **2011**, *40*, 6375–6377.

(6)　Godbert, N.; Pugliese, T.; Aiello, I.; Bellusci, A.; Crispini, A.; Ghedini, M. Efficient, Ultrafast, Microwave-Assisted Syntheses of Cycloplatinated Complexes. *Eur. J. Inorg. Chem.* **2007**, 5105–5111.

(7)　Che, C.-M.; Kwok, C.-C.; Lai, S.-W.; Rausch, A. F.; Finkenzeller, W. J.; Zhu, N.; Yersin, H. Photophysical Properties and OLED Applications of Phosphorescent Platinum(II) Schiff Base Complexes. *Chem. Eur. J.* **2010**, *16*, 233–247.

(8)　Knight, T. E.; Goldstein, A. P.; Brennaman, M. K.; Cardolaccia, T.; Pandya, A.; De Simone, J. M.; Meyer, T. J. Influence of the Fluid-to-Film Transition on Photophysical Properties of MLCT Excited States in a Polymerizable Dimethacrylate Fluid. *J. Phys. Chem. B* **2011**, *115,* 64–70.

(9)　Zanoni, K. P. S.; Kariyazaki, B. K.; Ito, A.; Brennaman, M. K.; Meyer, T. J. Blue-Green Iridium(III)

Emitter and Conprehensive Photopysical Elucidation of Heteroleptic Cyclometalated Iridium(III) Complexes. *Inorg. Chem.* **2014**, *53*, 4089–4099.

(10) Suzuki, K.; Kobayashi, A.; Kaneko, S.; Takehira, K.; Yoshihara, T.; Ishida, H.; Shiina, Y.; Oishi, S.; Tobita, S. Reevaluation of Absolte Luminescence Quantum Yields of Standard Solutions Using a Spectrometer with an Integrating Sphere and a Back-thinned CCD-detector. *Phys. Chem. Chem. Phys.* **2009**, *11*, 9850–9860.

(11) CrysAlisPro; Agilent Technologies Ltd. 2014, Abingdon, Oxfordshire.

(12) SHELXT; Sheldrick, G. M. *Acta Cryst. A* **2015**, *71*, 3–8.

(13) SHELX2013; Sheldrick, G. M. *Acta Crystallogr. Sect. A* **2008**, *64*, 112.

(14) Olex^2 1.2.7; Dolomanov, O. V.; Bourhis, L. J.; Gildea, R. J.; Howard, J. A. K.; Puschmann, H. *J. Appl. Cryst.* **2009**, *42*, 339–341.

(15) Kirakci, K.; Kubát, P.; Dušek, M.; Fejfarová, K.; Šícha, V.; Mosinger, J.; Lang, K. A Highly Luminescent Hexanuclear Molybdenum Cluster – A Promising Candidate toward Photoactive Materials. *Eur. J. Inorg. Chem.* **2012**, 3107–3111.

(16) Kirakci, K.; Kubát, P.; Langmaier, J.; Polívka, T.; Fuciman, M.; Fejfarová, K.; Lang, K. A Comparative Study of the Redox and Excited State Properties of (nBu$_4$N)$_2$[Mo$_6$X$_{14}$] and (nBu$_4$N)$_2$[Mo$_6$X$_8$(CF$_3$COO)$_6$] (X = Cl, Br, or I). *Dalton Trans.* **2013**, *42*, 7224–7232.

(17) Azumi, T.; Saito, Y. Electronic Structures of the Lower Excite Triplet Sublevels of Hexanuclear Molybdenum(II) Chloride Cluster. *J. Phys. Chem.* **1988**, *92*, 1715–1721.

(18) Kitamura, N.; Ueda, Y.; Ishizaka, S.; Yamada, Y.; Aniya, M.; Sasaki, Y. Temperature Dependent Emission of Hexarhenium(III) Clusters [Re$_6$(μ$_3$-S)$_8$X$_6$]$^{4-}$ (X = Cl$^-$, Br$^-$, and I$^-$): Analysis by Four Excited Triplet-State Sublevels. *Inorg. Chem.* **2005**, *44*, 6308–6313.

(19) Baudron, S. A.; Deluzet, A.; Boubekeur, K.; Batail, P. Jahn–Teller Distortion of the Open-shell 23-elecron Cgalcogenide Rhenium Cluster Cores in Crystals of the Series, {[Re$_6$Q$_8$]$^{3+}$(X$^-$)$_6$}$^{3-}$ (Q = S, Se; X = Cl, CN). *Chem. Commun.* **2002**, 2124–2125.

(20) Gray, T. G.; Rudzinski, C. M.; Meyer, E. E.; Nocera, D. G. Excite-state Distortion of Rhenium(III) Sulfide and Selenide Clusters. *J. Phys. Chem. A* **2004**, *108*, 3238–3243.

(21) Costuas, K.; Garreau, A.; Bulou, A.; Fontaine, B.; Cuny, J.; Gautier, R.; Mortier, M.; Molard, Y.; Duvail, J.-L.; Faulques, E.; Cordier, S. Combined Theoretical and Time-resolved Photoluminescence Investigations of [Mo$_6$Br$^i_8$Br$^a_6$]$^{2-}$ Metal Cluster Units: Evidence of Dual Emission. *Phys. Chem. Chem. Phys.* **2015**, *17*, 28574–28585.

(22) Gaussian 09, Revision A.02; Frisch, M. J.; Trucks, G. W.; Schlegel, H. B.; Scuseria, G. E.; Robb, M. A.; Cheeseman, J. R.; Scalmani, G.; Barone, V.; Petersson, G. A.; Nakatsuji, H.; Li, X.; Caricato, M.; Marenich, A.; Bloino, J.; Janesko, B. G.; Gomperts, R.; Mennucci, B.; Hratchian, H. P.; Ortiz, J. V.;

Izmaylov, A. F.; Sonnenberg, J. L.; Williams-Young, D.; Ding, F.; Lipparini, F.; Egidi, F.; Goings, J.; Peng, B.; Petrone, A.; Henderson, T.; Ranasinghe, D.; Zakrzewski, V. G.; Gao, J.; Rega, N.; Zheng, G.; Liang, W.; Hada, M.; Ehara, M.; Toyota, K.; Fukuda, R.; Hasegawa, J.; Ishida, M.; Nakajima, T.; Honda, Y.; Kitao, O.; Nakai, H.; Vreven, T.; Throssell, K.; Montgomery Jr., J. A.; Peralta, J. E.; Ogliaro, F.; Bearpark, M.; Heyd, J. J.; Brothers, E.; Kudin, K. N.; Staroverov, V. N.; Keith, T.; Kobayashi, R.; Normand, J.; Raghavachari, K.; Rendell, A.; Burant, J. C.; Iyengar, S. S.; Tomasi, J.; Cossi, M.; Millam, J. M.; Klene, M.; Adamo, C.; Cammi, R.; Ochterski, J. W.; Martin, R. L.; Morokuma, K.; Farkas, O.; Foresman, J. B.; Fox, D. J. Gaussian, Inc., Wallingford CT, **2016**.

(23) Fuentealba, P.; Preuss, H.; Stoll, H.; von Szentpály, L. A Proper Account of Core-polarization with Pseudopotentials: Single Valence-Electron Alkali Compounds. *Chem*. *Phys*. *Lett*. **1982**. *89*, 418–422

(24) Dunning Jr., T. H.; Hay, P. J. *Modern Theoretical Chemistry*, Plenum: New York, **1977**, *3*, 1–28.

(25) Krishnan, R.; Binkley, J. S.; Seeger, R.; Pople, J. A. Self-consistent Molecular Orbital Methods. XX. A Basis Set for Correlated Wave Functions. *J. Chem*. *Phys*. **1980**, *72*, 650–654.

(26) Yanai, T.; Tew, D. P.; Handy, N. C. A New Hybrid Exchange-correlation Functional Using the Coulomb-attenuating Method. *Chem*. *Phys*. *Lett*. **2004**, *393*, 51–57.

(27) NBO Version 3.1; Glendening, E. D.; Reed, A. E.; Carpenter, J. E.; Weinhold, F.

Chapter 3

Redox, Spectroscopic, and Photophysical

Properties of [{Mo$_6$X$_8$}Y$_6$]$^{2-}$ (X, Y = Cl, Br or I)

3-1. Introduction

Zero-magnetic-field splitting (zfs) in the lowest-energy excited triplet (T_1) state of a transition metal complex has been studied frequently[1-5] and, as an example, the zfs energies in the T_1 states of platinum(II) complexes have been studied systematically by Yersin and co-workers.[5] In contrast, the reports on the temperature(T)-dependent emission of octahedral hexametal clusters and its analysis based on the spin-sublevels model in the T_1 state, providing the zfs parameters described in Chapter 1, are limited to the following five complexes: $[\{M_6Cl_8\}Cl_6]^{2-}$ (M = Mo(II) or W(II)) and $[\{Re_6S_8\}X_6]^{4-}$ (X = Cl, Br, or I).[6-8] For systematic and detailed investigations on the T_1 state of an octahedral hexanuclear metal cluster, it is therefore necessary to check the validity of the four-spin-sublevel (Φ_n) model.[6] To confirm the applicability of the four-spin-sublevel (Φ_n) model to other octahedral hexametal clusters, this thesis focuses on terminal halide hexamolybdenum(II) clusters $[\{Mo_6X_8\}Y_6]^{2-}$ (X, Y = Cl, Br, or I. nX), since the clusters possess simple ligand structures and this enables one to neglect complicated structural factors represented by steric effects of the terminal ligands on the electronic structure of the cluster. Furthermore, a series of the clusters are advantageous to allow systematic combinations of X and Y in $[\{Mo_6X_8\}Y_6]^{2-}$: 3×3 combinations of the bridging and terminal ligands; see Chart 3-1.

An octahedral hexamolybdenum(II) has been known since 1960,[9] and the emission properties (maximum wavelength (λ_{em}), quantum yield (Φ_{em}), and lifetime (τ_{em})) have been first reported by Marverick et al. for $[\{Mo_6Cl_8\}Cl_6]^{2-}$ (**1Cl**).[10] After the first report on the emission properties of **1Cl**, those of analogous molybdenum(II) bromide ($[\{Mo_6Br_8\}Br_6]^{2-}$, **2Br**)[11-13] and iodide clusters ($[\{Mo_6I_8\}I_6]^{2-}$, **3I**)[12,13] in deaerated CH_3CN have been hitherto reported. Besides these three molybdenum(II) clusters, the λ_{em} values of $[\{Mo_6Br_8\}Y_6]^{2-}$ (**nBr**) in CH_2Cl_2 and the τ_{em} values of **nCl** and **nBr** in acetone have been also reported.[14,15] On the other hand, although the synthesis and the X-ray crystal structures of $[\{Mo_6I_8\}Cl_6]^{2-}$ (**1I**) and $[\{Mo_6I_8\}Br_6]^{2-}$ (**2I**) have been reported,[16] no emission data of these clusters is available until the date, despite these clusters have been also predicted to be luminescent in solution.[17] To the best of author's knowledge, although all of **nX** are reported to be emissive, the reported emission data[10–15] summarized in Table 1 are scatted between the literatures and are not enough for detailed discussions on the emission properties of the clusters. Therefore, there
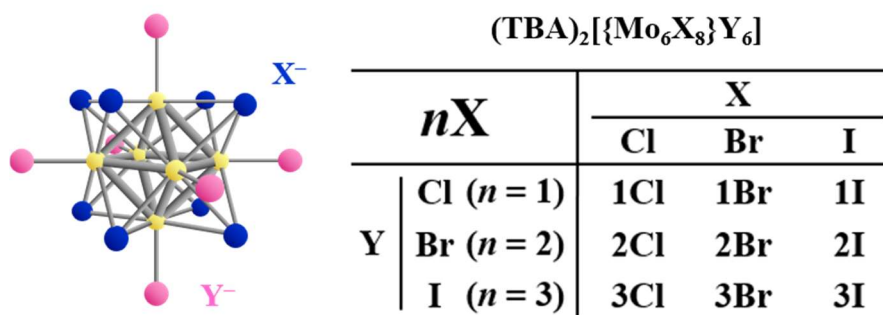
$(TBA)_2[\{Mo_6X_8\}Y_6]$

nX		X		
		Cl	Br	I
Y	Cl ($n=1$)	1Cl	1Br	1I
	Br ($n=2$)	2Cl	2Br	2I
	I ($n=3$)	3Cl	3Br	3I

Chart 3-1. Structures and abbreviations of halide clusters $[\{Mo_6X_8\}Y_6]^{2-}$.

Table 3-1. Emission properties of *n*X in solution at ambient temperature reported in the literatures.[10-15]

$[\{Mo_6X_8\}Y_6]^{2-}$			X		
			Cl	Br	I
λ_{em} / nm	Y	Cl	744,[12] 805[11]	683[14]	–
		Br	–	696,[14] 757,[12], 825[11]	–
		I	–	705[14]	730[12]
Φ_{em}	Y	Cl	0.15,[12] 0.19[11,13]	–	–
		Br	–	0.13,[12] 0.23[11,13]	–
		I	–	–	0.12,[12] 0.16[13]
τ_{em} / μs	Y	I	180[12,13,15]	190[15]	–
		Br	140[15]	110,[11] 120,[15], 130[11], 135[12]	–
		I	86[15]	71[15]	84,[13] 90[12]

The data in ref 14 and 15 are those in CH_2Cl_2 and acetone, respectively.

is no systematic study on the spectroscopic and emission characteristics of *n*X under the same experimental conditions. It is clear that a systematic study on the spectroscopic and emission properties of *n*X is the fundamental basis for the discussion on the *T*-dependent emission characteristics of the clusters based on the spin-sublevel model.

In this chapter, the redox, spectroscopic, and photophysical properties of the terminal halide clusters $[\{Mo_6X_8\}Y_6]^{2-}$ (X, Y = Cl, Br, or I. *n*X) in solution and/or crystalline phases at ambient temperature are described. Furthermore, the *T*-dependences of the emissions from *n*X in polymer matrixes in 3–300 K and their analysis by the four-spin-sublevel (Φ_n) model are described. On the basis of such systematic studies, the emission characteristics of *n*X are discussed in special references to the zfs parameters.

3-2. Absorption and Redox Properties

3-2-1. Absorption Spectra of $[\{Mo_6X_8\}Y_6]^{2-}$ in CH_3CN at 298 K.

Figure 3-1a shows the absorption spectra of $[\{Mo_6X_8\}Y_6]^{2-}$ (*n*X: X = Cl, Br, or I; Y = Cl (*n* = 1), Br (*n* = 2), or I (*n* = 3)) in the wavenumber region of $\tilde{v}$ = (18–50) × 10^3 cm^{-1} (wavelength (λ) = 200–560 nm), while those in an expanded scale in the visible region ($\tilde{v}$ = (18–30) × 10^3 cm^{-1}, λ = 330–560 nm) are shown in Figure 3-1b. The lowest-energy absorption band energies ($\tilde{v}_a$) and the relevant molar absorption coefficients of the clusters (ε) are summarized in Table 3-2. For a given $\{Mo_6X_8\}^{4+}$-core cluster, $\tilde{v}_a$ was shifted to a lower-energy in the sequence Y = Cl > Br > I. As an example, the $\tilde{v}_a$ value of **1Cl**, **2Cl**, or **3Cl** was 29.2×10^3, 27.3×10^3, or 26.5×10^3 cm^{-1}, respectively, and the lower-energy shift similar to $\tilde{v}_a$ of X = Cl (*n*Cl) was also confirmed for that of X = Br (*n*Br) or X = I (*n*I). For given terminal ligands (Y_6), furthermore, the $\tilde{v}_a$ value was shifted to a lower-energy in the sequence $\{Mo_6Cl_8\}^{4+}$ < $\{Mo_6Br_8\}^{4+}$ < $\{Mo_6I_8\}^{4+}$ irrespective of Y as seen in Table 3-2. The lower-
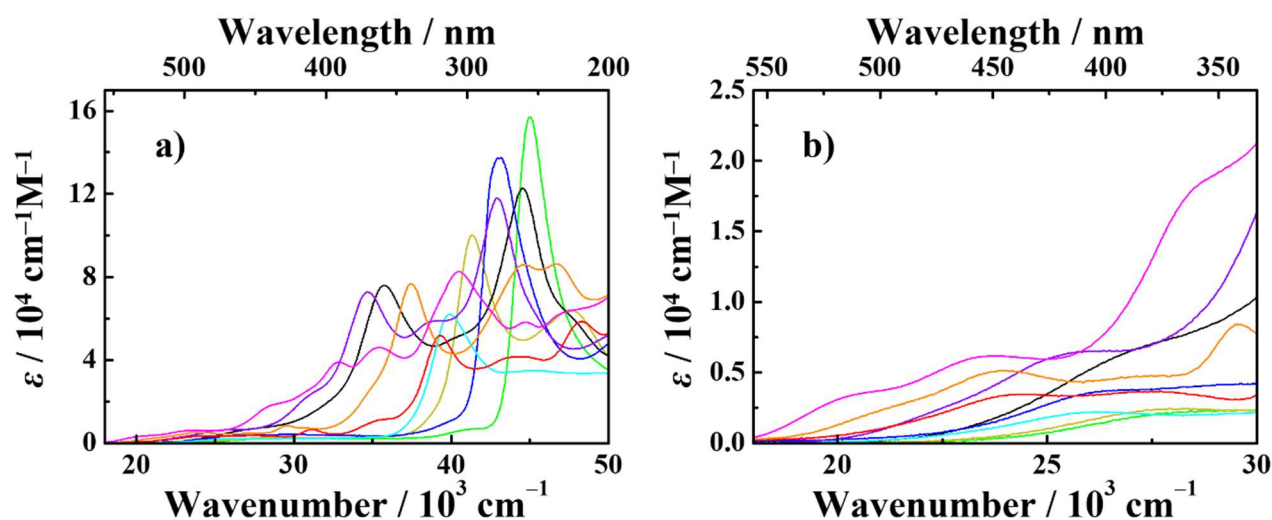
Figure 3-1. Absorption spectra of $[\{Mo_6X_8\}Y_6]^{2-}$ in CH_3CN at 298 K (a) and those in an expanded ε scale in the visible region (b). The color legend is as follows; black (**1Cl**), dark yellow (**2Cl**), green (**3Cl**), purple (**1Br**), cyan (**2Br**), blue (**3Br**), red (**1I**), orange (**2I**), and pink (**3I**).

energy shift of the absorption maximum ($\Delta\tilde{\nu}_a$) by an X variation in $[\{Mo_6X_8\}Y_6]^{2-}$ for given Y shown by $\Delta\tilde{\nu}_a(X)$ in Table 3-2 ($-3500 \sim -6500$ cm^{-1}) is much larger than that in a Y variation for given X: $\Delta\tilde{\nu}_a(Y) = -700 \sim -3900$ cm^{-1}. This will be very reasonable since the lowest-energy absorption band of the cluster is responsible for the metal-to-$\{Mo_6X_8\}^{4+}$-core electronic transition[17] and, thus, a variation of X should influence $\tilde{\nu}_a$ stronger than a Y variation in $[\{Mo_6X_8\}Y_6]^{2-}$. It is worth pointing out that the decreasing order of $\tilde{\nu}_a$ with X or Y in $[\{Mo_6X_8\}Y_6]^{2-}$ agrees very well with that of electronegativity (EN) of X/Y. The results demonstrate clearly that one of the factors governing $\tilde{\nu}_a$ is the π-electron-donating ability of X/Y.

3-2-2. Cyclic and Differential Voltammograms of $[\{Mo_6X_8\}Y_6]^{2-}$ in CH_3CN at 298 K.

In order to obtain information on the energy levels of the highest-energy occupied molecular orbital (HOMO) and the lowest-energy unoccupied MO (LUMO), electrochemical measurements of the clusters were conducted. In the present experiments, acetone was used as a solvent instead of using CH_3CN, since the solubility of the cluster in CH_3CN decreased in the sequence Y = Cl > Br > I for given X in $[\{Mo_6X_8\}Y_6]^{2-}$. In particular, the solubility of **3Cl** in CH_3CN was limited to $\sim 10^{-4}$ M, while those of the nine clusters in acetone were reasonably high enough for electrochemical measurements. It is worth nothing that the emission spectra of **nX** ($n = 1$–3. X = Cl, Br, or I) described in the following section §3-2-3 are insensitive to a solvent and the spectra in CH_3CN are almost comparable to those in acetone.

The CVs and DPVs of the clusters in acetone are shown in Figure 3-2, and the redox potentials determined by DPV are summarized in Table 3-3. Some of the clusters showed quasi-reversible oxidation waves (**1X**, **2Br**, and **2I**), while the oxidation waves of the other clusters (**2Cl**, and **3X**) were irreversible. Furthermore, all of the clusters exhibited irreversible reduction waves. The oxidation potential (E_{ox}) of the cluster was shifted to a

Table 3-2. Lowest-energy absorption band energies and the relevant molar absorption coefficients of $[\{Mo_6X_8\}Y_6]^{2-}$ in CH_3CN at 298 K.

$[\{Mo_6X_8\}Y_6]^{2-}$			X			$\Delta\tilde{v}_a(X)^{a)}$
			Cl	Br	I	/cm^{-1}
$\tilde{v}_a$ / 10^3 cm^{-1}	Y	Cl	29.2	25.9	23.9	−5300
(ε /10^3 M^{-1}cm^{-1})			(2.3) [342]	(3.5) [386]	(3.3) [419]	
[λ_a / nm]		Br	27.3	25.8	23.8	−3500
			(2.3) [366]	(2.1) [388]	(5.1) [421]	
		I	26.5	25.2	20.0	−6500
			(5.9) [377]	(6.1) [397]	(3.1) [500]	
$\Delta\tilde{v}_a(Y)^{a)}$ / 10^3 cm^{-1}			−2700	−700	−3900	–

a) The minus sign of the number represents the lower-energy shift of $\tilde{v}_a$ for an X ($\Delta\tilde{v}_a(X)$) or Y variation ($\Delta\tilde{v}_a(Y)$) for given Y or X, respectively, from the value for X, Y = Cl to that for I.

negative potential direction in X = Cl > Br > I (irrespective of Y) or in Y = Cl ≥ Br > I, though the values of **1Br** and **2Br** (X = Br) or **1I** and **2I** (X = I) were almost comparable with each other. The variation of E_{ox} with X for given Y ($\Delta E_{ox}(X) = -0.38 \sim -0.57$ in Table 3-3) is much larger than that of Y ($\Delta E_{ox}(Y) = -0.16 \sim -0.35$). This demonstrates that the oxidation of the cluster is responsible for that of the cluster core, $\{Mo_6X_8\}^{4+}$, whose assignment agrees very well with those by the literatures.[11,17] Although the E_{ox} values of (**1Br** and **2Br**) or (**1I** and **2I**) are exceptions as described above, the negative potential shift of E_{ox} by an X or Y variation agrees well with the decreasing order of EN(X/Y), demonstrating destabilization of the HOMO energy level with the decrease in the π-electron-donating ability of X or Y.

On the other hand, the reduction potential (E_{red}) of the cluster was shifted to a positive potential direction with a variation of Y irrespective of X in the sequence Y = Cl < Br < I with $\Delta E_{red}(Y) = +0.11 \sim +0.17$, while the potential was almost insensitive to a variation of X ($\Delta E_{red}(X) \leq 0.05$ in Table 3-3). The results indicate that the reduction of the cluster is governed primarily by nature of the terminal ligand, Y. The positive potential shifts of E_{red} with Y for given X in the decreasing order of EN(X/Y) is an opposite trend to the potential shift of E_{ox} with an X or Y variation. This indicates that the LUMO level of the cluster evaluated by E_{red} stabilizes in energy with the decrease in the π-electron-donating ability of X/Y. The (E_{ox}–E_{red}) value of the cluster, as a measure of the HOMO–LUMO energy gap, decreases in the sequence X, Y = Cl > Br > I: see Table 3-3. In practice, the $\tilde{v}_a$ value of the cluster correlates linearly with (E_{ox}–E_{red}) with the correlation coefficient (R^2) being 0.840 as seen in Figure 3-3. The present study therefore concludes that the absorption energy (or HOMO–LUMO energy gap) of the cluster is determined primarily by the π-electron-donating ability of X or Y in $[\{Mo_6X_8\}Y_6]^{2-}$; a stronger π-electron donating ability of X/Y gives rises to a larger HOMO–LUMO energy gap and, thus, a higher $\tilde{v}_a$ value.
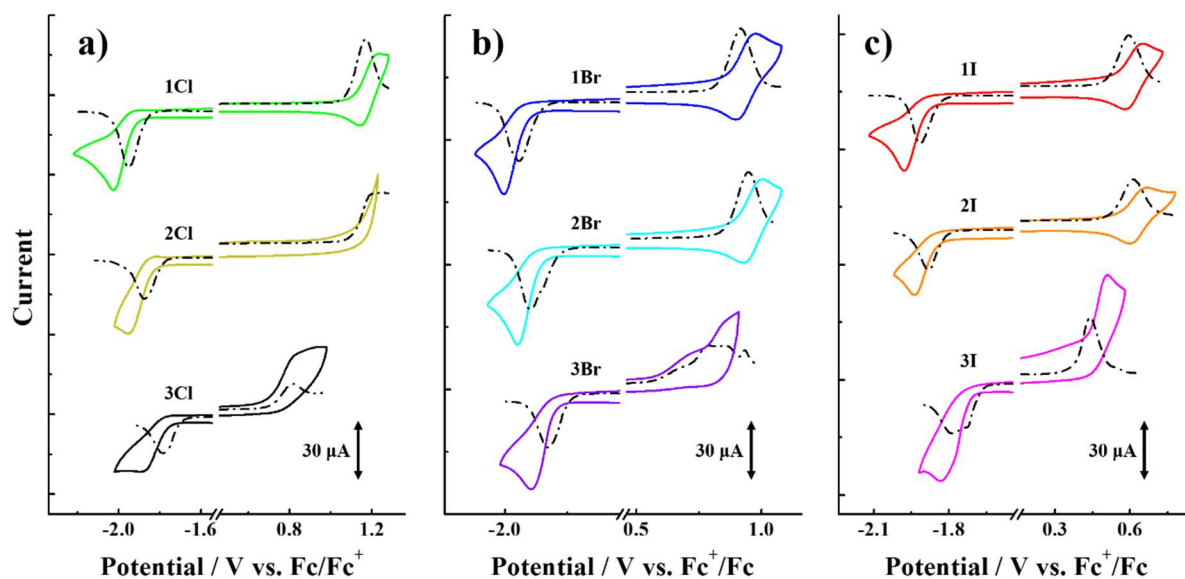
Figure 3-2. Cyclic voltammograms of (a) $[\{Mo_6Cl_8\}Y_6]^{2-}$, (b) $[\{Mo_6Br_8\}Y_6]^{2-}$, and (c) $[\{Mo_6I_8\}Y_6]^{2-}$ in acetone at 298 K. Differential pulse voltammograms are shown by the black broken curves. The color legend is the same with that in Figure 3-1.

3-3. Emission Properties

### 3-3-1. Emission Spectra of $[\{Mo_6X_8\}Y_6]^{2-}$ (X, Y = Cl, Br, or I) in CH₃CN at 298 K.

Figure 3-4 shows the emission spectra of **nX** in CH₃CN and crystalline phases, and the emission properties of **nX** are summarized in Table 3-4: emission maximum energy ($\tilde{v}_{em}$, wavelength (λ_{em})), full-width at half maximum (*fwhm*) of the spectrum, emission quantum yield (Φ_{em}), and emission lifetime (τ_{em}). As seen clearly in Figure 3-4, all of the clusters in both CH₃CN and crystalline phases at 298 K exhibit the structureless emission spectra. For a Y series (i.e., **nCl**, **nBr**, or **nI** series), the $\tilde{v}_{em}$ value in CH₃CN or crystalline phase was shifted to a lower-energy in Y = Cl > Br > I irrespective of X, which was in good accordance with the decreasing order of EN(Y). For an X series (i.e., (**1X**), (**2X**), or (**3X**) series), on the other hand, the $\tilde{v}_{em}$ value was shifted to a higher-energy in X = Cl ≤ Br < I irrespective of Y in both CH₃CN and crystalline phases, which was an opposite spectral shift to that by a Y variation: see Table 3-4. Reflecting such X/Y effects on $\tilde{v}_{em}$, the $\tilde{v}_{em}$ value by a variation of Y or X in $[\{Mo_6X_8\}Y_6]^{2-}$ shows a positive or negative correlation with (E_{ox}–E_{red}), respectively, as the data are shown in Figure 3-5. Despite the linear relationship between $\tilde{v}_a$ and (E_{ox}–E_{red}) irrespective of X and Y in Figure 3-3, that between $\tilde{v}_{em}$ and (E_{ox}–E_{red}) is categorized for a X or Y series. The result indicates that the $\tilde{v}_{em}$ value cannot be explained by EN(X/Y) alone and, thus, by the π-electron-donating ability of X/Y. This is due to the large *T*-dependences of the emission from $[\{Mo_6X_8\}Y_6]^{2-}$ clusters[6-8] and will be discussed in the following section §3-4.

The *fwhm* values of the emission spectra of the $\{Mo_6Cl_8\}^{4+}$- and $\{Mo_6Br_8\}^{4+}$-core clusters (**nCl** and **nBr**) shown in Table 3-5 were almost constant at around 4000 cm⁻¹ irrespective of Y and comparable with those

Table 3-3. Redox potentials of *n*X in acetone at 298 K.

$[\{Mo_6X_8\}Y_6]^{2-}$			X			$\Delta E_{ox}(X)^{a)}$ / V	$\Delta E_{red}(X)^{a)}$ / V	$(E_{ox}-E_{red})(X)^{b)}$ / V
			Cl	Br	I			
E_{ox} / V	Y	Cl	1.17	0.92	0.60	−0.57	−	−
		Br	1.03	0.95	0.61	−0.42	−	−
		I	0.82	0.79	0.44	−0.38	−	−
$\Delta E_{ox}(Y)^{a)}$ / V			−0.35	−0.16	−0.17	−	−	−
E_{red} / V	Y	Cl	−1.95	−1.94	−1.92	−	+0.03	−
		Br	−1.88	−1.90	−1.88	−	0.02$^{b)}$	−
		I	−1.78	−1.83	−1.79	−	0.05$^{b)}$	−
$\Delta E_{red}(Y)^{a)}$ / V			+0.17	+0.11	+0.13	−	−	−
$(E_{ox}-E_{red})(Y)$ / V	Y	Cl	3.12	2.86	2.52	−	−	0.60
		Br	2.91	2.85	2.49	−	−	0.42
		I	2.60	2.62	2.23	−	−	0.37
$\Delta E(E_{ox}-E_{red})(Y)^{b)}$ / V			0.52	0.24	0.29	−	−	−

a) The plus or minus sign of the number represents a positive or negative potential shift, respectively, for an X ($\Delta E_{ox}(X)$ or $\Delta E_{red}(X)$ for given Y) or Y variation ($\Delta E_{ox}(Y)$ or $\Delta E_{red}(Y)$ for given X) from the value for X, Y = Cl to that of I. b) Difference in the values for an X ($\Delta E(E_{ox}-E_{red})(X)$ for given Y) or Y variation ($\Delta E(E_{ox}-E_{red})(Y)$ for given X) from the value for X, Y = Cl to that of I.
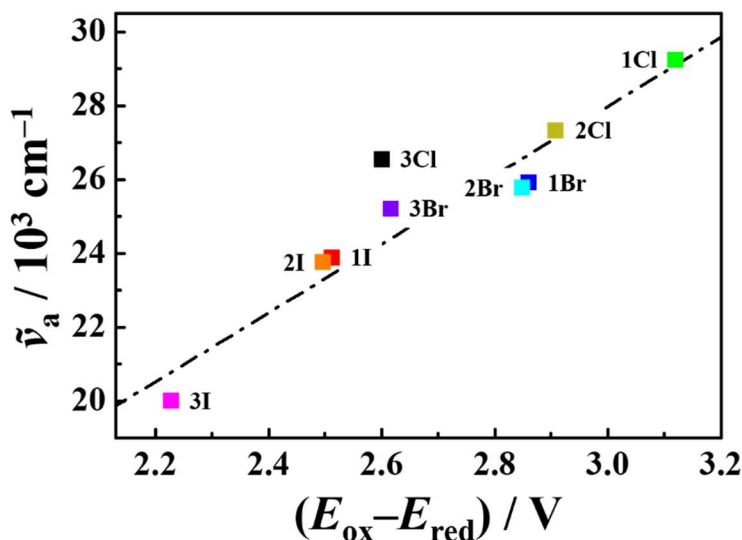
Figure 3-3. Relationship between $\tilde{v}_a$ in CH$_3$CN and $(E_{ox}-E_{red})$ in acetone at 298 K.

reported for various $[\{Mo_6X_8\}L_6]^{2-}$ clusters: X = Cl or Br, L = Cl, Br, aliphatic carboxylates, aromatic sulfonates, and so forth.[18,19] In the case of an $\{Mo_6I_8\}^{4+}$-core cluster series (*n*I), on the other hand, a variation of Y rendered that of *fwhm* in the sequence 2520 (**1I**) < 3230 (**2I**) < 4580 cm^{-1} (**3I**) in CH$_3$CN. It is worth emphasizing that,

although the *fwhm* values hitherto reported for $[\{Mo_6I_8\}L'_6]^{2-}$ (L' = aliphatic carboxylates, aromatic sulfonates, and so forth) are almost constant at 2170–3140 cm⁻¹,[18-23] the present study demonstrates that nature of Y also influences strongly the *fwhm* value of $[\{Mo_6I_8\}Y_6]^{2-}$. Since the emission spectrum of each cluster at 298 K is the sum of those of Φ_n and the contribution of the emission from each Φ_n to the spectrum at 298 K is determined by the zfs energies of the cluster.[6,8] Thus, the variation of the *fwhm* values of the clusters are also explained in terms of the zfs energies in the T_1 states of the clusters, which will be discussed in the following section §3-4.

3-3-2. Photophysical Properties of $[\{Mo_6X_8\}Y_6]^{2-}$ (X, Y = Cl, Br, or I) in CH₃CN at 298 K.

In CH₃CN at 298 K, a variation of X resulted in that of Φ_{em} in 0.09–0.19 (X = Cl: *n*Cl), 0.09–0.22 (X = Br: *n*Br), or 0.11–0.47 (X = I: *n*I), while that of Y gave rise to Φ_{em} to be 0.19–0.47 (Y = Cl: **1X**), 0.14–0.23 (Y = Br: **2X**), or 0.09–0.11 (Y = I: **3X**): see Table 3-4. Thus, all of the $[\{Mo_6X_8\}Y_6]^{2-}$ clusters are intense emitters and Φ_{em} of the cluster can be tuned in 0.09–0.47 by arbitrary choices of X and/or Y in $[\{Mo_6X_8\}Y_6]^{2-}$. Similar trends to those in CH₃CN can be also found in the crystalline phase as seen in Table 3-4. Among **nX**, $[\{Mo_6I_8\}Cl_6]^{2-}$ (**1I**) shows the highest Φ_{em} values in both CH₃CN (0.47) and crystalline phases (0.57). Furthermore, the cluster complexes in CH₃CN and crystalline phases showed single exponential decay as the temporal profiles being reported in Figure 3-6. The τ_{em} values of **nX** ranged in 85–300 or 50–170 μs in CH₃CN or crystalline phase, respectively. Thus, all of these clusters exhibit intense and long-lived emission at 298 K. Both Φ_{em} and τ_{em} values of the clusters for an X series (i.e., (**1X**), (**2X**), or (**3X**) series) in CH₃CN decrease in the sequence Y = Cl (Φ_{em} = 0.19–0.47, τ_{em} = 205–300 μs) > Br (0.14–0.23, 150–205 μs) > I (0.09–0.11, 85–100 μs), while those of a Y series (i.e., **nCl**, **nBr**, or **nI** series) increase in X = Cl (0.09–0.19, 100–205 μs) < Br (0.09–0.22, 85–220 μs) < I (0.11–0.47, 95–300 μs), though the Φ_{em} values of (**2Cl** and **2Br**) or (**3Cl** and **3Br**)
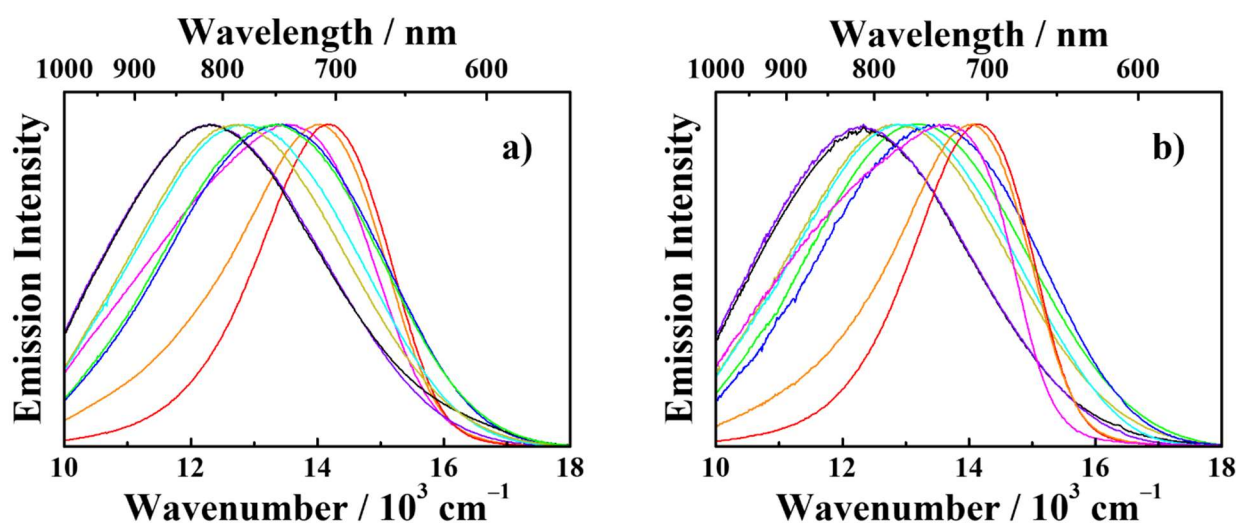

Figure 3-4. Corrected emission spectra of **nX** in CH₃CN (a) and crystalline phases (b) at 298 K under deaerated conditions. The color legend is the same with that in Figure 3-1.
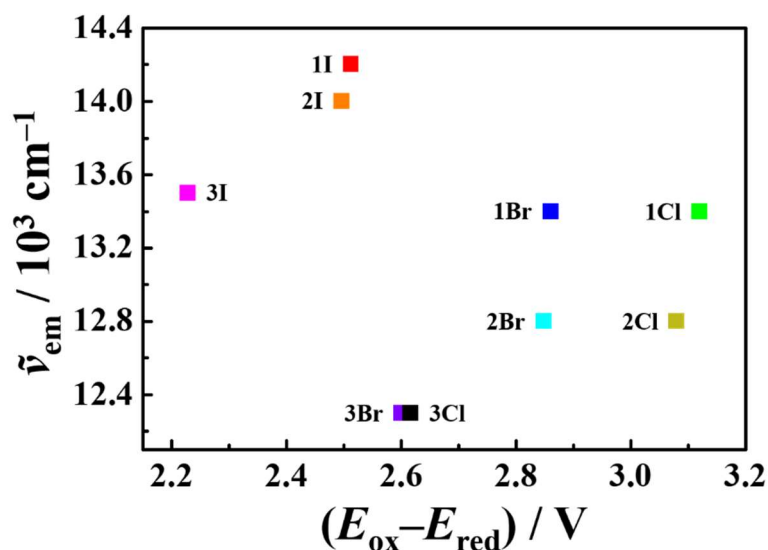
Figure 3-5. Relationship between $\tilde{\nu}_{em}$ in CH_3CN and (E_{ox}–E_{red}) in acetone.

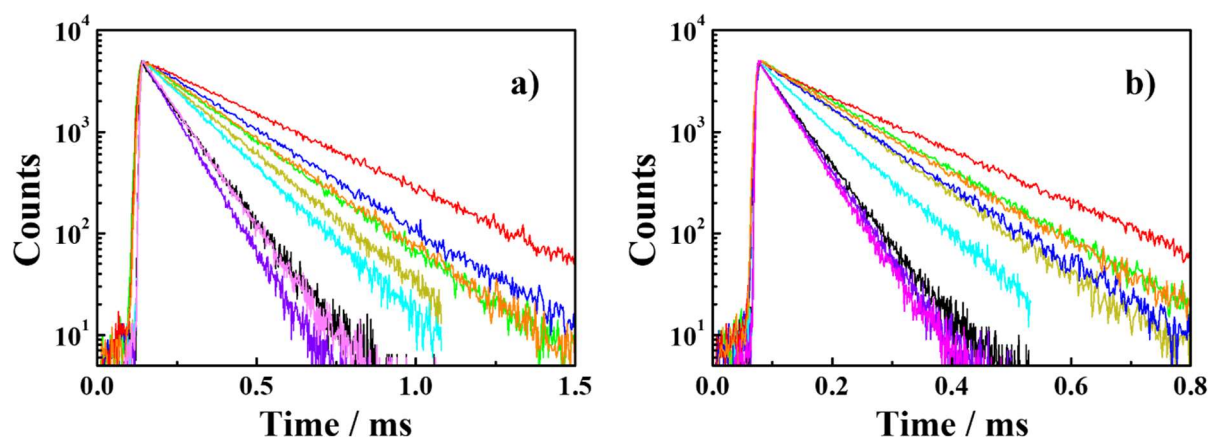**Figure 3-6**. Emission decay profiles of *n*X in CH_3CN (a) and crystalline phases (b) at 298 K under deaerated conditions. The color legend is the same with that in Figure 3-1.

are identical with each other (0.14 or 0.09, respectively) and τ_{em} of **3Br** (85 μs) is marginal between those of **3Cl** (100 μs) and **3I** (95 μs). It is worth emphasizing that the decreasing order of Φ_{em} or τ_{em} for a Y series for given X agrees very well with that of EN(Y), while the increasing order of Φ_{em} or τ_{em} for an X series for given Y shows an opposite trend to that of EN(X); the τ_{em} values of an X series for Y = Br (**2X**) and I (**3X**) are marginal (see Table 3-4). Although the X and Y dependences of Φ_{em} or τ_{em} exhibit an opposite trend against EN(X/Y) with one another, this can be explained reasonably in terms of the energy gap ($\tilde{\nu}_{em}$) dependence of the nonradiative decay rate constants of the clusters as described in §3-3-3.

3-3-3. Nonradiative Process in the T₁ States of [{Mo₆X₈}Y₆]²⁻ (X, Y = Cl, Br, or I).

The radiative rate constant of a hexamolybdenum(II) cluster (k_r) is insensitive to nature of the terminal

Table 3-4. Photophysical properties of n**X** in deaerated CH_3CN at 298 K.

[{Mo₆X₈}Y₆]²⁻			X			Δ(X)[a]
			Cl	Br	I	
$\tilde{\nu}_{em}$/ 10³ cm⁻¹	Y	Cl	**13.4 (4130) [748]**,	**13.4 (4120) [747]**,	**14.2 (2520) [705]**,	**+800**,
(*fwhm* / cm⁻¹)			13.2 (3830) [758]	13.5 (4210) [742]	14.1 (2320) [707]	+900
[λ$_{em}$/ nm]		Br	**12.7 (4000) [787]**,	**12.9 (4180) [778]**,	**14.0 (3230) [713]**,	**+1300**,
			12.9 (4040) [778]	12.9 (4030) [773]	14.0 (2850) [713]	+1100
		I	**12.3 (–)[c] [813]**,	**12.3 (–)[c] [812]**,	**13.6 (4580) [738]**,	**+1300**,
			12.3 (3820) [810]	12.3 (3840) [812]	13.6 (4530) [735]	+1300
Δ(Y)[a]			**−1100**, −1100	**−1100**, −1200	**−600**, −500	
Φ_{em}	Y	Cl	**0.19**, 0.20	**0.22**, 0.21	**0.47**, 0.57	**+0.28**, +0.37
		Br	**0.14**, 0.17	**0.14**, 0.15	**0.23**, 0.24	**+0.09**, +0.07
		I	**0.09**, 0.08	**0.09**, 0.10	**0.11**, 0.13	**+0.02**, +0.05
Δ(Y)[a]			**−0.10**, −0.12	**−0.13**, −0.11	**−0.36**, −0.47	
τ_{em}/ μs	Y	I	**205**, 130	**220**, 115	**300**, 170	**+95**, +40
		Br	**170**, 105	**150**, 85	**205**, 130	**+35**, +25
		I	**100**, 55	**85**, 50	**95**, 50	**−5**, −5
Δ(Y)[a]			**−95**, −75	**−135**, −65	**−205**, −120	
k_r / 10³ cm⁻¹	Y	Cl	**0.93**, 1.5	**1.0**, 1.8	**1.6**, 3.4	**+0.67**, +1.9
		Br	**0.82**, 1.6	**0.93**, 1.8	**1.1**, 1.9	**+0.28**, +0.30
		I	**0.90**, 1.5	**1.1**, 2.0	**1.2**, 2.6	**+0.30**, +1.1
Δ(Y)[a]			**−0.03**, 0.00	**−0.10**, −0.20	**−0.40**, −0.80	
k_{nr} / 10³ cm⁻¹	Y	Cl	**4.0**, 6.2	**3.6**, 6.9	**1.8**, 2.4	−2.2, −3.8
		Br	**5.1**, 7.9	**5.7**, 10	**3.8**, 5.9	−1.3, −3.8
		I	**9.1**, 17	**11**, 18	**9.4**, 17	−2.2, −3.8
Δ(Y)[a]			**+5.1**, +13	**+7.4**, +11	**+7.6**, +15	

a) The plus or minus sign of the number represents a higher- or lower-value shift of the data, respectively, for an X (Δ(X) for given Y) or Y variation (Δ(Y) for given X) from the value for X, Y = Cl to that of I. b) The numbers in bold and regular font represent the data in CH_3CN and crystalline phases, respectively.

ligands,[18-24] while the nonradiative decay rate constant (k_{nr}) varies considerably by a variation of the terminal ligands.[18-24] These results indicate that the Φ_{em} and τ_{em} values of the clusters are determined primarily by the k_{nr} values. In the present system, in practice, the k_r values in CH_3CN range in (0.82–1.6) × 10³ s⁻¹, which are much smaller than the range of k_{nr} ((1.8–11) × 10³ s⁻¹) irrespective of X and Y as seen in Table 3-4. Therefore, the Φ_{em} and τ_{em} values of n**X** are governed by k_{nr}. A close inspection of the data in Table 3-4 demonstrates that

the k_{nr} value increases in the sequence Y = Cl < Br < I for a given $\{Mo_6X_8\}^{4+}$-core cluster. For instance, the k_{nr} value of $[\{Mo_6I_8\}Y_6]^{2-}$ (**nI**) increases in Y = Cl (1.8×10^3) < Br (3.8×10^3) < I (9.3×10^3 s^{-1}). Similar trends to that of the $\{Mo_6I_8\}^{4+}$-core clusters are also found for the $\{Mo_6Cl_8\}^{4+}$- and $\{Mo_6Br_8\}^{4+}$-core clusters. For an ordinal transition metal complex, it has been reported that k_{nr} governs the Φ_{em} and τ_{em} values through the energy gap ($\tilde{v}_{em}$) dependence of k_{nr}: energy gap law (EGL).[25] The energy gap dependence of k_{nr} is given by eq. 3-1,[25]

$$\ln k_{nr} \propto -\frac{\gamma_0 \tilde{v}_{em}}{\hbar\omega} \tag{3-1a}$$

$$\gamma_0 = \ln \frac{\tilde{v}_{em}}{S\hbar\omega} \tag{3-1b}$$

where ω is the angular frequency of the vibration inducing radiationless transition from the T_1 state to the ground state (S_0), and S is the parameter related to the vibrational displacement between the T_1 and S_0 states. Although γ_0 is a function of $\tilde{v}_{em}$, since the contribution of γ_0 in eq. 3-1a has been reported to be minor,[25] eq. 3-1a is simplified to $\ln(k_{nr}) \propto -\tilde{v}_{em}$. Furthermore, reciprocal of the slope value of a $\ln(k_{nr})$ *vs.* $\tilde{v}_{em}$ plot corresponds to the vibrational mode ($\hbar\omega$) responsible for nonradiative decay from the T_1 state to S_0. To check an applicability of EGL to the present data, the $\tilde{v}_{em}$ values were plotted against the $\ln(k_{nr})$ values as the results were shown in Figure 3-7.

For a given $\{Mo_6X_8\}^{4+}$-core series, the $\ln(k_{nr})$ value decreased linearly with an increase in $\tilde{v}_{em}$, though the number of the data in each plot is limited to three: average R^2 values = 0.877. The results demonstrate that the τ_{em} value of the cluster is determined primarily by $\tilde{v}_{em}$: $\tau_{em} \propto k_{nr}$ where $k_{nr} \gg k_r$. Knowing $\Phi_{em} = k_r/(k_r + k_{nr}) = k_r\tau_{em}$ and $k_{nr} \gg k_r$, furthermore, the Φ_{em} value of the cluster will be also determined by k_{nr}. The $\hbar\omega$ value evaluated from the slope value of the EGL plot decreased in the sequence X = Cl (1350) > Br (971) > I (405

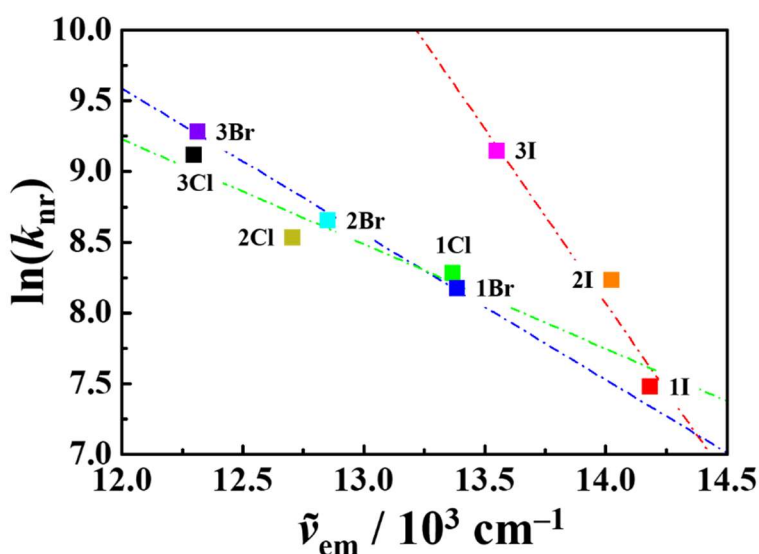**Figure 3-7**. Relationships between the $\ln(k_{nr})$ and $\tilde{v}_{em}$ values of **nX** in CH$_3$CN at 298 K. The broken lines show linear regression of the data for a given X in $[\{Mo_6X_8\}Y_6]^{2-}$.

cm^{-1}). The active vibrational frequencies (v_v) assigned to the Mo-X stretching modes have been reported to be v_v = 310–320, 203–212, and 148–154 cm^{-1} for X = Cl, Br, and I in $[\{Mo_6X_8\}X_6]^{2-}$,[16,26-28] respectively, and the decreasing order of v_v is in a good accordance with that of the observed $\hbar\omega$ values, though the absolute values of v_v and $\hbar\omega$ do not agree with each another. Such discussions suggest that the promoting mode inducing nonradiative decay from the T$_1$ states of **nX** will be the Mo-X stretching vibrations in the $\{Mo_6X_8\}^{4+}$-cores.

3-4. Temperature Dependent Emission Characteristics
3-4-1. Temperature Dependent Emission Spectra

The *T*-dependences of the emission spectra of $[\{Mo_6X_8\}Y_6]^{2-}$ (**nX**) in PEG-DMA matrixes are shown in Figure 3-8 and, those of the emission maximum energy ($\tilde{v}_{em}$) and full-width at half maximum of the spectrum (*fwhm*) of each cluster are summarized in Figure 3-9. The emission spectra of the $\{Mo_6Cl_8\}^{4+}$- (**nCl**), $\{Mo_6Br_8\}^{4+}$-core clusters (**nBr**), and $[\{Mo_6I_8\}I_6]^{2-}$ (**3I**) are shifted to the lower-energy on going from 3 to 60 K and, subsequently, the clusters show higher-energy emission shifts above 60 K. These seven clusters commonly showed the minima in the $\tau_{em} - T$ plots at around 60 K (left panels in Figure 3-9), while the behavior observed
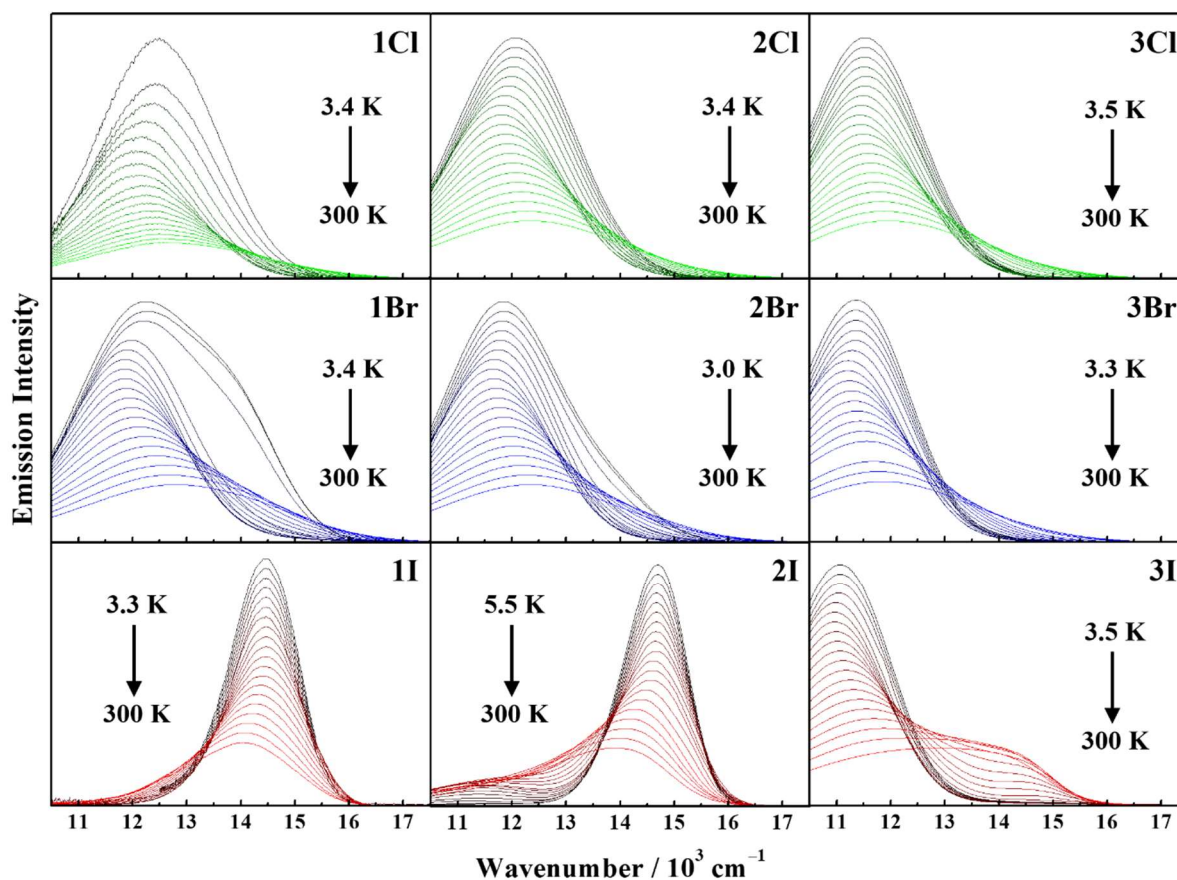

Figure 3-8. *T*-dependences of the emission spectra of $[\{Mo_6Cl_8\}Y_6]^{2-}$ (upper panel), $[\{Mo_6Br_8\}Y_6]^{2-}$ (middle panel), and $[\{Mo_6I_8\}Y_6]^{2-}$ (lower panel) in polymer matrixes in 3 K < *T* < 300 K. Temperature variations are shown by color gradation from black (3 K) to highlight (300 K).

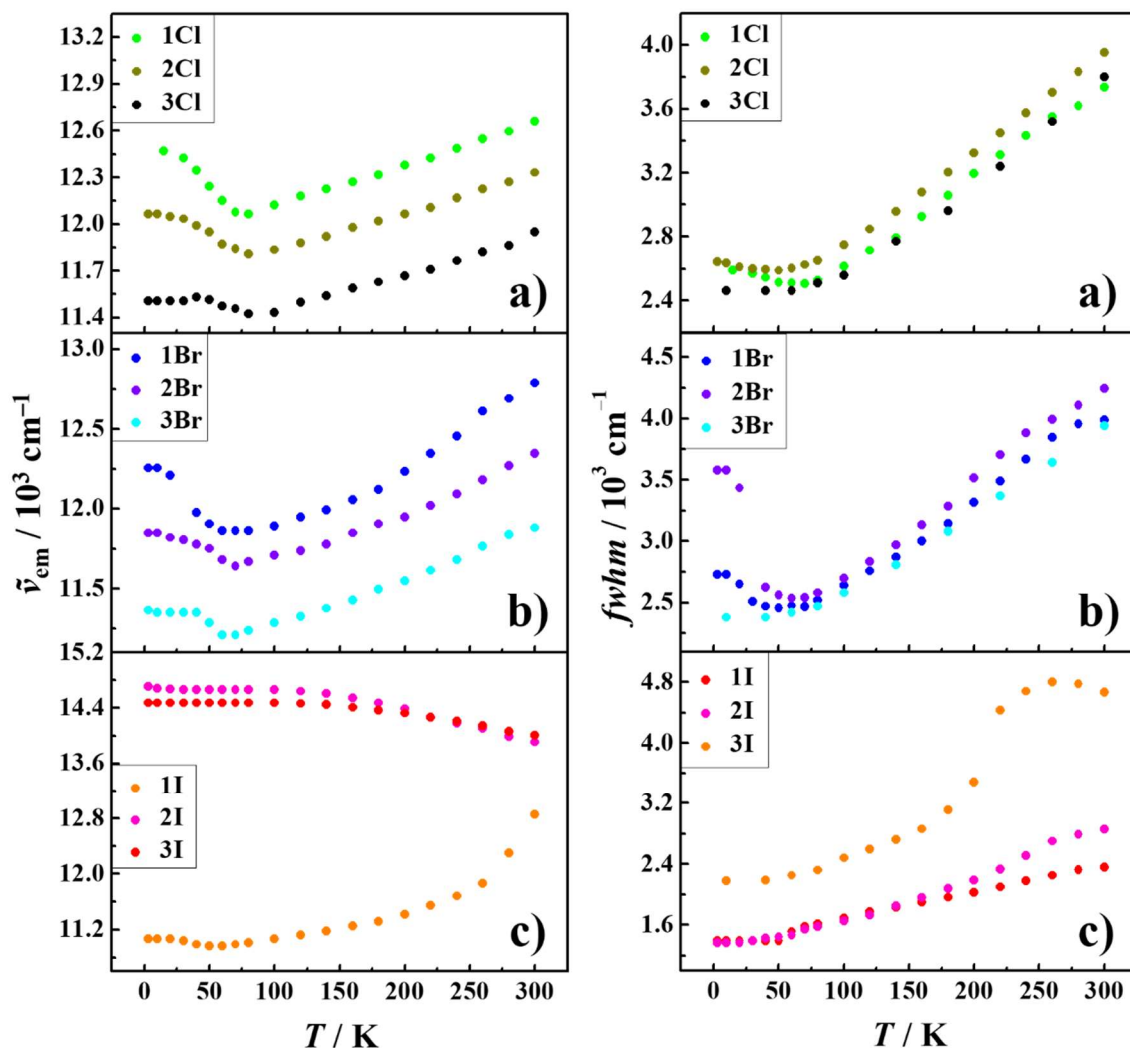**Figure 3-9**. *T*-dependences of the $\tilde{v}_{em}$ (left panel) and *fwhm* (right panel) values of (a) $[\{Mo_6Cl_8\}Y_6]^{2-}$, (b) $[\{Mo_6Br_8\}Y_6]^{2-}$, and (c) $[\{Mo_6I_8\}Y_6]^{2-}$ in polymer matrixes. The *fwhm* values of the clusters with Y = I (**3X**) at a given *T* are the approximated values as estimated by extrapolation of each spectrum by a Gaussian function.

for **3I** was marginal. These results indicate that the critical temperature, below and above which the clusters show lower- and higher-energy shifts upon *T*-elevation, respectively, is almost common for these clusters. Furthermore, such *T*-dependent emission shifts of the clusters accompanied the increases in *fwhm* of the spectra as seen in Figures 3-8 and 3-9. It is worth pointing that the *T*-dependent emission characteristics analogous to those of *n*Cl, *n*Br, and **3I** have been also confirmed for $[\{M_6Cl_8\}Cl_6]^{2-}$ (M = Mo(II) or W(II)) and $[\{Re_6S_8\}X_6]^{4-}$ (X = Cl, Br, or I).[6-8] In contrast, $[\{Mo_6I_8\}Cl_6]^{2-}$ (**1I**) and $[\{Mo_6I_8\}Br_6]^{2-}$ (**2I**) exhibited *T*-dependent emission characteristics completely different from other clusters. First, these two clusters showed the sharp (small *fwhm*) and higher-energy emission spectra compared to *n*Cl or *n*Br irrespective of *T* (3–300 K), indicating such emission characteristics of **1I** and **2I** were inherent to an $\{Mo_6I_8\}^{4+}$-core cluster. Second, the $\tilde{v}_{em}$ values of **1I** and **2I** were almost constant in 3 K < *T* < 100 K and, then, *T*-elevation above 100 K gave rise to gradual lower-

energy shifts of the spectra. On the other hand, the *T*-dependent emission characteristics of **3I** ([{Mo₆I₈}I₆]²⁻) were marginal between those of **1I/2I** and **nCl/nBr**.

3-4-2. Temperature Dependent Emission Lifetimes

The emission decay profiles of **nX** at several temperatures are shown in Figure 3-10. As a typical example, the emission decay profiles of [{Mo₆Br₈}Br₆]²⁻ (**2Br**) were fitted by single exponential functions irrespective of both *T* and the spectral shifts with *T* in Figure 3-8. The emission from the other clusters (**nCl, 1Br, 3Br**, and **nI**) also showed single exponential decay in the *T* range of 3–300 K. Costuas et al. reported recently that the emissions from the cesium and TBA salts of [{Mo₆Br₈}Br₆]²⁻ (**2Br**) in the solid states at low temperatures exhibited double exponential decay, and demonstrated that such emission characteristics were ascribed to the emissions from the structurally different two excited states (dual-emission model).[29] Under the present experimental conditions with each cluster being dispersed homogeneously in a polymer matrix, however, two components emission decay was not observed. Therefore, the two components emissions reported by Costuas et al. would be due to the intermolecular interactions between adjacent cluster molecules in the crystalline phase
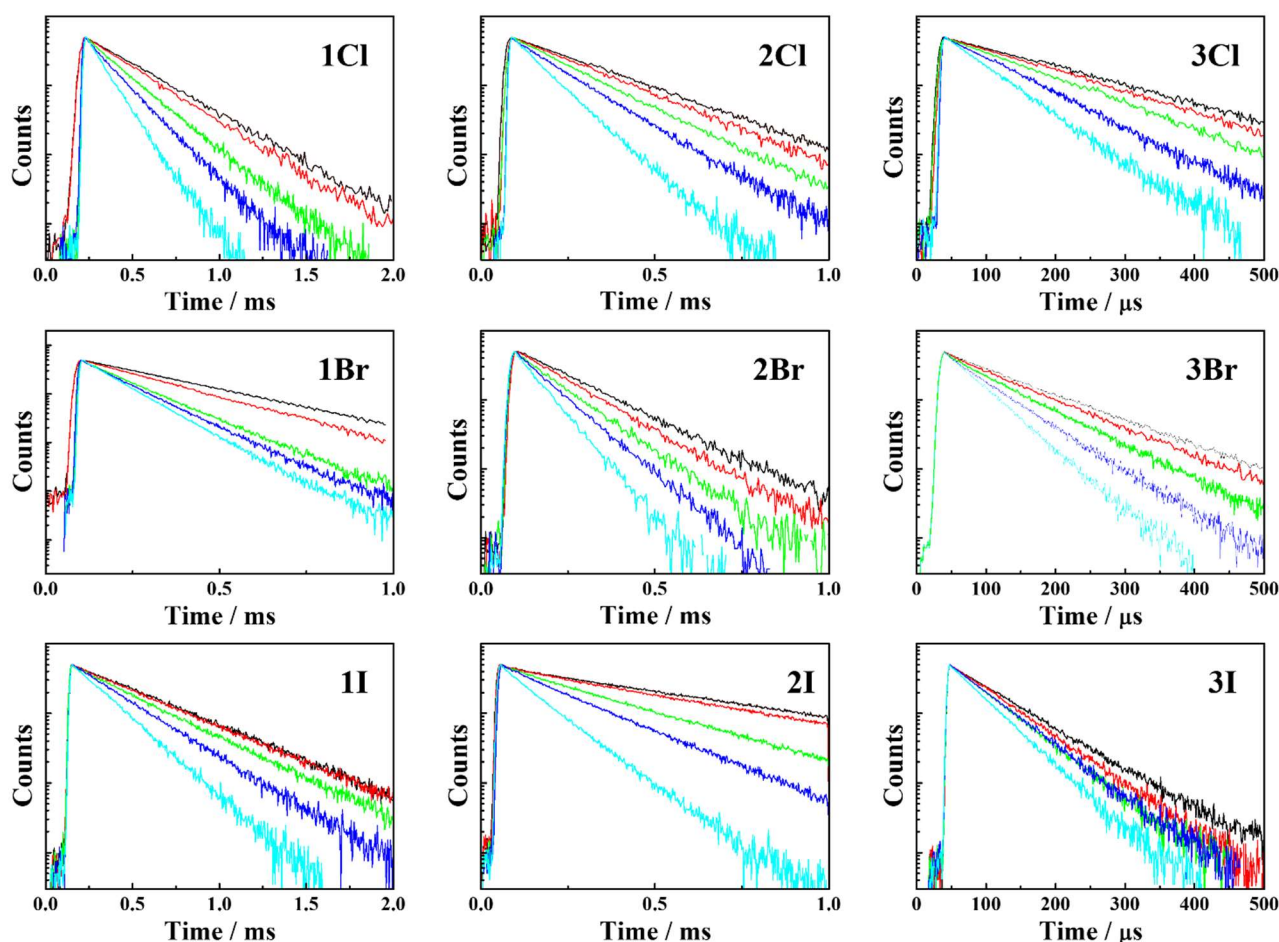

Figure 3-10. Emission decay profiles of [{Mo₆Cl₈}Y₆]²⁻ (upper panel**)**, [{Mo₆Br₈}Y₆]²⁻ (middle panel), and [{Mo₆I₈}Y₆]²⁻ (lower panel**)** in polymer matrixes at 10, 30, 100, 200, and 300 K.

Table 3-5. *T*-Dependences of the emission lifetimes of $[\{Mo_6X_8\}Y_6]^{2-}$ (*n*X) in PEG-DMA matrixes.

T / K	$\{Mo_6Cl_8\}^{4+}$			$\{Mo_6Br_8\}^{4+}$			$\{Mo_6I_8\}^{4+}$		
	1Cl	**2Cl**	**3Cl**	**1Br**	**2Br**	**3Br**	**1I**	**2I**	**3I**
3.0	–	–	–	–	203	–	–	–	–
3.3	–	–	–	–	–	167	–	–	110
3.4	555	335	–	350	–	–	–	–	–
3.5	–	–	–	–	–	–	–	628	–
3.6	–	–	222	–	–	–	–	–	–
5.5	–	–	–	–	–	–	433	–	–
10	410	240	164	251	182	124	426	551	78.0
15	328	–	–	–	–	–	–	–	–
20	–	227	149	225	166	114	426	525	71.0
30	293	218	143	199	154	111	423	490	68.0
40	278	211	139	179	147	109	409	447	63.0
50	257	205	135	160	140	107	398	411	62.0
60	244	196	127	149	135	97	388	374	61.0
70	226	189	121	147	135	94	385	350	59.6
80	219	186	118	145	134	92	371	332	59.3
100	218	182	113	141	132	89	360	300	58.7
120	205	177	111	139	128	85	343	278	58.4
140	198	171	105	133	123	82	328	259	58.0
160	189	154	99	128	118	77	312	235	57.8
180	179	156	94	128	112	73	297	220	57.5
200	168	146	87	127	105	69	280	214	57.2
220	158	137	78	126	100	64	266	195	56.2
240	147	129	68	123	95	60	249	177	54.9
260	137	120	61	121	89	57	230	153	53.2
280	126	109	53	117	83	52	210	140	51.5
300	114	95	48	110	77	50	196	123	48.9

as reported for **1Cl** in the crystalline phase.[6]

The *T*-dependences of τ_{em} evaluated for *n*X are summarized in Figure 3-11 and Tables 3-5. The τ_{em} values of *n*Cl and *n*Br decreased sharply upon *T*-elevation from 3 to 100 K, while those exhibited monotonous
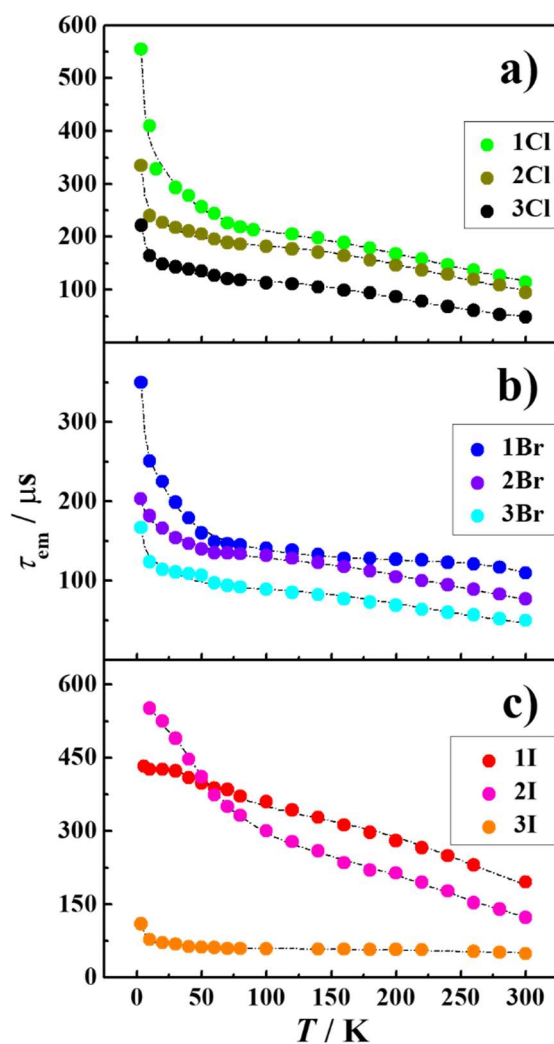
Figure 3-11. T-dependences of τ_{em} of (a) $[\{Mo_6Cl_8\}Y_6]^{2-}$, (b) $[\{Mo_6Br_8\}Y_6]^{2-}$, and (c) $[\{Mo_6I_8\}Y_6]^{2-}$ in polymer matrixes. The broken curves are the best fits of the observed data by eq. 2-2 with the fitting parameters, ΔE_{1n} and τ_n, being shown in Figure 3-12.

decreases above ~100 K. In contrast, the $\{Mo_6I_8\}^{4+}$-core clusters (nI) showed T-dependent τ_{em} different from nCl or nBr as seen in Figure 3-11. In practice, **1I** showed a gradual decrease in τ_{em} from 3 to 300 K (from 433 to 196 μs) and **2I** also exhibited moderate T-dependent τ_{em} (from 628 to 123 μs) compared to nCl or nBr: from 203 (3 K) to 77 μs (300 K) for **2Br** as an example. Importantly, furthermore, the τ_{em} value of **3I** was insensitive to T in the entire T-range studied: 110 (3 K)–48.9 μs (300 K). Since these clusters, nX, are isostructural and isoelectronic with one another, such T-dependent emission characteristics ($\tilde{\nu}_{em}$, τ_{em}, and *fwhm*) of the nine clusters should be explained by a common model.

3-4-3. Analysis of *T*-Dependent Emission Lifetimes by Spin-Sublevel Model.

The T-dependent τ_{em} data ($\tau(T)$) of the clusters in Figure 3-11 were analyzed based on the four-spin-sublevel (Φ_n) model and eq. 2-1 mentioned in §2-6. It has been reported that the ΔE_{12} value responsible for the
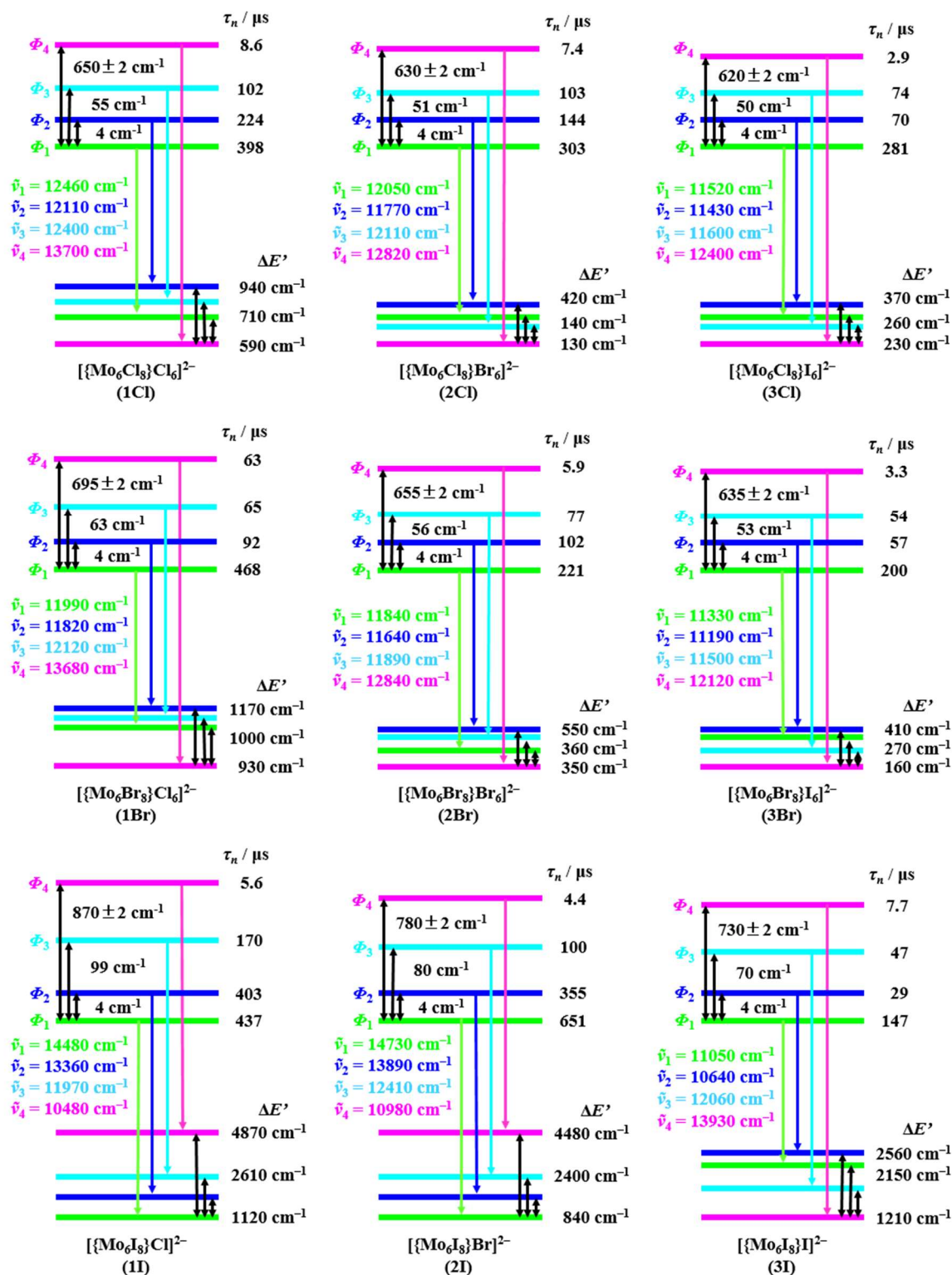
Figure 3-12. zfs parameters of $[\{Mo_6X_8\}Y_6]^{2-}$ (*n***X**).

participation of the Jahn-Teller distortion in the T_1 state of the cluster is essential to reproduce the experimentally observed $\tau(T)$ data though the ΔE_{12} value is much smaller than ΔE_{13} and ΔE_{14}.[6] In the case of **1Cl** in a poly(methyl methacrylate) matrix, the analysis of the $\tau(T)$ data by the three spin-sublevel φ_n model in Scheme
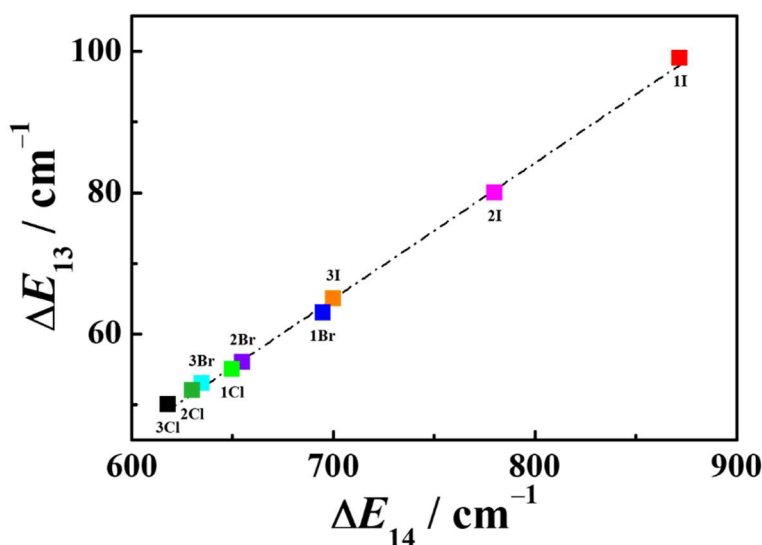
Figure 3-13. Relationship between ΔE_{14} and ΔE_{13} of $[\{Mo_6X_8\}Y_6]^{2-}$ (**nX**). The broken line represents the linear regression line.

2-1 (without assuming the Jahn-Teller effects in the T_1 state) failed to reproduce the experimental results as reported by Kitamura and co-workers.[6] Furthermore, they have demonstrated that the ΔE_{12} value being fixed at 4 cm^{-1} is adequate to reproduce the experimental observations.[6] Since **nX** possess the isoelectronic structure with each other, it is predicted that the ΔE_{12} value is insensitive to nature of the bridging or terminal ligands in **nX**. Therefore, the ΔE_{12} value is fixed at 4 cm^{-1} similar to that of **1Cl** for the following simulations.[6] As seen in Figure 3-11, the present simulations (broken curves) reproduced very well the observed $\tau(T)$ data on **nX** with the correlation coefficients (R^2) of the fittings being 0.982–0.999. The ΔE_{1n} and τ_n values thus evaluated by the analysis of the $\tau(T)$ data in Figure 3-11 are summarized in Figure 3-12.

The ΔE_{13} and ΔE_{14} values of the clusters, **nX**, were in the range of 50–99 and 620–870 cm^{-1}, respectively. It is worth emphasizing that the ΔE_{14} values are comparable to those evaluated by Ramirez-Tagle et al. based on relativistic TD-DFT calculations: 0.1–0.2 eV (ca. 800–1600 cm^{-1}).[17] Since ΔE_{14} and ΔE_{13} of the clusters are responsible for splitting of the degenerated T_1 state by the first- and second-order SOC, respectively (see also Scheme 2-1), the ΔE_{14} values should be proportional to the ΔE_{13} values. In practice, the present study found a linear relationship between ΔE_{14} and ΔE_{13} with R^2 being 0.998 as shown in Figure 3-13. The linear relationship in Figure 3-13 demonstrates clearly that the analysis of the $\tau(T)$ data for the nine clusters by the Φ_n model has been done satisfactorily and provides the zfs parameters in the T_1 states of the clusters.

3-4-4. Simulations of Emission Spectra by Spin Sublevel Model.

On the basis of the ΔE_{1n} values, the observed emission spectra of **nX** at a given T were simulated by eq. 2-2 in §2-6. Figure 3-14 shows the observed (shown by black curves) and simulated emission spectra (shown by
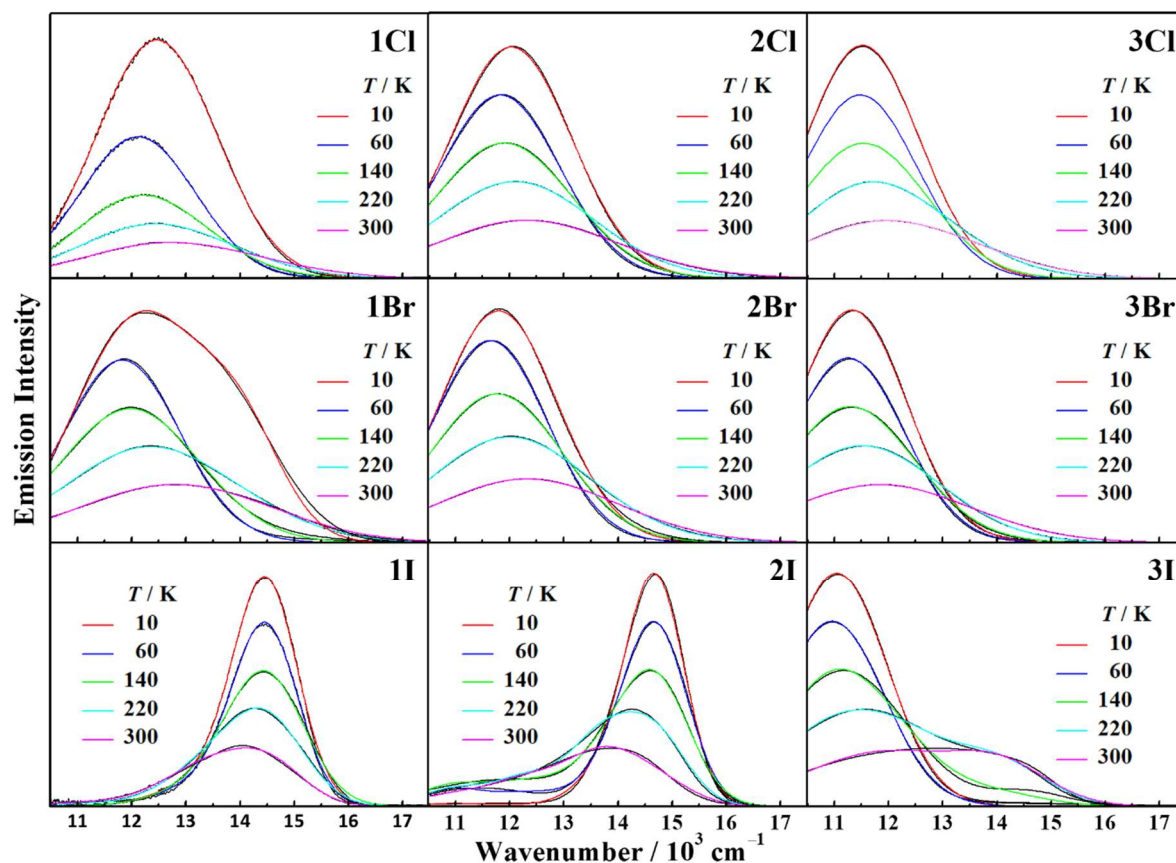
Figure 3-14. Simulations of the *T*-dependent emission spectra of $[\{Mo_6Cl_8\}Y_6]^{2-}$ (upper panel), $[\{Mo_6Br_8\}Y_6]^{2-}$ (middle panel), and $[\{Mo_6I_8\}Y_6]^{2-}$ (lower panel) in polymer matrixes. The spectra shown by the black curves are the observed ones, while the simulated spectra are shown by the colors indicated in the figures.

given colors) of *n*X at several *T*. The $\tilde{v}_n$ values simulated are included in Figure 3-12. Figure 3-14 demonstrates clearly that the observed spectrum is reproduced almost satisfactorily by ΔE_{1n}, $\tilde{v}_n$ (Figure 3-12), eqs. 2-2 and 2-3 irrespective of X, Y, and *T* with $R^2 \sim 0.999$. The *T*-dependent *fwhm*(Φ_n) values employed for the fittings of the spectra are summarized in Table 3-6. In the case of **2Br**, typically, the *fwhm*(Φ_n) value was necessary to vary from 2020 to 3220 cm^{-1} on going from 3 to 300 K, while that of **2I** varied from 1020 at 3 K to 1580 cm^{-1} at 300 K. It is worth noting that, although the *T*-dependent emission shifts and *fwhm* of *n*Cl, *n*Br, and **3I** are different largely from those of **1I** and **2I** as mentioned before, eqs. 2-2 and 2-3 reproduce very well the $I(\tilde{v}, T)$ data on *n*X based on the ΔE_{1n} values evaluated by the analysis of the $\tau(T)$ data in Figure 3-11. Therefore, both $\tau(T)$ and $I(\tilde{v}, T)$ data on a given cluster are analyzed properly by the common parameters and a single context of the present Φ_n model.

In order to show the validity of the present data analysis, the contribution percentage of each Φ_n ($\Phi_n\%$) in the emission spectra of *n*X at 300 K is summarized in Figure 3-15 and Table 3-7. In the case of $[\{Mo_6X_8\}Br_6]^{2-}$ (**2X**), as examples, the emission spectra of **2Cl** and **2Br** at 300 K are explained almost satisfactorily by the contributions from the Φ_3 and Φ_4 emissions (Φ_3 and Φ_4: 68 and 32% for **2Cl**, 53 and 47% for **2Br**) as seen in

Table 3-6. T-dependences of $fwhm(\Phi_n)$ of [{Mo$_6$X$_8$}Y$_6$]$^{2-}$ (**nX**) in polymer matrixes.

	$fwhm(\Phi_n)$ / cm^{-1}								
T / K	[{Mo$_6$Cl$_8$}Y$_6$]$^{2-}$			[{Mo$_6$Br$_8$}Y$_6$]$^{2-}$			[{Mo$_6$I$_8$}Y$_6$]$^{2-}$		
	1Cl	**2Cl**	**3Cl**	**1Br**	**2Br**	**3Br**	**1I**	**2I**	**3I**
10	2090	2240	2210	2020	2020	2020	1160	1020	1530
60	2100	2200	2130	2050	2090	2050	1160	1130	1540
140	2340	2490	2380	2360	2430	2370	1420	1270	1700
220	2600	2940	2720	2860	2920	2850	1400	1330	1820
300	2940	3300	3170	3120	3220	3310	1370	1580	1930

Figure 3-15b and 3-15e, while the Φ_1 (10%) and Φ_2 emissions (55%) also contribute to the spectrum of **2I** in addition to the contributions of the Φ_3 (25%) and Φ_4 emissions (11%): Figure 3-15h. Such tendencies have been also found for Φ_n% in the emission spectra of [{Mo$_6$X$_8$}Cl$_6$]$^{2-}$ (**1X**), [{Mo$_6$X$_8$}I$_6$]$^{2-}$ (**3X**) at 300 K as seen in Figure 3-15. According to the zfs parameters in Figure 3-12, it is easily predicted that the relatively large ΔE_{14} value of **2I** (780 cm^{-1}) compared to that of **2Cl** (630 cm^{-1}) or **2Br** (655 cm^{-1}) gives rise to the smaller contributions of the Φ_3 and Φ_4 emissions to the emission from **2I** at 300 K. In the case of a [{Mo$_6$I$_8$}Y$_6$]$^{2-}$ series (**nI**), on the other hand, the emission spectrum of **1I** at 300 K is characterized by relatively small Φ_3 (9%) / Φ_4 (2%) and large Φ_1 (49%) / Φ_2 (41%) contributions (Figure 3-15g), while that of **3I** is explained by large contributions of the Φ_3 (37%) and Φ_4 (42%) emissions: Figure 3-15i. The Φ_n% values of the emission from **2I** are marginal between those of **1I** and **3I** as seen in Table 3-7 and Figure 3-15h. It is worth noting that the Φ_3 and Φ_4% values increase in the sequence Y = Cl (**1I**) < Br (**2I**) < I (**3I**), which agrees very well with the decreasing order of ΔE_{13} and ΔE_{14}: Y = Cl (**1I**, 99 and 870 cm^{-1}) > Br (**2I**, 80 and 780 cm^{-1}) > I (**3I**, 70 and 730 cm^{-1}). The ΔE_{1n} and Φ_n% values mentioned above thus determine the emission spectrum of a given cluster at 300 K. Furthermore, since Φ_n% of the cluster is a function of T, the T-dependent emission shifts of the clusters will be also explained by the variation of Φ_n% with T as described later in detail: §3-4-5.

3-4-5. Origin of *T*-Dependent Emission Spectral Characteristics.

The curious T-dependent emission shifts, showing lower- and higher-energy shifts upon T-elevation from 3 to ~60 K and above ~60 K, respectively, observed for **nCl** or **nBr** (Figures 3-8 and 3-9), have been also reported for the T-dependent emission from [{M$_6$Cl$_8$}Cl$_6$]$^{2-}$ (M = Mo(II) or W(II)) and [{Re$_6$S$_8$}X$_6$]$^{4-}$ (X = Cl, Br, or I).[6-8] The {Mo$_6$I$_8$}$^{4+}$-core clusters, **1I** and **2I**, showed the T-dependent emission shifts different considerably from **nCl** or **nBr** as mentioned before. Such T-dependent emission shifts of **nX** can be explained in terms of the orders of the Φ_n and $\tilde{v}_n$ energies. Although the Φ_n energy increases in the sequence $\Phi_1 < \Phi_2 < \Phi_3 < \Phi_4$, the emission maximum energy of each Φ_n ($\tilde{v}_n$) does not coincide with this sequence and, thereby, the Φ_n energy levels cannot explain the T-dependent emission shifts. In the case of **2Br** as an example, $\tilde{v}_n$ ($\times 10^3$
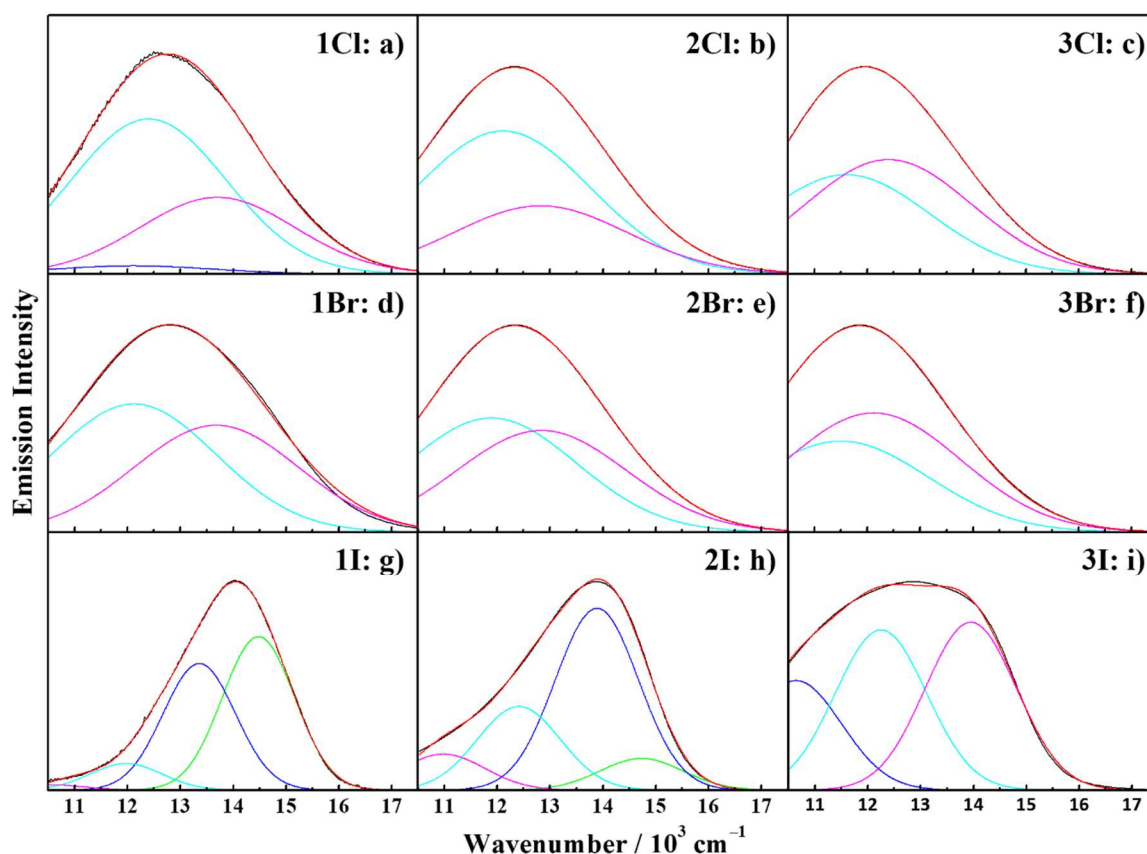
A Study on the Excited Triplet States of Octahedral Hexamolybdenum(II) Clusters

Figure 3-15. Observed and simulated emission spectra of $[\{Mo_6Cl_8\}Y_6]^{2-}$ (upper panel**)**, $[\{Mo_6Br_8\}Y_6]^{2-}$ (middle panel), and $[\{Mo_6I_8\}Y_6]^{2-}$ (lower panel**)** in polymer matrixes at 300 K. The observed and simulated emission spectra are shown by the black and red colors, respectively. The relative contributions of the Φ_n emission spectra to the observed spectrum of a given cluster are shown by green ($n = 1$), blue ($n = 2$), cyan ($n = 3$), and magenta ($n = 4$), respectively.

Table 3-7. Contribution percentages (Φ_n%) of the Φ_n emissions to the observed spectra of **nX** at 300 K.

	$[\{Mo_6Cl_8\}Y_6]^{2-}$			$[\{Mo_6Br_8\}Y_6]^{2-}$			$[\{Mo_6I_8\}Y_6]^{2-}$		
	1Cl	**2Cl**	**3Cl**	**1Br**	**2Br**	**3Br**	**1I**	**2I**	**3I**
Φ_1 / %	0	0	0	0	0	0	49.2	9.5	0
Φ_2 / %	3.2	0	0	0	0	0	40.6	54.6	21.4
Φ_3 / %	64.9	67.7	46.5	54.5	52.9	42.7	8.5	25.1	36.6
Φ_4 / %	31.9	32.3	53.5	45.5	47.1	57.3	1.7	10.8	42.0

cm^{-1}) increases in the sequence $\tilde{v}_2$ (11.64) $< \tilde{v}_1$ (11.84) $< \tilde{v}_3$ (11.89) $< \tilde{v}_4$ (12.84). Such sequence of $\tilde{v}_n$ can be also confirmed for **nCl**, **1Br**, **3Br**, and **3I**: see Figure 3-12. This indicates that the Franck-Condon (FC) ground state (S$_0$(FC)) responsible for each Φ_n emission transition is different. Knowing the energy difference between Φ_1 and Φ_n (ΔE_{1n}) and that between $\tilde{v}_1$ and $\tilde{v}_n$ ($\Delta \tilde{v}_n$), the energy differences between the S$_0$(FC) for the Φ_n emissions ($\Delta E'$) can be evaluated as the data are included in Figure 3-12. For **nCl**, **nBr**, and **3I**, the $\Delta E'$ values range in

- 59 -

130–2560 cm^{-1}. It is supposed that $\Delta E'$ will be determined by the displacement of the potential energy surface between the Φ_n level and the relevant S$_0$(FC) along vibrational coordinates. However, the absolute $\Delta E'$ values cannot be discussed in the present stage of the investigation, since the clusters show the intense emission, and this disturbs resonance Raman spectroscopy of the cluster providing the vibrational mode in the excited states. On the other hand, the $\Delta E'$ values of **1I** and **2I** were as large as 4530–4870 cm^{-1} and such large $\Delta E'$ values would not be explained by the difference in the vibrational modes between the T$_1$ and S$_0$ states. The participation of the ground states with different magnetic properties may explain such $\Delta E'$ values. In the case of **2Br** at 3 K, since the main contribution to the observed emission ($\tilde{v}_{em}$) is the Φ_1 emission, $\tilde{v}_{em}$ is predicted to be $\tilde{v}_{em} \approx \tilde{v}_1 = 11.84 \times 10^3$ cm^{-1}, which agrees very well with the experimental observation: $\tilde{v}_{em} = 11.85 \times 10^3$ cm^{-1} at 3 K, see Figure 3-9. Upon *T*-elevation above 3 K, the Φ_2 emission also participates in addition to the Φ_1 emission. Assuming simple average between $\tilde{v}_1$ and $\tilde{v}_2$, $\tilde{v}_{em}$ becomes ~11.74 × 10^3 cm^{-1}, leading to a higher-energy emission shift. Further *T*-elevation results in participation of the Φ_3 and Φ_4 emissions and, thus, the emission spectrum shifts gradually to the lower-energy, reflecting the increase in the contribution percentages of Φ_3 and Φ_4 to the observed spectrum. In contrast, since $\tilde{v}_n$ of **1I** or **2I** increases in the sequence $\tilde{v}_4 < \tilde{v}_3 < \tilde{v}_2 < \tilde{v}_1$ (see Figure 3-12), the cluster shows a gradual higher-energy shift upon *T*-elevation above 3 K. The Boltzmann population of Φ_n at a given *T*, the sequence of $\tilde{v}_n$, and the $\tilde{v}_n$ value explain very well the *T*-dependent emission shifts of **nX**.

3-4-6. Origin of the Terminal Ligand Dependences of the Emission Properties: $\tilde{v}_{em}$, τ_{em} , Φ_{em}, and *fwhm*.

A close inspection in the data in Figure 3-12 indicates that the $\tilde{v}_n$ values for a given X in **nX** increase in the sequence **3X** < **2X** < **1X**, while those of X = I (**nI**) are exceptional cases. In the case of **nBr** as an example, the $\tilde{v}_4$ or $\tilde{v}_3$ value (× 10^3 cm^{-1}) increases in the sequence **3Br** ($\tilde{v}_4$ or $\tilde{v}_3$ = 11.50 or 12.12) < **2Br** (11.89 or 12.84) < **1Br** ($\tilde{v}_4$ or $\tilde{v}_3$ = 12.12 or 13.68). It is worth noting that the terminal ligand substitution for a given X provides dramatic increases in the $\tilde{v}_n$ values, resulting in the $\tilde{v}_3$ value of **1X** being comparable to the $\tilde{v}_4$ value of **3X**: **1X** shows the $\tilde{v}_3$ value as large as the $\tilde{v}_4$ value of **3X**. As seen in Table 3-15, the present spectral analysis revealed that the emissions from **nCl** and **nBr** at 300 K are composed mainly of the Φ_3 and Φ_4 emissions and the increase in the zfs energy brings about smaller and larger contributions of the Φ_4 and Φ_3 emissions, respectively. Since the emission spectrum of the cluster at a given *T* is explained by the superposition of the Φ_n emissions as described in §3-4-5*,* this finding demonstrates that the large zfs energy for a given X leads to a higher-energy emission irrespective of *T*: see Figure 3-16 (a, b) for schematic illustration. Such discussions explain well the effects of the terminal ligand (Y) on the $\tilde{v}_{em}$ value at ambient temperature in Table 3-4, which cannot be explained by the electron-donating ability of the terminal ligand alone. Therefore, one of the factors governing the $\tilde{v}_{em}$ value is the zfs energy. It is worth emphasizing that Figure 3-16 (c, d) demonstrates that other photophysical properties (τ_{em} and Φ_{em}) at ambient temperature show the clear correlation with the zfs energy
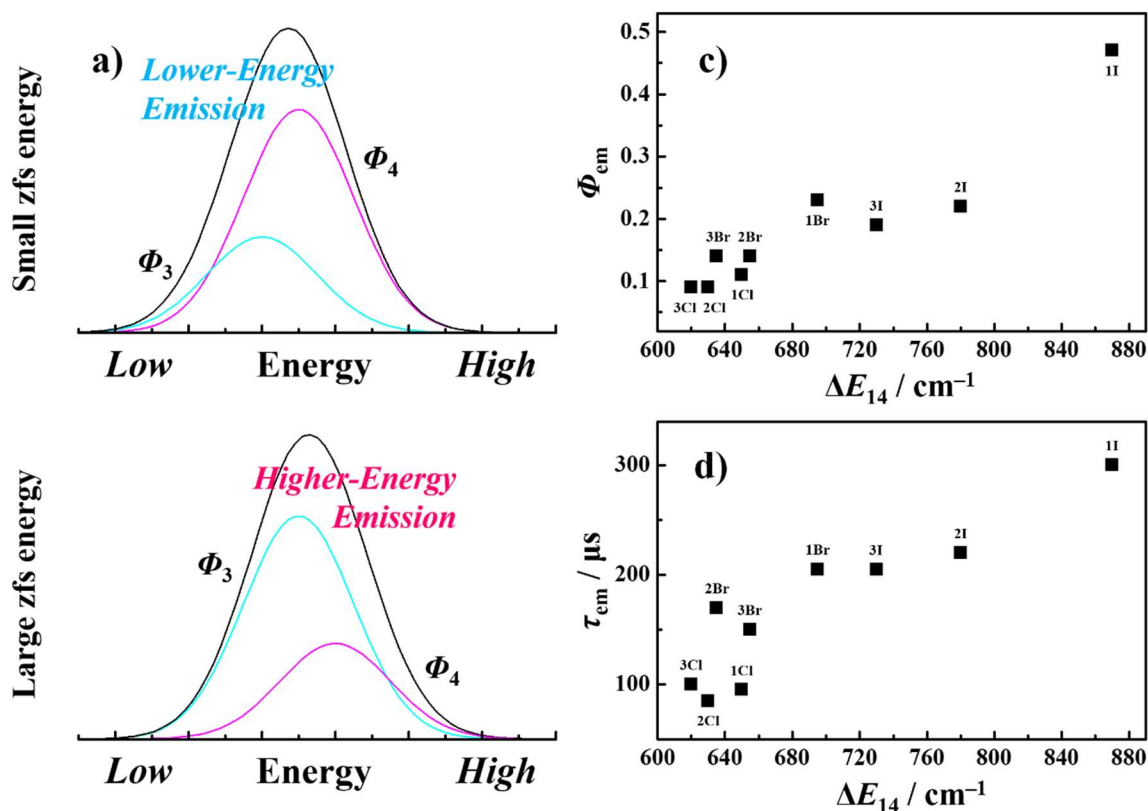
Figure 3-16. Schematic illustrations of the emission spectra of $[\{Mo_6X_8\}Y_6]^{2-}$ given by (a) a small zfs energy and (b) a large zfs energy. The relative contributions of the Φ_n emission to the total spetrum are shown by cyan ($n = 3$) and magenta ($n = 4$), respectively. Relationship between the ΔE_{14} value and (c) the Φ_{em} or (d) τ_{em} value.

similar to that of $\tilde{v}_{em}$, indicating the importance of zfs in the T_1 state as the governing factor of the photophysical properties of the octahedral hexametal cluster. Since the τ_{em} and Φ_{em} values of the cluster with a given X in n**X** are controlled synthetically based on the $\tilde{v}_{em}$ value through the energy gap dependence of k_{nr}, the zfs energy dependences of Φ_{em} and τ_{em} in Figure 3-16 (c, d) are very reasonable.

Another factor characterizing the emission spectra of n**X** is the *fwhm* value of each Φ_n: *fwhm*(Φ_n). As seen in Figure 3-9, the *fwhm* values of the observed spectra of n**Cl** and n**Br** show the minima at around 60 K, going from 3 to 300 K, the *fwhm* values of n**Cl** (X = Cl) and n**Br** (X = Br) vary from ~2600 to 3730–3950 cm^{-1} and from ~2500 to 3990–4240 cm^{-1}, respectively, while those of **1I** and **2I** (X = I) increase almost monotonically with T from ~1400 to 2300–2860 cm^{-1} with that of **3I** being an exceptional case: from 2180 to 4800 cm^{-1}. In contrast to the *fwhm* values, it is worth emphasizing the *fwhm*(Φ_n) value of **3I** at a given T is similar to that of **1I** or **2I**. For instance, at 300 K, the *fwhm*(Φ_n) value of **3I** (1930 cm^{-1}) is comparable to that of **1I** or **2I** (1370 or 1580 cm^{-1}, respectively) and much smaller than those of the $\{Mo_6Cl_8\}^{4+}$- and $\{Mo_6Br_8\}^{4+}$-core clusters (n**Cl** and n**Br**): 2940–3310 cm^{-1}. Although the relatively small *fwhm*(Φ_n) values of **3I** are inconsistent with the observed broad emission spectra of **3I** above 200 K, the large difference in $\tilde{v}_n$ explains well the observed data. Namely, the $\tilde{v}_n$ values of n**I** range in (10.5–14.7) × 10^3 cm^{-1} ($\Delta\tilde{v}_n = 3290–4000$ cm^{-1}), while those of n**Cl** and
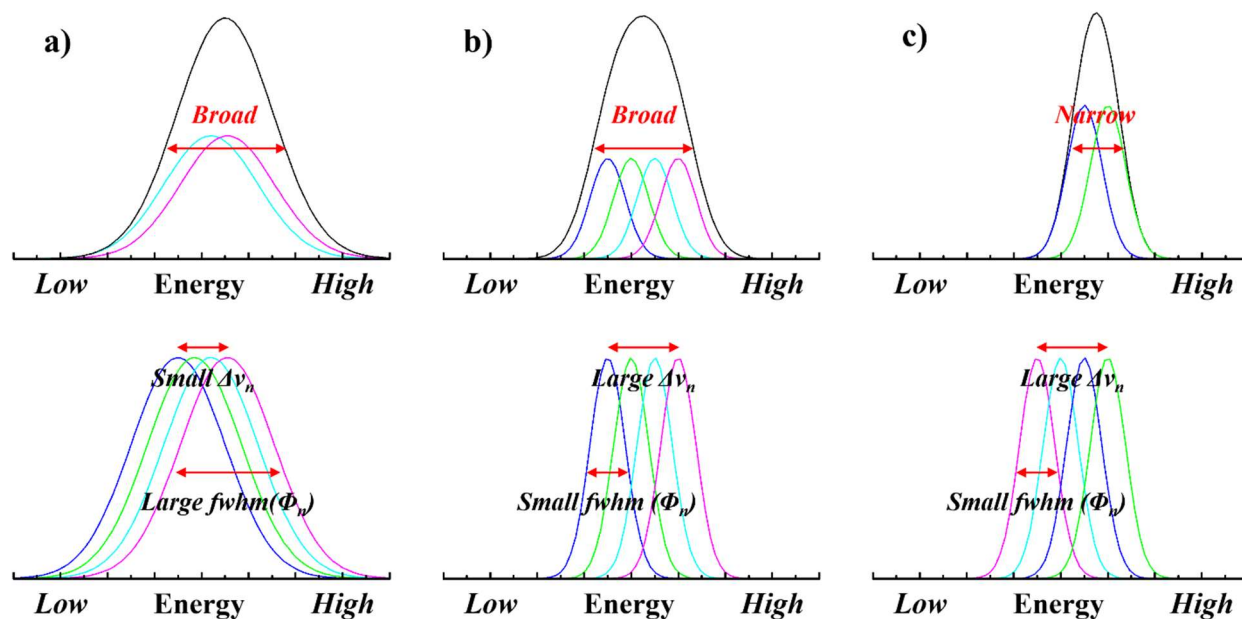
Figure 3-17. Schematic illustrations of the observed (upper panel) and Φ_n emissions (lower panel) from (a) ***n*Cl** or ***n*Br**, (b) **3I**, and (c) **1I** or **2I**. The relative contributions of the Φ_n emission spectra to the observed spectrum of a given cluster are shown by green ($n = 1$), blue ($n = 2$), cyan ($n = 3$), and magenta ($n = 4$).

***n*Br** lie in the narrow ranges: $\Delta\tilde{v}_n$ = 970–1590 and 980–1860 cm^{-1} for ***n*Cl** (X = Cl) and ***n*Br** (X = Br), respectively. As shown in Table 3-7 and Figure 3-15, the emission spectrum of **3I** at 300 K is reproduced by almost equal contributions from the Φ_2–Φ_4 emissions owing to the marginal ΔE_{1n} values between ***n*Cl**, ***n*Br** and **1I/2I**, resulting in the broad emission band shape of **3I**: see also Figure 3-17 for the schematic illustration. Therefore, the narrow spectral band shapes observed for the {Mo$_6$I$_8$}$^{4+}$-core clusters[12,18-23,31-33] are the inherent character to [{Mo$_6$I$_8$}Y$_6$]$^{2-}$.

3-5.   Conclusions

This chapter described the redox, spectroscopic, and photophysical properties of the terminal halide clusters [{Mo$_6$X$_8$}Y$_6$]$^{2-}$ (X, Y = Cl, Br, or I. ***n*X**) in solution and/or crystalline phases at ambient temperature. ***n*X** showed the clear X/Y dependences of the redox and several spectroscopic/ photophysical properties: E_{ox}, E_{red}, $\tilde{v}_a$, τ_{em}, and Φ_{em}. Since the (E_{ox}–E_{red}) value of the cluster determined by the π-electron-donating ability of X/Y (i.e., EN(X/Y)) is proportional to the (HOMO – LUMO) energy gap, the X/Y dependent E_{ox} and E_{red} values of ***n*X** resulted in the X/Y dependences of $\tilde{v}_a$. On the other hand, the X/Y dependences of the emission properties could not be explained by EN(X/Y) alone. In particular, the $\tilde{v}_{em}$ value of [{Mo$_6$X$_8$}Y$_6$]$^{2-}$ showed a higher- or lower-energy shift for an X (for given Y) or Y variation (for given X), respectively. The peculiar X/Y dependences of the $\tilde{v}_{em}$ were then discussed based on the zfs energies in the T$_1$ states of the clusters. On the basis of the investigations of the *T*-dependent emissions from ***n*X** in polymer matrixes in 3–300 K and their analysis

by the four-spin-sublevel (Φ_n) model, it was found that the splitting energies in the T_1 states (ΔE_{13} and ΔE_{14} values in cm^{-1}) increased in the sequences **3X < 2X < 1X** and **nCl < nBr < nI**, for a given Y and X, respectively. The larger is the ΔE_{14} value for a given X or Y series, the smaller is the contribution of the emission from the highest-energy spin sublevels (Φ_4) to the observed emission spectrum at 300 K with the sequence of Φ_4% being Y = I > Br > Cl or X = Cl > Br > I for given X or Y, respectively, and thus the larger is the contributions of the emissions from the lower-energy spin sublevels (Φ_3, Φ_2, or Φ_1). The variation of Φ_n% at 300 K with that of X or Y in [{Mo$_6$X$_8$}Y$_6$]$^{2-}$ (**nX**) mentioned above explained very well the $\tilde{v}_{em}$ value of the cluster as the sum of the emission from Φ_n.

3.6. References

(1)   Crosby, G. A.; Hipps, K. W.; Elfring Jr, W. H. On the Appropriateness of Assigning Spin Labels to Excited States of Inorganic Complexes. *J. Am. Chem. Soc*. **1974**, *96*, 629–630.

(2)   Westa, J.; Glasbeek, M. Localization of Optical Excitation in Crystalline Rh^{3+}-trisdiimine Chelates. *Chem. Phys. Lett*. **1990**, *166*, 535–538.

(3)   Yersin, H.; Strasser, J. Triplets in Metal-Organic Compounds. Chemical Tunability of Relaxation Dynamics. *Coord. Chem. Rev*. **2000**, *208*, 331–364.

(4)   Huber, P.; Yersin, H. Highly Resolved Emission of [Os(bpy-h$_8$)$_n$(bpy-d$_8$)$_{3-n}$]$^{2+}$ (*n* = 0–3): Evidence for Electronic Delocalization. *J. Phys. Chem*. **1993**, *97*, 12705–12709.

(5)   Yersin, H.; Rausch, A. F.; Czerwieniec, R.; Hofbeck, T.; Fischer, T. The Triplet State of Organo-transition Metal Compounds. Triplet Harvesting and Singlet Harvesting for Efficient OLEDs. *Coord. Chem. Rev*. **2011**, *255*, 2622–2652.

(6)   Kitamura, N.; Kuwahara, Y.; Ueda, Y.; Itoh, Y.; Ishizaka, S.; Sasaki, Y.; Tsuge, K.; Akagi, S. Excited Triplet States of [{Mo$_6$Cl$_8$}Cl$_6$]$^{2-}$, [{W$_6$Cl$_8$}Cl$_6$]$^{2-}$, and [{Re$_6$S$_8$}Cl$_6$]$^{4-}$ Clusters. *Bull. Chem. Soc. Jpn*. **2017**, *90*, 1164–1173.

(7)   Miki, H.; Ikeyama, T.; Sasaki, Y.; Azumi, T. Phosphorescence from the Triplet Spin Sublevels of a Hexanuclear Molybdenum(II) Chloride Cluster Ion, [Mo$_6$Cl$_{14}$]$^{2-}$. Relative Radiative Rate Constants for Emitting Sublevels. *J. Phys. Chem*. **1992**, *96*, 3236–3239.

(8)   Kitamura, N.; Ueda, Y.; Ishizaka, S.; Yamada, K.; Aniya, M.; Sasaki, Y. Temperature Dependent Emission of Hexarhenium(III) Clusters [Re$_6$S$_8$X$_6$]$^{4-}$ (X = Cl$^-$, Br$^-$, and I$^-$): Analysis by Four Excited Triplet-State Sublevels. *Inorg. Chem*. **2005**, *44*, 6308–6313.

(9)   Maverick, A. W.; Gray, H. B. Luminescence and Redox Photochemistry of the Molybdenum(II) Cluster Mo$_6$Cl$_{14}$$^{2-}$. *J. Am. Chem. Soc*. **1981**, *103*, 1298–1300.

(10)   Sheldon, J. C.; Chloromolybdenum(II) Compounds. *J. Chem. Soc*. **1960**, *0*, 1007–1014.

(11)   Maverick, A. W.; Najdzionek, J. S.; MacKenzie, D.; Nocera, D. G.; Gray, H. B. Spectroscopic,

Electrochemical, and Photochemical Properties of Molybdenum(II) and Tungsten(II) Halide Clusters. *J. Am. Chem. Soc.* **1983**, *105*, 1878–1882.

(12) Kirakci, K.; Kubát, P.; Langmaier, J.; Polívka, T.; Fuciman, M.; Fejfarová, K.; Lang, K. A Comprehensive Study of the Redox and Excited State Properties of (nBu₄N)₂[Mo₆X₁₄] and (nBu₄N)₂[{Mo₆X₈}(CF₃COO)₆] (X = Cl, Br, or I). *Dalton Trans.* **2013**, *42*, 7224–7232.

(13) Zietlow, T. C.; Hopkins, M. D.; Gray, H. B. Electronic Spectroscopy and Photophysics of d^4 Clusters. *J. Solid State Chem.* **1985**, *57*, 112–119.

(14) Malinak, S. M.; Maden, L. K.; Bullen, H. A.; McLeod, J. J.; Gaswick, D. C. Preparation of Tetrabutylammonium Octa-μ3-bromohexa(trifluoromethanesulfonato)octahedro-hexamolybdate(2–), (Bu₄N)₂[Mo₆Br$^i_8$(CF₃SO₃)$^a_6$] and Other Derivatives Containing the Mo₆Br₈⁴⁺ Core. *Inorg. Chim. Acta* **1998**, *278*, 241–244.

(15) Jackson, J. A.; Turro, C.; Newsham, M. D.; Nocera, D. G. Oxygen Quenching of Electronically Excited Hexanuclear Molybdenum and Tungsten Halide Clusters. *J. Phys. Chem.* **1990**, *94*, 4500–4507.

(16) Brückner, P.; Preetz, W.; Pünjer, M. Synthesis, Crystal Structure, NMR, Vibrational Spectra, and Normal Coordinate Analysis of the Cluster Anion [{Mo₆I$^i_8$}Y$^a_6$]²⁻, Y^a = F, Cl, Br, I. *Zeit. Anorg. Allg. Chem.* **1997**, *623*, 8–17.

(17) Ramirez-Tagle, R.; Arratia-Pérez, R. Electronic Structure and Molecular Properties of the [Mo₆X₈L₆]²⁻; X = Cl, Br, I; L = F, Cl, Br, I Clusters. *Chem. Phys. Lett.* **2008**, *460*, 438–441.

(18) Efremova, O. A.; Vorotnikov, Y. A.; Brylev, K. A.; Vorotnikova, N. A.; Novozhilov, I. N.; Kuratieva, N. V.; Edeleva, M. V.; Benoit, D. M.; Kitamura, N.; Mironov, Y. V.; Shestopalov, M. A.; Sutherland, A. J. Octahedral Molybdenum Cluster Complexes with Aromatic Sulfonate Ligands. *Dalton Trans.* **2016**, *45*, 15427–15435.

(19) Sokolov, M. N.; Mihailov, M. A.; Peresypkina, E. V.; Brylev, K. A.; Kitamura, N.; Fedin, V. P. Highly Luminescent Complexes [Mo₆X₈(n-C₃F₇COO)₆]²⁻ (X = Br, I). *Dalton Trans.* **2011**, *40*, 6375–6377.

(20) Sokolov, M. N.; Mikhailov, M. A.; Brylev, K. A.; Virovets, A. V.; Vicent, C.; Kompankov, N. B.; Kitamura, N.; Fedin, V. P. Alkynyl Complexes of High-Valence Clusters. Synthesis and Luminescence Properties of [Mo₆I₈(C≡CC(O)OMe)₆]²⁻, the First Complex with Exclusively Organometallic Outer Ligands in the Family of Octahedral {Mo₆X₈} Clusters. *Inorg. Chem.* **2013**, *52*, 12477–12481.

(21) Efremova, O. A.; Shestopalov, M. A.; Chirtsova, N. A.; Smolentsev, A. I.; Mironov, Y. V.; Kitamura, N.; Brylev, K. A.; Sutherland, A. J. A Highly Emissive Inorganic Hexamolybdenum Cluster Complex as a Handy Precursor for the Preparation of New Luminescent Materials. *Dalton Trans.* **2014**, *43*, 6021–6015.

(22) Miklailov, M. A.; Brylev, K. A.; Virovets, A. V.; Galyamov, M. R.; Novozhilov, I.; Sokolov, M. N. Complexes of {Mo₆I₈} with Nitrophenols: Synthesis and Luminescence. *New J. Chem.* **2016**, *40*, 1162–

1168.

(23)   Sokolov, M. N.; Mikhailov, M. A.; Virovets, A. V.; Brylev, K. A.; Bredikhin, R. A.; Maksimov, A. M.; Platonov, V. E.; Fedin, V. P. Synthesis, Structure, and Luminescence of the Octahedral Molybdenum Cluster $[Mo_6I_8(SC_6F_4H)_6]^{2-}$. *Russ. Chem. Bull.* **2013**, *62*, 1764–1767.

(24)   Szczepura, L. F.; Edwards, J. A.; Cedeño, D. L. Luminescent Properties of Hexanuclear Molybdenum(II) Chloride Clusters Containing Thiolate Ligands. *J. Clust. Sci.* **2009**, *20*, 105–112.

(25)   Caspar, J. V.; Meyer, T. J. Photochemistry of Tris(2,2'-bipyridine)ruthenium(2+) ion $(Ru(bpy)_3^{2+})$. Solvent Effects. *J. Am. Chem. Soc.* **1983**, *105*, 5583–5590.

(26)   Preetz, W.; Harder, K. Synthesis, Structure and Properties of the Cluster Anions $[(Mo_6Cl^i_8)X^a_6]^{2-}$ with X^a = F, Cl, Br, I. *J. Alloys Compds.* **1992**, *183*, 413–429.

(27)   Preetz, W.; Bublitz, D. Synthesis, Crystal Structure and Spectroscopic Properties of the Cluster Anions $[(Mo_6Br^i_8)X^a_6]^{2-}$ with X^a = F, Cl, Br, I. *Zeit. Anorg. Allg. Chem.* **1994**, *620*, 234–246.

(28)   Preetz, W.; Peters, G.; Bublitz, D. Preparation and Spectroscopic Investigations of Mixed Octahedral Complexes and Clusters. *Chem. Rev.* **1996**, *96*, 977–1026.

(29)   Costuas, K.; Garreau, A.; Bulou, A.; Fontaine, B.; Cuny, J.; Gautier, R.; Mortier, M.; Molard, Y.; Duvail, J.-L.; Faulques, E.; Cordier, S. Combined Theoretical and Time-resolved Photoluminescence Investigations of $[Mo_6Br^i_8Br^a_6]^{2-}$ Metal Cluster Units: Evidence of Dual Emission. *Phys. Chem. Chem. Phys.* **2015**, *17*, 28574–28585.

(30)   Finkenzeller, W. J.; Yersin, H. Emission of $Ir(ppy)_3$. Temperature Dependence, Decay Dynamics, and Magnetic Field Properties. *Chem. Phys. Lett.* **2003**, *377*, 299-305.

(31)   Kirakci, K.; Fejfarová, Kučeráková, M.; Lang, K. Haxamolybdenum Cluster Complexes with Pyrene and Anthracene Carboxylate: Ultrabright Red Emitters with the Antenna Effect. *Eur. J. Inorg. Chem.* **2014**, 2331–2336.

(32)   Kirakci, K.; Kubát, P.; Fejfarová, K.; Matinčík, J.; Nikl, M.; Lang, K. X-ray Inducible Luminescence and Singlet Oxygen Sensitization by an Octahedral Molybdenum Compound: A New Class of Nanoscintillators. *Inorg. Chem.* **2016**, *55*, 803–809.

(33)   Kirakci, K.; Šícha, V.; Holub, J.; Kubát, P.; Lang, K. Luminescen Hydrogel Particles Prepared by Self-Assembly β-Cyclodexrin Polymer and Octahedral Molybdenum Cluster Complexes. *Inorg. Chem.* **2014**, *53*, 13012–13018.

Chapter 4

Redox, Spectroscopic, and Photophysical Properties of

[{Mo$_6$X$_8$}(RCOO)$_6$]$^{2-}$ (X = Br or I, RCOO = Carboxylate)

4-1. Introduction

Chapter 3 of this thesis described the redox, spectroscopic, and photophysical properties of $[\{Mo_6X_8\}Y_6]^{2-}$ (X, Y = Cl, Br, or I) and demonstrated that these properties were largely affected by both bridging and terminal ligands. For example, the arbitrary combination of X and Y in $[\{Mo_6X_8\}Y_6]^{2-}$ can tune the emission lifetime (τ_{em}) and quantum yield (Φ_{em}) of the cluster in CH$_3$CN in the range of 85–300 μs and 0.09–0.47, respectively. Furthermore, it was demonstrated that the zero-magnetic-field splitting (zfs) parameters of $[\{Mo_6X_8\}Y_6]^{2-}$ (X, Y = Cl, Br, or I) evaluated by the *T*-dependent emissions of the clusters explained very well the emission properties of $[\{Mo_6X_8\}Y_6]^{2-}$ at ambient temperature. These results indicate that various properties arisen from the lowest-energy excited triplet (T$_1$) state of the cluster would be controlled more precisely or widely by an introduction of other terminal ligands to the $\{Mo_6X_8\}^{4+}$-core. Furthermore, since the discussion on the *T*-dependent emission from an octahedral hexametal cluster by the spin-sublevel model (Φ_n model described in Chapter 1) is still limited to the clusters having simple ligand structures (i.e., Mo$_6$, W$_6$, and Re$_6$ terminal halide clusters), the applicability of the spin-sublevel model to the emission properties of the cluster with relatively complicated ligand structures are worth studying in more detail. The thesis then focuses on aliphatic and aromatic carboxylates as the terminal ligands (L) in $[\{Mo_6X_8\}L_6]^{2-}$ (X = Cl, Br, or I) since these ligands show different electron-donating abilities, which is reflected on the acid dissociation constant of the carboxylate ($pK_a(L)$). Furthermore, the $pK_a(L)$ value can be expected to be used as a common parameter for systematic discussions on various properties of the cluster. Besides terminal carboxylate ligands in $[\{Mo_6X_8\}L_6]^{2-}$ (X = halide; L = carboxylate), the clusters with X = Br or I are interested since these clusters show in general intense emission compared to those with X = Cl as described in Chapter 3.

In this chapter, the X-ray crystal structures, redox, spectroscopic, and photophysical properties of terminal carboxylate clusters $[\{Mo_6X_8\}L_6]^{2-}$ (*n*Br or *n*I: See Chart 4-1 for the structures and abbreviations) in solution

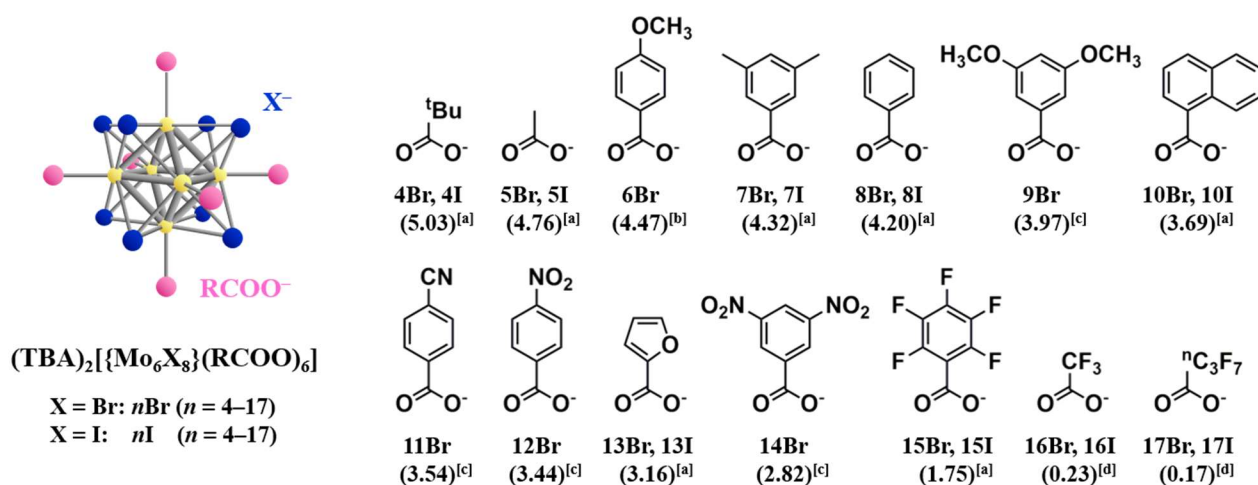**Chart 4-1.** Ligand structures and abbreviations of terminal carboxylate clusters $[\{Mo_6X_8\}(RCOO)_6]^{2-}$. The values in the brackets represent pK_a of the corresponding acid. a–d are the data taken from ref. 1–4, respectively.

at ambient temperature are described. Furthermore, the T-dependences of the emissions from $[\{Mo_6X_8\}(nC_3F_7COO)_6]^{2-}$ (X = Cl, Br, or I: **17X**) in polymer matrixes and $[\{Mo_6Br_8\}L_6]^{2-}$ (L = aromatic carboxylate: n_{AL}**Br**) in crystalline phases in 3–300 K are discussed based on the four-spin-sublevel (Φ_n) model to check the applicability of the model to the T-dependent emission of the clusters and to evaluate the zfs parameters.

4-2.   X-ray Crystal Structures

The X-ray crystal structures determined for the twenty new molybdenum(II) carboxylate clusters (**4Br**–**15Br**, **5I**, **7I**, **8I**, **10I**, **13I**, **15I**, and **17I**) are shown in Figures 4-1–4-3. The crystal structural data and selected average bond lengths in the crystals of n**X** are reported in Tables 4-1–4-3 and Table 4-4, respectively. The crystal structures of these clusters were obtained with a monoclinic or triclinic crystal system. As seen in Figures 4-1, tetra-n-butylammonium ions (TBA$^+$) as the counter cations locate between the cluster anions irrespective of X and L, and the main structural unit in the crystal structure is the cluster anion. Therefore, although some of n**X** possess the aromatic terminal ligands, no $\pi\pi$ stacking interaction between the aromatics is present in these crystals. Table 4-4 shows that the bond length between the ligating O atom in the carboxylate and Mo atom (d_{Mo-O}) decreases with increasing pK_a(L) for both X = Br and I clusters (n**Br** and n**I**), while that between Mo-Mo or Mo-X (d_{Mo-Mo} or d_{Mo-X}, respectively) is not influenced by nature of the carboxylate ligand. With a variation of the terminal carboxylate, the d_{Mo-O} value of the n**Br** or n**I** cluster varies from 2.076 to 2.118 Å or from 2.097 to 2.132 Å, respectively. Figure 4-4 shows the pK_a(L) dependence of the d_{Mo-O} value of n**Br** or n**I** including those of $(TBA)_2[\{Mo_6X_8\}(RSO_3)_6]^{2-}$ (RSO$_3^-$ = p-toluenesulfonate: **18X**, benzenesulfonate: **19X**)[5] and $(TBA)_2[\{Mo_6X_8\}(4\text{-nitrophenol})_6]^{2-}$ (**20I**).[6] The figure demonstrates that the d_{Mo-O} values of the clusters including those of the sulfonate and phenolate clusters correlate linearly with pK_a(L) with the correlation
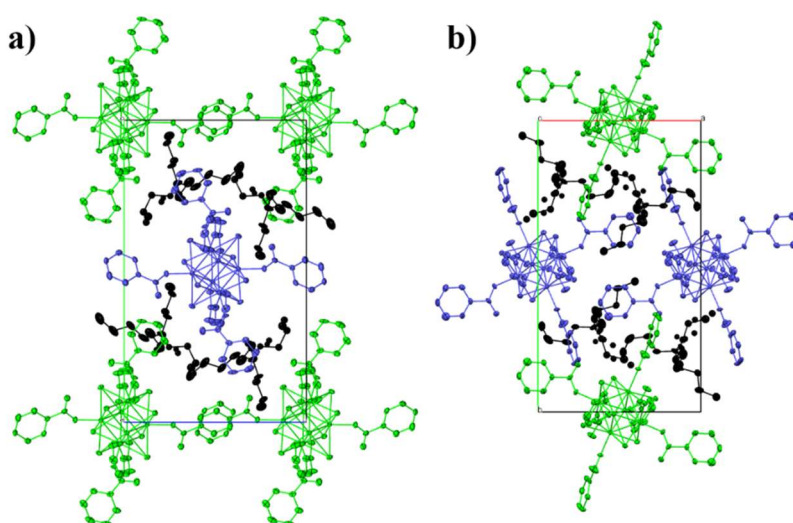

Figure 4-1. Packing structures of **7I** projected from (a) the a-axis and (b) the c-axis. The molecules shown by the colors are as follows: the counter cation TBA$^+$ (black) and non-equivalent clusters (green and blue).

coefficient (*cc*) being 0.834 or 0.750 for ***n*Br** or ***n*I**, respectively. The results demonstrate explicitly that the stronger σ-donating ability of the anionic terminal ligand gives rise to the shorter d_{Mo-O} value. For given L, furthermore, the d_{Mo-O} value of ***n*I** is longer than that of ***n*Br**. Similarly, since the π-donating ability of X increases in the sequence of $I^- < Br^- < Cl^-$ owing to the electronegativity of each atom, the shorter Mo-O bond length observed for ***n*Br** relative to that for ***n*I** for given L is the reasonable consequence. The results demonstrate clearly that the d_{Mo-O} value in $(TBA)_2[\{Mo_6X_8\}(RCOO)_6]$ can be tuned by $pK_a(L)$. To the best of author's knowledge, this is the first demonstration for the synthetic control of d_{Mo-O} in a hexamolybdenum(II) cluster.
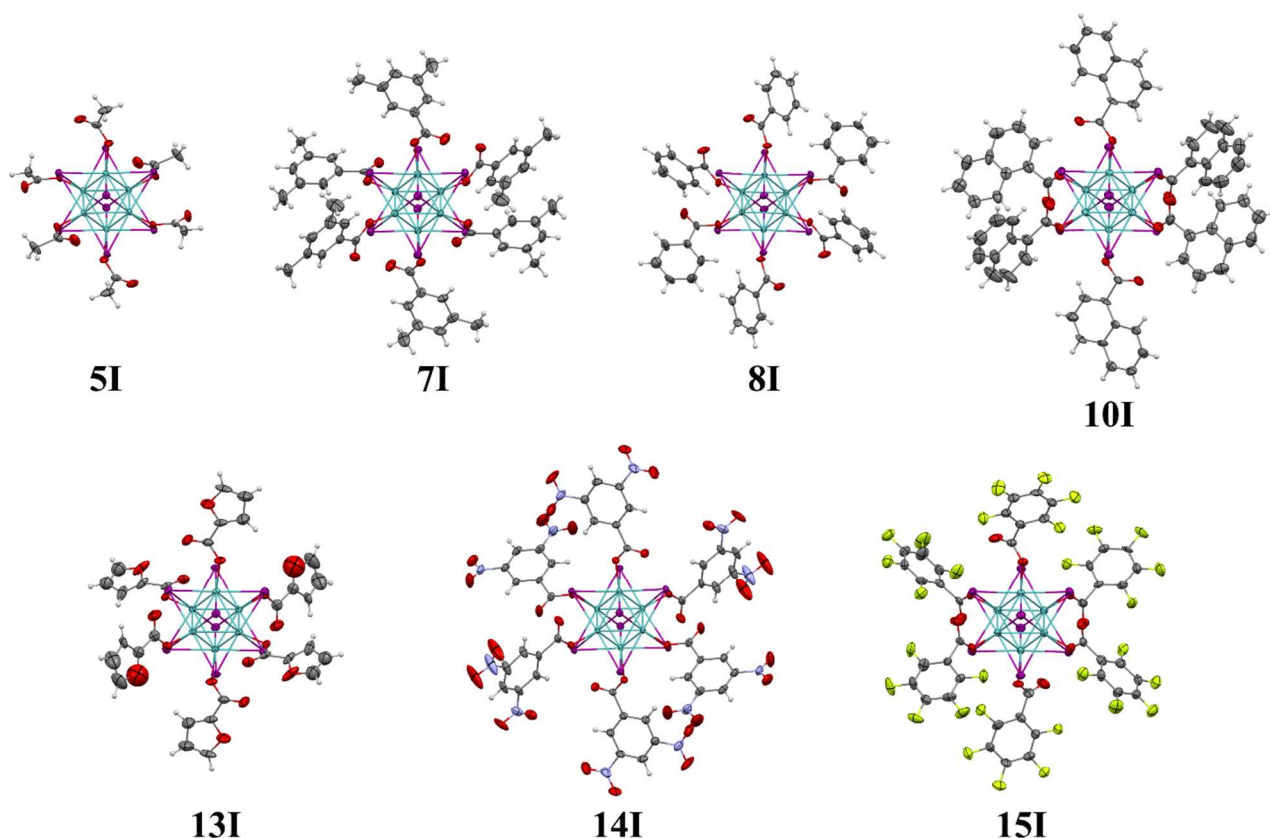

Figure 4-2. ORTEP drawings of **5I**, **7I**, **8I**, **10I**, and **13I**–**15I**. The thermal ellipsoids are displayed at the 50% probability level for the non-hydrogen atom. Atom color represents Mo (cyan), Br (orange), C (gray), N (blue), and O (red), and F (green). The counter cations TBA^+ in the structure were omitted to show the coordination structures of the ligands.
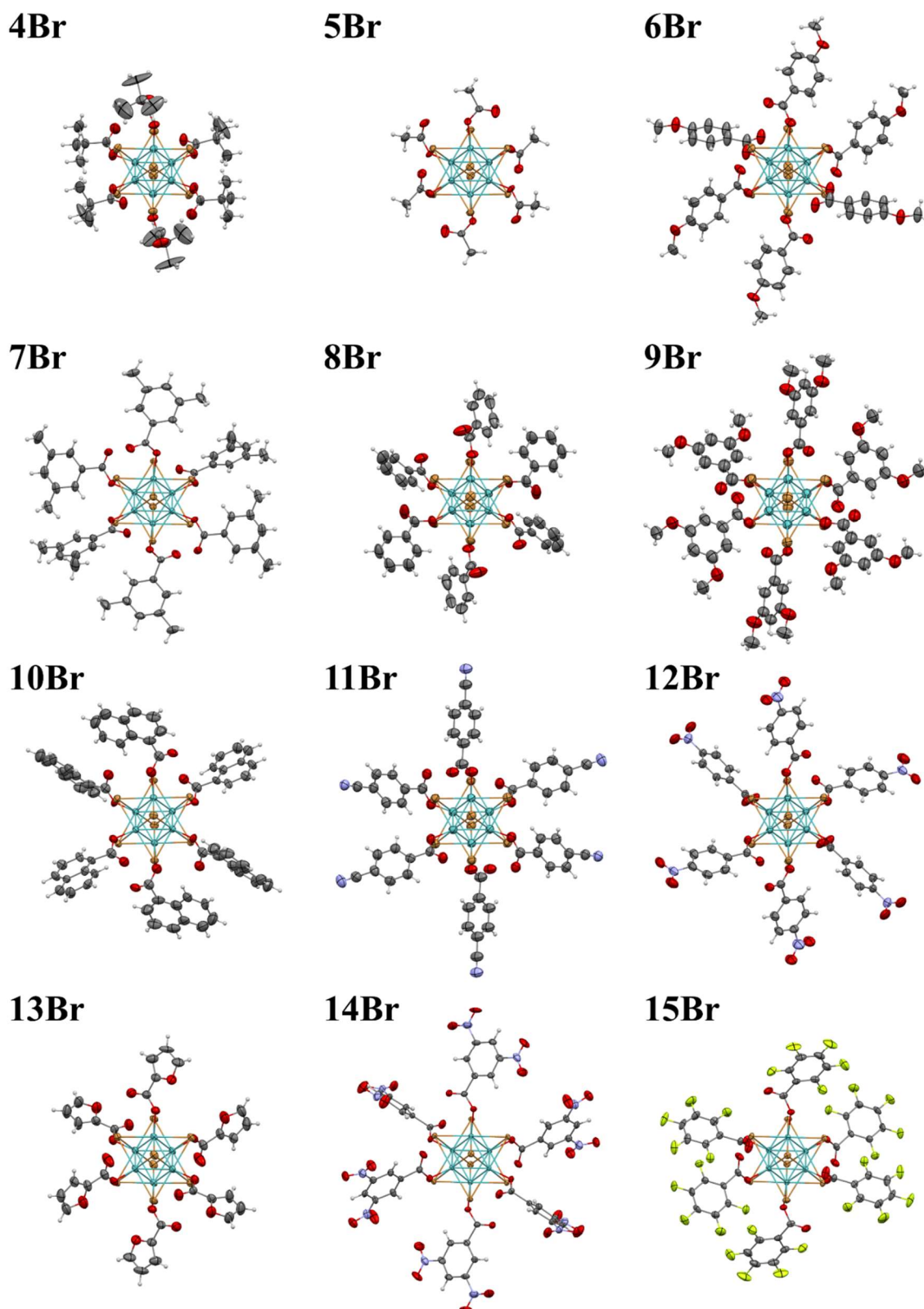
Figure 4-3. ORTEP drawings of **4Br–15Br**. The thermal ellipsoids are displayed at the 50% probability level for the non-hydrogen atom. Atom color represents Mo (cyan), Br (orange), C (gray), N (blue), O (red), and F (green). The counter cations TBA$^+$ in the structure were omitted to show the coordination structures of the ligands.

Table 4-1. Summary of the crystallographic data on **4Br**–**9Br**.

	4Br	5Br	6Br	7Br	8Br	9Br
T / K	150	150	150	150	150	150
Formula	$C_{74}H_{156}Br_8Mo_6N_2O_{17}$	$C_{44}H_{90}Br_8Mo_6N_2O_{12}$	$C_{74}H_{96}Br_8Mo_6N_8O_{24}$	$C_{86}H_{126}Br_8Mo_6N_2O_{12}$	$C_{80}H_{114}Br_8Mo_6N_2O_{14}$	$C_{86}H_{108}Br_8Mo_6N_8O_{14}$
fw	2654.80	2054.07	2696.50	2594.82	2542.66	2692.72
Crystal System	Monoclinic	Monoclinic	Triclinic	Monoclinic	Monoclinic	Monoclinic
Space Group	$C2/c$ (#15)	$P2_1/c$ (#14)	P-1 (#2)	$P2_1/c$ (#14)	$P2_1/n$ (#14)	$P2_1/n$ (#14)
a / Å	31.2648(10)	15.1335(12)	10.5647(3)	14.835(4)	13.450(5)	22.6128(4)
b / Å	15.856(4)	21.7459(16)	14.0336(5)	21.998(6)	23.923(8)	24.0823(2)
c / Å	26.184(8)	20.0844(11)	16.9473(6)	14.710(4)	14.435(5)	12.4409(2)
α /deg	90	90	82.058(3)	90	90	90
β / deg	90	90	72.306(3)	90	98.121(4)	131.921(3)
γ / deg	126.155(3)	90.920(3)	73.785(3)	96.950(4)	90	90
V / Å³	10481(4)	6608.8(8)	2294.63(14)	4765(2)	4598(3)	5041.0(2)
Z	4	4	1	2	2	2
measured refl.	76072	98944	40035	66707	58789	50835
unique refl.	11988	15138	8385	10939	10470	9160
R_{int}	0.0843	0.0817	0.0463	0.1044	0.0625	0.0430
GOF	1.141	1.116	1.023	1.078	1.058	1.080
$^a R_1$	0.0541	0.0820	0.0494	0.0771	0.0482	0.0590
$^b wR_2$	0.1170	0.1724	0.1388	0.1521	0.1360	0.1629

$^a R_1 = \Sigma||F_o| - |F_c|| / \Sigma|F_o|$. $^b wR_2 = [\Sigma(w(F_o^2 - F_c^2)^2) / \Sigma w(F_o^2)^2]^{1/2}$. $w = 1/ [\ \sigma^2(F_o^2) + (xP)^2 + yP]^{-1}$. $P = (F_o^2 - 2F_c^2)/3$

Table 4-2. Summary of the crystallographic data on **10Br**–**15Br**.

	10Br	11Br	12Br	13Br	14Br	15Br
T / K	150	150	150	150	150	150
Formula	$C_{98}H_{114}Br_8Mo_6N_2O_{12}$	$C_{86}H_{123}Br_8Mo_6N_2O_{24}$	$C_{160}H_{228}Br_{16}Mo_{12}N_4O_{36}$	$C_{62}H_{18}Br_8Mo_6N_2O_{18}$	$C_{74}H_{90}Br_8Mo_6N_{14}O_{36}$	$C_{82}H_{92}Br_8F_{30}Mo_6N_2O_{14}$
fw	2726.86	2783.78	5213.29	2293.70	2966.47	3114.46
Crystal System	Monoclinic	Triclinic	Monoclinic	Monoclinic	Monoclinic	Triclinic
Space Group	$P2_1$/c (#14)	P-1 (#2)	$P2_1$/c (#14)	$P2_1$/c (#14)	$P2_1$/n (#14)	P-1 (#2)
a / Å	13.288(2	15.0444(2)	21.8371(3)	13.130(3)	14.775(0)	12.4329(5)
b / Å	18.473(5)	15.2670(2)	19.0880(4)	14.212(3)	22.208(0)	14.5370(7)
c / Å	20.702(1)	22.4245(3)	25.6623(4)	21.114(5)	14.907(0)	14.6775(5)
α /deg	90	91.519(1)	90	90	90	82.676(9)
β / deg	90	93.540(1)	92.005(2)	90	97.717(0)	73.905(9)
γ / deg	106.5630(0)	101.662(1)	90	97.594(3)	90	87.9657(10)
V / Å³	4870(1)	5030.57(12)	10690.2(3)	3905.4(15)	4847.033(68)	2528.0(2)
Z	2	2	2	2	2	1
measured refl.	75884	99084	184948	29018	39631	39991
unique refl.	11135	17721	19422	8772	11117	11578
R_{int}	0.1425	0.0569	0.0524	0.0423	0.0548	0.0656
GOF	1.108	1.033	1.001	1.121	1.101	0.974
[a]R_1	0.1067	0.0842	0.0585	0.0544	0.0507	0.0376
[b]wR^2	0.2545	0.2426	0.1625	0.1416	0.1121	0.0850

[a]$R_1 = \Sigma||F_o| - |F_c|| / \Sigma|F_o|$. [b]$wR_2 = [\Sigma(w(F_o^2 - F_c^2)^2) / \Sigma w(F_o^2)^2]^{1/2}$. $w = 1/ [\sigma^2(F_o^2) + (xP)^2 + yP]^{-1}$. $P = (F_o^2 - 2F_c^2)/3$

Table 4-3. Summary of the crystallographic data on **10Br**–**15Br**.

	5I	7I	8I	10I	13I	15I	17I
T / K	100	150	150	150	150	150	150
Formula	$C_{44}H_{90}I_8Mo_6N_2O_{12}$	$C_{92}H_{138}I_8Mo_6N_2O_{14}$	$C_{74}H_{102}I_8Mo_6N_2O_{12}$	$C_{98}H_{114}I_8Mo_6N_2O_{12}$	$C_{62}H_{90}I_8Mo_6N_2O_{18}$	$C_{74}H_{72}I_8Mo_6N_2O_{12}$	$C_{50}H_{72}F_{30}I_8Mo_6N_2O_{12}$
fw	2430.02	3086.98	2802.41	3102.75	2742.19	3342.22	3053.93
Crystal System	Monoclinic	Triclinic	Monoclinic	Monoclinic	Monoclinic	Monoclinic	Monoclinic
Space Group	$P2_1/n$ (#14)	P-1 (#2)	$P2_1/n$ (#14)	$P2_1/n$ (#14)	$P2_1/n$ (#14)	$P2_1/c$ (#14)	$P2_1/n$ (#14)
a / Å	11.8966(4)	13.245(6)	13.4410(7)	14.2267(10)	13.4921(7)	21.733(6)	12.5244(5)
b / Å	20.0367(7)	14.904(6)	23.9391(12)	16.1895(12)	13.7589(7)	19.410(4)	21.0853(8)
c / Å	14.4535(5)	15.234(8)	14.5922(6)	21.9690(16)	21.9131(11)	22.799(5)	16.6103(5)
α /deg	90	73.897(19)	90	90	90	90	90
β / deg	95.478(1)	80.40(2)	94.5167(14)	96.476(2)	94.388(1)	90	105.959(1)
γ / deg	90	66.149(18)	90	90	90	91.697(3)	90
V / Å³	3429.5(2)	2637(2)	4680.7(4)	5027.7(6)	4055.9(4)	9613(4)	4217.4(2)
Z	2	2	2	2	2	4	2
measured refl.	30771	40685	31670	23179	22468	151008	45446
unique refl.	16290	12210	9995	14804	12140	22036	9699
R_{int}	0.034	0.0727	0.059	0.062	0.042	0.1032	0.034
GOF	1.01	1.076	0.95	0.94	1.00	1.173	1.06
[a]R_1	0.038	0.0630	0.038	0.062	0.042	0.0794	0.035
[b]wR_2	0.082	0.1706	0.084	0.173	0.101	0.1635	0.088

[a]$R_1 = \Sigma||F_o| - |F_c|| / \Sigma|F_o|$. [b]$wR_2 = [\Sigma(w(F_o^2 - F_c^2)^2) / \Sigma w(F_o^2)^2]^{1/2}$. $w = 1/ [\ \sigma^2(F_o^2) + (xP)^2 + yP]^{-1}$. $P = (F_o^2 - 2F_c^2)/3$

Table 4-4. Selected average bond lengths of (TBA)$_2$[{Mo$_6$I$_8$}(RCOO)$_6$] (**nI**, left panel) and (TBA)$_2$[{Mo$_6$Br$_8$}(RCOO)$_6$] (**nBr**, right panel). The values in the brackets represent the ranges of the observed values. The data on **16I** and **17I** are taken from ref. 7 and 8, respectively.

|	d_{Mo-O} / Å	d_{Mo-Mo} / Å	d_{Mo-I} / Å		d_{Mo-O} / Å	d_{Mo-Mo} / Å	d_{Mo-Br} / Å
5I	2.118 (2.098–2.149)	2.672 (2.665–2.679)	2.783 (2.771–2.800)	**4Br**	2.076 (2.069–2.082)	2.623 (2.620–2.629)	2.609 (2.588–2.629)
7I	2.099 (2.097–2.103)	2.663 (2.654–2.672)	2.779 (2.756–2.792)	**5Br**	2.093 (2.085–2.101)	2.629 (2.622–2.637)	2.605 (2.588–2.627)
8I	2.097 (2.084–2.107)	2.667 (2.660–2.673)	2.786 (2.764–2.806)	**6Br**	2.096 (2.085–2.103)	2.627 (2.621–2.630)	2.601 (2.583–2.620)
10I	2.111 (2.097–2.135)	2.674 (2.663–2.681)	2.786 (2.780–2.805)	**7Br**	2.091 (2.068–2.110)	2.629 (2.611–2.652)	2.605 (2.576–2.637)
13I	2.120 (2.111–2.128)	2.673 (2.666–2.682)	2.780 (2.762–2.811)	**8Br**	2.091 (2.085–2.103)	2.625 (2.619–2.632)	2.601 (2.589–2.625)
15I	2.124 (2.117–2.135)	2.664 (2.658 –2.669)	2.779 (2.771–2.795)	**9Br**	2.082 (2.065–2.089)	2.625 (2.616–2.636)	2.602 (2.584–2.618)
16I[7]	2.123 (2.115–2.132)	2.664 (2.659–2.670)	2.781 (2.771–2.800)	**10Br**	2.101 (2.097–2.103)	2.625 (2.619–2.630)	2.602 (2.585–2.619)
17I[8]	2.132 (2.120–2.141)	2.661 (2.658–2.666)	2.774 (2.762–2.788)	**11Br**	2.099 (2.084–2.108)	2.629 (2.624–2.631)	2.605 (2.585–2.618)
				12Br	2.113 (2.112–2.114)	2.633 (2.627–2.637)	2.603 (2.578–2.633)
				13Br	2.106 (2.096–2.112)	2.628 (2.620–2.639)	2.604 (2.591–2.608)
				14Br	2.116 (2.096–2.130)	2.630 (2.623–2.638)	2.600 (2.587–2.614)
				15Br	2.105 (2.094–2.118)	2.627 (2.623–2.635)	2.602 (2.592–2.601)
				16Br[7]	2.118 (2.121–2.121)	2.626 (2.618–2.631)	2.600 (2.593–2.606)
				17Br[8]	2.113 (2.105–2.118)	2.623 (2.620–2.628)	2.601 (2.585–2.617)
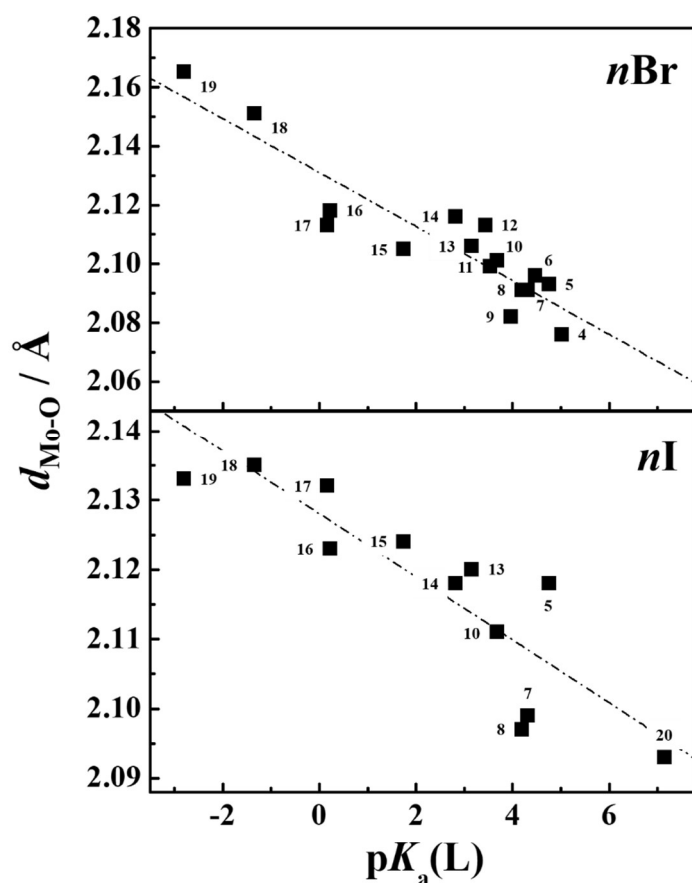
Figure 4-4. $pK_a(L)$ dependences of the d_{Mo-O} values of **nBr** (upper panel) and **nI** (lower panel): $[\{Mo_6X_8\}L_6]^{2-}$ with L: pivalate (**4X**), acetate (**5X**), 4-methoxybenzoate (**6Br**), 3,5-dimethylbenzoate (**7X**), benzoate (**8X**), 3,5-dimethoxybenzoate (**9Br**), 1-naphthoate (**10X**), 4-cyanobenzoate (**11Br**), 4-nitrobenzoate (**12Br**), 2-furoate (**13X**), 3,5-dinitorobenzoate (**14Br**), pentafluorobenzoate (**15X**), trifluoroacetate (**16X**),[7] *n*-heptafluorobutylate (**17X**),[8] *p*-toluenesulfonate (**18X**)[5], benzenesulfonate (**19X**)[5], 4-nitrophenolate (**20I**).[6] The $d_{Mo-O}/pK_a(L)$ data on **16X**–**20X** are taken from refs. 5–8. The $pK_a(L)$ values of *p*-toluenesulfonic acid, benzenesulfonic acid, and 4-nitrophenol are taken from refs. 9, 10, and 1, respectively. The broken line in the figure shows the regression line of the data.

4-3. Redox Properties

Figure 4-5 shows the cyclic voltammograms (CV) of **nBr** and **nI** in acetone, and the redox potentials of the clusters (E_{ox} and E_{red} vs. Fc⁺/Fc) determined by the relevant differential pulse voltammograms (DPVs) are summarized in Tables 4-5 and 4-6. All of the clusters show quasi-reversible oxidation waves irrespective of X and L. The E_{ox} value ranges in 0.56–1.33 or 0.34–0.91 V (vs. Fc/Fc⁺) for **nBr** or **nI**, respectively, and is shifted to a negative potential direction from +1.33 (**17Br**) to +0.59 V (**4Br**) or from +0.91 (**17I**) to +0.34 V (**4I**), respectively, with an increase in $pK_a(L)$ from 0.17 (n = **17**: heptafluorobutyric acid) to 5.03 (n = **1**: pivalic acid). It is worth pointing out that the E_{ox} values of both **nBr** and **nI**, responsible for the oxidation of the $\{Mo_6X_8\}^{4+}$-

cluster core, are proportional linearly with pK_a(L) with the correlation coefficient (*cc*) of 0.931 and 0.981 for *n*Br and *n*I, respectively, as shown in Figure 4-6a. The result indicates that coordination of stronger σ-donating carboxylate ligands (i.e., larger pK_a(L) ligand) to the $\{Mo_6X_8\}^{4+}$-core results in destabilization of the highest-energy occupied molecular orbital (HOMO) energy level of $[\{Mo_6X_8\}(RCOO)_6]^{2-}$. For given L, furthermore, E_{ox} of *n*Br is always more positive than that of *n*I. Since the σ-donating ability of X = Br is stronger than that of X = I, the E_{ox} value of *n*Br for given L should be more negative than that of the relevant *n*I, which is opposite to what is observed in Figure 4-6a. The shorter Mo-O bond length in *n*Br relative to that in *n*I for given L shown in Figure 4-4 indicates that more effective π-back donation in the $\{Mo_6Br_8\}^{4+}$-cluster core gives rise to the stabilization of the HOMO energy in *n*Br relative to that in *n*I and, thus, the E_{ox} values of *n*Br are more positive than those of *n*I.
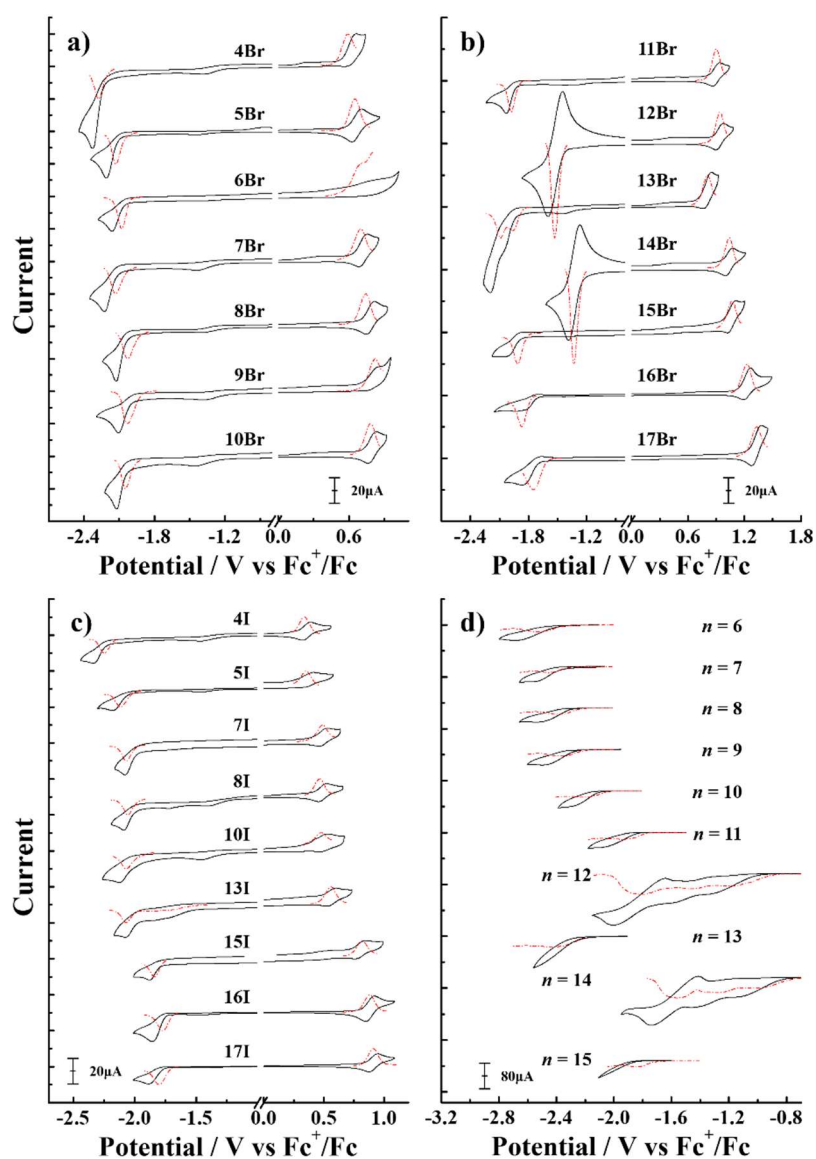

Figure 4-5. Cyclic voltammograms of (a) **4Br–10Br**, (b) **11Br–17Br**, (c) *n*I (*n* = 4, 5, 7, 8, 10, 13, and 15–17), and (d) RCOOH in acetone at 298 K. The broken red curves represent the differential pulse voltammograms.

Table 4-5. Redox properties of (TBA)$_2$[{Mo$_6$Br$_8$}(RCOO)$_6$] (*n*Br; $n = 4$–10 (upper panel) and $n = 11$–17 (lower panel)) in acetone at 298 K.

	4Br	5Br	6Br	7Br	8Br	9Br	10Br
pK_a(L)	5.03	4.76	4.47	4.32	4.20	3.97	3.69
E_{ox} / V	+0.59	+0.65	+0.70	+0.71	+0.74	+0.82	+0.78
E_{red} / V	–2.28	–2.13	–2.08	–2.12	–2.03	–2.03	–2.05
		(–2.39)[a]	(–2.54)	(–2.45)	(–2.39)	(–2.38)	(–2.20)
($E_{ox} - E_{red}$) / V	2.87	2.78	2.78	2.83	2.77	2.85	2.83

	11Br	12Br	13Br	14Br	15Br	16Br	17Br
pK_a(L)	3.55	3.44	3.16	2.82	1.75	0.23	0.17
E_{ox} / V	+0.90	+0.94	+0.81	+1.04	+1.07	+1.23	1.33
E_{red} / V	–1.98	–1.53	–2.09	–1.33	–1.87	–1.74	–1.75
	(–1.94)	(–1.81)	(–2.43)	(–1.57)	(–1.84)	(–1.81)[a]	
($E_{ox} - E_{red}$) / V	2.88	2.47	2.90	2.33	2.94	2.97	3.08

The values in the brackets represent the reduction potentials of the free ligands in the RCOOH form. Superscript a represents the data taken from ref. 11.

Table 4-6. Redox properties of (TBA)$_2$[{Mo$_6$I$_8$}(RCOO)$_6$] (*n*I) in acetone at 298 K.

	4I	5I	7I	8I	10I	13I	15I	16I	17I
pK_a(L)	5.03	4.76	4.32	4.20	3.69	3.16	1.75	0.23	0.17
E_{ox} / V	+0.34	+0.35	+0.49	+0.47	+0.48	+0.56	+0.75	+0.89	+0.91
E_{red} / V	–2.25	–2.12	–2.07	–2.06	–2.07	–2.07	–1.91	–1.77	–1.80
		(–2.39)[a]	(–2.45)	(–2.39)	(–2.20)	(–2.43)	(–1.84)	(–1.81)[a]	
($E_{ox} - E_{red}$) / V	2.59	2.47	2.56	2.53	2.55	2.63	2.66	2.66	2.71

The values in the brackets represent the reduction potentials of the free ligands in the RCOOH form. Superscript a represents the data taken from ref. 11.

Besides the oxidation waves and potentials, all of the clusters except for **12Br** and **14Br** show irreversible reduction waves, while **12Br** or **14Br** exhibits a reversible reduction wave. In the case of the clusters except for **12Br** and **14Br**, the E_{red} value of *n*I or *n*Br ranges from –2.25 to –1.80 or from –2.28 to –1.75 V (vs. Fc/Fc⁺), respectively, and is shifted to a negative potential direction from –1.80 (**17I**) to –2.25 V (**4I**) or from –1.75 (**17Br**) to –2.28 V (**4Br**), respectively, with an increase in pK_a(L), which is almost identical to the pK_a(L) dependence of the E_{ox} values. Different from the terminal ligand effects on the oxidation potential, on the other hand, the E_{red} values of both *n*I and *n*Br fall on a single line and that shifts linearly to the negative potential direction with an increase in pK_a(L) as seen clearly in Figure 4-6a: $cc = 0.890$. Furthermore, since the E_{red} value

of nX is similar to that of the corresponding terminal carboxylic acid, the reduction of the cluster is responsible for that of the terminal ligand(s), which indicates that the lowest-energy unoccupied MO (LUMO) energy level of the cluster is determined primarily by pK_a(L).

It is worth emphasizing that, as seen clearly in Figure 4-6, the reduction behavior of the clusters, **12Br** and **14Br**, are very much different from that of other clusters, where **12X** and **14X** show very large reduction currents relative to those of other clusters as well as to the relevant oxidation currents of **12X** and **14X**. As reported by Fujii et al., **12Br** and **14Br** exhibit quasi-one-step six-electron reduction,[12] while other clusters show one-electron reduction. The results in Figure 4-7 demonstrate that the E_{red} values of **12Br** and **14Br** are observed more positively than that predicted from the relevant pK_a(L) values probably due to the relatively small overpotential for the reduction. Furthermore, the ($E_{ox} - E_{red}$) value of the cluster, as a measure of the HOMO – LUMO energy gap, was plotted against the relevant pK_a(L) value as shown in Figure 4-6b. As seen clearly, the ($E_{ox} - E_{red}$) value correlated linearly with pK_a(L) (*cc* = 0.765 except for the data on **12Br** and **14Br**), while those of **12Br** and **14Br** deviated from the linear relationship in Figure 4-6a. The quasi-one-step six-electron reduction through the relatively small overpotentials compared to those other clusters[12] will be the principal reason for the positive E_{red} values of **12Br** and **14Br** relative to those predicted from the relevant pK_a(L) values.
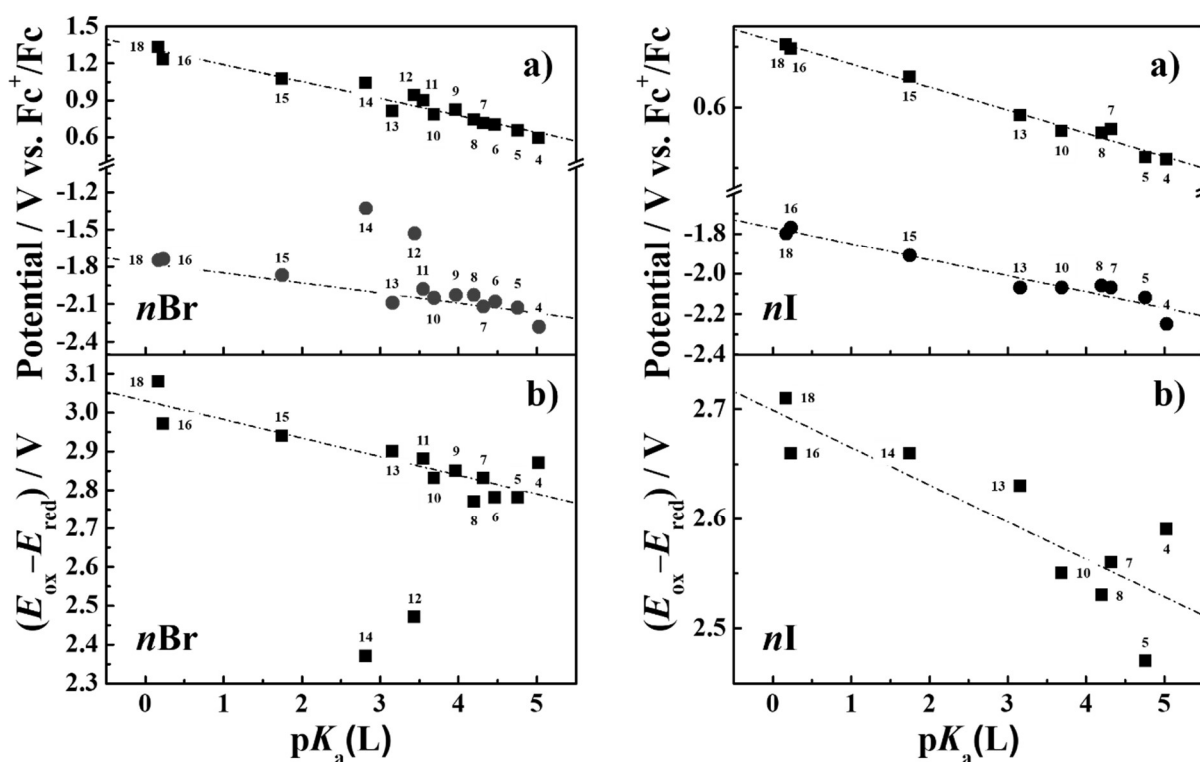

Figure 4-6. pK_a(L) dependences of (a) the E_{ox}, E_{red} and (b) ($E_{ox} - E_{red}$) values of n**Br** (left panel) and n**I** (right panel). Squares and circles in the panel (a) represent the data on E_{ox} and E_{red}, respectively. Numbering of the samples is the same with that in Chart 4-1 or Figure 4-4.

4-4. Emission Properties

Figures 4-7 and 4-8 show the emission spectra and emission decay profiles of **nBr** and **nI** in acetone, respectively, and the photophysical properties ($\tilde{v}_{em}$, Φ_{em}, and τ_{em}) are summarized in Tables 4-7 and 4-8. All of the clusters in acetone at 298 K exhibit near-infrared emission with $\tilde{v}_{em}$ of **nBr** and **nI** being ranged in $(13.87–14.31) \times 10^3$ cm⁻¹ (λ_{em} = 699–721 nm) and $(14.10–14.95) \times 10^3$ cm⁻¹ (669–709 nm), respectively. For both **nBr** and **nI**, an increase in $pK_a(L)$ gave rise to the lower energy shifts of $\tilde{v}_{em}$ and, the $\tilde{v}_{em}$ value of **nBr** or **nI** was correlated linearly with $pK_a(L)$ as shown in Figure 4-9a: cc = 0.886 and 0.975 for X = Br and I, respectively. The $pK_a(L)$ dependence of $\tilde{v}_{em}$ observed for **nI** was larger than that for **nBr**. This could be due to the weaker σ-donating ability of X = I relative to that of X = Br as discussed in Chapter 3. The emission energy of a $\{Mo_6I_8\}^{4+}$-core cluster would be thus influenced more strongly by $pK_a(L)$ compared to that of a $\{Mo_6Br_8\}^{4+}$-core cluster.
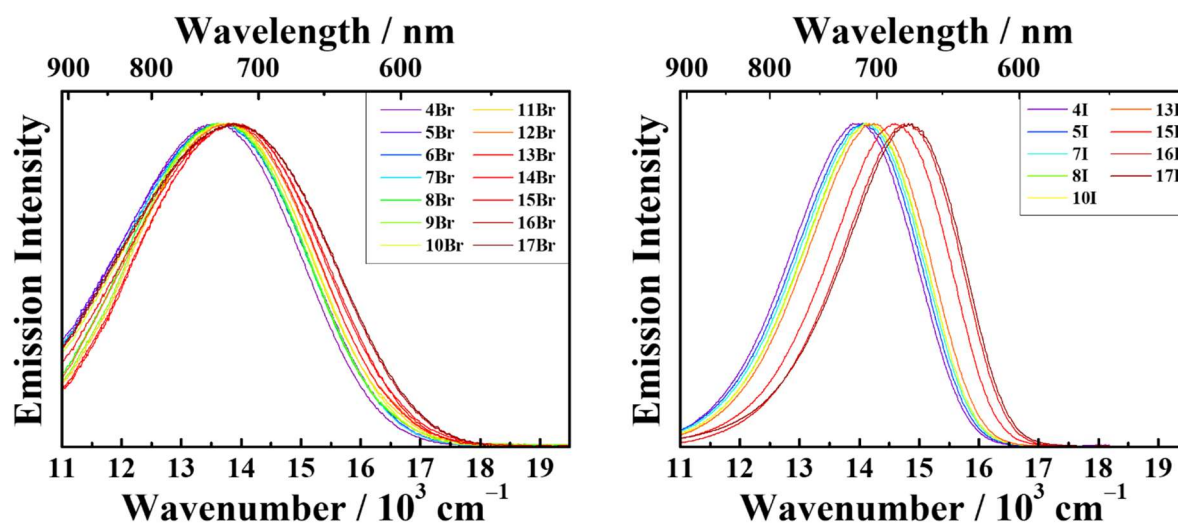

Figure 4-7. Corrected emission spectra of $[\{Mo_6Br_8\}(RCOO)_6]^{2-}$ (left panel) and $[\{Mo_6I_8\}(RCOO)_6]^{2-}$ (right panel) in deaerated acetone at 298 K. Color legend is indicated in the figure.
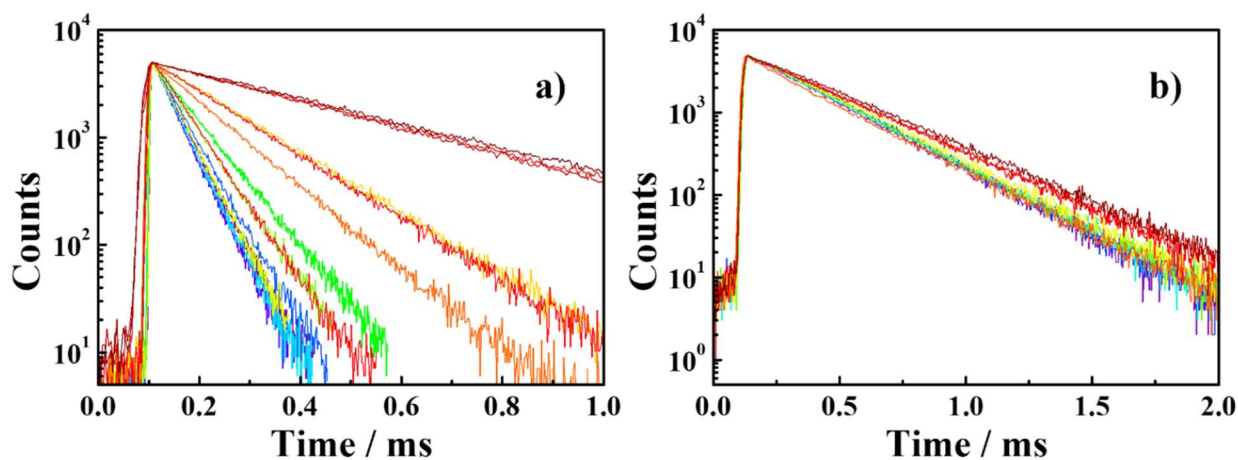

Figure 4-8. Emission decay profiles of $[\{Mo_6Br_8\}(RCOO)_6]^{2-}$ (left panel) and $[\{Mo_6I_8\}(RCOO)_6]^{2-}$ (right panel) in deaerated acetone at 298 K. Color legend is the same with that in Figure 4-7.

The Φ_{em} and τ_{em} values of n**I** range in 0.35–0.64 and 270–335 μs, respectively. Thus, the $\{Mo_6I_8\}^{4+}$-core clusters in acetone show intense and long-lived emission irrespective of nature of the terminal carboxylate ligand. On the other hand, n**Br** are weak emitters ($\Phi_{em} < 0.09$) with the short emission lifetimes ($\tau_{em} < 150$ μs), except for those with the perfluoro-carboxylate ligands (**15Br**–**17Br**), which exhibited relatively intense and long-lived emission: $\Phi_{em} = 0.23$–0.26 and $\tau_{em} = 350$–390 μs. According to Tables 4-9 and 4-10, one can easily find that the Φ_{em} and τ_{em} values of both n**Br** and n**I** are sensitive to the $pK_a(L)$ value and, thus, to the electronic properties of the terminal carboxylate ligand. Then, these parameters were plotted against the $pK_a(L)$ value as the results were shown in Figure 4-9b and 4-9c. Surprisingly, the Φ_{em} and τ_{em} values observed for n**Br** and n**I** show the clear $pK_a(L)$ dependences including the data on **15Br**–**17Br**. As seen in Figure 4-9b and 4-9c, both Φ_{em} and τ_{em} of the terminal carboxylate clusters correlate linearly with $pK_a(L)$: cc_Φ (cc_τ) = 0.859 (0.883) and 0.975 (0.990) for n**Br** and n**I** respectively.

Although the data in Figure 4-9 demonstrate explicitly that the spectroscopic ($\tilde{v}_{em}$) and photophysical properties (Φ_{em} and τ_{em}) of the clusters are controllable synthetically by $pK_a(L)$ and, thus, by the electron donating ability of the terminal carboxylate ligand, there is no theoretical rationale for the linear $pK_a(L)$

Table 4-7. Photophysical properties of $(TBA)_2[\{Mo_6Br_8\}(RCOO)_6]$ (n**Br**; $n = 4$–10 (upper panel) and $n = 11$–17 (lower panel)) in acetone at 298 K.

	4Br	5Br	6Br	7Br	8Br	9Br	10Br
$pK_a(L)$	5.03	4.76	4.47	4.32	4.20	3.97	3.69
$\tilde{v}_{em}$ / 10^3 cm^{-1}	13.87	13.97	13.95	13.97	14.03	13.99	13.97
($fwhm$ / cm^{-1})	(3580)	(3640)	(3570)	(3650)	(3410)	(3460)	(3720)
[λ_{em} / nm]	[721]	[716]	[717]	[716]	[713]	[715]	[716]
Φ_{em}	0.02	0.03	0.02	0.03	0.06	0.04	0.03
τ_{em} / μs	45	45	50	50	85	60	50
k_r / 10^3 s^{-1}	0.44	0.67	0.40	0.60	0.71	0.67	0.60
k_{nr} / 10^3 s^{-1}	22	22	20	19	11	16	19

	11Br	12Br	13Br	14Br	15Br	16Br	17Br
$pK_a(L)$	3.55	3.44	3.16	2.82	1.75	0.23	0.17
$\tilde{v}_{em}$ / 10^3 cm^{-1}	14.09	14.12	14.04	14.18	14.20	14.29	14.31
($fwhm$ / cm^{-1})	(3610)	(3400)	(3670)	(3460)	(3810)	(4060)	(4110)
[λ_{em} / nm]	[710]	[708]	[712]	[705]	[704]	[700]	[699]
Φ_{em}	0.09	0.07	0.09	0.05	0.24	0.23	0.26
τ_{em} / μs	150	110	150	65	290	355	390
k_r / 10^3 s^{-1}	0.60	0.64	0.60	0.77	0.83	0.65	0.67
k_{nr} / 10^3 s^{-1}	6.1	8.4	6.1	15	2.6	2.2	1.9

Table 4-8. Photophysical properties of $[\{Mo_6I_8\}(RCOO)_6]^{2-}$ (*n*I) in acetone at 298 K.

	4I	5I	7I	8I	10I	13I	15I	16I	17I
pK_a(L)	5.03	4.76	4.32	4.20	3.69	3.16	1.75	0.23	0.17
$\tilde{v}_{em}$ / 10^3 cm⁻¹	14.10	14.16	14.22	14.31	14.27	14.35	14.73	14.90	14.95
(*fwhm* / cm⁻¹)	(2400)	(2400)	(2380)	(2370)	(2350)	(2370)	(2320)	(2280)	(2300)
[λ_{em} / nm]	[709]	[706]	[703]	[699]	[701]	[697]	[679]	[671]	[669]
Φ_{em}	0.35	0.38	0.42	0.42	0.45	0.46	0.56	0.60	0.64
τ_{em} / μs	270	275	280	280	285	290	315	330	335
k_r / 10^3 s⁻¹	1.30	1.38	1.50	1.50	1.58	1.59	1.78	1.82	1.91
k_{nr} / 10^3 s⁻¹	2.41	2.25	2.07	2.07	1.93	1.86	1.40	1.21	1.07
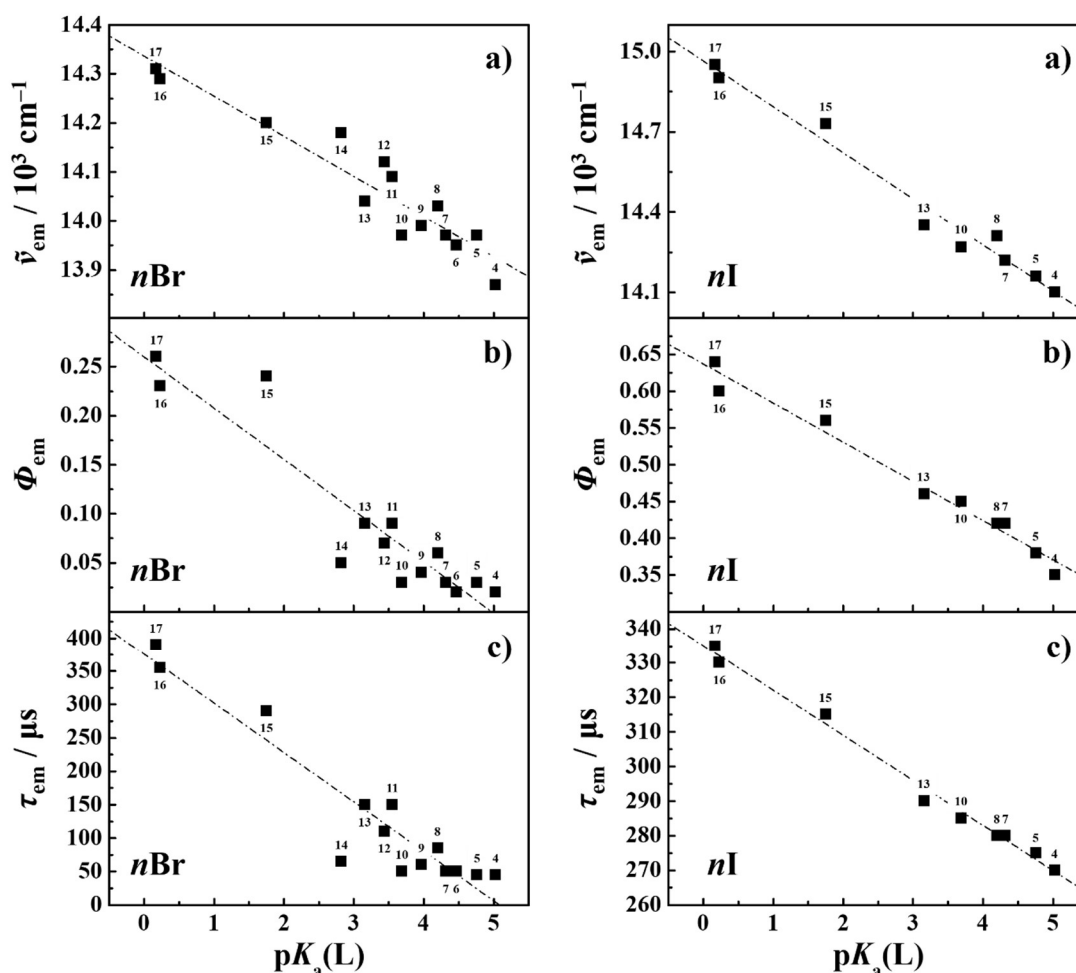
Figure 4-9. pK_a(L) dependences of (a) $\tilde{v}_{em}$, (b) Φ_{em}, and (c) τ_{em} of *n*Br (left panel) and *n*I (right panel). Numbering of the samples is the same with that in Chart 4-1 or Figure 4-4.

dependences of Φ_{em} and τ_{em}. However, since the $\tilde{v}_{em}$ values of both *n*Br and *n*I correlate linearly with pK_a(L) as seen in Figure 4-9a, the following explanation could be made. According to the energy gap law mentioned in §3-3-3, the natural logarithm of k_{nr} is proportional to $\tilde{v}_{em}$ when the vibrational mode inducing nonradiative decay
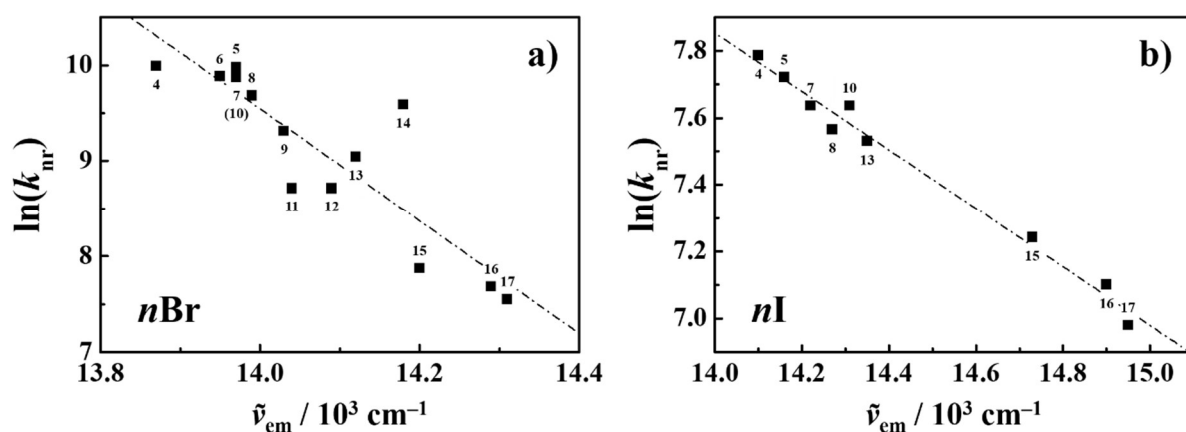
Figure 4-10. Relationship between the $\ln(k_{nr})$ and $\tilde{v}_{em}$ values of (a) $[\{Mo_6Br_8\}(RCOO)_6]^{2-}$ and (b) $[\{Mo_6I_8\}(RCOO)_6]^{2-}$ in deaerated acetone at 298 K. The broken lines show the linear regression of the data.

from the T_1 state to the electronically ground state (S_0) is identical among a series of compounds. In practice, for a given X, linear correlations between $\ln(k_{nr})$ and $\tilde{v}_{em}$ can be found for both n**Br** and n**I** as the data are shown in Figure 4-10: $cc = 0.763$ and 0.981 for n**Br** and n**I**, respectively. It is worth emphasizing that the $\tilde{v}_{em}$ values of both n**Br** and n**I** correlate linearly with $pK_a(L)$ as shown in Figure 4-9a and, thus, the $\ln(k_{nr})$ value also correlates with $pK_a(L)$: $k_{nr} \propto pK_a(L)$. In the present case, since the variation of k_r by the terminal carboxylate ligand ((0.44–0.83) $\times$ 10^3 or (1.30–1.91) $\times$ 10^3 s^{-1} for the n**Br** or n**I**, respectively) is smaller than that of k_{nr} ((1.9–22) $\times$ 10^3 or (1.1–2.4) $\times$ 10^3 s^{-1}, respectively) as seen in Tables 4-7 and 4-8, both Φ_{em} and τ_{em} values of the clusters are governed by k_{nr}: Φ_{em} and $\tau_{em} \propto k_{nr}^{-1}$. The linear $pK_a(L)$ dependences of $\tilde{v}_{em}$ of the clusters thus provide those of Φ_{em} and τ_{em} in Figure 4-10. Furthermore, the $h\omega$ values evaluated from the slopes of the energy gap plots for n**Br** and n**I** are different significantly with each other and are 170 and 1145 cm^{-1}, respectively. In the case of $[\{Mo_6Br_8\}Y_6]^{2-}$ (**1Br**–**3Br**), since the vibrational frequency assigned to the Mo-Br stretching mode in the $\{Mo_6Br_8\}^{4+}$-core (203–212 cm^{-1}) is comparable to the $h\omega$ value observed for n**Br**,[13] nonradiative decay from the T_1 state of n**Br** is determined primarily by the Mo-Br stretching mode. In contrast, since the $h\omega$ value observed for n**I** agrees well with the vibrational frequency of the C-O stretching mode of the carboxylate (1200–1300 cm^{-1}), nonradiative decay from the T_1 state of n**I** would be originated from the carboxylate ligand. Judging from Figure 4-4, the carboxylate coordinates strongly to the $\{Mo_6I_8\}^{4+}$-core relative to that to the $\{Mo_6Br_8\}^{4+}$-core and, therefore, the various properties of n**I** are strongly affected by the terminal carboxylate ligand compared to those of n**Br**, resulting in the dramatic $pK_a(L)$ dependences of the crystallographic, redox, spectroscopic, and emission properties of n**I**.

4-5. Bridging Ligand Effects on Temperature Dependent Emission Characteristics of [{Mo₆X₈}-(C₃F₇COO)₆]²⁻ (X = Cl, Br, or I)

4-5-1. Temperature Dependent Emission Spectra

Figure 4-11 shows the *T*-dependences of the emission spectra of **17X** in PEG-DMA matrixes, and those of $\tilde{v}_{em}$ and the full-width at half maximum of the spectrum (*fwhm*) are summarized in Figure 4-12. The emission spectrum of **17Cl** was shifted to the lower-energy on going from 3 ($\tilde{v}_{em} = 12.9 \times 10^3$ cm^{-1}, $\lambda_{em} = 776$ nm) to 70 K (12.5×10^3 cm^{-1}, 800 nm). Subsequently, *T*-elevation above 70 K gave rise to an increase in $\tilde{v}_{em}$ (upto ~13.2×10^3 cm^{-1} or ~756 nm at 300 K). Such spectral shifts upon *T*-elevation accompanied the increase in the *fwhm* value of the spectrum from 2460 cm^{-1} (at 3 K) to 3870 cm^{-1} (at 300 K). The cluster complex, **17Br**, also showed analogous trends to those of **17Cl**: typically, $\tilde{v}_{em} = 12.7 \times 10^3$ ($\lambda_{em} = 787$ nm), 12.2×10^3 (821 nm), and 13.1×10^3 cm^{-1} (763 nm) at 3, 70, and 300 K, respectively, and *fwhm* varied from 2570 to 3790 cm^{-1} on going from 3 to 300 K. Such *T*-dependent emission shifts have been commonly observed for (TBA)₄[{Re₆S₈}X₆] (X = Cl, Br, and I), (TBA)₂[{W₆Cl₈}Cl₆], and (TBA)₂[{Mo₆X₈}Y₆] (X = Cl or Br: **nCl** or **nBr** in Chapter 3) in the crystalline
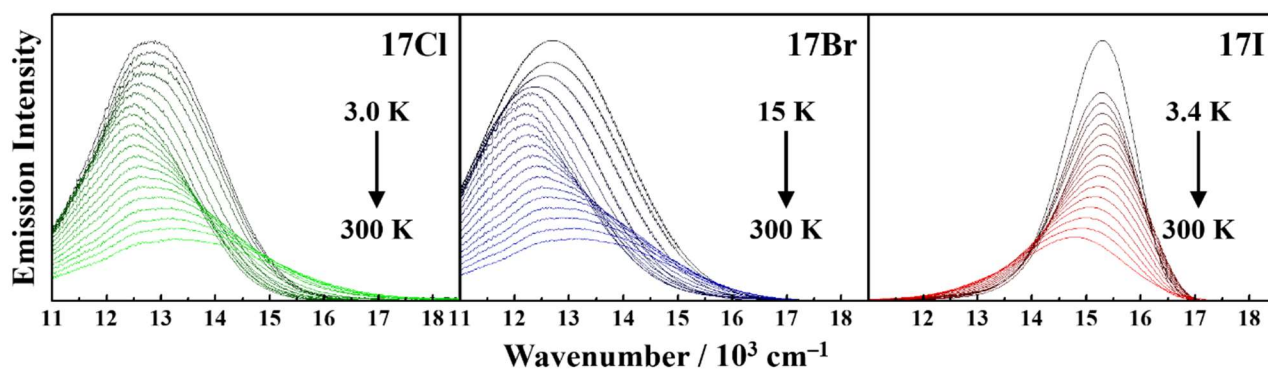
Figure 4-11. *T*-Dependences of the emission spectra of [{Mo₆X₈}(nC₃F₇COO)₆]²⁻ (left: X = Cl, center: X = Br, right: X = I) in polymer matrixes in 3 K < *T* < 300 K. Temperature variation is shown by the color gradation from black (3 K) to highlight (300 K).

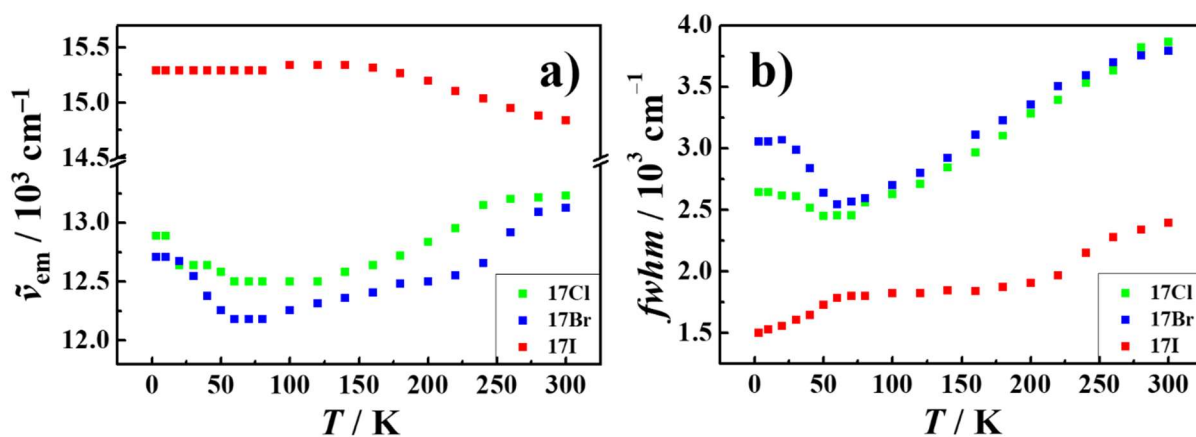**Figure 4-12**. *T*-Dependences of (a) the $\tilde{v}_{em}$ (b) and *fwhm* values of **17X** in polymer matrixes.
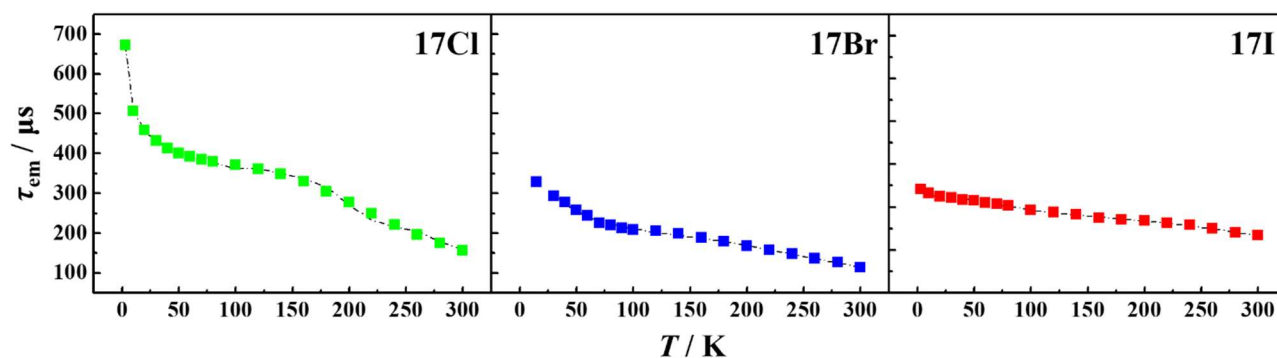
Figure 4-13. *T*-Dependences of τ_{em} of $[\{Mo_6X_8\}(nC_3F_7COO)_6]^{2-}$ (left: X = Cl, center: X = Br, right: X = I) in polymer matrixes. The broken curves are the best fits of the $\tau(T)$ data by eq. 2-2 with the fitting parameters, ΔE_{1n} and τ_n values, being shown in Figure 4-14.

Table 4-9. *T*-Dependences of the emission lifetimes of $[\{Mo_6X_8\}(nC_3F_7COO)_6]^{2-}$ (**17X**) in polymer matrixes.

T / K	**17Cl**	**17Br**	**17I**
3.0	671	–	–
3.4	–	–	341
10	508	–	332
15	–	328	–
20	456	293	325
30	432	278	322
40	417	257	317
50	402	244	315
60	393	226	310
70	383	219	307
80	377	213	303
100	362	209	293
120	362	205	288
140	350	198	283
160	338	189	275
180	316	179	271
200	271	168	268
220	233	158	263
240	215	147	258
260	205	137	249
280	179	126	240
300	151	114	234

phases and/or polymer matrixes.[14–16] In contrast, **17I** exhibited T-dependent emission characteristics different totally from those of **17Cl** and **17Br**. As seen in Figures 4-11 and 4-12, the $\tilde{v}_{em}$ value of **17I** was almost constant at 15.3×10^3 cm^{-1} (654 nm) in 3 K $<$ T $<$ 100 K, while that was shifted to the lower-energy above 100 K, which was an opposite T-dependent shift to that of **17Cl** or **17Br** as seen clearly in Figure 4-12. Furthermore, the *fwhm* value of **17I** (1500 and 2400 cm^{-1} at 3 and 300 K, respectively) was much smaller than that of **17Cl** or **17Br** (~2500 cm^{-1} at 3 K and ~3900 cm^{-1} at 300 K) in the entire T-range studied (Figure 4-12). Therefore, the small *fwhm* value of **17I** compared to that of **17Cl** or **17Br** is an inherent character of an $\{Mo_6I_8\}^{4+}$-core cluster as described in Chapter 3.

4-5-2. Temperature Dependent Emission Lifetimes

The emission decay profiles of the complexes can be fitted by single exponential functions irrespective of X and T (3 – 300 K), and the T-dependences of τ_{em} observed for **17X** are summarized in Figure 4-13 and Table 4-9. In the case of **17Cl** or **17Br**, the τ_{em} value decreased sharply upon T-elevation from 3 to ~30 K and, then, decreased gradually above 30 K. From 3 to 300 K, the τ_{em} values of **17Cl** and **17Br** decreased from 670 to 160 μs and from 330 to 115 μs, respectively. On the other hand, **17I** showed a relatively monotonous decrease in τ_{em} from 340 μs at 3 K to 235 μs at 300 K. It is worth emphasizing that the change in τ_{em} observed for **17I** upon T-variation from 3 (340 μs) to 300 K (235 μs) is as small as 105 μs. Such a small T-dependence of τ_{em} in the T range of 3–300 K has observed only for the $\{Mo_6I_8\}^{4+}$-core cluster in §3-4-2 (**1I–3I**). Since **17X** is isoelectronic with $[\{Mo_6X_8\}Y_6]^{2-}$ (**1X–3X**) described in Chapter 3, the T-dependent $\tilde{v}_{em}$, *fwhm*, and τ_{em} of the clusters (Figures 4-11–4-13) should be explained by a common emission model.
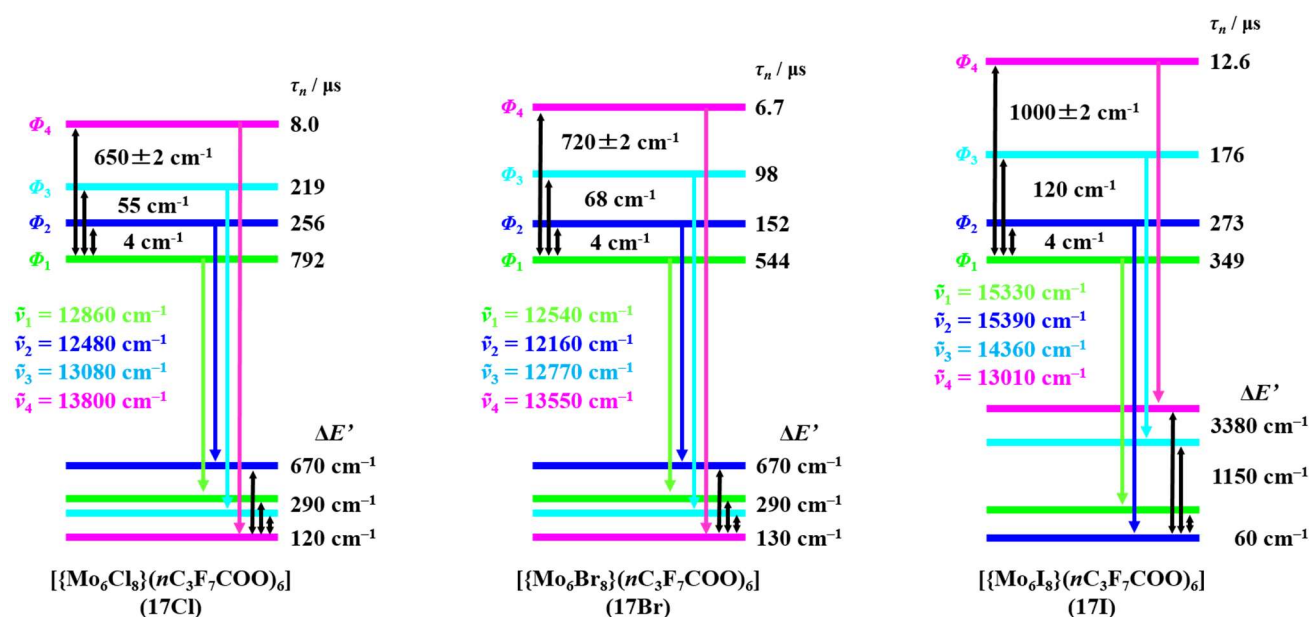

Figure 4-14. zfs parameters of $[\{Mo_6X_8\}(nC_3F_7COO)_6]^{2-}$.

4-5-2. Analysis of *T*-Dependent Emission Lifetimes by Spin-sublevel Model.

Similar to the *T*-dependences of the emission lifetimes and spectra of **1X–3X** in §3-4-3 and 3-4-4, those of **17X** were analyzed based on the Φ_n model. As seen in the Figure 4-13, the $\tau(T)$ data of **17X** were fitted very well by the ΔE_{1n} and τ_n values shown in Figure 4-14: the correlation coefficients (R^2) of the fittings were 0.998 for all of the $\tau(T)$ data. The ΔE_{13} and ΔE_{14} values were in the ranges of 55–120 and 650–1000 cm^{-1}, respectively. For a given X, the ΔE_{13} and ΔE_{14} values of **17X** are comparable to those of $[\{Mo_6X_8\}Y_6]^{2-}$. For example, the ΔE_{13} and ΔE_{14} values of **17Br** (68 and 720 cm^{-1}, respectively) agree with the relevant values of $[\{Mo_6Br_8\}Y_6]^{2-}$ (**1Br–3Br**, 53–63 and 635–695 cm^{-1}, respectively). Furthermore, the ΔE_{13} and ΔE_{14} values increased in the sequence **17Cl** (55 and 650 cm^{-1}) < **17Br** (68 and 720 cm^{-1}) < **17I** (120 and 1000 cm^{-1}) similar to those of $[\{Mo_6X_8\}Y_6]^{2-}$ despite the completely different terminal ligands (i.e., organic and inorganic terminal ligands). These findings demonstrate that one of the important factors governing the zfs energies (ΔE_{1n}, n = 3 and 4) is nature of the $\{Mo_6X_8\}$-core structure. The detailed discussion on the zfs energy are described in Chapter 5.

4-5-3. Simulation of Emission Spectra by Spin-sublevel Model.

On the basis of the ΔE_{1n} values, furthermore, the emission spectrum of **17X** at a given *T* was analyzed as the results were shown in Figure 4-15. The $\tilde{v}_n$ values evaluated are included in Figure 4-14. Figure 4-15 demonstrates clearly that the observed spectrum can be fitted very well by eqs. 2-2 and 2-3 irrespective of X and *T* with R^2 being ~1.00. Although the *T*-dependent emission shift of **17I** is different largely from those of **17Cl** or **17Br**, the Φ_n model explains successfully such different *T*-dependent emission characteristics of **17X**. As shown in Figure 4-16 and Table 4-10, the present spectral analysis demonstrates that the major contributions to the emission spectra of **17Cl** and **17Br** at 300 K are the emissions from Φ_3 and Φ_4 (Φ_3 = 45 % and Φ_4 = 55 % for **1**; Φ_3 = 72 % and Φ_4 = 28 % for **2**), while the emission spectrum of **17I** is explained by the large contributions of the emissions from Φ_2 and Φ_3: Φ_2 = 50 %, Φ_3 = 47 %, and Φ_4 = 3 %. Thermal population from Φ_1 to Φ_4 at a given *T* is governed by ΔE_{14} and, thereby, the contribution of the Φ_4 emission to an observed spectrum at 300 K should become smaller with an increase in ΔE_{14}. In practice, the contribution of the Φ_4 emission to the observed spectrum at 300 K decreases in the sequence **17Cl** (ΔE_{14} = 650 cm^{-1}, Φ_4 = 55%) > **17Br** (720 cm^{-1}, 28%) > **17I** (1000 cm^{-1}, 3%). It is worth noting that these results coincide well with the relationship between ΔE_{14} and the Φ_n contribution percentage to an observed emission spectrum at 300 K for a given X in $[\{Mo_6X_8\}Y_6]^{2-}$ (**1X–3X**) as described in §3-4-4.

The percentages of Φ_n contributed to the emission spectrum of each cluster (Φ_n%) mentioned above explain very well the emission characteristics of **17X** reported by Sokolov et al. in 2011.[8] Almost equal contributions of Φ_3 ($\tilde{v}_3$ = 13.1×10^3 cm^{-1}) and Φ_4 ($\tilde{v}_4$ = 13.8×10^3 cm^{-1}) or Φ_2 ($\tilde{v}_2$ = 15.4×10^3 cm^{-1}) and Φ_3 ($\tilde{v}_3$ = 14.4×10^3 cm^{-1}) to the emission spectrum of **17Cl** or **17I**, respectively, demonstrate the relevant average $\tilde{v}_{em}$ value to be 13.4×10^3 (λ_{em} = 744 nm) or 14.9×10^3 cm^{-1} (672 nm), respectively, which agrees very well with the observed $\tilde{v}_{em}$ reported by Sokolov et al.: 13.4×10^3 cm^{-1} (745 nm) for **17Cl** and 15.0×10^3 cm^{-1} (668 nm) for **17I**.[8] On the basis of the simulated *fwhm*(Φ_n) values of **17Cl** (3260 cm^{-1}) and **17I** (1460 cm^{-1}) at 300 K shown in Figure 4-
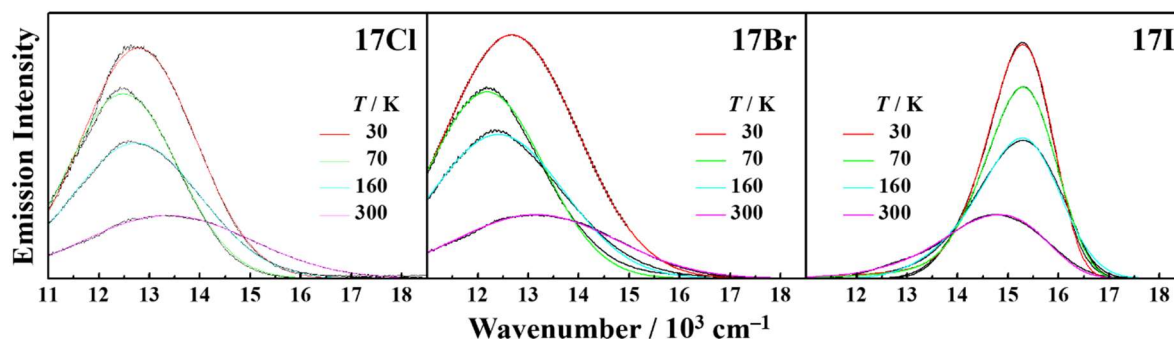
Figure 4-15. Simulations of the *T*-dependent emission spectra of $[\{Mo_6X_8\}(nC_3F_7COO)_6]^{2-}$ in polymer matrixes. The spectra shown by the black curves are the observed ones, while the simulated spectra are shown by the colors indicated in the figures.

16, furthermore, the *fwhm* values of the whole spectra of **17Cl** and **17I** in CH_3CN at 298 K are predicted to be 3980 and 2390 cm⁻¹, respectively, which is also in good agreement with the observed values: 3870 and 2400 cm⁻¹ for **17Cl** and **17I**, respectively. Similarly, the observed $\tilde{v}_{em}$ and *fwhm* values of **17Br** can be also reproduced very well by the Φ_n percentage and $fwhm(\Phi_n)$ as reported in Figure 4-16 and Table 4-10. It is worth pointing out that the $fwhm(\Phi_n)$ value of **17I** is much smaller than that of **17Cl** or **17Br**: **17Cl** (3260 cm⁻¹) ~ **17Br** (3420 cm⁻¹) > **17I** (1460 cm⁻¹). The results demonstrate clearly that the small $fwhm(\Phi_n)$ value is the origin of a sharp emission band of an $\{Mo_6I_8\}^{4+}$-core cluster relative to that of an $\{Mo_6Cl_8\}^{4+}$- or $\{Mo_6Br_8\}^{4+}$-core cluster as described in §3-4-6. The *fwhm* value of an emission spectrum observed at 3 K will be determined primarily by the slope of the potential energy curve in S_0 at the T_1 geometry. In the present case, the broad Φ_n emission spectra of an $\{Mo_6Cl_8\}^{4+}$- or $\{Mo_6Br_8\}^{4+}$-core cluster will be ascribed to the radiative transition from Φ_n to the potential curve in the relevant ground state with a rather steep slope, while the sharp Φ_n spectrum of an $\{Mo_6I_8\}^{4+}$-core cluster indicates the radiative transition occurs from T_1 to near the bottom of the potential curve in S_0. Such simple considerations on $fwhm/fwhm(\Phi_n)$ demonstrate that the T_1 states of $\{Mo_6Cl_8\}^{4+}$- or $\{Mo_6Br_8\}^{4+}$-core cluster are considerably distorted probably due to Jahn-Teller effects, while the T_1 geometry in an $\{Mo_6I_8\}^{4+}$-core cluster is less distorted.

The characteristic *T*-dependent emission shifts of **17Cl** and **17Br**, showing lower- and subsequent higher-energy shifts from 3 to 300 K, have been also observed for $[\{Mo_6Cl_8\}Y_6]^{2-}$ (**1Cl–3Cl**), $[\{Mo_6Br_8\}Y_6]^{2-}$ (**1Br–3Br**), and $[\{Mo_6I_8\}I_6]^{2-}$ (**3I**) and, thus, its origin can be explained by the similar arguments to those described in §3-4-5. Briefly, the emission maximum energy of each Φ_n ($\tilde{v}_n$ in cm⁻¹) does not increase in the sequence, $\tilde{v}_1 < \tilde{v}_2 < \tilde{v}_3 < \tilde{v}_4$, but increases in the order of $\tilde{v}_2$ (12.5×10³) < $\tilde{v}_1$ (12.9×10³) < $\tilde{v}_3$ (13.1×10³) < $\tilde{v}_4$ (13.8×10³) for **17Cl** or $\tilde{v}_2$ (12.2×10³) < $\tilde{v}_3$ (12.4×10³) < $\tilde{v}_1$ (12.5×10³) < $\tilde{v}_4$ (13.5×10³) for **17Br**. The energy order of $\tilde{v}_n$ observed for **17Cl** is essentially the same with that for $[\{Mo_6Cl_8\}Cl_6]^{2-}$: common for an $\{Mo_6Cl_8\}$-core structure.
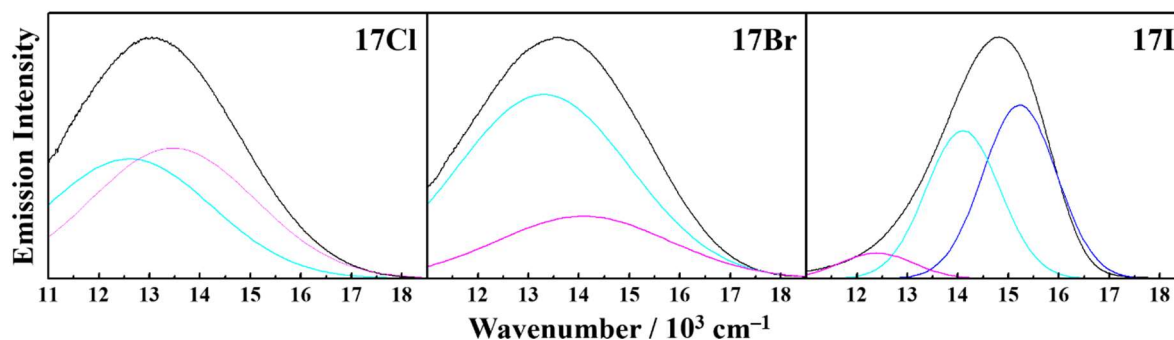
Figure 4-16. Observed and simulated emission spectra of $[\{Mo_6X_8\}(nC_3F_7COO)_6]^{2-}$ in CH_3CN at 298 K. The observed spectra shown by the black color are taken from ref. 8. The relative contributions of the Φ_n emission spectra to the observed spectra of a given cluster are shown by blue ($n = 2$), cyan ($n = 3$), and magenta ($n = 4$), respectively. The $fwhm(\Phi_n)$ values used to reproduce the data are 3260, 3420, and 1460 cm^{-1} for **17Cl**, **17Br**, and **17I**, respectively.

Although the main contribution of the emission from **17Cl** or **17Br** at 3 K is that from Φ_1 ($\tilde{v}_1 = 12.9 \times 10^3$ or 12.5×10^3 cm^{-1} for **17Cl** or **17Br**, respectively), T-elevation to 70 K gives rise to the increase in the contribution of the Φ_2 emission ($\tilde{v}_2 = 12.5 \times 10^3$ or 12.2×10^3 cm^{-1} for **17Cl** or **17Br**, respectively) and, thus, the observed $\tilde{v}_{em}$ is shifted to the lower-energy. Since further T-elevation leads to the participation of the Φ_3 and Φ_4 emissions, the observed emission spectrum of **17Cl** or **17Br** as the sum of the emissions from Φ_n ($n = 1$–4) shifts to the lower-energy as expected from the $\tilde{v}_3$ and $\tilde{v}_4$ values of **17Cl** or **17Br**: see Figure 4-15. In the case of **17I**, on the other hand, since the energy order of $\tilde{v}_n$ (in cm^{-1}) is $\tilde{v}_4$ (13.5×10^3) $< \tilde{v}_3$ (14.4×10^3) $< \tilde{v}_1$ (15.3×10^3) $\leq \tilde{v}_2$ (15.4×10^3) and ΔE_{13} (120 cm^{-1}) is relatively large compared to that of **17Cl** (55 cm^{-1}) or **17Br** (68 cm^{-1}), the main contributions to the emission spectrum of **17I** in 3 K $< T <$ 70 K are the Φ_1 and Φ_2 emissions and, thus, the $\tilde{v}_{em}$ value of the cluster is almost unchanged as seen in Figures 4-11 and 4-12. The emission spectrum of **17I** shifts to the lower-energy owing to the participations of the Φ_3 and Φ_4 emissions above 70 K. These discussions demonstrate that the Φ_n model explains satisfactorily the emission characteristic of **17X** in 3 K $< T <$ 300 K and, therefore, the analysis of T-dependent emissions by the Φ_n model provides satisfactorily the zfs parameters. The detailed discussion on the zfs parameters are described in Chapter 5.

The difference in $\tilde{v}_n$ between Φ_1 and Φ_n ($\Delta\tilde{v}_n$) is governed by ΔE_{1n} and the energy of the Franck-Condon ground state ($S_0(FC)$) responsible for each Φ_n emission transition. Knowing ΔE_{1n} and Δv_n, the energy differences between the ($S_0(FC)$) for the Φ_n emissions ($\Delta E'$) are evaluated as the data are included in Figure 4-14. As mentioned in §3-4-5, $\Delta E'$ will be determined by the displacement of the potential surface between the Φ_n level and the relevant ($S_0(FC)$) along a vibrational coordinate. Ramirez-Tagle et al. have reported the computational calculations on the vibrational frequencies of $[\{Mo_6X_8\}Y_6]^{2-}$, and these clusters show active vibrations assigned to the Mo-Mo and Mo-X stretching modes in the ranges of 136–350 and 151–399 cm^{-1}, respectively.[13]

Table 4-10. Contribution percentages (Φ_n%) of the Φ_n emissions to the observed spectra of [{Mo_6X_8}(n-C_3F_7COO)$_6$]$^{2-}$ in CH_3CN at 298 K.

	17Cl	**17Br**	**17I**
Φ_1 / %	0	0	0
Φ_2 / %	0	0	53.1
Φ_3 / %	44.9	71.5	47.4
Φ_4 / %	55.1	28.5	3.5

Furthermore, while the stretching vibrational frequency of the Mo-O bond (coordinated O atom in the terminal ligand) has been reported to be 670 cm^{-1},[17] the present clusters show the IR bands at around 670 cm^{-1} irrespective X. In the case of **17Cl** and **17Br**, the ΔE' values were evaluated to be ~130, 290, and 670 cm^{-1}, which might correspond roughly to the Mo-Mo, Mo-X, and Mo-O stretching frequencies, respectively. Since the excited state of the octahedral hexametal cluster has been reported to be best characterized by the {Mo_6X_8}-core centered excited state,[13,18,19] the observation of ΔE' relevant to the Mo-Mo, Mo-X, and Mo-O stretching modes might be reasonable. On the other hand, the ΔE' values observed for **17I** are very large (1090–3380 cm^{-1}), though the Mo-I stretching mode in {Mo_6I_8}$^{4+}$ is 152–154 cm^{-1}.[19-22] Similar to [{Mo_6X_8}Y_6]$^{2-}$ described in Chapter 3, the participation of the ground states with different magnetic properties may explain such ΔE' values.

4-6. Terminal Ligand Effects on Temperature Dependent Emission Characteristics of [{Mo₆Br₈}-(RCOO)₆]²⁻

4-6-1. Temperature Dependences of Emission Spectra

Figure 4-17 shows the *T*-dependent emission spectra of the {Mo_6Br_8}$^{4+}$ terminal aromatic carboxylate clusters (n_{AL}**Br**: **6Br**, **8Br**, **9Br**, **11Br**, **12Br**, and **14Br**) in the crystalline phases, and the *T*-dependences of the $\tilde{v}_{em}$ and *fwhm* values are shown in Figure 4-18. The $\tilde{v}_{em}$ values of n_{AL}**Br** except for **14Br** were shifted to the lower-energy upon heating from 3 to ~70 K and, then, to the higher-energy above 70 K. Although the amounts of the *T*-dependent $\tilde{v}_{em}$ shifts in 3 K < *T* < 300 K are different between the clusters, the general features of the *T*-dependent emission shifts are common for these six clusters. In the case of **14Br**, the *T*-dependent $\tilde{v}_{em}$ shift from 3 to 50 K was very small ((14.29–14.33) × 10^3 cm^{-1}, $\Delta\tilde{v}_{em}$ = 40 cm^{-1}), while the $\tilde{v}_{em}$ value varied largely at around 50–60 K: 14.29 × 10^3 and 12.63 × 10^3 cm^{-1} at 50 and 60 K, respectively, $\Delta\tilde{v}_{em}$ = 1660 cm^{-1}. Above 60 K, $\tilde{v}_{em}$ of **14Br** was shifted gradually to the higher-energy accompanying by broadening of the spectrum much larger than the spectra of other clusters. Although the *T*-dependent emission shifts of **14Br** are thus somewhat different from those of the other clusters, the general characteristics of the *T*-dependent emission shifts (i.e., lower-energy and subsequent higher-energy shifts upon *T*-elevation) are common for all clusters as mentioned above.
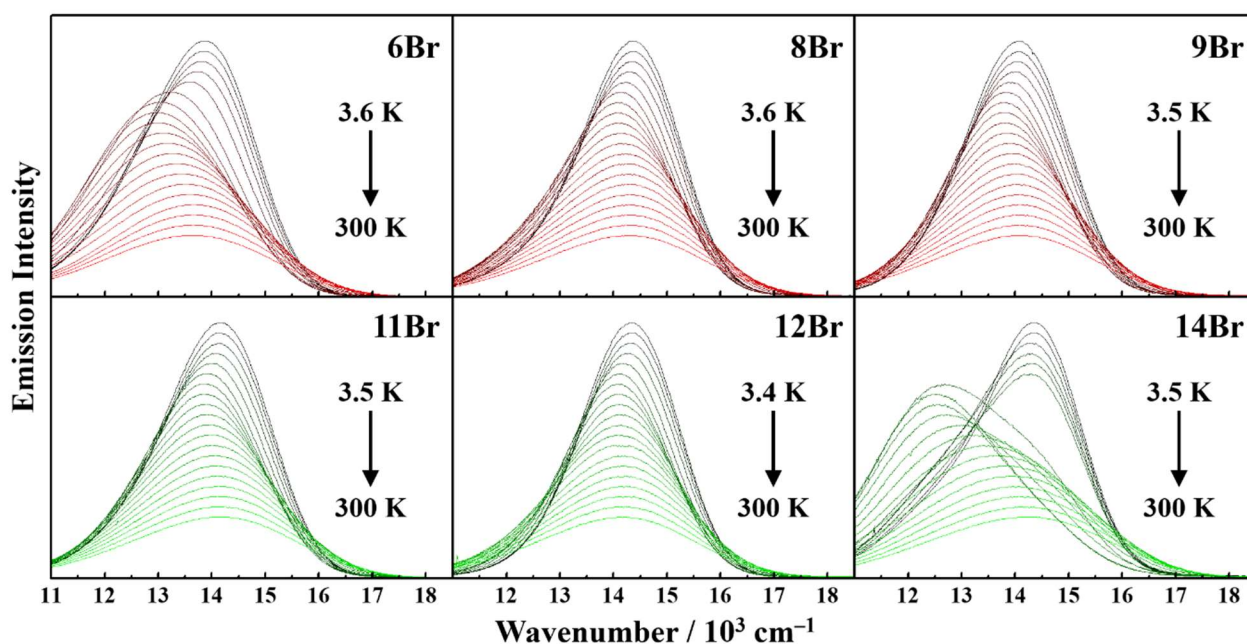
Figure 4-17. *T*-Dependences of the emission spectra of $[\{Mo_6Br_8\}(RCOO)_6]^{2-}$ in the crystalline phases in 3 K < *T* < 300 K. Temperature variation is shown by the color gradation from black (3 K) to highlight (300 K).

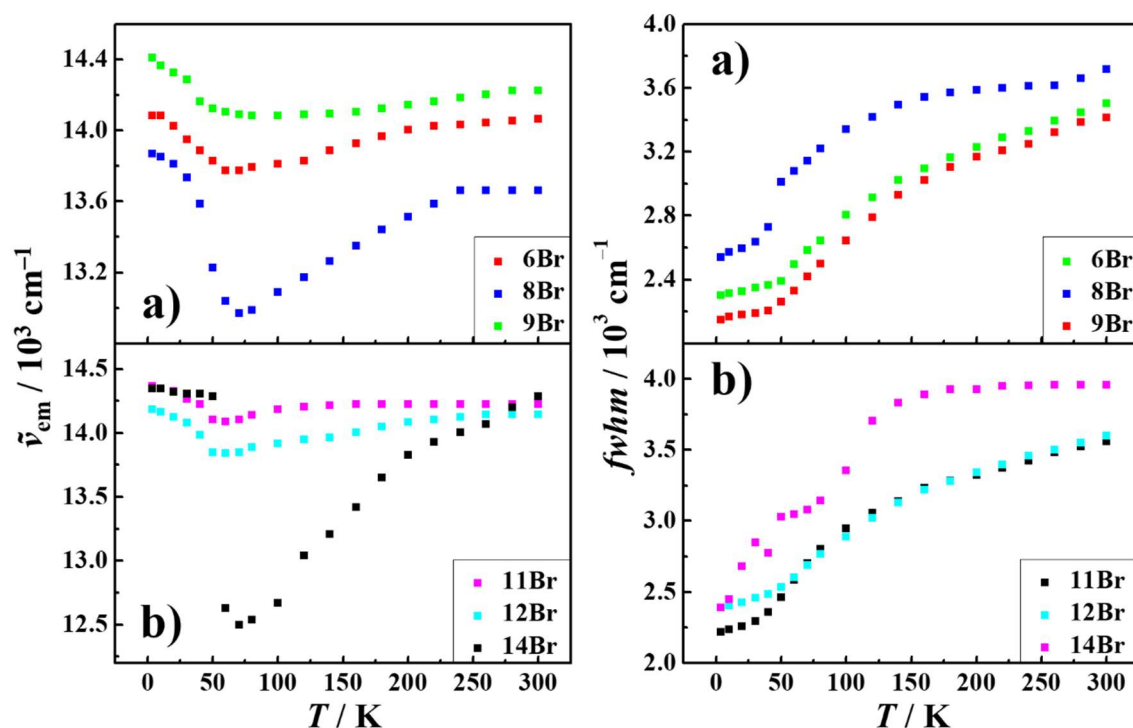**Figure 4-18**. *T*-Dependences of the $\tilde{v}_{em}$ (left panel) and *fwhm* (right panel) values of (a) **6Br**, **8Br**, **9Br**, (b) **11Br**, **12Br**, and **14Br** in crystalline phases.

4-6-2. Temperature Dependent Emission Lifetimes

Although the emissions from $\boldsymbol{n}_{\mathbf{AL}}\mathbf{Br}$ in acetone at 300 K show single-exponential decay, those in the crystalline phases exhibit double-exponential decay irrespective of T (3 K $< T <$ 300 K) as the emission decay profiles in acetone at 300 K and in the crystalline phases at several temperatures are reported in Figures 4-8 and 4-19, respectively. Single-exponential emission decay of $\boldsymbol{n}_{\mathbf{AL}}\mathbf{Br}$ in acetone indicates that double-exponential emission decay of the clusters in the crystalline phases would not be due to impurities in the samples, but to the crystal packing effects on the emission decay profiles. In the case of $[\{Mo_6Cl_8\}Cl_6]^{2-}$ (**1Cl**) and $[\{Mo_6Br_8\}Br_6]^{2-}$ (**5Br**) in the crystalline phases, the $\tilde{v}_{em}$ values of the clusters have been reported to be dependent on nature of the counter cations (TBA/tetraethylammonium ion and TBA/Cs⁺ for the former and latter complexes, respectively),[14,18] which demonstrates participation of intermolecular interactions in the crystalline phases. Such intermolecular interactions sometimes result in an appearance of a short-lifetime component owing to excitation energy migration between the cluster molecules and subsequent energy trap at the defect sites in the crystals. Furthermore, excited triplet–triplet (T_1–T_1) annihilation is likely to proceed under pulsed-laser excitation to the crystalline cluster sample and this might result in an appearance of a short-lifetime component, although the excitation laser power in the present experiments is set as low as possible: < 10 μJ/pulse. In the present case, it is supposed that the short-lifetime components observed for the emission decay profiles in Figure 4-19 would be due to intermolecular interactions and/or T–T annihilation in the crystalline phase. Therefore, the long-lifetime components were employed as τ_{em} in the following data analysis and discussion. The τ_{em} values of $\boldsymbol{n}_{\mathbf{AL}}\mathbf{Br}$ in the crystalline phases thus evaluated at a given T are summarized in Table 4-11 and the T-dependences of τ_{em} are shown in Figure 4-20. As seen in the figure, the τ_{em} values of the clusters at 3 K (740–
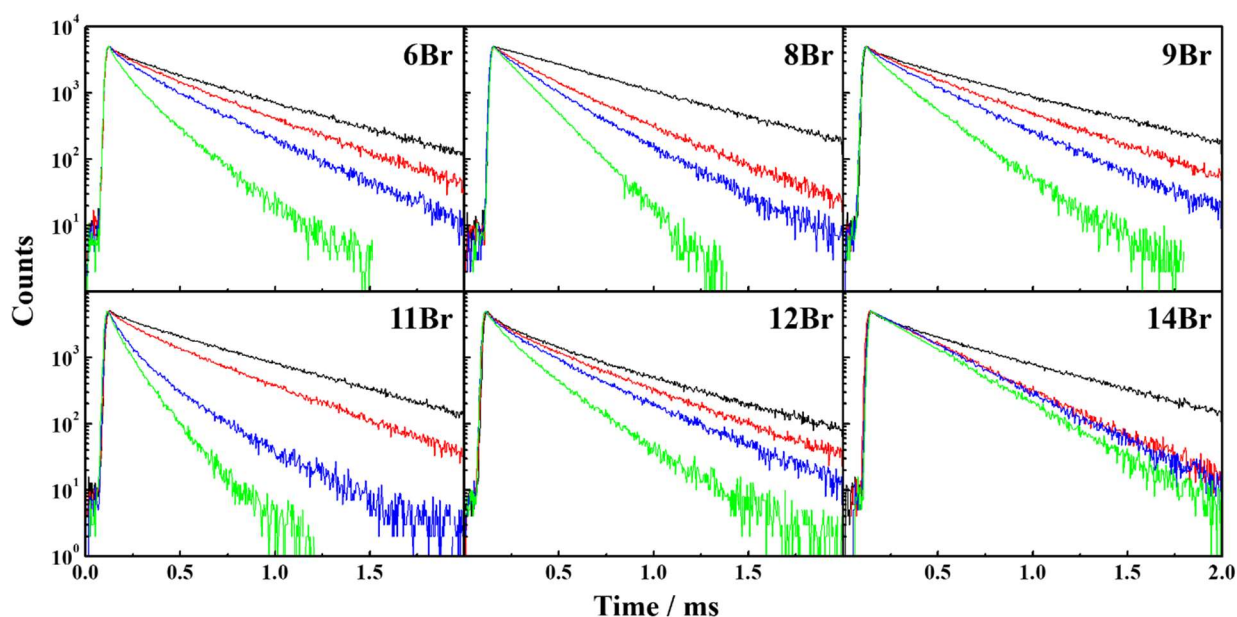

Figure 4-19. Emission decay profiles of $\boldsymbol{n}\mathbf{Br}_{\mathbf{AL}}$ in crystalline phases at 10, 100, 200, and 300 K.
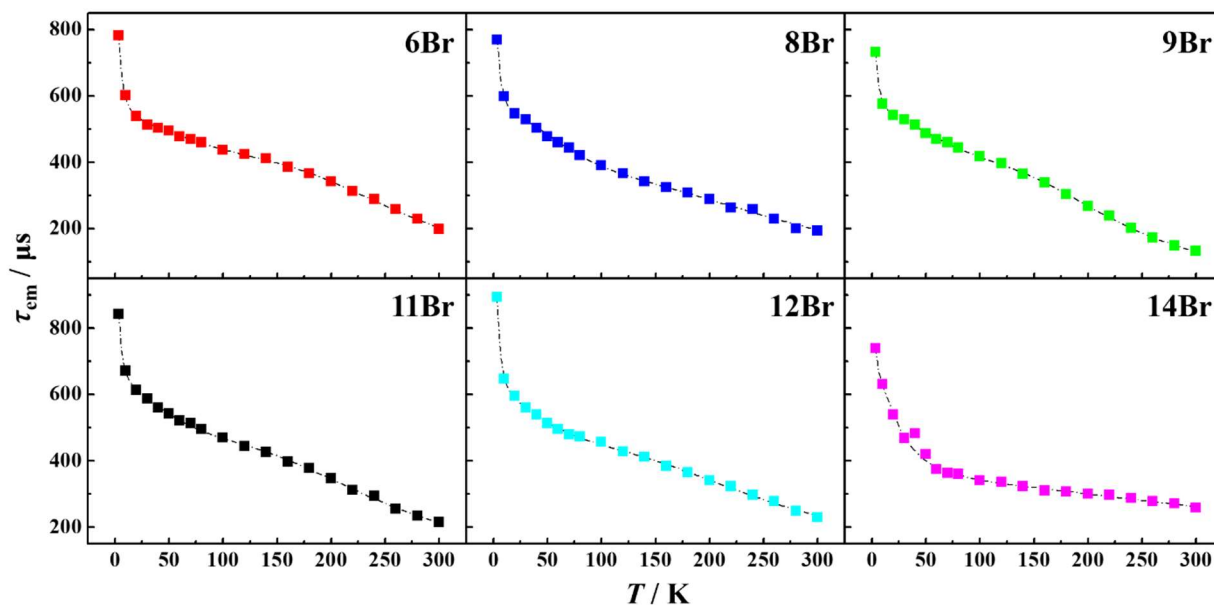
Figure 4-20. *T*-Dependences of τ_{em} of $\boldsymbol{n}\mathbf{Br_{AL}}$ in the crystalline phases. The broken curves are the best fits of the $\tau(T)$ data by eq. 2-1 with the fitting parameters, ΔE_{1n} and τ_n values, being shown in Figure 4-21.

840 µs) decrease sharply upon *T*-elevation to 40–50 K (400–500 µs) and, then, decrease gradually with increasing *T* to 300 K (200–250 µs). Since such *T*-dependent τ_{em} characteristics have been also observed for $[\{Mo_6X_8\}Y_6]^{2-}$, $[\{Mo_6X_8\}(n\text{-}C_3F_7COO)_6]^{2-}$, $[\{Re_6S_8\}X_6]^{4-}$ (X, Y = Cl, Br, or I), and $[\{W_6Cl_8\}Cl_6]^{2-}$, the $\tau(T)$ data of $\boldsymbol{n}_{\mathbf{AL}}\mathbf{Br}$ are also analyzed based on eq. 2-1.[14–16,24]

**4-6-3. Analysis of *T*-Dependent Emission Lifetimes by Spin-Sublevel Model.**

The results of the fittings of the $\tau(T)$ data on $\boldsymbol{n}_{\mathbf{AL}}\mathbf{Br}$ by eq. 2-1 are shown by the broken curves in Figure 4-20. As seen in Figure 4-20, the simulations reproduced very well the experimental observations with *cc* being 0.998–0.999, affording the ΔE_{1n} values of each cluster. The fitting parameters, ΔE_{1n} (n = 3, 4), evaluated by the $\tau(T)$ data on $\boldsymbol{n}_{\mathbf{AL}}\mathbf{Br}$ are summarized in Figure 4-21. It is worth pointing out that a series of the terminal carboxylates in $\boldsymbol{n}_{\mathbf{AL}}\mathbf{Br}$ give the completely different ΔE_{13} and ΔE_{14} values: 40–120 and 545–810 cm^{-1}, respectively. The ΔE_{13} and ΔE_{14} values increase in the sequence **14Br** (40 and 545 cm^{-1}) < **12Br** (80 and 620 cm^{-1}) < **11Br** (85 and 640 cm^{-1}) < **9Br** (110 and 710 cm^{-1}) < **8Br** (115 and 745 cm^{-1}) < **6Br** (120 and 810 cm^{-1}). The ΔE_{13} and ΔE_{14} values observed for **14Br** are the smallest (40 and 555 cm^{-1}, respectively), while those for **6Br** are the largest (120 and 810 cm^{-1}, respectively) among the relevant values of $\boldsymbol{n}_{\mathbf{AL}}\mathbf{Br}$. Furthermore, since other $\{Mo_6Br_8\}^{4+}$-core clusters show the ΔE_{14} values in the range of 635–720 cm^{-1}, the ΔE_{13} and ΔE_{14} values of **14Br** and **6Br** are the smallest and largest, respectively, among those of $\{Mo_6Br_8\}^{4+}$-core clusters. The detailed discussions on the factors governing the zfs energies will be described in Chapter 5.

Table 4-11. T-Dependences of the emission lifetimes (longer-lifetime components) of $[\{Mo_6Br_8\}(RCOO)_6]^{2-}$ ($n_{AL}Br$) in crystalline phases.

T / K	6Br	8Br	9Br	11Br	12Br	14Br
3.4	–	893	–	–	–	–
3.5	738	–	841	732	–	–
3.6	–	–	–	–	781	769
10	738	647	671	732	601	598
20	631	595	613	576	538	547
30	538	559	586	542	512	529
40	467	538	559	529	503	503
50	482	512	542	512	495	478
60	419	495	521	486	478	460
70	374	478	512	469	469	443
80	362	473	495	460	460	421
100	359	456	469	443	437	390
120	341	428	443	417	424	365
140	335	411	426	396	411	341
160	322	383	396	364	386	324
180	310	364	377	338	365	271
200	306	341	347	302	341	268
220	300	322	312	268	312	263
240	296	297	293	238	288	258
260	287	278	254	201	258	249
280	278	249	233	172	228	240
300	270	228	215	149	198	234

4-6-4. Simulation of Emission Spectra by Spin-sublevel Model.

On the basis of the ΔE_{1n} data, one must reproduce the $I(\tilde{v}, T)$ data in Figure 4-17. Therefore, the $I(\tilde{v}, T)$ data were analyzed with the ΔE_{1n} values and eqs. 2-2 and 2-3 as the results were shown in Figure 4-22, while the $\tilde{v}_n$ values were included in Figure 4-21. Similar to the T-dependences of **1X–3X** and **17X,** the observed emission spectra at a given T were reproduced almost satisfactorily ($cc = 0.999$) by the sum of those of the Φ_n spin-sublevels. It is worth emphasizing that, although the energy order of Φ_n is $\Phi_1 < \Phi_2 < \Phi_3 < \Phi_4$, the sequence of $\tilde{v}_n$ is $\tilde{v}_2 < \tilde{v}_3 < \tilde{v}_1 < \tilde{v}_4$ irrespective of the cluster complex as seen in Figure 4-21. This indicates that the emission
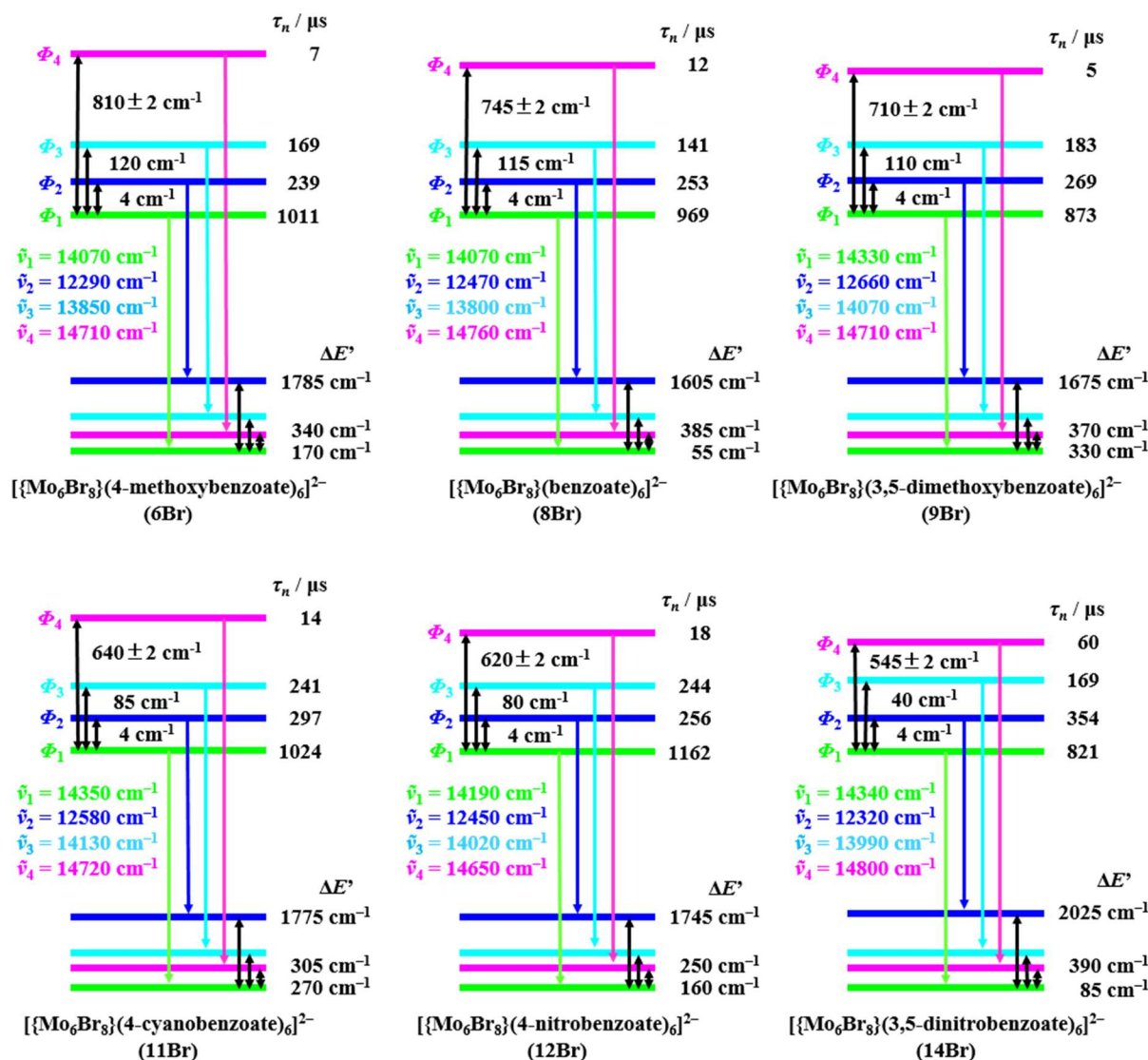
Figure 4-21. zfs parameters of $[\{Mo_6Br_8\}(RCOO)_6]^{2-}$.

transition from each Φ_n to S_0 proceeds to the individual Franck-Condon vibrational level in S_0 (S_0(FC)) and each cluster complex possesses own energy gap between the S_0(FC) levels: $\Delta E'$ in Figure 4-21. The $\Delta E'$ values with the relatively low frequencies (55–390 cm^{-1}) could be assigned to the Mo-Mo and Mo-Br stretching modes in $\{Mo_6Br_8\}^{4+}$-core.[33,34] High-resolution vibrational spectroscopy of the cluster would provide more detailed information on the vibrational modes characterizing the $\Delta E'$ values. In the present stage of the investigations, however, it is difficult to assign the origin of the larger $\Delta E'$ values ((1606–2025) cm^{-1}) observed for nBr$_{AL}$ since the clusters show the intense emission and this disturbs resonance Raman spectroscopy.

4-6-5. Origin of the Terminal Ligand Dependences of the Emission Properties: $\tilde{\nu}_{em}$, τ_{em} , and Φ_{em}.

The observed and simulated spectra of the clusters at 300 K are shown in Figure 4-23, while the contribution percentage of the Φ_n emissions to the observed spectrum are reported in Table 4-12. The emission
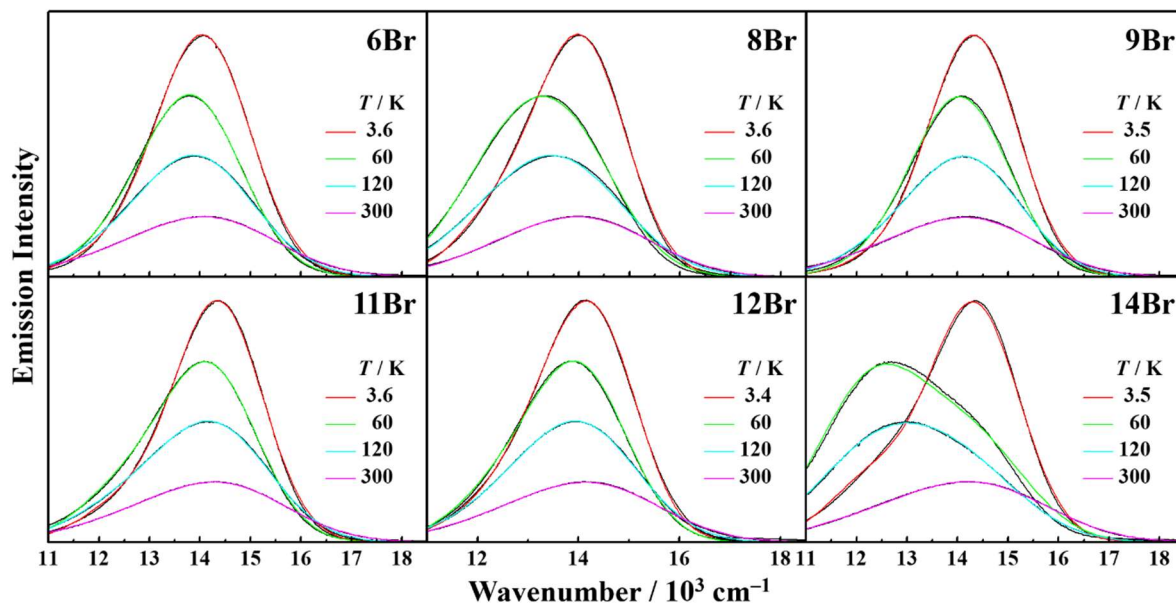
Figure 4-22. Simulations of the *T*-dependent emission spectra of $[\{Mo_6Br_8\}(RCOO)_6]^{2-}$ in crystalline phases. The spectra shown by the black curves are the observed ones, while the simulated spectra are shown by the colors indicated in the figures.

spectrum for a given terminal carboxylate cluster can be explained by the major contributions from the Φ_3 and Φ_4 emissions (30–40 and 40–45%, respectively) with the minor contribution from the Φ_2 emission (20–25%). In the case of **6Br**, for example, the contributions of the Φ_3 and Φ_4 emissions to the observed spectrum are comparable (38 and 42%, respectively) and dominant, while that from the Φ_2 emission is almost half (20%) compared to the Φ_3 and Φ_4 percentages as mentioned above. Focusing on the contribution percentage of the Φ_4 emission (Φ_4%), one can find that the Φ_4% value depends on nature of the terminal carboxylate ligand and decreases in the sequence **14Br** (44%) > **12Br** (43%) > **11Br** (42%) > **9Br** (40%) ∼ **8Br** (40%) > **6Br** (38%). It is worth emphasizing that the tendency mentioned above agrees well with the increasing order of the ΔE_{14} value and, thus, **14Br** (545 cm⁻¹) < **12Br** (620 cm⁻¹) < **11Br** (640 cm⁻¹) < **9Br** (710 cm⁻¹) < **8Br** (745 cm⁻¹) < **6Br** (810 cm⁻¹). The contribution of the emission from each Φ_n to the observed spectrum is determined by the thermal Boltzmann distribution at a given *T*. Furthermore, since present spectral analysis of the *T*-dependence of the

Table 4-12. Contribution percentages (Φ_n%) of the Φ_n emissions to the observed spectra of **nBr$_{AL}$** at 300 K.

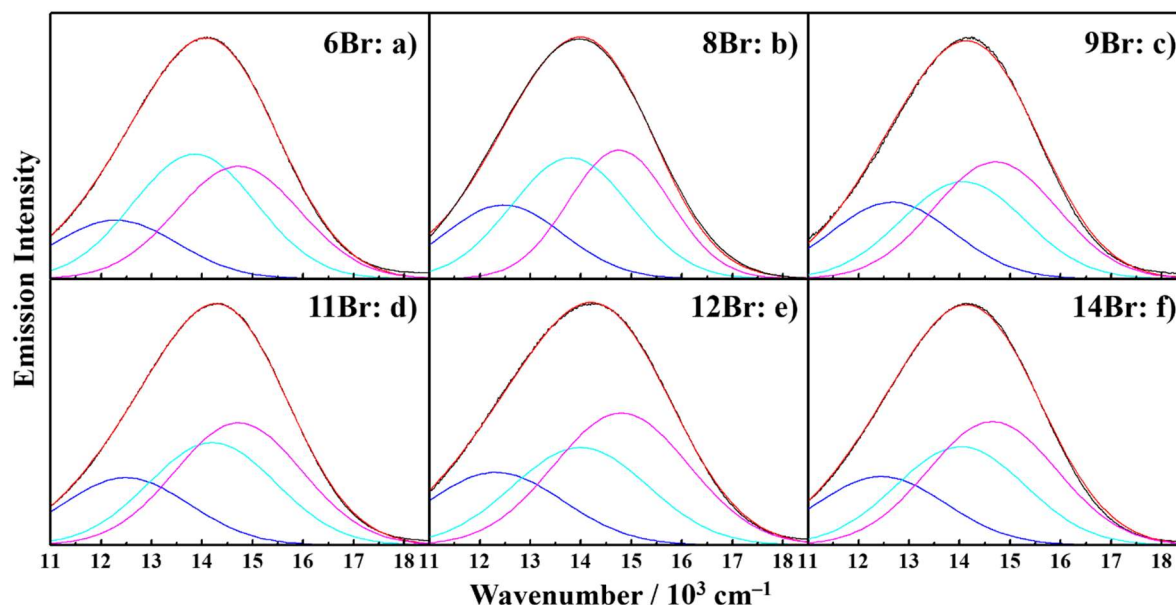|	6Br	8Br	9Br	11Br	12Br	14Br
Φ_1 / %	0	0	0	0	0	0
Φ_2 / %	19.8	22.8	26.4	23.1	23.6	24.1
Φ_3 / %	42.2	37.4	33.4	35.1	33.9	32.3
Φ_4 / %	38.0	39.8	40.2	41.8	42.5	43.6

Figure 4-23. Observed and simulated emission spectra of $[\{Mo_6Br_8\}(RCOO)_6]^{2-}$ in crystalline phases at 300 K. The observed and simulated spectra are shown by the black and red colors, respectively. The relative contributions of the Φ_n emission spectra to the observed spectra of a given cluster are shown by blue ($n = 2$), cyan ($n = 3$), and magenta ($n = 4$).

emission spectra demonstrates that $\boldsymbol{n_{AL}}\textbf{Br}$ possess the almost identical $\tilde{v}_4$ values (i.e., $\Delta\tilde{v}_4(\textbf{14Br–6Br}) = 90$ cm^{-1}, while $\Delta\tilde{v}_{em} = 230$ cm^{-1}) and $\tilde{v}_4$ is the highest energy emission, the larger $\Phi_4\%$ value leads to the higher energy emission at ambient temperature. The large population of Φ_4 is the primary reason for the pK_a(L) dependence of $\tilde{v}_{em}$ at ambient temperature shown in Figure 4-7.

4-7. Conclusion

This chapter described the X-ray structure, redox, spectroscopic, and photophysical properties of the terminal carboxylate clusters $[\{Mo_6X_8\}L_6]^{2-}$ (X = Br or I, L = carboxylate, $\boldsymbol{n}\textbf{Br}$ or $\boldsymbol{n}\textbf{I}$) in solution at ambient temperature. Both $\boldsymbol{n}\textbf{Br}$ and $\boldsymbol{n}\textbf{I}$ showed the large terminal carboxylate dependences of the X-ray structural, redox, and several photophysical properties: d_{Mo-O}, E_{ox}, E_{red}, $\tilde{v}_{em}$, τ_{em}, and Φ_{em}. The present study found that these properties showed the clear correlations with pK_a(L), while those of the E_{red} and ($E_{ox} - E_{red}$) values observed for **12Br** and **14Br** showing quasi-one-step six-electron electrochemical reduction were exceptions. For example, the larger is the pK_a(L) value (i.e., the stronger σ-donating ability of the terminal carboxylate), the HOMO energy level evaluated by the E_{ox} value is more destabilized since the E_{ox} value corresponds to the Mo^{2+}/Mo^{3+} potential. According to the energy gap ($\tilde{v}_{em}$) dependence of k_{nr}, furthermore, the ln(k_{nr}) values of $\boldsymbol{n}\textbf{Br}$ or $\boldsymbol{n}\textbf{I}$ correlated linearly with $\tilde{v}_{em}$ and, thereby, those are also governed by pK_a(L). Such circumstances resulted in almost linear pK_a(L) dependences of Φ_{em} and τ_{em} observed for both $\boldsymbol{n}\textbf{Br}$ and $\boldsymbol{n}\textbf{I}$. However, the terminal ligand
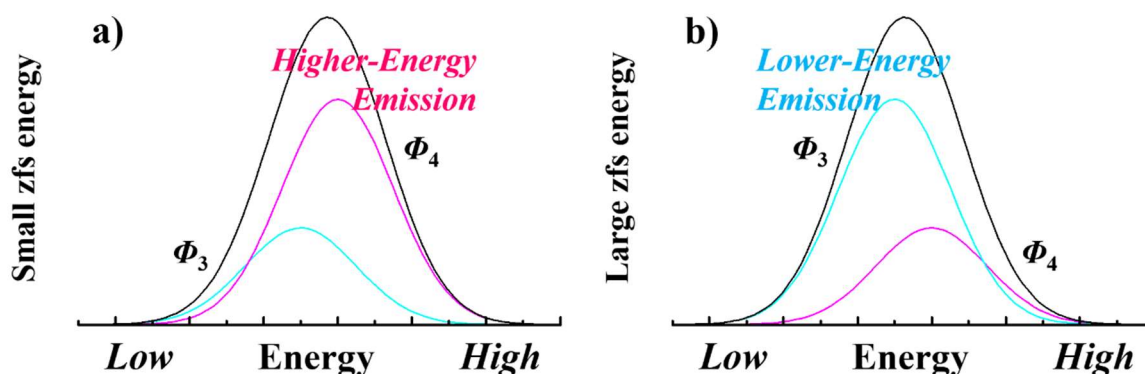
Figure 4-24. Schematic illustrations of the emission spectra of [{Mo$_6$Br$_8$}(RCOO)$_6$]$^{2-}$ given by (a) a small zfs energy and (b) a large zfs energy. The relative contributions of the Φ_n emission are shown by cyan ($n = 3$) and magenta ($n = 4$).

dependence of $\tilde{\nu}_{em}$ of **nBr** or **nI** itself, which was the origin of pK_a(L) dependent photophysical properties, could not be explained by the σ-donating ability of the terminal carboxylate alone and was needed to be discussed based on the relevant zfs parameters. All of the clusters studied in this chapter ({Mo$_6$X$_8$}$^{4+}$-core clusters having *n*-perfluorobutylate terminal ligands ([{Mo$_6$X$_8$}(*n*-C$_3$F$_7$COO)$_6$}]$^{2-}$: **17X**) and {Mo$_6$Br$_8$}$^{4+}$-core clusters with the terminal aromatic carboxylates ([{Mo$_6$Br$_8$}(RCOO)$_6$}]$^{2-}$: n_{AL}**Br**)) showed large *T*-dependent emission characteristics ($\tilde{\nu}_{em}$ and τ_{em}) in 3 K < *T* < 300 K analogous to [{Mo$_6$X$_8$}Y$_6$]$^{2-}$ described in Chapter 3. The Φ_n model explained satisfactory the *T*-dependences of the emission characteristics of **17X** and n_{AL}**Br**, providing the zfs parameters. It was found that the splitting energies in the T$_1$ states (ΔE_{13} and ΔE_{14} values) increased in the sequences X = Cl < Br < I for **17X** and L = 3,5-dinitrobenzoate < 4-nitrobenzoate < 4-cyanobenzoate < 3,5-dimethoxybenzoate < benzoate < 4-methoxybenzoate for n_{AL}**Br**. The energy order of ΔE_{13} or ΔE_{14} shown above for **17X** or n_{AL}**Br** coincides with the size/mass of X or pK_a(L) value, respectively. The larger is the ΔE_{14} value for a given L in n_{AL}**Br** or X in **17X**, the smaller is the contribution of the emission from the highest-energy spin sublevels (Φ_4) to the observed emission spectrum at 300 K with the sequence of Φ_4% being L = 3,5-dinitrobenzoate > 4-nitrobenzoate > 4-cyanobenzoate > 3,5-dimethoxybenzoate > benzoate > 4-methoxybenzoate and X = Cl > Br > I. The $\tilde{\nu}_4$ value of n_{AL}**Br** is insensitive to nature of the terminal carboxylate ligand compared to the $\tilde{\nu}_{em}$ value of n_{AL}**Br** (i.e., $\Delta\tilde{\nu}_4$(**14Br**–**6Br**) = 90 cm^{-1}, $\Delta\tilde{\nu}_{em}$ = 230 cm^{-1}). Furthermore, since $\tilde{\nu}_4$ is the highest energy emission, the larger Φ_4% leads to the higher energy emission at ambient temperature. For a given X, the weak σ-donation from the terminal ligand thus gives rise to the high-energy emission, resulting in the pK_a(L) dependences of Φ_{em} or τ_{em} through the energy gap ($\tilde{\nu}_{em}$) dependence of k_{nr}.

4-8.   References

(1)   Haynes, W. M. *CRC Handbook of Chemistry and Physics, 92nd ed.*; CRC Press: Boca Raton, **2011**.

(2)   Perrin, D. D. *Dissociation Constants of Organic Bases in Aqueous Solution*; Butterworths: London, **1965**.

(3)   Harding, A. P.; Wedge, D. C.; Popelier, P. L. A. pK_a Prediction from "Quantum Chemical Topology" Descriptors. *J. Chem. Int. Model.*, **2009**, *49*, 1914–1924.

(4)   Henne, A. L.; Fox, C. J. Ionization Constants of Fluorinated Acids. *J. Am. Chem. Soc.* **1951***, 73*, 2323–2325.

(5)   Efremova, O. A.; Vorotnikov, Y. A.; Brylev, K. A.; Vorotnikova, N. A.; Novozhilov, I. N.; Kuratieva, N. V.; Edeleva, M. V.; Benoit, D. M.; Kitamura, N.; Mironov, Y. V.; Shestopalov, M. A.; Sutherland, A. J. Octahedral Molybdenum Cluster Complexes with Aromatic Sulfonate Ligands. *Dalton Trans*. **2016**, *45*, 15427–15435.

(6)   Miklailov, M. A.; Brylev, K. A.; Virovets, A. V.; Galyamov, M. R.; Novozhilov, I.; Sokolov, M. N. Complexes of {Mo_6I_8} with Nitrophenols: Synthesis and Luminescence. *New J. Chem*. **2016**, *40*, 1162–1168.

(7)   Kirakci, K.; Kubát, P.; Langmaier, J.; Polívka, T.; Fuciman, M.; Fejfarová, K.; Lang, K. A Comprehensive Study of the Redox and Excited State Properties of (nBu$_4$N)$_2$[Mo_6X_{14}] and (nBu$_4$N)$_2$[{Mo_6X_8}(CF_3COO)$_6$] (X = Cl, Br, or I). *Dalton Trans*. **2013**, *42*, 7224–7232.

(8)   Sokolov, M. N.; Mihailov, M. A.; Peresypkina, E. V.; Brylev, K. A.; Kitamura, N.; Fedin, V. P. Highly Luminescent Complexes [Mo_6X_8(n-C_3F_7COO)$_6$]$^{2-}$ (X = Br, I). *Dalton Trans*. **2011**, *40*, 6375–6377.

(9)   Dinius, R. H.; Choppin, G. R. N.M.R. Study of the Ionization of Aryl Sulfonic Acids. *J. Phys*. *Chem.* **1962**, *66*, 268–270.

(10)   Guthrie, J. P. Hydrolysis of Esters of Oxy Acids: pK_a Values for Strong Acids; Brønsted Relationship for Attack of Water at Methyl; Free Energies of Hydrolysis of Esters of Oxy Acids; and a Linear Relationship between Free Energy of Hydrolysis and pK_a Holding over a Range of 20 pK Units. *Can. J. Chem.* **1978**, *56*, 2342–2354.

(11)   McCarthy, B. D.; Martin, D. J.; Rountree, E. S.; Ullman, A. C.; Dempsey, J. L. Electrochemical Reduction of Brønsted Acids by Glassy Carbon in Acetonitrile–Implications for Electrocatalytic Hydrogen Evolution. *Inorg. Chem.* **2014**, *53*, 8350–8361.

(12)   Fujii, S.; Horiguchi, T.; Akagi, S.; Kitamura, N. Quasi-One-Step, Six-Electron Electrochemical Reduction of an Octahedral Hexanuclear Molybdenum(II) Cluster. *Inorg. Chem.* **2016**, *55*, 10259–10266.

(13)   Ramirez-Tagle, R.; Arratia-Pérez, R. Electronic Structure and Molecular Properties of the [$Mo_6X_8L_6$]$^{2-}$; X = Cl, Br, I; L = F, Cl, Br, I Clusters. *Chem. Phys*. *Lett*. **2008**, *460*, 438–441.

(14)   Kitamura, N.; Kuwahara, Y.; Ueda, Y.; Itoh, Y.; Ishizaka, S.; Sasaki, Y.; Tsuge, K.; Akagi, S. Excited Triplet States of [{Mo$_6$Cl$_8$}Cl$_6$]$^{2-}$, [{W$_6$Cl$_8$}Cl$_6$]$^{2-}$, and [{Re$_6$S$_8$}Cl$_6$]$^{4-}$ Clusters. *Bull. Chem. Soc. Jpn.* **2017**, *90*, 1164–1173.

(15)   Miki, H.; Ikeyama, T.; Sasaki, Y.; Azumi, T. Phosphorescence from the Triplet Spin Sublevels of a Hexanuclear Molybdenum(II) Chloride Cluster Ion, [Mo$_6$Cl$_{14}$]$^{2-}$. Relative Radiative Rate Constants for Emitting Sublevels. *J. Phys. Chem.* **1992**, *96*, 3236–3239.

(16)   Kitamura, N.; Ueda, Y.; Ishizaka, S.; Yamada, K.; Aniya, M.; Sasaki, Y. Temperature Dependent Emission of Hexarhenium(III) Clusters [Re$_6$S$_8$X$_6$]$^{4-}$ (X = Cl$^-$, Br$^-$, and I$^-$): Analysis by Four Excited Triplet-State Sublevels. *Inorg. Chem.* **2005**, *44*, 6308–6313.

(17)   Hardcastle, F. D.; Wachs, I. E. Determination of Molybdenum–Oxygen Bond Distances and Bond Order by Raman Spectroscopy. *J. Raman Spectrosc.* **1990**, *21*, 683-691.

(18)   Ramirez-Tagle, R.; Arratia-Pérez, R. The Luminescent [Mo$_6$X$_8$(NCS)$_6$]$^{2-}$ (X = Cl, Br, I) Clusters?: A Computational Study Based on Time-Dependent Density Functional Theory Including Spin-Orbit and Solvent-Polarity Effects. *Chem. Phys. Lett.* **2008**, *455*, 38-41.

(19)   Ramirez-Tagle, R.; Arratia-Pérez, R. Pyridine as Axial Ligand on the [Mo$_6$Cl$_8$]$^{4+}$ Core Switches off Luminescence. *Chem. Phys. Lett.* **2009**, *475*, 232-234.

(20)   Preetz, W.; Harder, K. Synthesis, Structure and Properties of the Cluster Anions [{Mo$_6$Cl$^i_8$}X$^a_6$]$^{2-}$ with X^a ≡ F, Cl, Br, I*. *J. Alloys Compds.* **1992**, *183*, 413-429.

(21)   Preetz, W.; Bublitz, D. Darstellung, Kristallstruktur und spektroskopische Eigenschaften der Clusteranionen [{Mo$_6$Br$^i_8$}X$^a_6$]$^{2-}$ mit X^a = F, Cl, Br, I. *Zeit. Anorg. Allg. Chem.* **1994**, *620*, 234-246.

(22)   Brückner, P.; Preetz, W.; Pünjer, M. Darstellung, Kristallstruktur, NMR-Schwingungsspektren und Normalkoordinatenanalyse der Clusteranionen [{Mo$_6$I$^i_8$}X$^a_6$]$^{2-}$, X^a = F, Cl, Br, I. *Zeit. Anorg. Allg. Chem.* **1997**, *623* 8-17.

(23)   Costuas, K.; Garreau, A.; Bulou, A.; Fontaine, B.; Curry, J.; Gautier, R.; Mortier, M.; Molard, Y.; Duvail, J.-L.; Faulques, E.; Cordier, S. Combined Theoretical and Time-resolved Phosphorescence Investigations of [Mo$_6$Br$_8$Br$_6$]$^{2-}$ Metal Cluster Units: Evidence of Dual Emission. *Phys. Chem. Chem. Phys.* **2015**, *17*, 28574–28585.

(24)   Saito, Y.; Tanaka, H. K.; Sasaki, Y.; Azumi, T. Temperature Dependence of the Luminescence Lifetime of Hexanuclear Molybdenum(II) Chloride Cluster. Identification of Lower Excited Triplet Sublevels. *J. Phys. Chem.* **1985**, *89*, 4413–4415.

Chapter 5

General Factors Governing Zero-Magnetic-Field

Splitting of Transition Metal Complex and

Implications of zfs to Phosphorescence Properties

5-1.   Introduction

Chapters 3 and 4 of the thesis described the photophysical properties of the terminal halide and carboxylate hexamolybdenum(II) clusters, $[\{Mo_6X_8\}Y_6]^{2-}$ (X, Y = Cl, Br, or I) and $[\{Mo_6X_8\}(RCOO)_6]^{2-}$ (X = (Cl), Br or I, RCOO = aromatic or aliphatic carboxylate) at various temperatures (T = 3–300 K). These chapters have demonstrated that the spin-sublevel Φ_n model can explain almost satisfactorily the T-dependences of the emission characteristics of the hexamolybdenum(II) clusters. Furthermore, the emission properties of these clusters at 298 K were explained very well by the zero-magnetic-field splitting (zfs) parameters estimated by the analysis of the T-dependent emission data based on the Φ_n model. In the case of these clusters, since it has been demonstrated that the zfs parameters primarily determine the emission properties at a given T in 3–300 K, the factors governing the zfs parameters of the clusters would be similar to those of the emission properties. When one can elucidate the factors governing the zfs parameters in the lowest-energy excited triplet (T$_1$) state, it is expected that the emission properties of a hexamolybdenum(II) cluster would be controlled synthetically and, therefore, these are worth discussing and elucidating in detail.

This chapter focuses on the zfs energies (ΔE_{1n}) among several zfs parameters. To elucidate the factors governing the zfs parameters, the bridging and terminal ligand effects on the zfs energies of $[\{Mo_6X_8\}Y_6]^{2-}$, $[\{Mo_6X_8\}(nC_3F_7COO)_6]^{2-}$, and $[\{Mo_6Br_8\}(RCOO)_6]^{2-}$ (see Figures 3-12, 4-14, and 4-21 in Chapters 3 and 4, respectively) are described in special references to the electronic structures of the clusters. Furthermore, it is of broad interests whether the experimental findings for the octahedral hexamolybdenum(II) cluster can also explain the zfs energy (the energy difference between the lowest- and highest-energy lying spin-sublevels) and relevant phosphorescence properties of an ordinary transition metal complex or not. This chapter therefore describes the general factors governing zfs in the T$_1$ states of several platinum(II) complexes and their implications to the phosphorescence properties of the complexes: [Pt(*C^N*)(*O^O*)] and [Pt(*C^N*)(*C^N*)] (*C^N* and *O^O* = single cyclometalating and non-cyclometalating ligand, respectively; see Chart 5-1 for the structures and abbreviations).

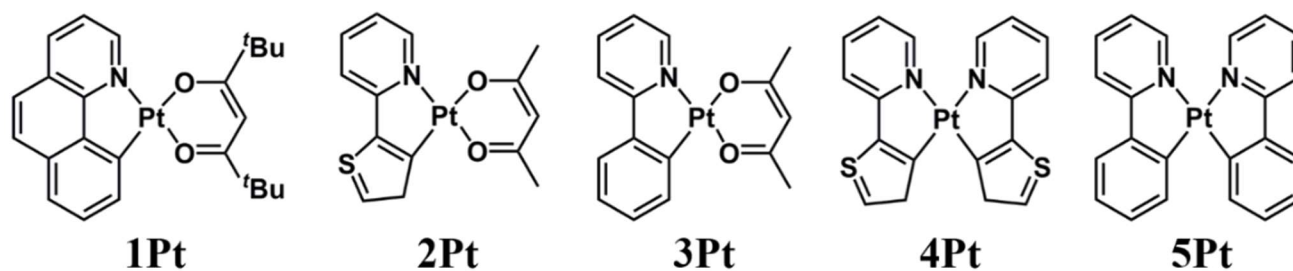**Chart 5-1**. Structures and abbreviations of platinum(II) complexes [Pt(*O^O*)(*C^N*)] and [Pt(*C^N*)(*C^N*)].

5-2.   Factors Governing the zfs Energies in the T_1 States of Hexamolybdenum(II) Clusters

5-2-1. Bridging Ligand Effects on the zfs Energies in the Excited Triplet States

The ΔE_{1n} values ($n = 3$ and 4) described in Figures 3-12, 4-14, and 4-21 in Chapters 3 and 4, respectively, are summarized in Table 5-1. A close inspection of the data in Table 5-1 indicates that, for a given terminal ligand, the cluster having heavier (i.e., larger atomic number, Z) X atoms shows larger ΔE_{1n} ($n = 3$, 4) values. In the case of an $[\{Mo_6X_8\}Br_6]^{2-}$ (**2X**) or $[\{Mo_6X_8\}(nC_3F_7COO)_6]^{2-}$ (**17X**) series as an example, ΔE_{13} and ΔE_{14} increase in the sequence X = Cl (**2Cl**, $\Delta E_{13} = 51$ and $\Delta E_{14} = 630$ cm^{-1}) < Br (**2Br**, 56 and 655 cm^{-1}) < I (**2I**, 80 and 780 cm^{-1}) or X = Cl (**17Cl**, 55 and 650 cm^{-1}) < Br (**17Br**, 68 and 720 cm^{-1}) < I (**17I**, 120 and 1000 cm^{-1}), respectively. Similar bridging ligand effects on ΔE_{13} or ΔE_{14} to those of **2X** or **17X** can be also found for a **1X** and **3X** series, whose ΔE_{14} (ΔE_{13}) values range in 620–650 (50–55) and 730–1000 (70–120) cm^{-1}, respectively. The results demonstrate clearly that the ΔE_{13} and ΔE_{14} values of the clusters, whose values are determined by the second- and first-order spin-orbit coupling (SOC), respectively, depend primarily on nature of the $\{Mo_6X_8\}^{4+}$-core, and the heavier bridging ligands give rise to larger ΔE_{13} or ΔE_{14} values. The results will be very reasonable, since it has been reported theoretically that the T_1 state of $[\{Mo_6X_8\}X_6]^{2-}$ (X = Cl, Br, or I) is localized on the $\{Mo_6X_8\}^{4+}$-core and the photophysical characteristics of the cluster are determined primarily by the electronic structures of the cluster-core.[1-17]

An SOC parameter, ξ, is known to relate to the atomic number (Z) of a constituted atom in a molecule through eq. 5-1,[18,19]

Table 5-1. zfs energies in the excited triplet states (ΔE_{13} and ΔE_{14}) of $[\{Mo_6X_8\}Y_6]^{2-}$ (**1X–3X**) and $[\{Mo_6X_8\}(RCOO)_6]^{2-}$ (**6Br, 8Br, 9Br, 11Br, 12Br, 14Br**, and **17X**).

$[\{Mo_6X_8\}L^n{}_6]$		ΔE_{14} (ΔE_{13}) / cm^{-1}		
		X = Cl	X = Br	X = I
$n = 1$–3	**1**: 1Cl	650 (55)[a]	695 (63)[a]	730 (70)[a]
L = halide	**2**: 1Br	630 (51)[a]	655 (56)[a]	780 (80)[a]
	3: 1I	620 (50)[a]	635 (53)[a]	870 (99)[a]
$n = 4$–17	**17**: *n*-perfluorobutylate	650 (55)[b]	720 (68)[b]	1000 (120)[b]
L = carboxylate	**6**:1 4-methoxybenzoate	–	810 (120)[b]	–
	8: 1benzoate	–	745 (115)[b]	–
	9: 13,5-dimethoxybenzoate	–	710 (110)[b]	–
	11: 4-cyanobenzoate	–	640 (85)[b]	–
	12: 4-nitrobenzoate	–	620 (80)[b]	–
	14: 3,5-dinitrobenzoate	–	545 (40)[b]	–

a and b represent the data taken from Chapter 3 and Chapter 4, respectively.

$$\zeta_{nl} = \frac{e^2 \hbar^2}{2m^2 c^2 a_0^3} \left[\frac{Z^4}{n^3 (l+1)(l+\frac{1}{2})l} \right] \tag{5-1}$$

where e, $\hbar$, m, a_0, n, and l are the elementary electron charge, the reduced Planck constant, the mass of an electron, the Bohr radius, the principal and azimuthal quantum numbers of a molecule, respectively. Eq. 5-1 demonstrates that the ζ value is proportional to the fourth power of an atomic number (Z). In the case of the T_1 state of $[Ru(bpy)_3]^{2+}$ or $[Os(bpy)_3]^{2+}$ (bpy = 2,2'-bipyridine), the ΔE_{13} value has been reported to be 61 or 210 cm^{-1},[20,21] respectively. According to the Z and ζ values of a Ru ($Z = 44$, $\zeta = 1042$ cm^{-1}) or Os atom (76, 3381 cm^{-1}),[19] the relatively small ΔE_{13} value of $[Ru(bpy)_3]^{2+}$ compared to that of $[Os(bpy)_3]^{2+}$ will be the reasonable consequence. It is worth emphasizing again that the ΔE_{14} value of $n\mathbf{X}$ increases in the sequence X = Cl ($\mathbf{1X}$) < Br ($n\mathbf{Br}$) < I ($n\mathbf{I}$), whose sequence agrees very well with those of the Z and ζ values of X: $Z = 17$ (Cl) < 35 (Br) < I (53) and ζ (in cm^{-1}) = 587 (Cl) < 2460 (Br) < 5069 (I).[19] In order to check the relationship between the ΔE_{1n} and Z^4 values, the observed ΔE_{1n} values were plotted against the Z^4 values of X: ΔE_{1n} *vs.* $\{Z(X)\}^4$. As the results are shown in Figure 5-1, one obtains good linear correlations between ΔE_{1n} (n = 3 and 4) and $\{Z(X)\}^4$

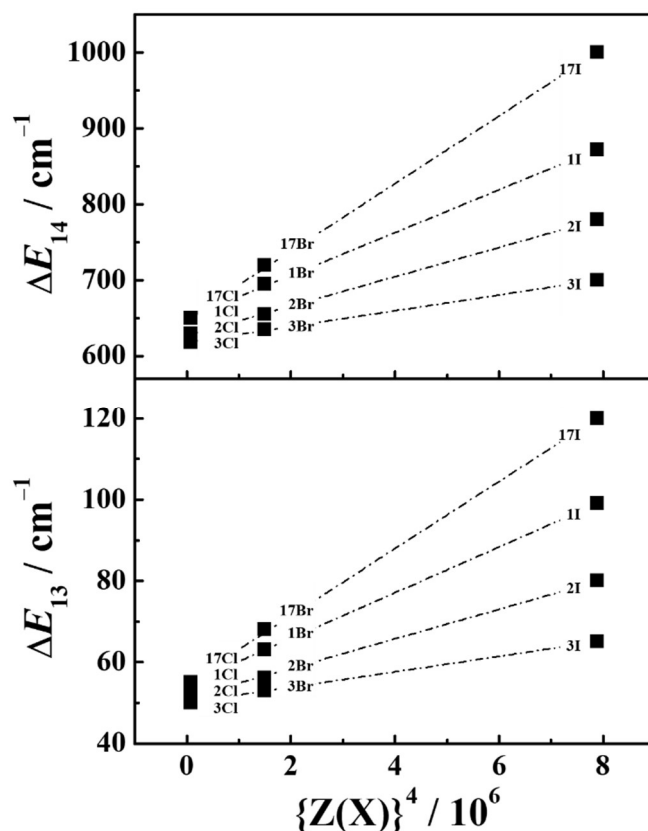**Figure 5-1**. Relationships between the zfs energies in the excited triplet states (ΔE_{13} and ΔE_{14}) of $[\{Mo_6X_8\}Y_6]^{2-}$ ($\mathbf{1X–3X}$) or $[\{Mo_6X_8\}(nC_3F_7COO)_6]^{2-}$ ($\mathbf{17X}$) and the fourth power of the atomic number of the bridging ligand ($\{Z(X)\}^4$). The broken lines represent regression between the two parameters.

irrespective of nature of the terminal ligands with R^2 being 0.987–0.999 for the ΔE_{13} and ΔE_{14} data, respectively, demonstrating that SOC of the excited state cluster is determined primarily by nature of the bridging ligands (X) and, thus, $\{Z(X)\}^4$.

5-2-2. Terminal Ligand Effects on the zfs Energies in the Excited Triplet States

Figure 5-1 and Table 5-1 demonstrate explicitly that the ΔE_{13} and ΔE_{14} values for a given $\{Mo_6X_8\}^{4+}$-core cluster depend on nature of the terminal ligands. In the case of the $\{Mo_6Br_8\}^{4+}$-core clusters (**nBr**), as an example, the ΔE_{13} and ΔE_{14} values increase in the sequence Y = I (**3Br**, 53 and 635 cm^{-1}) < Br (**2Br**, 56 and 655 cm^{-1}) < Cl (**1Br**, 63 and 695 cm^{-1}) for the terminal halide as well as L = 3,5-dinitrobenzoate (**14Br**, 40 and 545 cm^{-1}) < 4-nitrobenzoate (**12Br**, 80 and 620 cm^{-1}) < 4-cyanobenzoate (**11Br**, 85 and 640 cm^{-1}) < 3,5-dimethoybenzoate (**9Br**, 110 and 710 cm^{-1}) < benzoate (**8Br**, 115 and 745 cm^{-1}) < 4-methoxybenzoate (**6Br**, 120 and 810 cm^{-1}) for the terminal aromatic carboxylate. The π or σ-donating ability of the terminal halide or carboxylate, respectively, increases in the sequence Y = I < Br < Cl or L = 3,5-dinitrobenzoate < 4-nitrobenzoate < 4-cyanobenzoate < 3,5-dimethoybenzoate < benzoate < 4-methoxybenzoate, respectively, and, thus, a decrease or increase in the ionic size of the halide or acid dissociation constant of the terminal RCOOH (pKa(L)),
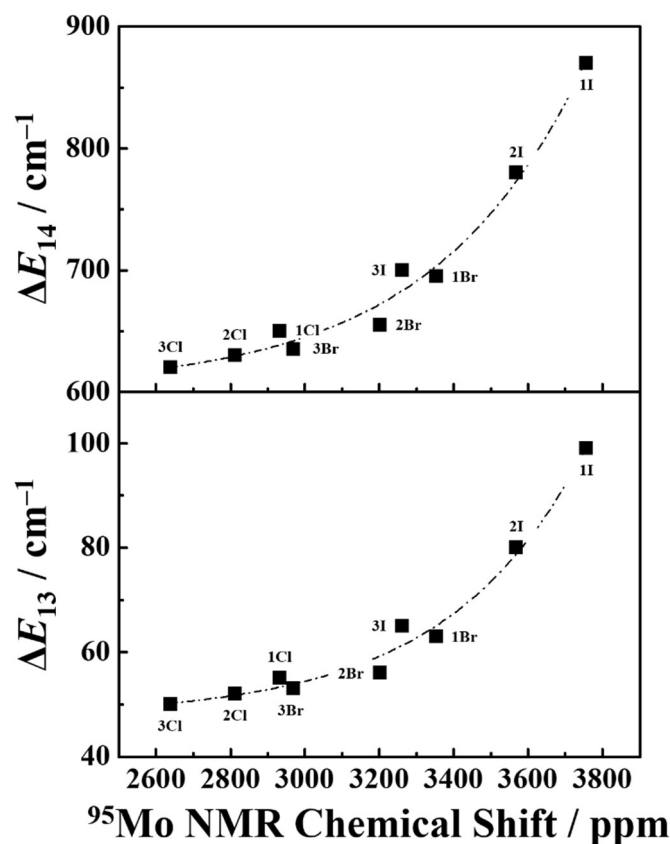

Figure 5-2. Relationships between the zfs energies in the excited triplet states (ΔE_{13} and ΔE_{14}) of $[\{Mo_6X_8\}Y_6]^{2-}$ (**1X–3X**) and the ^{95}Mo NMR chemical shift of $[\{Mo_6X_8\}Y_6]^{2-}$ whose data are taken from ref. 22–24. The broken curves represent regression between the two parameters.

respectively. It is worth noting that the stronger π/σ-donating ability of the terminal ligand gives rise to the larger ΔE_{13} and ΔE_{14} values. The results indicate that the zfs energies in the T_1 state of the cluster are related closely to the electronic structures of the terminal ligands. Therefore, the relationship between the effective nuclear charge of the Mo atom(s) (Z_{eff}) in the cluster and the zfs energies is worth discussing in detail.

In the case of a non-hydrogen like atom, Z in eq. 5-1 should be replaced by $Z_{eff} = (Z - \sigma)$, where σ is a screening constant to the electron in an atomic orbital interested. Unfortunately, since the actual Z_{eff} values of the Mo atoms in **nX** are not known, the ^{95}Mo NMR chemical shifts of **nX** ($n = 1$–3) reported by Preetz and co-workers[22-24] or pK_a values of RCOOH in **nBr** ($n = 6, 8, 9, 11, 12,$ and 14) are employed as a measure of Z_{eff} of the Mo atom in the cluster for the following discussion. Then, the $\Delta E_{14}/\Delta E_{13}$ values of **nX** ($n = 1$–3) or **nBr** ($n = 6, 8, 9, 11, 12,$ and 14) are plotted against the ^{95}Mo NMR chemical shifts of the clusters or pK_a(L), respectively. In the case of **nX** ($n = 1$–3), the ΔE_{14} and ΔE_{13} values increase with an increase in the ^{95}Mo NMR chemical shift as shown in Figure 5-2 and, thus, a decrease in the d-electron density on the Mo atom in the cluster. For a given X, since the π-donating ability of a halide depends on its ionic size and increases in the sequence Y = I < Br < Cl, it is expected that the cluster with Y = Cl shows the highest d-electron density compared to the corresponding cluster with Y = Br or I, which is an opposite trend to what shown by the ^{95}Mo NMR chemical shifts of **nX** (n
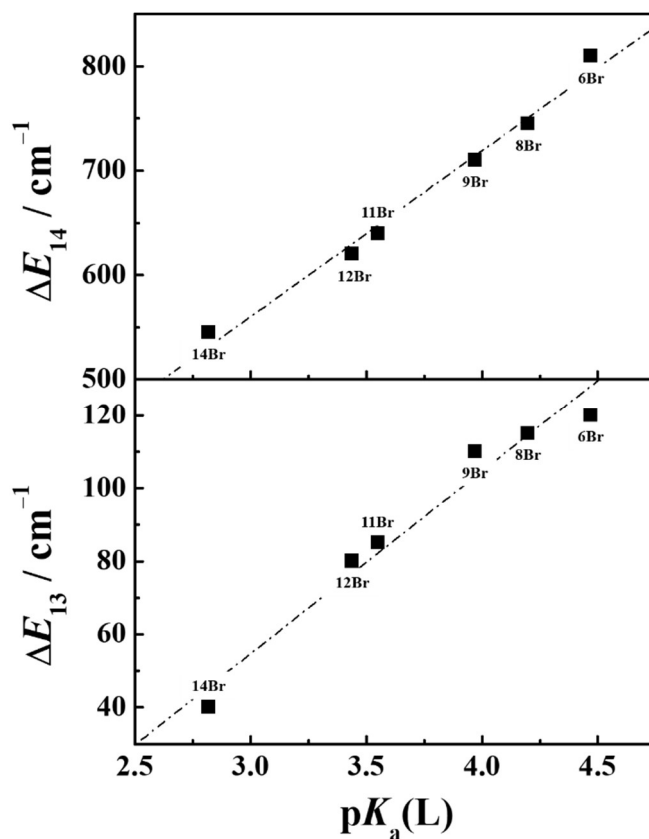

Figure 5-3. Relationships between the zfs energies in the excited triplet states (ΔE_{13} and ΔE_{14}) of $[\{Mo_6X_8\}(RCOO)_6]^{2-}$ (**6Br**, **8Br**, **9Br**, **11Br**, **12Br**, and **14Br**) and the pK_a(L) values. The broken lines represent regression between the two parameters.

= 1–3). In the case of a $[\{Mo_6X_8\}Y_6]^{2-}$ family, the smallest-sized terminal halide gives the shortest bond length between Mo and Y (d_{Mo-Y}) irrespective of X.[23-25] The shorter is the Mo-Y bond distance, the more effective is donation-back-donation between the Mo(II) and Y atoms, resulting in the lowest d-electron density of **1X** (Y = Cl) as shown by the ^{95}Mo NMR chemical shift of the cluster and, thus, leading to the largest zfs energies of **1X** among those of **nX** (n = 1–3).

In the case of $[\{Mo_6Br_8\}(RCOO)_6]^{2-}$, similarly, the ΔE_{14} and ΔE_{13} values increase with an increase in the $pK_a(L)$ value and, thus, an increase in the σ-donating ability of the terminal carboxylate. Very importantly, both ΔE_{13} and ΔE_{14} values are found to correlate very well with $pK_a(L)$ as shown in Figure 5-3. Since the $\{Mo_6Br_8\}^{4+}$-core is common in the present system, the variations of $\Delta E_{13/14}$ with $pK_a(L)$ will be also responsible for that of the effective nuclear charge (Z_{eff}) of the Mo atom or $\{Mo_6Br_8\}^{4+}$-core. In particular, the Z_{eff} value of the Mo atom ($Z_{eff}(Mo)$) coordinated with the O atom in RCOO would play important roles in determining $\Delta E_{13/14}$ through σ-donation and π-back-donation between the Mo and O atoms. The stronger is the σ-donating ability of the terminal carboxylate ligand and, thus, the larger is the $pK_a(L)$ value, the stronger is π-back donation from the Mo metal center to the coordinating O atom. Therefore, the $Z_{eff}(Mo)$ will increase with an increase in $pK_a(L)$. The larger $Z_{eff}(Mo)$ or $Z_{eff}(\{Mo_6Br_8\})$ thus leads to the larger zfs energies between Φ_n in the emitting T_1 state of the cluster.

5-3.   Implications of zfs Energies to the Emission Properties of Hexamolybdenum(II) Clusters

This thesis has demonstrated that the zfs parameters primarily determine the emission properties of the octahedral hexametal cluster. Knowing the factors governing the zfs parameters, one might control synthetically the emission properties of the clusters through tuning of the zfs parameters. Furthermore, since an octahedral hexametal cluster is used as luminophores in various photoluminescence researches owing to the high chemical/thermal stabilities and relatively easy synthetic procedures, detailed discussion on the implications of the zfs parameters to the phosphorescence properties of the clusters would receive broad interests. The emission properties (emission maximum energy ($\tilde{v}_{em}$), quantum yield (Φ_{em}), and lifetime (τ_{em})) of **1X**–**3X** or **nBr$_{AL}$** are thus plotted against the ^{95}Mo NMR chemical shift or $pK_a(L)$. As shown in Figure 5-4, the photophysical properties of the clusters show the good correlations with ^{95}Mo NMR chemical shift or $pK_a(L)$. Figure 5-4 demonstrates that an increase in the d-electron density on the Mo atom(s) (i.e., large ^{95}Mo NMR chemical shift) in **1X**–**3X** accompanies the long-lived and bright emission from the cluster. In the case of **nBr$_{AL}$**, in contrast, the high d-electron density (i.e., large $pK_a(L)$) on the Mo atom(s) gives rise to the short-lived and weak emission. Such discussions indicate that the photophysical properties of the cluster cannot be explained by a single parameter, ^{95}Mo NMR chemical shift or $pK_a(L)$.

It is worth noting, however, that the marginal ^{95}Mo NMR chemical shift or $pK_a(L)$ dependences of $\tilde{v}_{em}$, Φ_{em}, and τ_{em} in Figure 5-4 are not fortuitous. The populations to the spin-sublevels in the T_1 state of the cluster are
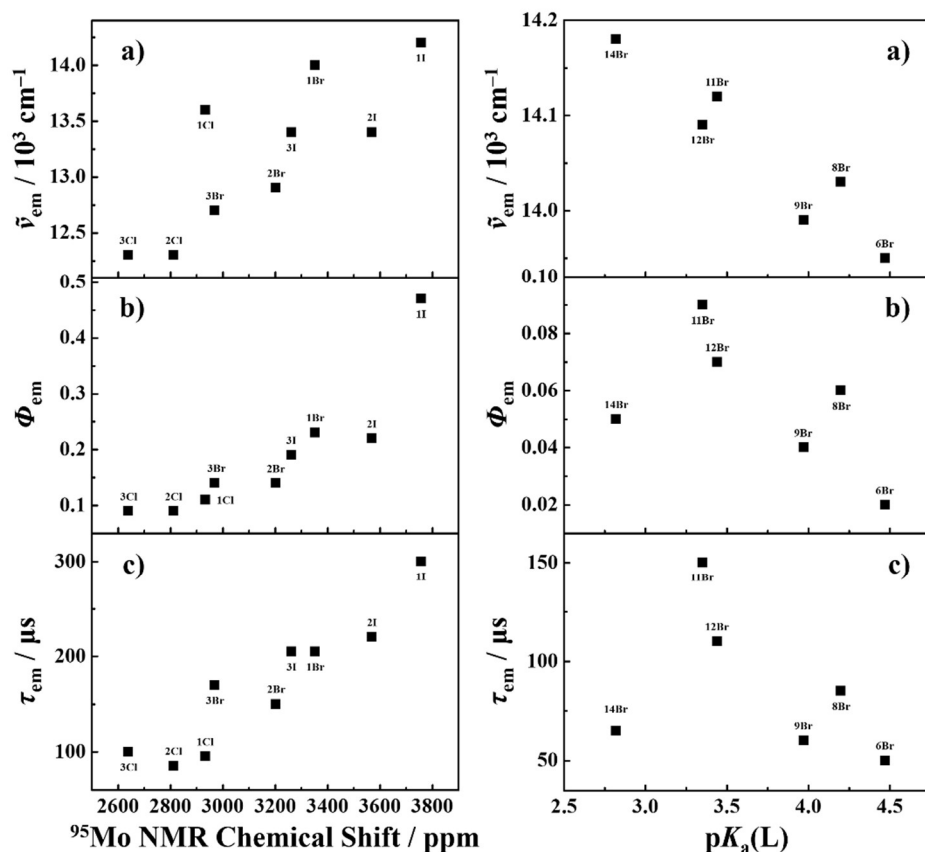
Figure 5-4. Relationships between the emission properties ((a)emission maximum energy, (b) quantum yield, and (c) lifetime) of $[\{Mo_6X_8\}Y_6]^{2-}$ (**1X–3X**) and the ^{95}Mo NMR chemical shift (left panel) or those of $[\{Mo_6Br_8\}(RCOO)_6]^{2-}$ (***n*Br$_{AL}$**) and the pK_a(L) value (right panel).

determined by thermal Boltzmann distributions at a given *T*. Different from an ordinary transition metal complex, the zfs energy of the octahedral hexamolybdenum(II) cluster, in particular ΔE_{14}, is much larger than the thermal Boltzmann factor (k_{BT}, k_B = Boltzmann constant) at ambient temperature. For instance, the $k_B T$ value at 300 K and the ΔE_{14} values of the present clusters are 209 cm^{-1} and 545–1000 cm^{-1}, respectively. In the case of an octahedral hexamolybdenum(II) cluster at 300 K, therefore, all of the spin-sublevels in the T$_1$ state cannot contribute equally to the observed emission and the relative population percentages to each spin-sublevel   at a given *T* should be considered. For a given X in the terminal halide cluster $[\{Mo_6X_8\}Y_6]^{2-}$, as examples, the emission spectra of $[\{Mo_6Br_8\}Y_6]^{2-}$ (***n*Br**) at 300 K are the sum of the Φ_3 and Φ_4 emissions with different contribution percentages: Φ_3 and Φ_4 = 54.5 and 45.5% for **1Br**; 52.9 and 47.1% for **2Br**; 42.7 and 57.3% for **3Br**. Furthermore, the large zfs energies (i.e., ΔE_{13} and ΔE_{14}) of the cluster give rise to the higher-energy Φ_3 and Φ_4 emissions from $[\{Mo_6Br_8\}Y_6]^{2-}$. The small and large contributions from the lower-energy Φ_3 and higher-energy Φ_4 lying spin-sublevels, respectively, to the observed emission spectrum thus leads to the lower-energy emissions from **1X–3X**: see Figure 3-16 in Chapter 3. For a given X in the terminal carboxylate cluster $[\{Mo_6Br_8\}(RCOO)_6]^{2-}$ (***n*Br$_{AL}$**) similar to the terminal halide clusters, the emission spectra at 300 K are

composed of the Φ_3 and Φ_4 emissions and the contribution of the Φ_3 emission to the observed spectrum decreases with an increase in the zfs energy. In the case of the terminal carboxylate cluster, however, the $\tilde{v}_3$ and $\tilde{v}_4$ values are almost comparable contrarily to those of the terminal halide clusters. The small Φ_3 and large Φ_3 contributions to the observed emission spectra originated from the large zfs energies thus lead to the lower-energy emissions from $n\mathbf{Br_{AL}}$: see Figure 4-24 in Chapter 4. Such discussions described in §3-4-6 and §4-6-5 explain very well the $\tilde{v}_{em}$ values of $\mathbf{1X}$–$\mathbf{3X}$ and $n\mathbf{Br_{AL}}$ at 300 K. Furthermore, it has been also demonstrated that the Φ_{em} and τ_{em} values of $\mathbf{1X}$–$\mathbf{3X}$ for a given X or $n\mathbf{Br_{AL}}$ are determined by the relevant $\tilde{v}_{em}$ values since the radiative rate constant (k_r) of the octahedral hexamolybdenum(II) cluster is rather insensitive to the terminal ligand structure, while the nonradiative rate constant (k_{nr}) of the cluster shows a $\tilde{v}_{em}$ dependence: energy gap dependences of k_{nr} in Figures 3-5 and 4-10. The primary origin of the opposite d-electron density dependences of the emission properties between those of the terminal halide and terminal carboxylate clusters is thus the different effects of the zfs energies on $\tilde{v}_{em}$ (or $\tilde{v}_n$).

5-4.   Origin of the Characteristic zfs Energies of Hexamolybdenum(II) Clusters

The ΔE_{14} values of the present hexamolybdenum(II) clusters range in 545–1000 cm^{-1}, while the zfs energies in the T_1 states of ordinary mononuclear transition metal complexes are in the range of ~0–170 cm^{-1}.[21] For example, the zfs energy of [Rh(bpy)$_3$]$^{2+}$, [Pt(ppy)$_2$], [Ru(bpy)$_3$]$^{2+}$, or [Ir(ppy)$_3$] (bpy = 4,4'-bipyridine, ppy = 2-phenylpyridine) is reported to be 0.04, 32, 61, or 170 cm^{-1}, respectively.[25–28] Since the zfs energies in the T_1 states of hexatungsten(II) and hexarhenium(III) clusters are comparable to those of the hexamolybdenum(II) clusters,[29,30] the surprisingly large zfs energy of an octahedral hexametal cluster demonstrated in the present study would be the inherent character to a polynuclear transition metal complex.

The main structural unit of a hexamolybdenum(II) or hexatungsten(II) cluster is $\{M_6X_8\}^{4+}$ (M = Mo(II) or W(II), X = Cl, Br, or I), and the very heavy six metal atoms sit closely in the $\{M_6X_8\}^{4+}$-core to form the metal-metal bonds. Furthermore, the molecular orbitals of the clusters are responsible for the delocalized electrons in the $\{M_6X_8\}^{4+}$-core, where the electrons are distributed equally to each metal atom or bridging ligand owing to high molecular symmetry.[15,31] These structural and electronic characteristics indicate that the $\{M_6X_8\}^{4+}$-core would behave as a single atom or a superatom reported sometimes for a polynuclear metal complex having metal-metal bonds.[32–35] In the case of Au clusters, as an example, a closed shell electronic structure similar to that of a noble gas atom is necessary to confine the electrons in the polynuclear metal unit.[34] In contrast, the number of the total valence electrons in a metal octahedron (M$_6$ unit) or cluster core ($\{M_6X_8\}^{4+}$ unit) is 24 or 40, respectively, which is a closed shell structure different from that of a noble gas atom. Therefore, although the $\{M_6X_8\}^{4+}$-core is not a perfect superatom, the $\{M_6X_8\}^{4+}$-core could behave as a pseudo-superatom owing to the electrons confined in the $\{M_6X_8\}^{4+}$-core.

According to the second-order perturbation theory described in Chapter 1, spin-orbit coupling (SOC) is the

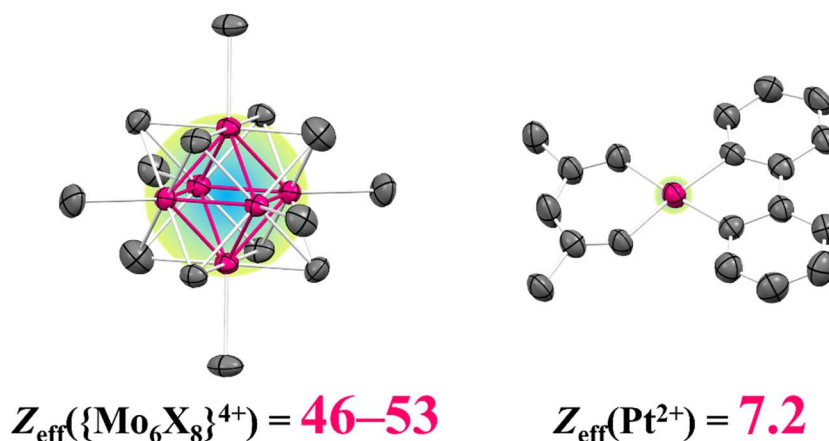$$Z_{eff}(\{Mo_6X_8\}^{4+}) = 46–53 \qquad Z_{eff}(Pt^{2+}) = 7.2$$

Figure 5-5. Schematic illustrations of H_{SO} of an octahedral hexamolybdenum(II) cluster and a platinum(II) complex. The Z_{eff} value was calculated based on the ionization energy of the metal ion (IE_{Mo2+} = 27 eV, IE_{Pt2+} = 28 eV)[39] and the electron affinity of the halide (EA_{Cl-} = 3.6 eV, EA_{Br-} = 3.4, EA_{I-} = 3.1)[39] through the following equation; IE or EA = $-(Z_{eff}^2/n^2)R_y$, where Ry is the Rydberg constant (13.61 eV). The background colors of the structures represent the significance of H_{SO}. Metal and other atoms are colored in red and gray, respectively.

dominant factor determining the zfs energy in the T_1 state of a transition metal complex,[36,37] and Hamiltonian of SOC (H_{SO}) is given by eq. 5-2,[38]

$$H_{SO} = \left(\frac{\alpha^2}{2}\right)\sum_i\sum_A\left(\frac{Z_{eff}(A)}{r_{iA}^3}\right)L_{iA}\cdot S_i$$

(5-2)

where α is a fine structure constant, S and L are orbital and angular momentum operators for an electron i and a nucleus A, respectively.[36] Since eq. 5-2 demonstrates H_{SO} in a multi-electron configuration system is given by the sum of Z_{eff} of the atoms constituting of an molecule, the heavier is the atom(s) constituting an molecule, the stronger is the strength of SOC generated. Indeed, under the assumption that an $\{M_6X_8\}^{4+}$-core is a pseudo-superatom, the sum of Z_{eff} of the atoms constituting a hexamolybdenum(II) cluster explains well the differences in the zfs energies of the hexamolybdenum(II) cluster and the mononuclear platinum complex as demonstrated in Figure 5-5. Superatom-like behavior of the $\{M_6X_8\}^{4+}$-core therefore increases the effective nuclear charge, leading to the very large zfs energies in the T_1 state of the octahedral hexametal clusters relative to those of other mononuclear transition metal complexes.

5-5.   Factors Governing zfs Energies in the T_1 States of Platinum(II) Complexes
5-5-1. ^{195}Pt NMR Spectroscopy of Luminescent Platinum(II) Complexes

The zfs energies in the T_1 states of **1Pt–5Pt** reported by Yersin et al. are summarized in Table 5-2.[21] The zfs energies of **1Pt–5PT** are sensitive to nature of the ligand structure and vary in ~0–36 cm^{-1}. In general, the combination of an *O^O* or *C^N* ligand with a Pt(II) ion provides the small zfs energy compared to those of other

Table 5-2. zfs energies and [195]Pt NMR chemical shifts of **nPt** in $CDCl_3$ relative to that of K_2PtCl_4 in D_2O.

Complexes	1Pt	2Pt	3Pt	4Pt	5Pt
zfs / cm^{-1}	~1[a]	4.3[a]	11.5[a]	16[a]	32[a]
δ([195]Pt) / ppm	−1148	−1165	−1219	−1524[b]	−1518[b]

a, b) The data taken from ref. 21 and 40, respectively.

ligand–Pt(II) ion combinations, and the complex having two *C^N* ligands (i.e., homoleptic complex) shows the largest zfs energy among those of the platinum(II) complexes hitherto reported.[21] For a given ligand in the heteroleptic *O^O-C^N* and homoleptic *C^N-C^N* platinum(II) complexes, furthermore, the zfs energy increases in the sequence benzo[*h*]quinoline < 2-(2-thienyl)pyridine < 2-phenylpyridine. The zfs energy of an ordinary transition metal complex has been reported to correlate closely to the d-electron character in the T_1 state and increases in the sequence $^3(\pi\pi^*)$ < admixture of $^3(\pi\pi^*)/^3$(MLCT = metal-to-ligand charge transfer) < ^{3}(MLCT) excited states.[21] Furthermore, it was demonstrated that the zfs energies of the octahedral hexamolybdenum(II) cluster show the [95]Mo NMR chemical shift or pK_a(L) dependence through variation of the effective nuclear charge on the Mo(II) atom(s) and, thus, the d-electron density on Mo(II). The present study has therefore focused on the NMR chemical shift of the metal atom in a transition metal complex as a measure of the d-electron density on the metal atom.

Figure 5-6a shows the [195]Pt NMR spectra of **1Pt**–**3Pt** in $CDCl_3$ at ambient temperature, and the [195]Pt NMR chemical shifts of **1Pt**–**5Pt** are summarized in Table 5-2, together with the relevant zfs energies reported by Yersin et al.[21] As seen in Table 5-2, the heteroleptic *O^O-C^N* platinum(II) complexes (**1Pt**–**3Pt**) show the [195]Pt NMR signals in the higher magnetic field side compared to that of the homoleptic *C^N-C^N* platinum(II) complex (**4Pt** or **5Pt**) though the complexes possess the same *C^N* ligand. For a given ligand in the heteroleptic
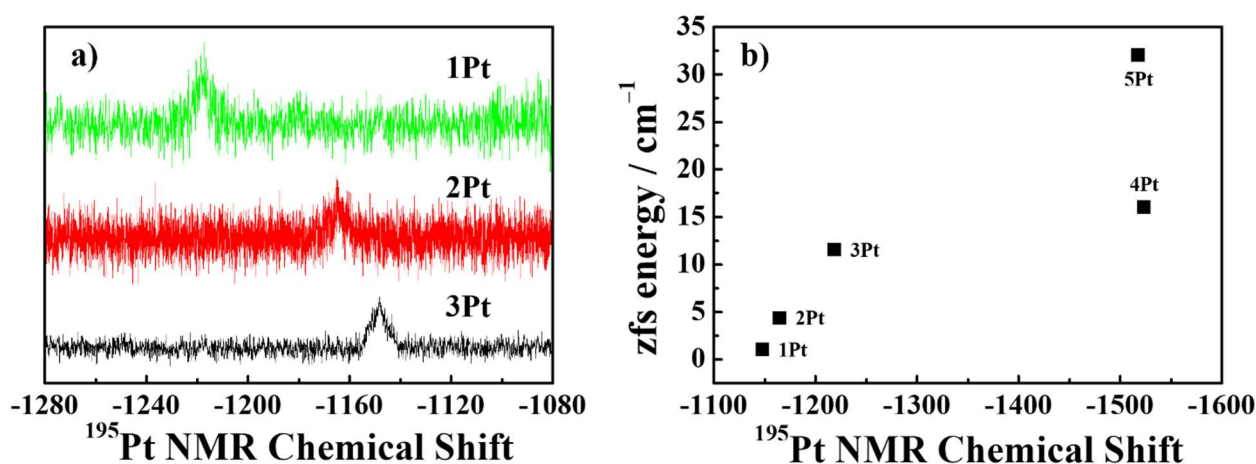

Figure 5-6. (a) [195]Pt NMR spectra of **1Pt** (green), **2Pt** (red), and **3Pt** (black) in $CDCl_3$ at 293 K. (b) Relationship between [195]Pt NMR chemical shift and zfs energy of **1Pt**–**5Pt**. The chemical shift is relative to that of K_2PtCl_4 in D_2O at 293 K.

$O{\wedge}O$ or homoleptic $C{\wedge}N$ platinum(II) complex, furthermore, the [195]Pt NMR chemical shifts of **1Pt–5Pt** increase in the sequence benzo[*h*]quinoline(**1Pt**) < 2-(2-thienyl)pyridine (**2Pt, 4Pt**) < 2-phenylpyridine (**3Pt, 5Pt**). It is worth noting that the tendency in the ligand dependence of the zfs energy or [195]Pt NMR chemical shift coincides very well with each other. Thus, the [195]Pt NMR chemical shifts of **1Pt–5Pt** were plotted against the relevant zfs energies. As seen in Figure 5-6b, an increase in the [195]Pt NMR chemical shift gives rise to an increase in the zfs energy with the clear correlation between the two parameters. It is worth emphasizing that the results in Figure 5-6b are quite similar to those observed for the octahedral hexamolybdenum(II) clusters shown in Figure 5-2, indicating that the zfs energy of an ordinary mononuclear transition metal complex is also closely related to the d-electron density on the metal atom similar to that of the octahedral hexamolybdenum(II) cluster. Chapter 5 has described that the origin of the NMR chemical shift dependence of the zfs energy is the effective nuclear charge of a metal center. Since the effective nuclear charge of a metal ion is predictable by fundamental density functional theory (DFT) calculations, the correlation between the zfs energy and effective nuclear charge of the metal center in a transition metal complex is worth discussing based on the DFT calculations on Z_{eff}.

5-5-2. DFT Calculations of the Structures and Effective Nuclear Charges in the T_1 States of the Platinum(II) Ions in Luminescent Platinum(II) Complexes

The structure optimizations of **1Pt–5Pt** by DFT calculations were conducted based on the X-ray crystal structures of the complexes.[40,41] The selected bond lengths in the optimized structures of **1Pt–5Pt** are summarized in Table 5-3. Although the present calculation level of the theory (i.e., CAM-B3LYP/SDD, 6-311G++(d,p)) has resulted in the slightly elongated bond length compared to the relevant value in the X-ray crystal structures, the calculated bond length is qualitatively in good agreement with the relevant value in the X-ray crystal structure. In the case of the $O{\wedge}O$-$C{\wedge}N$ complexes (**1Pt–3Pt**), as an example, the bond length between the platinum atom and the ligating carbon, nitrogen or oxygen ($d_{\text{Pt-C}}$, $d_{\text{Pt-N}}$, or $d_{\text{Pt-O}}$, respectively) decreases in the sequence **2Pt** < **3Pt** < **1Pt** for $d_{\text{Pt-C}}$(DFT) and $d_{\text{Pt-N}}$(DFT), **1Pt** < **2Pt** < **3Pt** for $d_{\text{Pt-O}}$(DFT), **2Pt** < **1Pt** for $d_{\text{Pt-C}}$(X-ray) and $d_{\text{Pt-N}}$(X-ray), or **1Pt** < **2Pt** for $d_{\text{Pt-O}}$(X-ray). The results demonstrate that the present

Table 5-3. Selected average bond lengths in the optimized and X-ray crystal structures of **1Pt–5Pt**.

	SDD, 6-311G++(d,p)			Crystal Structure		
	$d_{\text{Pt-C}}$ / Å	$d_{\text{Pt-N}}$ / Å	$d_{\text{Pt-O}}$ / Å	$d_{\text{Pt-C}}$ / Å	$d_{\text{Pt-N}}$ / Å	$d_{\text{Pt-O}}$ / Å
1Pt	1.989	2.032	2.070	1.989[a]	1.983[a]	2.031[a]
2Pt	1.974	2.034	2.074	n.d.	n.d.	n.d.
3Pt	1.979	2.019	2.082	1.948[a]	1.979[a]	2.036[a]
4Pt	2.062	2.223	–	n.d.	n.d.	–
5Pt	2.064	2.203	–	1.993[b]	2.128[b]	–

a, b) The data compiled from ref. 40 and 41, respectively.

Table 5-4. Calculated and reported Z_{eff} values of several 4d-metal atoms (left; Mo–Rh, right; Pd–Cd).

	Effective nuclear charge (4d)				Effective nuclear charge (4d)	
	Present method	Reported[42]			Present method	Reported[42]
Mo	4.2505	3.1110		Pd	6.8500	3.6476
Tc	4.9008	3.2205		Ag	7.5001	3.8064
Ru	5.5505	3.3470		Cd	8.1500	3.9692
Rh	6.2009	3.4937				

calculation level of the theory reproduced adequately the experimentally observed structures and, therefore, these optimized structures are employed for further detailed DFT calculations.

It has been shown that the zfs energies (ΔE_{13} and ΔE_{14}) of the octahedral hexamolybdenum(II) cluster correlate very well with the relevant ^{95}Mo NMR chemical shift. This has demonstrated that the ΔE_{13} or ΔE_{14} value is determined primarily by the d-electron density on the Mo atom(s) and, thus, by the effective nuclear charge on the Mo atom(s) (Z_{eff}(Mo)). Similar to the octahedral hexamolybdenum(II) clusters, since the zfs energies of the present platinum(II) complexes show clear correlation with the relevant ^{195}Pt NMR chemical shifts, the Z_{eff}(Pt) values of a series of the platinum(II) complexes are interested and worth investigating in more detail. Koseki has reported that the DFT calculations of the Z_{eff} values of heavy diatomic molecules based on effective core potential (ECP) basis sets, though the calculations involve 30% errors compared to the experimental values due to the absence of relativistic effects considerations.[38] Since the present study focuses on the demonstration of the importance of Z_{eff} in determining the zfs energy in the T_1 state of a transition metal complex, rough evaluation of the Z_{eff} value of a targeted complex will be enough for the present purpose of the study. Therefore, the present study has employed the method analogous to the report by Koseki and, thus, employed the combination of ECP based DFT calculations and the Slater's rule. Briefly, the number of the electron in the core and valence orbitals (4d) of a platinum ion is estimated by the natural population analysis in the ECP-based DFT calculations and, then, the Z_{eff} value of the Pt(II) ion is calculated based on the Slater's rule. Since such a method has not been hitherto reported, the validity of the present method is worth checking to discuss the results on the Pt(II) complexes. Therefore, the Z_{eff} values of several 4d-metal atoms in the valence orbitals (4d orbitals) have been estimated by the present method as the results are summarized in Table 5-4, together with those reported by Clementi et al.[42] As seen in Table 5-4, the present method overestimated the Z_{eff} value and the error of the results increases with an increase in the atomic number owing to the absence of relativistic effects in the calculations. However, since the Z_{eff} values calculated by the SCF method reported by Clementi et al. and the present method correlate very well with each other as shown in Figure 5-7 ($cc = 0.995$), the Z_{eff} value evaluated by the present method is qualitatively reasonable and could be employed to discuss the
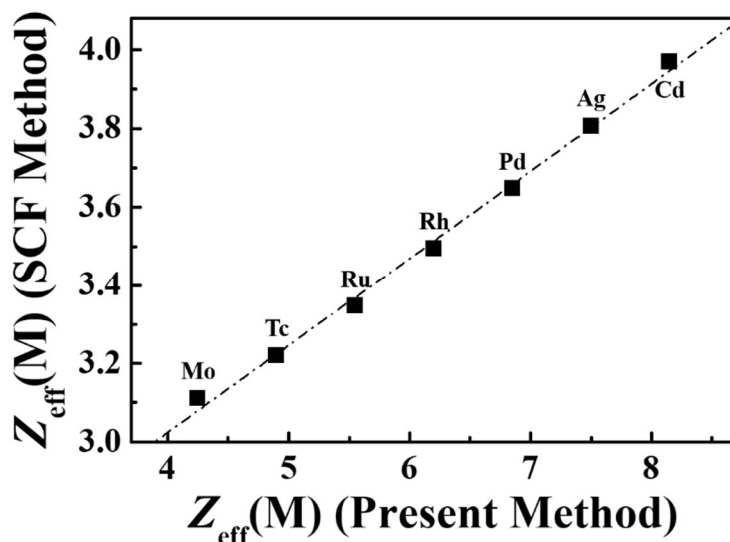
Figure 5-7. Relationship between the calculated Z_{eff} values by SCF[42] and the present method.

relationship between the Z_{eff} value and the zfs energy of the Pt(II) complex. The Z_{eff} values of the platinum atoms (Z_{eff}(Pt)) in **1Pt–5Pt** have been therefore calculated based on ECP-based DFT calculations.

The Z_{eff}(Pt) values of **1Pt–5Pt** in the T_1 states estimated by the present method are summarized in Table 5-5. The calculated Z_{eff}(Pt) value ranges in 3.72–3.90 and the ligand dependence of the value is not significant. However, the variation of the Z_{eff}(Pt) value by the ligand and/or ligand combination gives the different Z_{eff}(Pt) values. For a given ligand in the heteroleptic *O^O-C^N* or homoleptic *C^N-C^N* platinum(II) complex, as an example, the Z_{eff}(Pt) value increases in the sequence benzo[*h*]quinoline(**1Pt**) < 2-(2-thienyl)pyridine (**2Pt**, **4Pt**) < 2-phenylpyridine (**3Pt**, **5Pt**). Furthermore, the homoleptic *C^N-C^N* platinum(II) complex (**4Pt** or **5Pt**) shows the larger Z_{eff}(Pt) value than that of the heteroleptic *O^O-C^N* platinum(II) (**1Pt–3Pt**). It is worth emphasizing that the ligand dependence of Z_{eff}(Pt) is analogous to that of the ^{195}Pt NMR chemical shift. Since the ligand dependence of the zfs energy shown in Table 5-2 would be originated from the d-electron density on the Pt(II) ion and is reflected by the effective nuclear charge, the Z_{eff}(Pt) values of **1Pt–5Pt** are plotted against the relevant zfs energies. As seen clearly in Figure 5-8, the larger Z_{eff}(Pt) value gives rise the larger zfs energy. The results demonstrate that the zfs energy in the T_1 state of a transition metal complex is determined by the effective nuclear charge of the metal center, irrespective of a metal atom and a ligand structure. Furthermore, the present study has demonstrated that the zfs energy of a transition metal complex could be evaluated and predicted based on simple DFT calculations though the accuracy of the present method should be improved in near future to compare the zfs energies of various transition metal complexes having different metal atoms and ligands.

Table 5-5. Calculated Z_{eff}(Pt) values of **1Pt–5Pt** in the T_1 states.

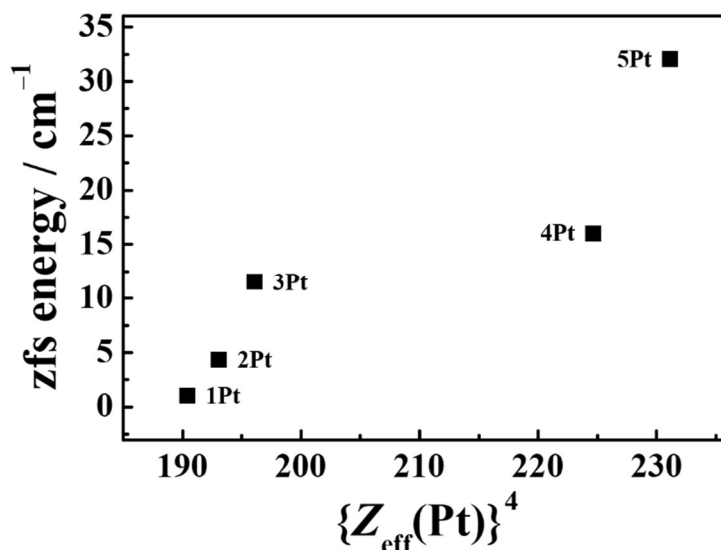| Complexes	**1Pt**	**2Pt**	**3Pt**	**4Pt**	**5Pt**
Z_{eff}(Pt)	3.7149	3.7278	3.7422	3.8716	3.8992

Figure 5-8. Relationship between the fourth power of the effective nuclear charges on the platinum atoms in the excited triplet states of **1Pt–5Pt** and the relevant zfs energies.

5-6. Implications of the zfs Energies to the Phosphorescence Properties of the Platinum(II) Complexes

This study has demonstrated experimentally that zfs in the T_1 state of a transition metal complex is related strongly with the effective nuclear charge of the metal atom(s) concerned and this determines the zfs energy(ies). In the case of an octahedral hexametal cluster, it has been also shown that the zfs energies determine the emission characteristics of the clusters as described in §3-4-6 and §4-6-5. Furthermore, the photophysical properties of the octahedral hexamolybdenum(II) cluster at 298 K are determined primarily by the emission maximum energy ($\tilde{v}_{em}$) through the energy gap dependence of k_{nr} (i.e., $\ln(k_{nr}) \propto \tilde{v}_{em}$) as described in §3-3-3 and §4-4, leading to the [95]Mo NMR chemical shift or pK_a(L) dependence of the emission properties as shown in Figure 5-4. It is expected that the photophysical properties of the platinum(II) complex are also governed and explained by the factors governing zfs in the T_1 states similar to those of the octahedral hexamolybdenum(II) cluster. Furthermore, the elucidation of the factors governing the photophysical properties of an ordinary transition metal complex, represented by a Pt(II) complex, will be received broad interests, which is worth investigating in detail.

The emission spectra and decay profiles of **1Pt–3Pt** in acetonitrile at 298 K are shown in Figure 5-9, while the photophysical properties of the complexes are summarized in Table 5-6, together with those of **4Pt** reported by Maestri et al.[19] Unfortunately, the emission data on **5Pt** have not been collected since the complex is non-emissive at ambient temperature.[22] As seen in Table 5-6, the emission maximum energy ($\tilde{v}_{em}$), lifetime (τ_{em}) and quantum yield (Φ_{em}) of **1Pt–4Pt** vary in $\tilde{v}_{em} = (17.30–20.62) \times 10^3$ cm^{-1}, $\tau_{em} = 2.2–20.3$ μs, and $\Phi_{em} = 0.095–0.305$, respectively, and decreased in the sequences $\tilde{v}_{em} = $ **3Pt** > **1Pt** > **2Pt** > **4Pt**, $\tau_{em} = $ **2Pt** > **1Pt** > **3Pt** > **4Pt**, and $\Phi_{em} = $ **2Pt** > **4Pt** > **3Pt** > **1Pt**. In these data, one cannot find any common tendency in the ligand dependences or the correlation with the relevant zfs energy of the complex. It is worth noting that, on the other hand, the radiative rate constant (k_r) of the complex increases with an increase in the zfs energy in the sequence $k_r = $ **1Pt**

Table 5-6. Emission properties of **1Pt**–**4Pt** in nitrile solvent at ambient temperature.

	1Pt	2Pt	3Pt	4Pt[43]
$\tilde{v}_{em}$/ 10^3 cm^{-1}	19.53	17.92	20.62	17.30
(λ_{em}/ nm)	(512)	(558)	(485)	(578)
τ_{em} / μs	18.4	20.3	3.3	2.2
Φ_{em}	0.095	0.305	0.200	0.30
k_r / 10^3 s^{-1}	0.52	1.50	6.06	13.6
k_{nr} / 10^3 s^{-1}	4.92	3.42	24.2	31.8

(zfs = ~1 cm^{-1}) < **2Pt** (4.3) < **3Pt** (11.5) < **4Pt** (16). In practice, the k_r values of **1Pt**–**4Pt** show the linear correlation with the relevant zfs energies as shown in Figure 5-11a. Furthermore, interestingly, Figure 5-11 (b, c) demonstrates that the ^{195}Pt NMR chemical shift and the $Z_{eff}(Pt)^4$ value evaluated by the DFT calculations also show the clear correlation with the k_r value and, therefore, with the zfs energy. Analogous to the octahedral hexamolybdenum(II) cluster, the results clearly demonstrate that zfs in the T_1 state is the significant factor determining the emission properties of the Pt(II) complexes and this suggests that the phosphorescence properties of a platinum(II) complex could be also controlled synthetically based on the zfs in the T_1 state.

The population to each spin-sublevel in the T_1 state of a complex is determined by the thermal Boltzmann distribution at a given T. In the case of a transition metal complex, the thermal Boltzmann factor ($k_B T$) at ambient temperature is in general larger than the zfs energy of the complex. For instance, the $k_B T$ value at 298 K and the zfs energies of ordinary transition metal complexes are 207 cm^{-1} and 1–170 cm^{-1}, respectively.[21] This indicates that all of the spin-sublevels of the complex contribute almost equally to the observed emission at 298 K and, thereby, the emission properties of the complex at 298 K are characterized directly by the zfs parameters.
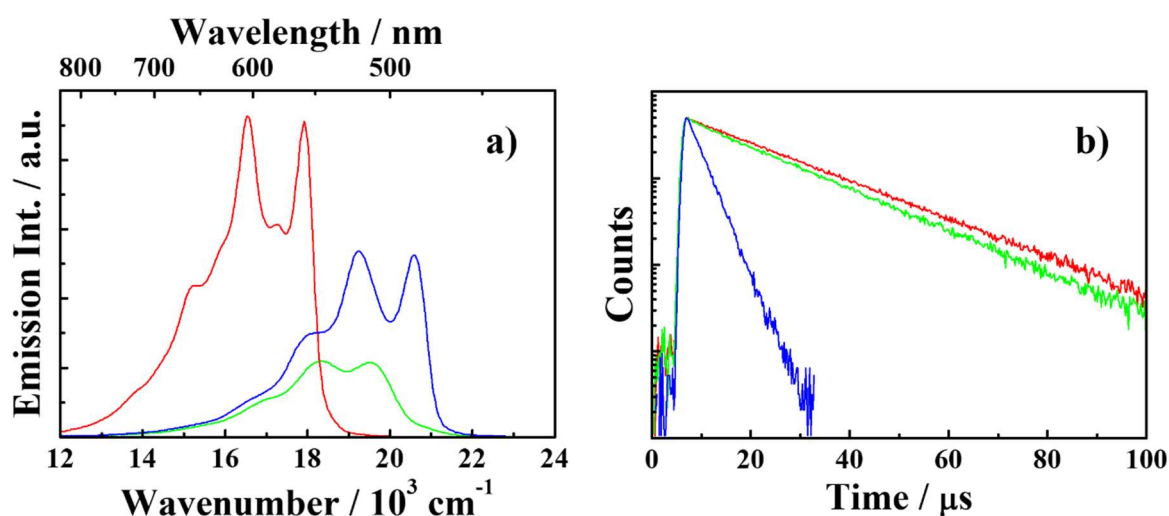

Figure 5-10. Emission spectra (a) and decay profiles (b) of **1Pt**–**3Pt** (**1Pt**, green; **2Pt**, red; **3Pt,** blue) in CH$_3$CN at 298 K. The areas of the emission spectra correspond to the emission quantum yields.
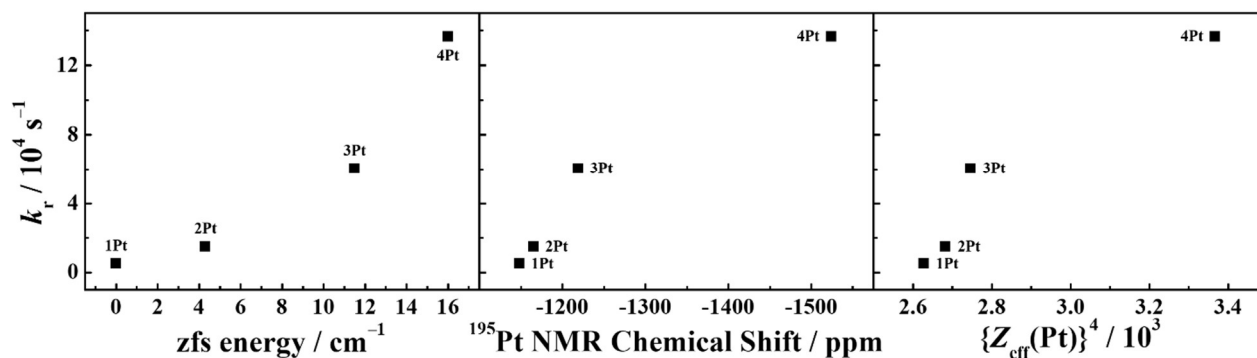
Figure 5-11. Relationships between the radiative rate constant and (a) the zfs energy, (b) the ^{195}Pt NMR chemical shift, and (c) the fourth power of the effective nuclear charge of the platinum atom in the T_1 state.

According to the perturbation theory, the electronically singlet (S_n, $n = 1, 2, 3, \cdots$) and lowest-energy emitting excited triplet (T_1) states are mixed and coupled by SOC and, when one considers the lowest-energy S_1 and T_1 states for simplicity, the mixing coefficient is given by eq. 5-3,[21]

$$a = \frac{\langle \Phi(^1S_1) | H_{SO} | \Phi(^3T_1) \rangle}{E(^1S_1) - E(^3T_1)}$$

(5-3)

where H_{SO}, $\Phi(^1S_1 \text{ or } ^3T_1)$, and $E(^1S_1 \text{ or } ^3T_1)$ are the Hamiltonian for SOC, the wave function of the S_1 or T_1 state, and the energy of the S_1 or T_1 states, respectively. Eq. 5-3 demonstrates that the stronger SOC and the smaller S_1–T_1 energy gap leads to more efficient mixing of the S_1 and T_1 states. As seen in eq. 5-2, H_{SO} is closely related to $Z_{eff}(M)$ (M = metal) and $Z_{eff}(M)$ determines the zfs energy. Furthermore, since the phosphorescence process of a transition metal complex with the rate constant, k_r, involves spin-inversion, more effective mixing between the S_1 and T_1 states leads to the larger k_r value. Furthermore, since the platinum(II) complex with a larger k_r value shows a shorter τ_{em} value, it is thus reasonable that a larger zfs energy (i.e., stronger SOC) accompanies a larger k_r value.

5-7.   Conclusions

This chapter described the factors governing the zfs energies and the implications of the zfs energies to the phosphorescence properties of the octahedral hexamolybdenum(II) clusters and the platinum(II) complexes. For a given terminal ligand in the octahedral hexamolybdenum(II) cluster, the zfs energies (ΔE_{13} and ΔE_{14}) increased with an increase in the atomic number of the bridging ligand irrespective of the terminal ligands. Furthermore, for a given bridging ligand, the stronger electron-donating terminal ligand in the cluster gave rise to the larger zfs energies. The ^{95}Mo NMR chemical shift or $pK_a(L)$ dependences of the zfs energies of the clusters demonstrate that the d-electron density on the Mo atom(s) primarily determines the zfs energies. Very importantly, the findings similar to the octahedral hexametal clusters were also confirmed for the mononuclear

platinum(II)) complexes, demonstrating that one of the factors governing the zfs energy(ies) of the transition metal complex is the electron density on the metal atom(s). In the case of the octahedral hexamolybdenum(II) cluster, reflecting the zfs energies sensitive to the d-electron density on the Mo atom, the photophysical properties showed the clear ^{95}Mo NMR chemical shift or pK_a(L) dependence. The terminal halide cluster becomes strongly emissive with an increase in the d-electron density on the Mo atom(s) (i.e., increase in the zfs energies), while the terminal carboxylate cluster with the low d-electron density on the Mo atom(s) results in a weak emitter. The opposite trend seen in the zfs energy dependences of the photophysical properties of the hexamolybdenum(II) clusters was explained satisfactorily by the different contribution percentages of the Φ_n emissions to the observed emission. In the case of the terminal halide cluster, the small and large contributions from Φ_4 and Φ_3 owing to the large zfs energies gives rise to the higher energy emission, since the larger is the zfs energies for a given bridging ligand, the higher is the emission energy of the spin-sublevel. For a given X in the terminal carboxylate cluster, the contribution of the Φ_3 emission to the observed spectrum decreases with a decrease in the zfs energies similar to the results on the terminal halide clusters. In the case of the terminal carboxylate cluster, however, the emission energy of the spin-sublevel is not affected by the carboxylate terminal ligands, leading to the lower-energy emission of the cluster due to the larger zfs energies. Interestingly, it has been demonstrated furthermore that the radiative rate constant of the platinum(II) complex is shown to correlate very well with the relevant zfs energy, which is explained by both the almost equal contributions of the spin-sublevels to the observed emission and strong SOC induced by the low d-electron density on the platinum atom.

5-8. References

(1) Maverick, A. W.; Gray, H. B. Luminescence and Redox Photochemistry of the Molybdenum(II) Cluster $Mo_6Cl_{14}^{2-}$. *J. Am. Chem. Soc.* **1981**, *103*, 1298–1300.

(2) Maverick, A. W.; Najdzionek, J. S.; MacKenzie, D.; Nocera, D. G.; Gray, H. B. Spectroscopic, Electrochemical, and Photochemical Properties of Molybdenum(II) and Tungsten(II) Halide Clusters. *J. Am. Chem. Soc.* **1983**, *105*, 1978–1882.

(3) Zietlow, T. C.; Hopkins, M. D.; Gray, H. B. Electronic Spectroscopy and Photophysics of d^4 Clusters. *J. Solid State Chem.* **1985**, *57*, 112–119.

(4) Sokolov, M. N.; Mihailov, M. A.; Peresypkina, E. V.; Brylev, K. A.; Kitamura, N.; Fedin, V. P. Highly Luminescent Complexes $[Mo_6X_8(n\text{-}C_3F_7COO)_6]^{2-}$ (X = Br, I). *Dalton Trans.* **2011**, *40*, 6375–6377.

(5) Kirakci, K.; Kubát, O.; Dušek, M.; Fejfarová, K.; Šicha, V.; Mosinger, J.; Lang, K. A Highly Luminescent Haxanuclear Molybdenum Cluster: A Promising Candidate toward Photoactive Materials. *Eur. J. Inorg. Chem.* **2012**, 3107–3111.

(6) Kirakci, K.; Kubát, P.; Langmaier, J.; Polívka, T.; Fuciman, M.; Fejfarová, K.; Lang, K. A Comparative Study of the Redox and Excited State Properties of $(nBu_4N)_2[Mo_6X_{14}]$ and $(nBu_4N)_2[Mo_6X_8(CF_3COO)_6]$

(X = Cl, Br, or I). *Dalton Trans.* **2013**, *42*, 7224–7232.

(7) Sokolov, M. N.; Mikhailov, M. A.; Brylev, K. A.; Virovets, A. V.; Vicent, C.; Kompankov, N. B.; Kitamura, N.; Fedin, V. P. Alkynyl Complexes of High-Valence Clusters. Synthesis and Luminescence Properties of $[Mo_6I_8(C\equiv CC(O)OMe)_6]^{2-}$, the First Complex with Exclusively Organometallic Outer Ligands in the Family of Octahedral $\{Mo_6X_8\}$ Clusters. *Inorg. Chem.* **2013**, *52*, 12477–12481.

(8) Efremova, O. A.; Shestopalov, M. A.; Chirtsova, N. A.; Smolentsev, A. I.; Mironov, Y. V.; Kitamura, N.; Brylev, K. A.; Sutherland, A. J. A Highly Emissive Inorganic Hexamolybdenum Cluster Complex as a Handy Precursor for the Preparation of New Luminescent Materials. *Dalton Trans.* **2014**, *43*, 6021–6015.

(9) Kirakci, K.; Fejfarová, K.; Kučeráková, M.; Lang, K. Hexamolybdenum Cluster Complexes with Pyrene and Anthracene Carboxylates: Ultrabright Red Emitters with Antenna Effects. *Eur. J. Inorg. Chem.* **2014**, 2331–2336.

(10) Miklailov, M. A.; Brylev, K. A.; Virovets, A. V.; Galyamov, M. R.; Novozhilov, I.; Sokolov, M. N. Complexes of $\{Mo_6I_8\}$ with Nitrophenols: Synthesis and Luminescence. *New J. Chem.* **2016**, *40*, 1162–1168.

(11) Kirakci, K.; Kubát, P.; Kučeráková, M.; Šicha, V.; Gbelcová, H.; Lovecká, P.; Grznárová, P.; Ruml, T.; Lang, K. Water-Soluble Octahedral Molybdenum Cluster Compounds $Na_2[Mo_6I_8(N_3)_6]$ and $Na_2[Mo_6I_8(NCS)_6]$: Synthesis, Luminescence, and in vitro Studies. *Inorg. Chim. Acta* **2016**, *441*, 42–49.

(12) Riehl, M.; Ströbele, M.; Enselig, D.; Jüstel, T.; Meter, H.-J. Molecular Oxygen Modulated Luminescence of an Octahedral-Hexamolybdenum Iodide Cluster Having Six Apical Thiocyanate Ligands. *Zeit. Anorg. Allg. Chem.* **2016**, *642*, 403–408.

(13) Efremova, O. A.; Vorotnikov, Y. A.; Brylev, K. A.; Vorotnikova, N. A.; Novozhilov, I. N.; Kuratieva, N. V.; Edeleva, M. V.; Benoit, D. M.; Kitamura, N.; Mironov, Y. V.; Shestopalov, M. A.; Sutherland, A. J. Octahedral Molybdenum Cluster Complexes with Aromatic Sulfonate Ligands. *Dalton Trans.* **2016**, *45*, 15427–15435.

(14) Vorotnikov, Y. A.; Efremova, O. A.; Novozhilov, I. N.; Yanshole, V. V.; Kuratieva, N. V.; Brylev, K. A.; Kitamura, N.; Mironov, Y. V.; Shestopalov, M. A. Hexaazide Octahedral Molybdenum Cluster Complexes: Synthesis, Properties and the Evidence of Hydrolysis. *J. Mol. Struc.*, **2017**, *1134*, 237–243.

(15) Ramirez-Tagle, R.; Arratia-Pérez, R. Electronic Structure and Molecular Properties of the $[Mo_6X_8L_6]^{2-}$; X = Cl, Br, I; L = F, Cl, Br, I Clusters. *Chem. Phys. Lett*. **2008**, *460*, 438-441.

(16) Ramirez-Tagle, R.; Arratia-Pérez, R. The Luminescent $[Mo_6X_8(NCS)_6]^{2-}$ (X = Cl, Br, I) Clusters?: A Computational Study Based on Time-Dependent Density Functional Theory Including Spin-Orbit and Solvent-Polarity Effects. *Chem. Phys. Lett*. **2008**, *455*, 38-41.

(17) Ramirez-Tagle, R.; Arratia-Pérez, R. Pyridine as Axial Ligand on the $[Mo_6Cl_8]^{4+}$ Core Switches off

Luminescence. *Chem. Phys. Lett*. **2009**, *475*, 232-234.

(18)   Condon, E. U.; Shortley, G. H. *The Theory of Atomic Spectra*; Cambridge University Press: London, **1953**.

(19)   Montalti, M.; Credi, A.; Prodi, L.; Gandolfi, M. T. *Handbook of Photochemistry*, 3rd ed.; Taylor & Francis: Boca Raton, **2006**.

(20)   Crosby, G. A.; Hipps, K. W.; Elfring Jr, W. H. On the Appropriateness of Assigning Spin Labels to Excited States of Inorganic Complexes. *J. Am. Chem. Soc*. **1974**, *96*, 629-630.

(21)   Yersin, H.; Strasser, J. Triplets in Metal-Organic Compounds. Chemical Tunability of Relaxation Dynamics. *Coord. Chem. Rev*. **2000**, *208*, 331-364.

(22)   Preetz, W.; Harder, K. Synthesis, Structure and Properties of the Cluster Anions $[\{Mo_6Cl^i_8\}X^a_6]^{2-}$ with $X^a \equiv$ F, Cl, Br, I*. *J. Alloys Compds*. **1992**, *183*, 413-429.

(23)   Preetz, W.; Bublitz, D. Darstellung, Kristallstruktur und spektroskopische Eigenschaften der Clusteranionen $[\{Mo_6Br^i_8\}X^a_6]^{2-}$ mit X^a = F, Cl, Br, I. *Zeit. Anorg. Allg. Chem*. **1994**, *620*, 234-246.

(24)   Brückner, P.; Preetz, W.; Pünjer, M. Darstellung, Kristallstruktur, NMR-Schwingungsspektren und Normalkoordinatenanalyse der Clusteranionen $[\{Mo_6I^i_8\}X^a_6]^{2-}$, X^a = F, Cl, Br, I. *Zeit. Anorg. Allg. Chem*. **1997**, *623* 8-17.

(25)   Humbs, W.; Yersin, H. Characterization of the Lowest Excited States of $[Rh(bpy\text{-}h_8)_n(bpy\text{-}d_8)_{3-n}]^{3+}$ by Highly Resolved Emission and Excitation Spectra. *Inorg. Chem*. **1996**, *35*, 2220–2228.

(26)   Hager, G. D.; Crosby, G. A. Charge Transfer Excited States of Ruthenium(II) Complexes. I. Quantum Yield and Decay Measurement. *J. Am. Chem. Soc*. **1975**, *97*, 7031–7037.

(27)   Finkenzeller, W. J.; Yersin, H. Emission of Ir(ppy)$_3$. Temperature Dependence, Decay Dynamics, and Magnetic Field Properties. *Chem. Phys. Lett*. **2003**, *377*, 229–305.

(28)   Strasser, J.; Donges, D.; Humbs, W.; Kulikova, M. V.; Balashev, K. P.; Yersin, H. Dynamical Processes between Triplet Sublevels of Metal-Organic Pt(II) Compounds. *J. Luminescence* **1998**, *76–77*, 611–614.

(29)   Kitamura, N.; Kuwahara, Y.; Ueda, Y.; Itoh, Y.; Ishizaka, S.; Sasaki, Y.; Tsuge, K.; Akagi, S. Excited Triplet States of $[\{Mo_6Cl_8\}Cl_6]^{2-}$, $[\{W_6Cl_8\}Cl_6]^{2-}$, and $[\{Re_6S_8\}Cl_6]^{4-}$ Clusters. *Bull. Chem. Soc. Jpn*. **2017**, *90*, 1164–1173.

(30)   Kitamura, N.; Ueda, Y.; Ishizaka, S.; Yamada, K.; Aniya, M.; Sasaki, Y. Temperature Dependent Emission of Hexarhenium(III) Clusters $[Re_6S_8X_6]^{4-}$ (X = Cl$^-$, Br$^-$, and I$^-$): Analysis by Four Excited Triplet-State Sublevels. *Inorg. Chem*. **2005**, *44*, 6308–6313.

(31)   Gray, T. G. Divergent Electronic Structures of Isoelectronic Metalloclusters: Tungsten(II) Halides and Rhenium(III) Chalcogenide Halides. *Chem. Eur. J*. **2009**, *15*, 2581–2593.

(32)   Xu, L.; Sevov, S. C. Oxidative Coupling of Deltahedral $[Ge_9]^{4-}$ Zintl Ions. *J. Am. Chem. Soc*. **1999**, *121*, 9245–9246.

(33) Bergeron, D. E.; Castleman Jr., A. W.; Morisato, T.; Khanna, S. N. Formation of $Al_{13}I^-$: Evidence for the Superhalogen Character of Al_{13}. *Science* **2004**, *304*, 84–87.

(34) Negishi, Y.; Nobusada, K.; Tsukuda, T. Glutathione-protected Gold Clusters Revisited: Bridging the Gap between Gold(I)–thiolate Complexes ad Thiolate-protected Gold Nanocrystals. *J. Am. Chem. Soc.* **2005**, *127*, 5261–5270.

(35) Esenturk, E. N.; Fettinger, J.; Eichhorn, B. The Pb_{12}^{2-} and Pb_{10}^{2-} Zintl Ions and the $M@Pb_{12}^{2-}$ and $M@Pb_{10}^{2-}$ Cluster Series Where M = Ni, Pd, Pt. *J. Am. Chem. Soc.* **2006**, *128*, 9178–9186.

(36) Griffith, J. S. *The Theory of Transition Metal Ions*; Cambridge University Press: Cambridge, **1964**.

(37) Vrjamasu, V. V.; Bominaar, E. L.; Meyer, J.; Münck, E. Mössbauer Study of Reduced Rubredoxin As Purified and in Whole Cells. Structural Correlation Analysis of Spin Hamiltonian Parameters. *Inorg. Chem.* **2002**, *41*, 6358–6371.

(38) Koseki, S. Main Group Effective Nuclear Charge for Spin-orbit Calculations. *J. Chem. Phys.* **1995**, *99*, 12764–12772.

(39) Haynes, W. M. *CRC Handbook of Chemistry and Physics, 92nd ed.*; CRC Press: Boca Raton, **2011**.

(40) Chassot, L; von Zelewsky, A. Cyclometalated Complexes of Platinum(II): Homoleptic Compounds with Aromatic C, N Ligands. *Inorg. Chem.* **1987**, *26*, 2814–2818.

(41) Bossi, A.; Rauch, A. F.; Leitl, M. J.; Czerwieniec, R.; Whited, M. T.; Djurovich, P. I.; Yersin, H.; Thompson, M. E. Photophysical Properties of Cyclometalated Pt(II) Complexes: Counterintuitive Blue Shift in Emission with an Expanded Ligand π System. *Inorg. Chem.* **2013**, *52*, 12403–12415.

(42) Clementi, E.; Raimonde, D. L.; Reinhardt, W. P. Atomic Screening Constants from SCF Functions. II. Atom with 37 to 86 Electrons. *J. Chem. Phys.* **1967**, *47*, 1300–1307.

(43) Maestri, M.; Sandrini, D.; Balzani, V.; Chassot, L.; Jolliet, P.; von Zelewsky, A. Luminescence of Ortho-metallated Platinum(II) Complexes. *Chem. Phys. Lett.* **1985**, *122*, 375–379.

Chapter 6

General Conclusions

6-1. General Conclusions

In the present study, thirty-four octahedral hexamolybdenum(II) clusters including twenty-one new and novel clusters were synthesized, and the X-ray structural, redox, spectroscopic, and photophysical properties of these hexamolybdenum(II) clusters at ambient temperature were described in detail. Among these thirty-four clusters, furthermore, the temperature (T)-dependences of the emission characteristics of the seventeen $[\{Mo_6X_8\}Y_6]^{2-}$ or $[\{Mo_6X_8\}L_6]^{2-}$ clusters having a series of the bridging (X = Cl, Br, or I) or terminal ligands (Y = Cl, Br, or I; L = carboxylate) were investigated in the T range of 3 K < T < 300 K. The analysis of the T-dependent emission data of these clusters were successful by the four spin-sublevel (Φ_n) model and this provided the factors determining zero-magnetic-field splitting (zfs) in the lowest-energy excited triplet (T_1) state of the cluster.

Zfs in the T_1 state of a transition metal complex is responsible for spin-orbit coupling (SOC) and the strength of SOC is determined by nature of the atoms composed of a molecule. Furthermore, it has been demonstrated that the emission lifetime of a transition metal complex correlates with the relevant zfs energy in the T_1 state. These results indicate that the emission characteristics of a transition metal would be controlled by the relevant zfs energy in the T_1 state and, thus, nature of the constituting atoms of the complex, though a quantitative discussion on such a relationship has not been hitherto reported. Besides the interpretation of the emission characteristics of a transition metal complex, various guidelines on design of phosphorescent transition metal complexes have been hitherto reported toward development of further bright luminescent materials. Unfortunately, however, these are phenomenological results predicted from the relationship between the molecular structures and their properties. Different from these studies, the investigation on zfs in the T_1 state of a transition metal complex enables one to provide deep insight into the origin of the emission characteristics of a transition metal complex and, therefore, is worth investigating in detail. These research back grounds and the experimental procedures including the synthesis of the cluster samples were described in Chapters 1 and 2, respectively. The principal experimental results and conclusions are as follows.

In Chapter 3, the redox, spectroscopic, and photophysical properties of the terminal halide clusters $[\{Mo_6X_8\}Y_6]^{2-}$ (X, Y = Cl, Br, or I) in solution and/or crystalline phases at ambient temperature were described. The redox, spectroscopic and photophysical properties of these clusters depended highly on nature of the bridging (X) and terminal halide ligands (Y). As an example, the redox potential difference of the complex, (E_{ox}–E_{red}), for given X and Y decreased in the sequence X, Y = Cl > Br > I. Therefore, the stronger π-electron donating ability of X/Y gives rises to a larger (HOMO – LUMO) energy gap, resulting in the X/Y dependence of the lowest-energy absorption band. The X/Y dependences of the emission properties, on the other hand, could not be explained by the π-electron donating ability of X/Y alone. In particular, the emission maximum energy ($\tilde{\nu}_{em}$) showed a higher- or lower-energy shift for an X (for given Y) or Y variation (for given X), respectively, which was then discussed based on the zfs energies in the T_1 states of the clusters. The investigations of the T-

dependent emissions and their analysis by the four-spin-sublevel (Φ_n) model revealed that the zfs energies in the T_1 states (ΔE_{13} and ΔE_{14} values) increased in the sequences X = Cl < Br < I and Y = I < Br < Cl for given Y and X, respectively. The larger ΔE_{14} value for a given X or Y series gave rise to the smaller contribution of the emission from the highest-energy spin-sublevels (Φ_4) to the observed emission spectrum at 300 K with the sequence of Φ_4% being X = Cl > Br > I or Y = I > Br > Cl for given X or Y, respectively. The results demonstrate that the larger zfs energy in the T_1 state of the cluster leads to a higher-energy emission. Furthermore, the emission lifetime (τ_{em}) and the emission quantum yield (Φ_{em}) of the cluster with a given X were shown to be controlled synthetically by the $\tilde{v}_{em}$ value through the energy gap ($\tilde{v}_{em}$) dependence of the nonradiative rate constant (k_{nr}) and, thus, this explained the zfs energy dependences of Φ_{em} and τ_{em}.

Chapter 4 described the X-ray structural, redox, spectroscopic, and photophysical properties of the terminal carboxylate clusters $[\{Mo_6X_8\}L_6]^{2-}$ (X = Br or I, L = carboxylate) in solution and/or crystalline phases at ambient temperature. These clusters showed the large terminal carboxylate dependences of the X-ray structural, redox, and several photophysical properties: d_{Mo-O} (bond length between the ligating O atom in the carboxylate and the Mo atom), E_{ox}, E_{red}, $\tilde{v}_{em}$, τ_{em}, and Φ_{em}, irrespective of X. For example, the smaller is the acid dissociation constant of a carboxylate ($pK_a(L)$) value and, thus, the weaker is the σ-donating ability of a carboxylate, the higher are $\tilde{v}_{em}$ and Φ_{em} and the longer is τ_{em} of the cluster, leading to a long-lived and bright higher-energy emission. Furthermore, the k_{nr} value of the cluster showed a clear and linear correlation with $\tilde{v}_{em}$ for a given bridging ligand (X). The results demonstrate that the k_{nr} value is also governed by $pK_a(L)$, resulting in almost linear $pK_a(L)$ dependences of Φ_{em} and τ_{em}. However, the terminal ligand dependence of $\tilde{v}_{em}$ could not be explained by the σ-donating ability of the terminal carboxylate alone similar to that of $[\{Mo_6X_8\}Y_6]^{2-}$, indicating that the *T*-dependent emission characteristics should be considered to explain the terminal ligand dependence of $\tilde{v}_{em}$. Through the analysis of the *T*-dependent emission characteristics, the zfs energies in the T_1 states were found to increase in the sequences X = Cl < Br < I and L = 3,5-dinitrobenzoate < 4-nitrobenzoate < 4-cyanobenzoate < 3,5-dimethoxybenzoate < benzoate < 4-methoxybenzoate for a given L and X, respectively. Similar to $[\{Mo_6X_8\}Y_6]^{2-}$, the larger is the ΔE_{14} value, the smaller is the contribution of the emission from the highest-energy spin sublevels (Φ_4) to the observed emission spectrum at 300 K with the sequence of Φ_4% being X = Cl > Br > I and L = 3,5-dinitrobenzoate > 4-nitrobenzoate > 4-cyanobenzoate > 3,5-dimethoxybenzoate > benzoate > 4-methoxybenzoate for a given L and X, respectively. In the case of the clusters for a given X, the emission maximum energy of Φ_4 ($\tilde{v}_4$) was insensitive to nature of the terminal carboxylate ligand, while the $\tilde{v}_{em}$ value was dependent on L. Since $\tilde{v}_4$ is the highest energy emission among $\tilde{v}_n$ (n = 1–4), the higher energy emission at ambient temperature is accompanied by a larger Φ_4%. For a given X, the weak σ-donation from the terminal carboxylate thus gives rise to a high-energy emission, resulting in the $pK_a(L)$ dependence of Φ_{em} or τ_{em} through the energy gap dependence of k_{nr}.

To elucidate the factors governing the zfs energies in the T_1 states of the octahedral hexamolybdenum(II)

clusters, Chapter 5 discussed the zfs energies of a series of $[\{Mo_6X_8\}Y_6]^{2-}$ and $[\{Mo_6X_8\}L_6]^{2-}$ described in Chapters 3 and 4 in special references to the electronic structures of the targeted clusters: the ^{95}Mo NMR chemical shift of the cluster or $pK_a(L)$. Furthermore, to pursue tuning of the emission characteristics based on the zfs energy in the T_1 state, implications of the zfs energies of the octahedral hexamolybdenum(II) clusters and platinum(II) complexes to their phosphorescence properties were discussed. The zfs energies of $[\{Mo_6X_8\}Y_6]^{2-}$ or $[\{Mo_6X_8\}L_6]^{2-}$ were dependent on the ^{95}Mo NMR chemical shift of the cluster or $pK_a(L)$, respectively, which demonstrated that the d-electron density on the Mo atom(s) primarily determined the zfs energies. Furthermore, it is worth emphasizing that the zfs energies of the mononuclear platinum(II) complexes have been shown to be explained satisfactorily by the similar context to that of the octahedral hexamolybdenum(II) clusters and, thus, by the ^{195}Pt NMR chemical shift of the complex. These results demonstrate clearly that one of the factors governing the zfs energy(ies) of a transition metal complex is the electron density on the metal atom(s). The higher d-electron density on the Mo atom(s) in $[\{Mo_6X_8\}Y_6]^{2-}$ accompanied the long-lived and bright higher-energy emission as described above, while that in $[\{Mo_6X_8\}L_6]^{2-}$ gave poor luminescence. However, the opposite trend seen in the effects of the d-electron density on the emission properties of $[\{Mo_6X_8\}Y_6]^{2-}$ and $[\{Mo_6X_8\}L_6]^{2-}$ were demonstrated to be explained satisfactorily by the different contribution percentages of the Φ_n emissions to the observed emission. Among several photophysical properties of the platinum(II) complex, importantly, the radiative rate constant (k_r) of the platinum(II) complex showed a good correlation with the relevant zfs energy though the zfs energy was not the decisive factor of other emission properties ($\tilde{\nu}_{em}$, τ_{em}, and Φ_{em}). The zfs energy dependence of the k_r value of the platinum(II) complex is responsible essentially for both the almost equal contributions of the spin-sublevels to the observed emission and strong SOC induced by the high d-electron density on the platinum atom. These findings demonstrate clearly that the effective nuclear charge(s) on the metal atom(s) in a transition metal complex is one of the decisive factors of its zfs energy(ies) and photophysical properties of the complex

6-2.   Future Perspective

The present study has revealed that the effective nuclear charge(s) on the metal atom(s) in a transition metal complex governs the zfs energy and photophysical properties in the T_1 state of the complex and that these properties can be controlled synthetically by tuning the effective nuclear charge on the metal atom(s). Since the effective nuclear charges on a metal can be determined by NMR spectroscopy on the relevant metal nucleus or conventional DFT calculations as demonstrated in Chapter 5, the present findings indicate that the phosphorescence properties of a transition metal complex would be predicted by the conventional DFT calculations or NMR spectroscopy. Some groups have reported that the relativistic DFT calculations based on Amsterdam Density Functional (ADF) software are very powerful to evaluate the phosphorescent lifetimes of transition metal complexes.[1–2] However, the calculations require relatively long time and special techniques on

the software as well as on knowledge on photophysics. Furthermore, these calculations assist only phenomenological interpretations on a phosphorescence process based on the relationship between the molecular structures and the emission properties, since one can extract only the targeted properties from the calculation results without any knowledge on the important and decisive factors determining the properties. On the other hand, the experimental approaches and analytical methods demonstrated in the present thesis can provide deeper insights into the origin of the luminescence from a transition metal complex based on the elucidation of the decisive factor of the luminescence properties through the effective nuclear charge(s) on a metal atom(s), facile DFT calculations, and NMR spectroscopy. The author convinces that the present study will offer a novel guideline for developments of luminescent materials in near future.

6-3.   References

(1)   Mori, K.; Goumans, T. P. M.; van Lenthe, E.; Wang, F. Predicting Phosphorescent Lifetimes and Zero-Field Splitting of Organometallic Complexes with Time-Dependent Density Functional Theory Including Spin-Orbit Coupling. *Phys. Chem. Chem. Phys.* **2014**, *16*, 14523–14530

(2)   Li, E. Y.-T.; Jiang, T.-Y.; Chi, Y.; Chou, P.-T. Semi-quantitative Assessment of the Intersystem Crossing Rate: An Extension of the El-Sayed Rule to the Emissive Transition Metal Complexes. *Phys. Chem. Chem. Phys.* **2014**, *16*, 26184–26192.

Acknowledgement

The studies presented in the thesis were carried out under the supervise of Prof. Noboru Kitamura at the department of chemical sciences and engineering, graduate school of chemical sciences and engineering, analytical chemistry laboratory, Hokkaido University during April 2013 to March 2019.

First and foremost, the author would like to express the greatest profound appreciation to Professor Noboru Kitamura (Hokkaido University) for the best research environment along with his continuous and warm encouragements, kind guidance, and valuable comments throughout the work. The author is grateful deeply to Associate Professor Eri Sakuda (Nagasaki University), Lecture Akitaka Ito (Kochi University of Technology), Assistant Professor Sho Fujii (Hokkaido University), and Associate Professor Atsushi Miura (Hokkaido University) for their numerous discussions and devoted attitude to education. The author would like to express greatest appreciation to Dr. Konstantin Brylev (Nikolaev Institute of Inorganic Chemistry) for supervision and warm hospitality during visiting their research group, and valuable discussions of the sample preparations. The author acknowledgements gratefully to Professor Masako Kato, Associate Professor Atsushi Kobayashi, and Assistant Professor Masaki Yoshida (all Hokkaido University) for their kind help to NMR and single crystal X-ray measurements. The author would like to express gratitude to Professor Yukio Hinatsu (Hokkaido University) for the sample preparations. The author is deeply grateful to Professor Masako Kato, Professor Tetsuya Taketsugu, and Professor Yasuchika Hasegawa (all Hokkaido University) for reviewing the thesis. Last but not least, the author expresses special thanks to my parents, Hiromori Akagi and Ikuko Akagi.

March 2019,
Soichiro Akagi

Publication List

Related publications for this thesis

(1) **Akagi, S.**; Fujii, S.; Horiguchi, T.; Kitamura, N. pK_a(L) Dependences of Structural, Electrochemical, and Photophysical Properties of Octahedral Hexamolybdenum(II) Clusters: [Mo$_6$X$_8$L$_6$]$^{2-}$ (X = Br or I; L = Carboxylate). *J. Clust. Sci.* **2017**, *28*, 757–772.

(2) **Akagi, S.**; Fujii, S.; Kitamura, N. Zero-Magnetic-Field Splitting in the Excited Triplet States of [{Mo$_6$X$_8$}(n-C$_3$F$_7$COO)$_6$]$^{2-}$ (X = Cl, Br, or I). *J. Phys. Chem. A* **2017**, *121*, 7148–7156.

(3) **Akagi, S.**; Fujii, S.; Kitamura, N. A Study on the Redox, Spectroscopic, and Photophysical Characteristics of a Series of Octahedral Hexamolybdenum (II) Clusters: [{Mo$_6$X$_8$}Y$_6$]$^{2-}$ (X, Y = Cl, Br, or I). *Dalton Trans.* **2018**, *47*, 1131–1139.

(4) **Akagi, S.**; Fujii, S.; Kitamura, N. Zero-Magnetic-Field Splitting in the Excited Triplet States of Octahedral Hexanuclear Molybdenum(II) Clusters: [{Mo$_6$X$_8$}Y$_6$]$^{2-}$ (X, Y = Cl, Br, I). *J. Phys. Chem. A* **2018**, *122*, 9014–9024.

(5) **Akagi, S.**; Horiguchi, T.; Fujii, S.; Kitamura, N. Terminal Ligand (L) Effects on Zero-Magnetic-Field Splitting in the Emissive Excited Triplet State of [{Mo$_6$Br$_8$}L$_6$]$^{2-}$ (L = Aromatic Carboxylates). *Inorg. Chem.* **2019**, *51*, 703–714.

(6) **Akagi, S.**; Fujii, S.; Kitamura, N. Prediction of Zero-Magnetic-Field Splitting in the Excited Triplet States and Phosphorescence Properties of Emissive Platinum Complexes Based on [195]Pt NMR and DFT Calculations. *To be Submitted.*

Other Publications

(1) Shimada, K.; Kobayashi, A.; Ono, Y.; Ohara, H.; Hasegawa, T.; Taketsugu, T.; Sakuda, E.; **Akagi, S.**; Kitamura, N.; Kato, M. Core-structure-dependent Luminescence of Thiolato-bridged Copper(I) Cluster Complexes. *J. Phys. Chem. C* **2016**, *120*, 16002–16011.

(2) Fujii, S.; Horiguchi, T.; **Akagi, S.**; Kitamura, N. Quasi-One-Step, Six-Electron Electrochemical Reduction of an Octahedral Hexanuclear Molybdenum(II) Cluster. *Inorg. Chem.* **2017**, *55*, 10259–10266.

(3) Mikhailov, M. A.; Brylev, K. A.; Abramov, P. A.; Sakuda, E.; **Akagi, S.**; Ito, A.; Kitamura, N.; Sokolov, M. N. Synthetic Tuning of Redox, Spectroscopic, and Photophysical Properties of {Mo$_6$I$_8$}$^{4+}$ Core Cluster Complexes by Terminal Carboxylate Ligands. *Inorg. Chem.* **2017**, *55*, 8437–8445.

(4) Kitamura, N.; Kuwahara, Y.; Ueda, Y.; Ito, Y.; Ishizaka, S.; Sasaki, Y.; Tsuge, K.; **Akagi, S.** Excited Triplet States of [{Mo$_6$Cl$_8$}Cl$_6$]$^{2-}$, [{Re$_6$S$_8$}Cl$_6$]$^{4-}$, and [{W$_6$Cl$_8$}Cl$_6$]$^{2-}$ Clusters. *Bull. Chem. Soc. Jpn.* **2017**, *90*, 1164–1173.

Appendix

Table A-1. Cartesian coordinates of the optimized structure of **1Pt** in the excited triplet state. The coordinates of the hydrogen atoms in the complex were omitted.

Atom	Cartesian coordinate		
C	1.65417	1.29259	0.00028
C	2.91087	0.69290	0.00047
C	1.61234	2.71423	0.00029
C	2.90560	–0.73136	0.00045
C	4.13886	1.41471	0.00067
C	2.79489	3.45669	0.00048
C	4.13105	–1.47028	0.00063
C	5.32358	0.70875	0.00084
C	4.03543	2.84457	0.00067
C	4.01261	–2.89957	0.00059
C	5.30497	–0.74387	0.00082
C	1.61065	–2.68188	0.00022
C	2.74451	–3.46740	0.00039
C	–2.57789	–1.25115	–0.00042
C	–2.53644	1.25441	–0.00038
C	–3.18216	0.01547	–0.00050
Pt	0.15987	0.01232	0.00003
O	–1.32989	-1.46681	–0.00023
O	–1.27754	1.44865	–0.00018
N	1.70571	-1.30712	0.00025
C	–3.33450	2.56739	–0.00049
C	–3.42517	-2.53311	–0.00058
C	–4.85188	2.37052	–0.00073
C	–2.93323	3.35786	–1.25651
C	–2.93362	3.35783	1.25568
C	–4.93456	–2.28240	–0.00083
C	–3.05068	–3.33687	–1.25627
C	–3.05110	–3.33689	1.25523

Table A-2. Cartesian coordinates of the optimized structure of **2Pt** in the excited triplet state. The coordinates of the hydrogen atoms in the complex were omitted.

Atom	Cartesian coordinate		
C	1.06431	–1.32936	–0.00010
C	2.38882	–0.65775	–0.00010
C	2.40829	0.72312	–0.00003
C	3.53808	1.58242	-0.00001
C	3.36309	2.93601	0.00006
C	0.97588	2.60059	0.00011
C	2.05512	3.46590	0.00012
C	–3.13229	1.22462	0.00016
C	–3.09358	–1.28010	0.00001
C	–3.73832	–0.03899	0.00010
Pt	–0.39983	–0.05186	0.00001
O	–1.88755	1.45504	0.00014
O	–1.84181	–1.49483	–0.00004
N	1.12108	1.27792	0.00003
C	–3.92208	–2.53635	–0.00004
C	–4.00345	2.45259	0.00026
S	3.69996	–1.79263	–0.00019
C	2.52502	–3.14129	–0.00023
C	1.21512	–2.71043	–0.00017

Table A-3. Cartesian coordinates of the optimized structure of **3Pt** in the excited triplet state. The coordinates of the hydrogen atoms in the complex were omitted.

Atom	Cartesian coordinate		
C	–1.37802	–1.03379	0.00000
C	–0.83385	–2.41678	0.00000
C	–2.76129	–0.85604	0.00000
C	0.54867	–2.51019	0.00000
C	–3.61768	–1.93745	0.00000
C	–3.08850	–3.27150	0.00000
C	2.69461	–3.62799	0.00000
C	2.53988	–1.21605	0.00000
C	3.32265	–2.35412	0.00000
C	1.45995	2.98410	0.00000
C	–1.04084	3.11648	0.00000
C	0.24087	3.67567	0.00000
Pt	0.00000	0.33081	0.00000
O	1.60398	1.72668	0.00000
O	–1.33943	1.88198	0.00000
N	1.20954	–1.26251	0.00000
C	1.33628	–3.69823	0.00000
C	–1.75392	–3.51740	0.00000
C	–2.23758	4.02900	0.00000
C	2.74454	3.76942	0.00000

Table A-4. Cartesian coordinates of the optimized structure of **4Pt** in the excited triplet state. The coordinates of the hydrogen atoms in the complex were omitted.

Atom	Cartesian coordinate		
C	1.01347	–1.26808	0.65096
C	2.34306	–0.94531	0.72288
C	2.90205	0.10822	–0.09388
C	4.23535	0.52541	–0.08603
C	4.63089	1.55207	–0.91835
C	2.39485	1.69539	–1.71497
C	3.69620	2.15681	–1.75242
N	2.00207	0.70290	–0.91291
S	3.21491	–1.92598	1.87399
C	1.76396	–2.77433	2.25751
C	0.69177	–2.32881	1.54477
Pt	–0.05283	–0.12967	–0.77220
N	–1.05444	1.25718	0.66428
C	–2.38506	1.02421	0.75285
C	–1.21326	3.02881	2.24136
C	–3.17418	1.80862	1.60195
C	–2.58605	2.80986	2.34406
C	–1.96559	–0.74402	–0.89212
C	–2.84405	–0.05696	–0.07869
C	–2.64395	–1.79472	–1.58654
S	–4.47537	–0.66234	–0.17223
C	–3.97254	–1.86245	–1.30579
C	–0.48904	2.22366	1.38650

Table A-5. Cartesian coordinates of the optimized structure of **5Pt** in the excited triplet state. The coordinates of the hydrogen atoms in the complex were omitted.

Atom	Cartesian coordinate		
C	2.32149	–1.16634	0.76319
C	0.36242	–2.28244	1.36709
C	2.87806	–0.07805	-0.04634
C	1.03579	–3.14397	2.20607
C	2.41639	–3.00117	2.31698
C	4.71346	1.30223	–0.78658
C	2.48409	1.69501	–1.61974
C	3.82926	2.02252	–1.58866
C	4.23523	0.25921	–0.01728
C	3.05688	–2.01407	1.59801
Pt	0.03859	0.08079	–0.73684
C	–0.94853	1.28044	0.69867
N	–2.04693	–0.60742	–0.87068
C	–2.33308	1.07075	0.80392
C	–0.36537	2.25829	1.49983
C	–2.91634	0.02450	–0.05377
C	–2.47541	–1.57530	–1.68689
C	–3.10283	1.83231	1.68908
C	–1.13089	3.01010	2.38116
C	–4.26550	–0.33684	–0.06474
C	–3.79458	–1.97726	–1.73976
C	–2.50337	2.79903	2.47639
C	–4.70519	–1.33717	–0.90792
C	1.97049	0.63313	–0.86352
N	0.98603	–1.33279	0.66788